Slamming of High Speed Craft: A Parametric Study of Severe Cases

Robert J Van Erem

Thesis submitted to the Faculty of the

Virginia Polytechnic Institute and State University

in partial fulfillment of the requirements for the degree of

Masters of Science

in

Ocean Engineering

Christine Gilbert, Chair

Stefano Brizzolara

Craig Woolsey

Nathan Alexander

April 23rd, 2024

Blacksburg, Virginia

Keywords: Slamming, Planing Vessels, Controlled Motion

Slamming of High Speed Craft: A Parametric Study of Severe Cases

Robert J Van Erem

(ABSTRACT)

High-speed planing craft slamming into waves can cause structural damage to the vessel as well as hinder or injure personnel onboard. As a result, it is one of the primary constraints that limit the operating envelope of high-speed surface vessels. The controlled motion experiments presented in this thesis were designed to be an intermediate step between vertical water entry tests of a wedge and a traditional tow tank experiment of a planning hullform in waves. This allowed a deeper study of the hydrodynamic loads that occur during slamming. A planing hull model was subjected to controlled motions in the vertical plane to replicate the types of slamming motions that a vessel may experience in the ocean. The slamming events investigated were chosen based on towing tank experiments previously conducted at the U.S. Naval Academy. Hydrodynamic forces were measured globally and also at particular locations near the bow. The vertical motions were programmed into a pair of linear actuators that were rigidly mounted to the towing carriage. The towing carriage prescribed the horizontal motion. Each actuator was independently controlled and capable of moving at 1.3 m/s and 15 m/s^2. Pressure sensors were used to measure the pressure time history at discrete points on the model. Force sensors mounted beneath the actuators were used to compute the overall slamming load and moments induced by the slam event. A combination of other sensors were used to verify the accuracy of the prescribed motion profile. The results suggested that total impact velocity is correlated with the load growth rate. In addition, the velocity normal to the keel was found to be most impactful on the magnitude of the peak force.

Slamming of High Speed Craft: A Parametric Study of Severe Cases

Robert J Van Erem

(GENERAL AUDIENCE ABSTRACT)

The goal of this thesis was to understand the effect of high-speed boats impacting waves. These wave slamming events can harm the boat and make people sea sick onboard. Consequently, the top speed at which these high-speed boats can operate safely is often limited by these wave impacts. The approach taken for this study involved using a model boat that had similar features to high-speed boats seen in the real world. The model underwent specific movements to replicate the impact that occurs when a real boat encounters waves at sea. This method sought to identify important parameters that determine the severity of the slam event. A Vertical Planar Motion Mechanism simulated the slamming motion, allowing the model boat to move at high speeds relative to its size. A variety of sensors located throughout the model collected data on the slam event. The combination of these sensors helped paint a picture of what is occurring during the entire slam event. This study focused on the dynamics that are measured by the sensors. This included the pressure at important locations, the force on the whole model, and the way that the model moves. The Office of Naval Research provided both financial and intellectual support that makes this research possible. Beyond the ONR, many other academic, commercial, and military groups had given their support for this work.

Dedication

To all my friends and family; thank you for always being by my side.

Acknowledgments

I would like to first thank my parents for giving me every opportunity to succeed with this project. They were supportive every day no matter what happened. This was only possible because of their gentle push and massive safety net.

I also couldn't haven't done this without my close friends. They kept me going when things were good and made me laugh when things were not.

I want to thank all those part of the Hydroelasticity lab group that helped me through the many challenging problems. Special thanks to everyone involved with the seaplane project that greatly propelled the lab forward.

I would like to thank Dr. Gilbert and all the members of my committee for being attentive and motivating. Your incredible expertise helped me expand what I thought was possible.

To the Office of Naval Research, thank you for the support and funding of Grant N00014-20-1-225.

Contents

List of Figures

List of Tables

List of Abbreviations

ϕ	Sum of Running Trim and Wave Impact Angle
ρ	Density of water
τ	Running Trim Angle
θ	Wave Impact Angle
A0	Linear Actuator 0 Force (reactionary)
A1	Linear Actuator 1 Force (reactionary)
C	Towing Carriage Force (reactionary)
CAD	Computer Aided Design
G	Force of Gravity
g	Acceleration of Gravity
GPPH	Generic Prismatic Planing Hull
LCG	Longitudinal Center of Gravity
M	Moment induced by Force
N	Normal Force
S	Slamming Force
S_w	Wetted Surface Area

USNA United States Naval Academy

V Total Impact Velocity

V_H Heave Velocity

V_S Surge Velocity

$V_{Z'}$ Velocity in the Z' direction

VPMM Vertical Planar Motion Mechanism

Chapter 1

Introduction

The effects of slamming continue to be one of the primary constraints on the operating envelope of high-speed planing craft. Slamming between the hull body and the free surface occurs when the high-speed vessel encountering waves emerges from the surface and then re-enters. Frequent slamming events cause structural damage to the vessel, damage instrumentation on board, and increase the risk of injury and seasickness among the crew. Most classification societies have little to no regard for hydroelasticity in their current design criteria for high-speed craft. This leads to designs that are overly conservative in their structural thickness to handle slamming and therefore have a heavier weight. Further understanding of the physics of slamming events and the hydroelasticity of the hull can allow for designs that are lighter in weight, mitigate the severity of slamming events, and increase the operation envelope.

1.1 Major Stakeholders of the Slamming Problem

Planing hullforms take advantage of hydrodynamic forces to allow the vessel to sustain higher speeds. The rise in popularity of planing hull boats has made this slamming problem increasingly relevant to government, private, and commercial stakeholders that need to have high-speed vessels. The coast guard is one such stakeholder that uses these planing vessels regularly in situations where time is limited and high-speed is necessary. Imagine the scenario of a coast guard vessel that receives a call to rescue passengers onboard a sinking boat in a

storm. In this life saving mission, the time it takes to make it to the sinking boat will be critical. The coast guard cannot afford to delay their arrival to be successful. However, the current overly conservative slamming models used in design result in reduced top speed. As a result, these current models can directly limit mission success.

The slamming problem is something that recreational high-speed boat owners face often. Repeated wave slamming causes frequent acceleration spikes that will make passengers uncomfortable and possibly sea sick. This forces the owner to either significantly reduce their speed or turn home and end the day on the water. The scenario reduces the value of the vessel for the customer and the reputation of the boat maker.

The slamming problem also extends to the world of autonomy, with the recently increasing desire for unmanned high-speed vessels. The autonomous vessels rely on control systems that are reactive since models to predict the ship dynamics of these slam events are limited. Further understanding of the physics behind the slamming problem can allow for better models to be developed and faster reacting feed forward controls to be implemented. These are just a small set of examples of the many scenarios that are severely impacted by wave slamming events.

The Office of Naval Research has made it a priority to develop better models to predict the effects of wave slamming events, particularly on high-speed planing hullforms. This research is a small part of the ONR slamming research project being carried out by multiple naval offices and universities across the country. Being a part of such a large and organized effort has provided this novel research with the necessary resources and foundation to further the understanding of these slamming events from a new perspective.

1.2 Approach

Slamming tests performed at the Virginia Tech Impact Basin will utilize a deterministic approach to increase the understanding of slamming events. Utilizing a dynamic model that sets the water surface as the reference point, the relative surge, heave, and pitch of the boat can be calculated for a particular type of slam. These relative motion parameters applied to the vessel slamming into calm water simulate an equivalent slam of a moving vessel into a traveling wave. This relative dynamics model allows for equivalent physical data to be collected on the slamming event without the use of a wavemaker. Currently, the Virginia Tech Advanced Towing Facility is equipped with a carriage that allows for controlled surge motion on an attached model. The Vertical Planar Motion Mechanism (VPMM), which is attached to the carriage, will allow for simultaneous control of surge, heave, and pitch motion of an attached model. This thesis pertains to surface models; however, the VPMM is capable of subsurface model control as well. The control of these key motion parameters will allow for more complexity to be incorporated into the dynamics involved in slamming events compared to the traditional wedge drop experiments. The data collected during this study will be used to determine key motion parameters in slamming events and the severity of their effects.

1.3 Thesis Overview

The introduction of these thesis includes a discussion on who is impacted by the slamming problem and an approach to further understand it. This discussion was just presented here in Chapter 1. Chapter 2 contains a literature review on relevant background information collected in previous research. The next chapter, Chapter 3, goes over the dynamic theory

and equations used to develop the novel test method. Chapter 4 discusses the experimental setup of the towing tank carriage, vertical planar motion mechanism, data acquisition system, and generic prismatic planing hull model. All the systems and associated equipment are reviewed in detail. Chapter 5 presents the collected data and a discussion of the results. Also included in that chapter are the limitations of the system that were discovered through testing. Chapter 6 contains the conclusions drawn from the collected data and suggestions for future work to move this research forward.

Chapter 2

Literature Review

The broad impact and complexity of the wave slamming problem have led to many researchers attempting to gain a better understanding. The following chapter will dive into the past research that laid the groundwork for the work presented in this thesis.

2.1 Early Work Using Momentum Theory

2.1.1 The von Karman Approach

Early research to study the water entry of seaplanes laid the groundwork for studying planing hull vessels slamming into waves. von Karman (1929) utilized momentum theory to devise a method for estimating the peak pressure during water entry [1]. The von Karman method was applied to a horizontal cylindrical body with a wedge shaped submerged section as it struck a horizontal surface of water. The added mass applied to the wedge as it enters the water is approximated as half the mass of fluid contained in a cylinder with a diameter equal to the width of the wedge. von Karman assumed the effect of air suction as the wedge enters the water to be negligible, thereby halving the overall mass by discounting the added mass. After a mathematical derivation using momentum theory, von Karman arrived at the conclusion that the average pressure seen on the wedge is equal to

$$p = \frac{P}{2x} = \frac{\rho \mathrm{v}_0^2}{2} \frac{\pi \cot(\alpha)}{\left(\frac{\gamma \pi \mathrm{x}^2}{2W} + 1\right)^3},$$

where P is the force of impact, x is the width of the wedge, g is the acceleration of gravity, ρ is the density of water, v_0 is the velocity at the moment of first contact, α is the deadrise angle, $\gamma = \rho \mathrm{g}$, and W is the weight of the body per unit length. The term $\frac{pv_0^2}{2}$ represents the dynamic pressure corresponding to the impact velocity, and the term $\pi \cot(\alpha)$ is the theoretical factor of increase. This average pressure formula implies that the maximum pressure occurs along the centerline of the wedge, where the width approaches zero. The formula for the maximum pressure on the plate is

$$p_{\max} = \frac{\rho \mathrm{v}_0^3}{2} \pi \cot(\alpha).$$

This method assumed a horizontal water surface, or calm water. von Karman predicted that the waves may cause pressure of the same order as the results calculated using this pressure formula. In the conclusion of the 1929 paper, von Karman suggested future research on the variation of the pressure with time and the variation of the pressure over the length of the wedge would be of importance. This thesis work will cover both of these topics in the results and discussion contained in Chapter 5.

2.1.2 The Wagner Method

Soon after von Karman derived these equations, the theory was applied to the landing of seaplanes in rough sea conditions. The report "Landing of Seaplanes" written by Wagner (1932) discussed the theoretical and practical aspects of seaplanes landing on water [2]. Wagner noted that significant forces occur in the early moments of the slam event. When the keel of a seaplane touches the water surface, it experiences an initial impact force. This impact force is a function of the velocity profile, the angle of impact, and the properties of the

water surface. After the initial impact, hydrodynamic forces become more prominent. These hydrodynamic forces are also functions of the velocity of the seaplane as it moves through the water. At the end of the report, Wagner emphasizes the importance of understanding the slamming forces to ensure the safe design and use of seaplanes operating in harsh sea states.

2.1.3 The Vorus Method

Vorus (1996) improved upon the early theories to predict the hydrodynamic effects during slamming events by incorporating computation [3]. Vorus sought to find the balance between direct numerical simulation of complex governing equations and the asymptotic theories developed by Wagner (1932) [2]. Unlike asymptotic methods, this method produced one solution space due to the governing analytical equations. Vorus's theory assumed uniform first-order geometric linearity, in line with Wagner's asymptotic theory. In addition, the theory incorporated the hydrodynamic nonlinearity and transverse flow perturbations found in the governing equations. This meant that as objects became flatter and approached geometric linearity, their transverse velocity increased. Linear asymptotic theories did not previously account for this phenomenon. The theory allowed for numerical simulations that were both stable and computationally feasible. In his 1996 paper, Vorus applied this theory to the study of a flat-cylinder impacting water. This work demonstrated the evolution of early theories to incorporate modern analytical and numerical techniques. This evolution has further progressed today with the inclusion of computational fluid dynamic simulations that continue to develop and improve. These computational methods provide an alternative to physical experiments and provide new insights into slamming phenomena.

Wagner's and Vorus's findings can be applied to planing craft because of the close similarity

in geometry and wave interaction to seaplanes. The Wagner and Vorus methods can be used to predict the hydrodynamic effects on an infinitesimally thin slice of the boat's transverse cross section. In this model, only the downward motion of the vessel is considered. The hydrodynamic effect on the whole hullform can later be calculating with the use of 2D + t theory or strip theory.

2.2 Findings From Towing Tank Testing

2.2.1 Early Parametric Study on Planing Hulls

In later years, surface vessels would develop the planing hullform to more efficiently achieve high speeds by utilizing hydrodynamic effects. While this planing hullform performed exceptionally in calm water, Fridsma (1969) noticed that this hullform often had reduced performance in rough sea states [4]. Fridsma sought to identify what hullform parameters led to the reduction in performance through a series of towing tank tests on planing hull models. The models were towed through calm water, regular waves, and irregular waves. Fridsma found that as the vessel progressed from displacement speeds to planing speeds, the vessel's motions transitioned from following the wave to skimming across the crests of the wave. This change in hull-wave interaction led to the severe slamming phenomena.

As the vessel moved at planing speeds, the bow of the vessel naturally emerged from the water. This crest impact into the exposed bow led to an increase in acceleration due to slamming and more violent motions seen by the vessel. The collected data revealed that, in general, the added resistance, motion response, and accelerations are nonlinear functions of the wave height. The collected data revealed exceptions to this trend, especially when the wave lengths were significantly shorter or longer than the vessel's length. For example, there

was a tendency for the accelerations to be linear with wave height when the wavelength was relatively long. Fridsma found that even when the wave height was relatively small, large and intolerable accelerations could develop on the hull. This phenomenon was particularly evident when the deadrise angle was low, specifically 10° for this testing. The data revealed that the accelerations increase as the square of the velocity for the 10° deadrise model but are linear with speed for the 30° deadrise model. The VT Impact Basin can be used to validate this finding by controlling both the model's experienced velocity and acceleration.

2.2.2 Towing Tank Tests with Further Complexity

A straightforward method to test the slamming impact on a particular model is to perform tow tank experiments in combination with a wavemaker. Unfortunately, this method can be challenging because it requires extensive and high quality equipment to reliably capture the physics of the slam event. Judge *et al.* sought to overcome these hurdles and conduct extensive model testing using this method at the USNA towing tank [5, 6, 7]. A deterministic approach was taken that sought to analyze each slamming event individually rather than statistically. Multiple models were tested under a variety of test conditions. The models were towed at various Froude numbers through calm water, regular waves, and irregular waves. A variety of sensors and a high-speed camera were used to capture data for each run. The model motion and the spray root were recorded using high-speed video. The impact pressures were recorded using both point pressure sensors and pressure pad sensors. The model accelerations were recorded at the bow, at a midpoint between the bow and the center of gravity, and at the center of gravity. The model heave and trim angle were recorded using potentiometers.

The Judge *et al.* experiments were able to correlate particular pre-impact motion parameters

with higher accelerations and peak pressures. The results of their testing suggest that large pitch angles just before impact lead to more severe accelerations and pressures. The results also suggest that the peak accelerations occur near the minimum pitch angle. The time of the peak pressure measurements at each of the point sensors suggests a relationship between the peak pressure and the spray root propagation. The peak pressure occurs slightly after the spray root has propagated past the sensor. The peak pressure value also decreases slightly along the bottom of the hull. Pressure sensors located near the keel see higher peaks than pressure sensors located near the chine.

One goal of this research is to verify this novel test by validating its data against the results collected by Judge *et al.* Careful note of the planing hull model dimensions and its data collection system has been taken to maintain consistency. The model used for this thesis was developed to be as similar as possible to the 1.22 m generic prismatic planing hull (GPPH) model used by Judge *et al.* In addition, the point pressure sensors are located in the same positions. The data collected for the model motion parameters will be used to ensure the same dynamics occur during this thesis testing. More specifics about the experimental setup for this thesis are presented in the Methodology sections located in Chapter 4.

2.3 Developing Relationships to the Spray Root Propagation

2.3.1 Spray Root Analysis on Flat Plates

The propagation of the spray root and its relation to pressure are key to understanding the physics of the slamming problem. As such, spray root propagation is a primary focus of Wang and Duncan at the University of Maryland [8, 9]. In order to properly study the

propagation rate of the spray root, Wang and Duncan use a system of controlled motors to ensure a constant speed throughout the test trial. Motors mounted on a towing tank carriage attach to the flat plate. The motors provide controlled heave motion, and the carriage provides controlled surge motion. A computer-based control system drives the plate through a programmable motion profile throughout the impact. This allows for consistent motion throughout the changing loading of the slam event. This novel system allows for the study of spray formation within a highly controllable parameter space.

Wang and Duncan noted trends that suggest that the location of the spray root is synonymous with the location of the peak pressure as the vessel enters the water. In the collected data, an interesting region of spray root propagation presented itself. The region is where the local inclination angle is lower than the deadrise angle. Within this region, a more severe local impact is created by a greater local peak pressure due to the greater dimensionless pressure at smaller inclination angles. In addition, the reduced inclination also results in a faster propagation speed of the spray root and a greater expansion rate of the area under hydrodynamic pressure.

Wang and Duncan's fundamental approach analyzes each of these phenomena individually with their flat plate experimentation. When more complex geometry is considered, such as a modern planing hullform, these phenomena can occur in culmination. The use of the GPPH model should allow for new analysis of the coupled nature of these spray root phenomena.

2.3.2 Spray Root Analysis on V-Shaped Wedges

Another approach to understanding the hydroelasticity of slamming events is to study the vertical impact of a V-shaped wedge on calm water. This approach greatly simplifies the dynamics of a real world slamming event to isolate the fluid-structure interaction. Javaherian

et al. sought to understand the role of structural deformation on the spray root propagation [10, 11]. Experimentation was performed on a flexible wedge with a 20° deadrise angle at the Virginia Tech Hydroelasticity Lab. The flexible wedge was dropped in free fall at even keel in calm water to experimentally determine the relationship between the spray root, peak pressure, and structural response. The rigid wedge was dropped in the same manner to allow for comparative analysis of the effect of flexibility. Data collected from this experiment show that the spray root propagation is almost identical at the initial stages of penetration until roughly 20% of the time duration of the wedge entry into the free surface has passed. However, after this moment, the spray root propagation for the flexible wedge lags behind the rigid one. Since the deflection causes a curvature in the bottom plating of the wedge, the spray root attached to the flexible wedge must travel longer compared to the rigid one. The nondimensional speed for propagation of the spray root on the flexible wedge is reduced up to 4% due to fluid-structure interactions. These results highlight the coupled relationship between structural flexibility, the spray root propagation, and the pressure distribution.

2.4 Categorizing the Slamming Events

A key aspect of all slamming events is the dynamics of the high-speed vessel and the waves it impacts. Slamming events can occur in many variations, and this creates the need for categorization. Riley and Coats (2017) proposed three basic categories of slamming events observed on-board small craft, referred to as Alpha, Bravo, and Charlie events [12]. The formation of these categories was based on several characteristics seen in the acceleration time history. Type Alpha is characterized by a free fall with a stern first landing, which causes a downward pitching motion just prior to impact. Type Bravo events are similar; however, the stern may remain in the water with negligible bow down pitching motion prior

to impact. Propeller emergence may result in a reduction of thrust for both Alpha and Bravo events. In a Charlie slam, the boat remains in the water, there is little to no bow-down pitching motion before impact, and there is no loss of thrust. Rather than landing on the wave, the vessel runs into the wave and has a rapid bow up pitching motion.

The first section of the slamming event is primarily influenced by the initial motion parameters of the vessel. The next phase includes the rapid spike in vertical acceleration governed by the wave impact. After the wave impact, buoyancy plays a key role in determining the vessel motion. In seemingly random wave patterns in different sea states, the response motions observed by the vessel follow repeatable patterns that are consistently observed in acceleration data. Riley comments on the limitations of full scale trials based on the limited ability to measure the cause-effect relationship of slamming and the availability of weather conditions to generate sea states. To address this issue with sea state generation the relative dynamics model will be used to allow for these slamming events to occur in calm water.

Riley and Coats (2017) also explain that acceleration data collected during rough water seakeeping trials is routinely used for comparing wave impact severity. This data is used to compare different crafts, different locations in a craft, different speeds, with or without ride control systems, and different sea states and heading conditions. The database has revealed important lessons, but the seakeeping trials are limited in scope, as previously mentioned. Riley claims that scale model testing and computational fluid dynamics (CFD) are needed to research and determine how varying parameters affect cause and effect relationships. Model scale testing often relies on a deterministic approach used to study wave impacts one at a time to determine the physics behind individual responses to wave impact loads. Alternatively, the development of CFD evolved with a reliance on statistical parameters to quantify the wave impact environment. Riley emphasizes the necessity of utilizing both methods to further understand slamming events. The Virginia Tech Advanced Towing Facility, with the

addition of the VPPM, will be able to provide useful data on model scale testing that can be used to study the physics of slamming events and verify and validate CFD programs.

2.5 Summary

The slamming problem has been studied scientifically for almost a hundred years, yet there is still much to learn. The early work by von Karman used momentum theory to analyze the pressure on a simple wedge geometry during water entry. This method laid the groundwork for the analysis of the slamming event using mathematics and physics. The work that followed von Karman's research on the slamming event involved more complex experiments that incorporated additional physical phenomena. Fridsma noted that slamming events were especially impactful on planing hull forms. As vessels transitioned from displacement speeds to planing speeds, they went from following a wave to skimming across the crests. This change led to severe slamming phenomena, even when the wave was relatively small. Judge *et al.* led an extensive multi-institution project to test various aspects of a planing slamming event simultaneously. Their experiment was able to correlate particular pre-impact motion parameters with post impact accelerations and pressures. Wang and Duncan's work closely examined the peak pressures generated by the spray root, a prominent physical phenomenon. They found that the location of the spray root is synonymous with the location of the peak pressure as the vessel enters the water. Their work also found a geometric relationship between the deadrise angle and the spray root inclination angle that led to increased peak pressure magnitudes. In a broader scope, Riley and Coats researched the correlation between the type of impact and the accelerations that ensued. From this correlation, Riley and Coats developed three categories that can be used as a basis for further analysis. Their work also stressed the limitations of existing data sets and that more model scale testing and CFD

are needed. The following chapters describe a novel model scale test method developed at Virginia Tech that builds on this previous work for further understanding. The chapter immediately proceeding describes the theory behind the novel testing method.

Chapter 3

Relative Dynamics Model

Currently, the Virginia Tech Advanced Towing Tank does not have an operational wavemaker. Therefore, a novel testing method is needed in order to perform research on a high-speed boat slamming into waves without a wavemaker. This novel testing method relies on the principles of relative motion dynamics. Relative motion dynamics refers to the study of how objects in a system move in relation to each other. Instead of focusing on the absolute motion of each object, relative dynamics looks at how their positions, velocities, and accelerations change concerning one another. A key factor in finding the relative motion of each object in the system is the reference point. In relative motion dynamics, the reference point can be thought of as stationary and all objects in the system have their motion described relative to this point. While the position of this reference point can vary, the physics of the system will remain equivalent regardless of the position.

3.1 Setting the Point of Reference

Relative dynamics principles can be applied to approximate the incoming wave as calm water. By placing the reference point at the location of impact between the vessel and the traveling wave, the traveling wave becomes stationary in the body reference frame. Following the principles of relative motion dynamics, the vessel's motion will be calculated relative to this reference point. Since the traveling wave is stationary in this model, a calm water surface

will be used to approximate the traveling wave in the system. The calm water surface does not contain the curvature of a wave, so this aspect of the problem will need to be simplified. The curvature of the wave at the impact point can be approximated by taking another point that is an infinitesimally small step along the curvature of the wave from this impact point and making a line between these two points. This line is tangent to the curvature of the wave at the point of impact and has some particular slope value. This particular slope value has an associated angle relative to the surge axis, which will be denoted as angle theta, θ. In a similar way, the calm water surface can be thought of as a line with a slope of zero relative to the surge axis. This model's stationary impact point also serves as an effective rotational point for the system. Rotating the system about the impact point by the angle θ makes the wave tangent line equivalent to the calm water surface line. Figure 3.1 below visualizes this manipulation of the frame of reference.

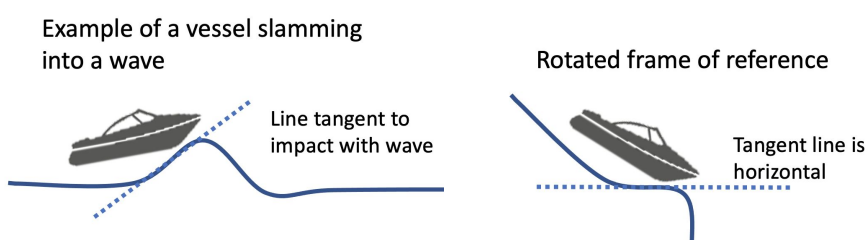

Figure 3.1: Visual Representation of the Reference Frame Rotation

3.2 Equating the Inertial Frame to the Body Frame

The starting point of the model is the inertial reference frame. The free body diagram in the inertial reference frame for the GPPH in a traditional towing tank test is shown below in Figure 3.2.

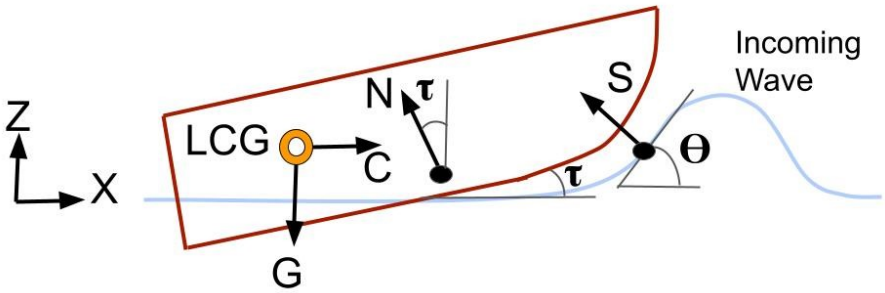

Figure 3.2: Traditional Towing Tank Experimental Setup in the Inertial Frame

In this free body diagram, G represents the force of gravity, C represents the force of the towing carriage, N represents the normal force due to hydrodynamic effects and buoyancy, and S represents the force of slamming. τ represents the running trim angle, and θ represents the angle of the wave at the point of impact. The LCG represents the location of the longitudinal center of gravity. Note that the traditional towing tank test mounting configuration applies the towing carriage force at the LCG. The X and Z represent the orientation of the axes in this reference frame. The sum of the forces and moments applied to the GPPH in this frame are as follows

$$\Sigma \text{ F}_X = C - N\sin(\tau) \text{ - S } \sin(\theta)$$

$$\Sigma \text{ F}_Z = N\cos(\tau) \text{ - S } \cos(\theta)$$

$$\Sigma \text{ M}_{LCG} = M_N + M_S$$

This inertial reference frame can be transformed into a body reference frame. In this case, the impact point on the wave is selected as the reference point. The body reference frame is also rotated such that the tangent line wave approximation is parallel to the calm water surface. Figure 3.3 visualizes the free body diagram in the body reference frame.

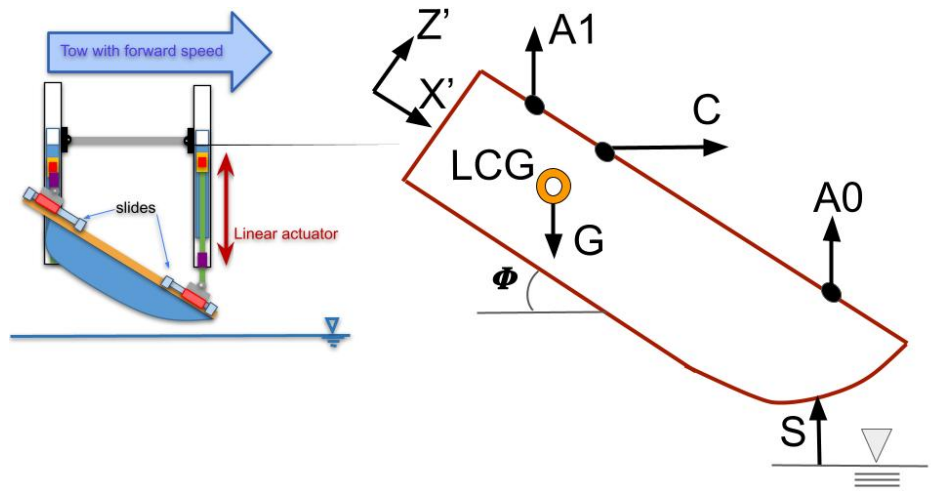

Figure 3.3: Virginia Tech Experimental Setup in the Body Reference Frame

This body reference frame free body diagram has a new list of variables. The X' and Z' represent the new axis orientation in this body reference frame. $A0$ and $A1$ represent the forces applied by the linear actuators. C represents the force applied by the towing carriage. G represents the force due to gravity, and S represents the force of slamming. The symbol ϕ represents the angle of impact where $\phi = \theta - \tau$ from the inertial frame. Once again, the LCG represents the longitudinal center of gravity. Notice that the mounting configuration for this setup changes where the towing carriage force is applied, inducing a moment that must be accounted for. The sum of the forces and moments applied to the GPPH in this frame are as follows

$$\Sigma \mathrm{F}_{X'} = (G - A0 - A1 - S)\sin(\phi) + C\cos(\phi)$$
$$\Sigma \mathrm{F}_{Z'} = (A0 + A1 + S - G)\cos(\phi) + C\sin(\phi)$$
$$\Sigma \mathrm{M}_{LCG} = M_{A0} + M_{A1} + M_S + M_C$$

In order for this dynamic model to be valid, the forces in the inertial reference frame need to be accounted for in the body reference frame. The mathematical proof that relates the

reference frames is displayed below. The rotation matrix R is used to apply the reference frame rotation.

$$\text{R}=\begin{pmatrix} \cos(\phi) & -\sin(\phi) \\ \sin(\phi) & \cos(\phi) \end{pmatrix}$$

$$\begin{pmatrix} \Sigma\text{F}_X \\ \Sigma\text{F}_Z \end{pmatrix} = R(\phi) \begin{pmatrix} \Sigma\text{F}_{X'} \\ \Sigma\text{F}_{Z'} \end{pmatrix}$$

Equating the forces in the X direction of the inertial frame to the body reference yields

$$\Sigma\text{F}_X = \Sigma\text{F}'_X \cos(\phi) - \Sigma\text{F}'_Z \sin(\phi)$$

$$\text{C - N}\sin(\tau) - S\sin(\theta) =$$
$$((\text{G-A0-A1-S})\sin(\phi) + C\cos(\phi))\cos(\phi)$$
$$\text{-}((\text{A0+A1+S-G})\cos(\phi) + C\sin(\phi))\sin(\phi)$$

The equality can be simplified by applying double angle trigonometry identities. Basic algebra is then used to group the controllable force terms on the left side and the physical forces on the right side.

$$(\text{A0+A1})\ \sin(2\phi) + 2C\sin^2(\phi) =$$
$$\text{G}\ \sin(2\phi) + N\sin(\tau) + S(\sin(\theta) - \sin(2\phi))$$

This same method is applied to the forces in the Z direction of the inertial reference frame. The equality to the body reference frame is as follows

$$\Sigma \mathrm{F}_Z = \Sigma \mathrm{F}'_X \sin(\phi) + \Sigma \mathrm{F}'_Z \cos(\phi)$$

$$\begin{gathered}\mathrm{N}\cos(\tau) - S\cos(\theta) = \\ ((\text{G-A0-A1-S})\sin(\phi) + C\cos(\phi))\sin(\phi) \\ +((\text{A0+A1+S-G})\cos(\phi) + C\sin(\phi))\cos(\phi)\end{gathered}$$

Once again, double angle trigonometry identities are used to simplify the equality. The controllable forces are grouped on the left side and the physical forces are grouped on the right side.

$$\begin{gathered}(\text{A0+A1})\ \cos(2\phi) + C\sin(2\phi) = \\ \text{G}\ \cos(2\phi) + N\cos(\tau) - S(\cos(\theta) + \cos(2\phi))\end{gathered}$$

A MATLAB code, presented in Appendix C, performs the necessary calculations to translate a vessel's motion relative to the point of impact on a regular wave and rotate the frame of reference accordingly. The inputs for the vessel's motion and the parameters for the wave can be varied to study different slamming events. The output of this relative motion code is the surge, heave, and impact angle the model needs to have to capture the same physics of the slam event. A visual representation of this model applied to an arbitrary slam event is shown below in Figure 3.4.

3.3 VPMM Verification Study Experimental Matrix

The VPMM and carriage software can use the motion requirements calculated by the relative motion dynamics model as inputs to perform a specific slam event. The validity of this novel testing method and the VPMM setup can be verified by matching test results collected by the VT Impact Basin with those of another trusted facility. The testing conducted by Judge

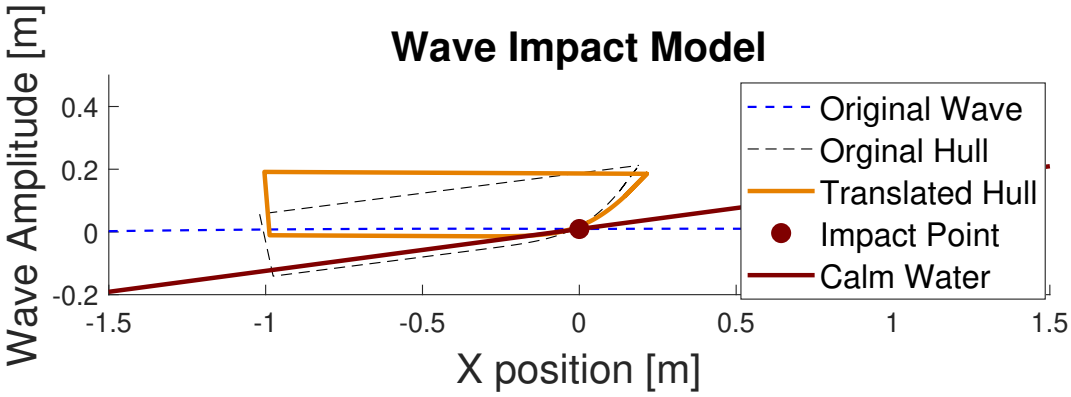

Figure 3.4: Visualization of Relative Dynamic Model MATLAB Calculation

et al. [5, 6, 7] at the USNA will be used to verify the experimental setup here at Virginia Tech. The USNA used a traditional testing method to measure the slamming severity on a 1.22 m GPPH model. As previously mentioned, the USNA GPPH served as the mold for the VT GPPH, resulting in nearly identical models.

The raw data collected during the USNA testing was reanalyzed to identify the vessel motion parameters, the wave characteristics, and the impact point between the vessel and the traveling wave. The first step to collecting these parameters was to identify the moment of impact from the USNA high-speed camera video. The three snapshots below show the selected frame of impact, with the identified point of impact circled in orange.

This impact moment gave the time of impact relative to the data collected. This time of impact was then used to extract the DAQ data associated with that particular slam event. Table 3.1, presented below, displays the key parameters extracted from the collected USNA DAQ data at the time of impact.

Figure 3.5: USNA Run 81 Impact Moment

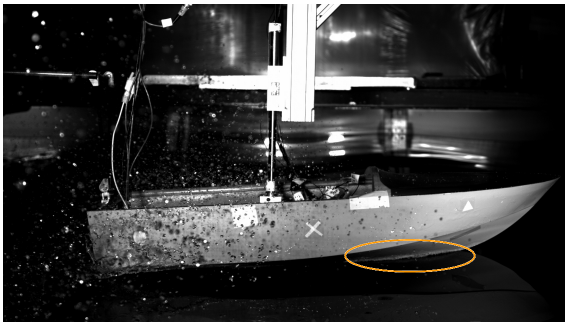

Figure 3.6: USNA Run 90 Impact Moment

Figure 3.7: USNA Run 97 Impact Moment

Table 3.1: Key Parameters Taken from USNA DAQ Data

	Run 81	Run 90	Run 97
Surge (m/s)	6.39	6.39	6.39
Initial Trim (°)	4.89	4.43	7.32
Impact Time (s)	1.52	2.14	2.26
λ / L Ratio	1.55	1.55	3.7
Wave Celerity (m/s)	1.72	1.72	2.65
Wave Type	Regular	Regular	Irregular

These parameters were input into the relative motion dynamics model to translate the motion from an inertial reference frame to a body reference frame. Three unique runs conducted at USNA are selected as representative cases. The motion parameters that are translated into the body reference frame that need to be run at the VT Impact Basin are presented below.

Table 3.2: Translated Motion Parameters for Body Reference Frame

	Condition 1 (Run 81)	Condition 2 (Run 90)	Condition 3 (Run 97)
Surge (m/s)	8.09	8.07	8.96
Heave (m/s)	0.59	0.68	1.20
Initial Trim (°)	-3.95	-4.77	-7.60

The velocity limits of the Virginia Tech towing tank carriage and VPMM are discussed in detail in Chapter 4, but a brief discussion is needed here. The carriage is capable of producing a maximum surge velocity of 7 m/s. Unfortunately, the Virginia Tech facility is not capable

of producing the required surge velocities to match the USNA testing. By eliminating the wave celerity from the system, the relative velocity of the GPPH in the body frame falls within the capabilities of the carriage. The approximation that the wave celerity is equal to 0 m/s is taken to proceed with testing. Note that this is a significant approximation and further separates the physics between the USNA and Virginia Tech setups. Recalculating the translated motion parameters to be tested at Virginia Tech yields the following values displayed in Table 3.3.

Table 3.3: Translated Motion Parameters for Body Reference Frame, Eliminating Wave celerity

	Condition 1 (Run 81)	Condition 2 (Run 90)	Condition 3 (Run 97)
Surge (m/s)	6.37	6.37	6.33
Heave (m/s)	0.44	0.53	0.85
Initial Trim (°)	-3.95	-4.77	-7.60

3.4 Kinematic Motion Parametric Study Experimental Matrix

Controlled surge, heave, and pitch motion are achievable by combining the VPMM with the towing tank carriage. There has not been any recorded research on a generic prismatic planing hullform undergoing controlled slamming identified in the literature. The relationship between the motion parameters and slamming severity has yet to be identified in this test case. A Parametric Study of the motion parameters and their effect on slamming severity will be conducted to identify key parameters and notable trends. Tabletop testing has

identified the limits for the motions that can be performed on the GPPH by the current VPMM setup. This Parametric Study will test these limit cases along with several test cases between the limits. The motion parameters that will be varied for this experiment are the surge velocity, heave velocity, and impact trim angle. The table of values for each of the parameters is shown below in Table 4.3. All combinations of the parameters will be tested. Each combination will be run three times to demonstrate repeatability.

Table 3.4: Parametric Study Experimental Matrix

Trim (°)	Heave (m/s)	Surge (m/s)
0	0.25	5
-5	0.5	7
-10	0.75	
-15	1	

Both the Verification Study and the Parametric Study experimental matrices were tested and their results are presented in 5. The next chapter will explain the experimental setup used to conduct all the testing for these studies.

Chapter 4

Methodology

The methodology section of this report will define the experimental set up for the slamming of the generic prismatic planing hull into calm water using the Virginia Tech Advanced Towing Facility, carriage, and vertical planar motion mechanism. The description of the capabilities of the mechanical and electrical components that comprise these devices will be discussed in detail. First the Advanced Towing Tank and VPMM will be characterized. Then, the planing hull model and its mounting configuration are discussed. The description of the measurement equipment and data collection system will follow. Finally, experimental matrices will be shown.

4.1 Virginia Tech Advanced Towing Tank and Carriage

Donald L. Blount and Associates (DLBA), a Gibbs and Cox Division, a Leidos Company, collaborated with Edinburgh Designs to design and build the Advanced Towing Carriage System Modernized 2022. Figure 4.1 displays the CAD rendering of the carriage shaded light gray. The carriage is capable of a maximum velocity of 7 m/s for a 1 s data window, along with a maximum acceleration of 5 m/s^2 and a maximum jerk of 20 m/s^3. The Advanced Towing Carriage System runs on rails that were designed and constructed by Kempf and Remmers, a Cussons' Marine Hydrodynamics division. There is an allowable tolerance for rail height of 0.1 millimeters.

The carriage achieves its high velocity with a belt drive system with an electric motor on each of the two rails. The brakes are electromagnetic and provide enough braking force for the high acceleration and deceleration loads. The Advanced Towing Carriage System allows for inputs for desired destination position, movement speed, acceleration, and jerk. The position of the carriage is constantly measured by the Pepperl and Fuchs linear code reader. The code reader assesses a unique matrix encoded tape identifying the device's position. The tape has been installed on the IGUS tray, which runs along the tank. The carriage position is derived from this device and translated to have the 0 m position on the outside wall of the basin behind the wavemaker.

Polyurethane-painted reinforced concrete forms the towing tank basin. The facility is 29.9 m long, 1.8 m wide, and 1.5 m deep. The current operation limits of the carriage are set between 5.525 m and 24.365 m, allowing for a 1 m buffer to the mechanical buffer.

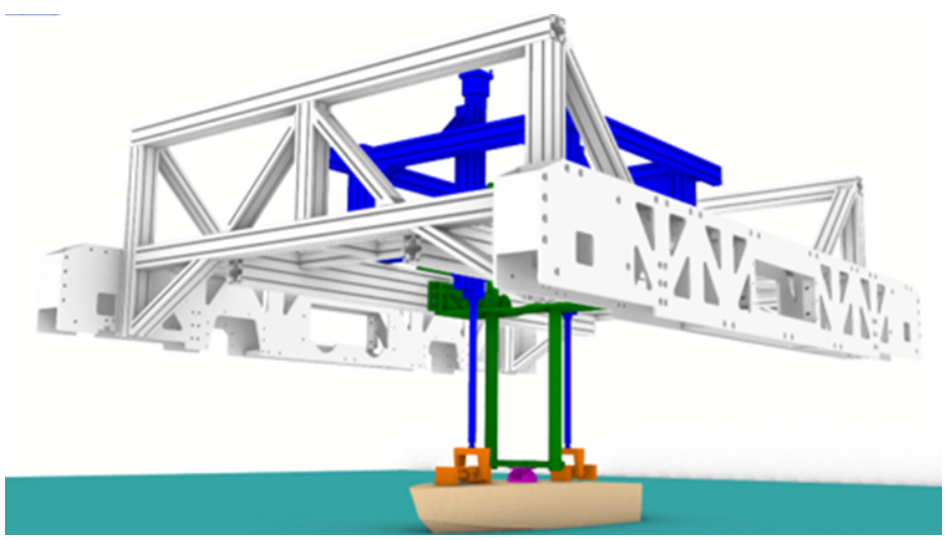

Figure 4.1: Virginia Tech Towing Tank Carriage and VPMM Setup, Courtesy of DLBA.

4.2 Vertical Planar Motion Mechanism

4.2.1 Linear Actuator Design

Attached to the carriage is the Vertical Planar Motion Mechanism (VPMM). The VPMM is composed of three modules: the linear actuator assembly, the heave staff assembly, and the attachable subsurface assembly. The linear actuator assembly is a combination of mechanical and electronic components mounted to the towing tank carriage that drive the heave and pitch motion of the vessel. The linear actuators are attached to the support structure with aluminum angle brackets and stainless steel screws placed above and below horizontal aluminum rails. The configuration of the linear actuators and their support structure are shown in blue in Figure 4.2. The heave staff assembly, which helps support the forces on the linear actuators, is shown in green.

The structural support system is designed to handle 2400 N along the z-axis for the surface configuration and a bending moment of 990 N-m around the y-axis. The estimated loads and moments calculated by the designers along each of the x-y-z axes are shown in Table 4.1.

	F_x	F_y	F_z	M_x	M_y	M_z
Subsurface Vessel	1454	N/A	1610	N/A	989	N/A
Surface Vessel	204	427	2424	195	97	3.2

Table 4.1: Vertical Planar Motion Mechanism Load Estimates, Courtesy of DLBA.

The linear actuators drive the vertical motion of the vessel to control both heave and pitch. The Parker ETH050 High-Force Screw Drive Electric Actuator was selected to perform the necessary operations to control heave and pitch. The actuator has a maximum stroke length of 600 mm, a maximum operating speed of 1.3 m/s, and a maximum acceleration of 15

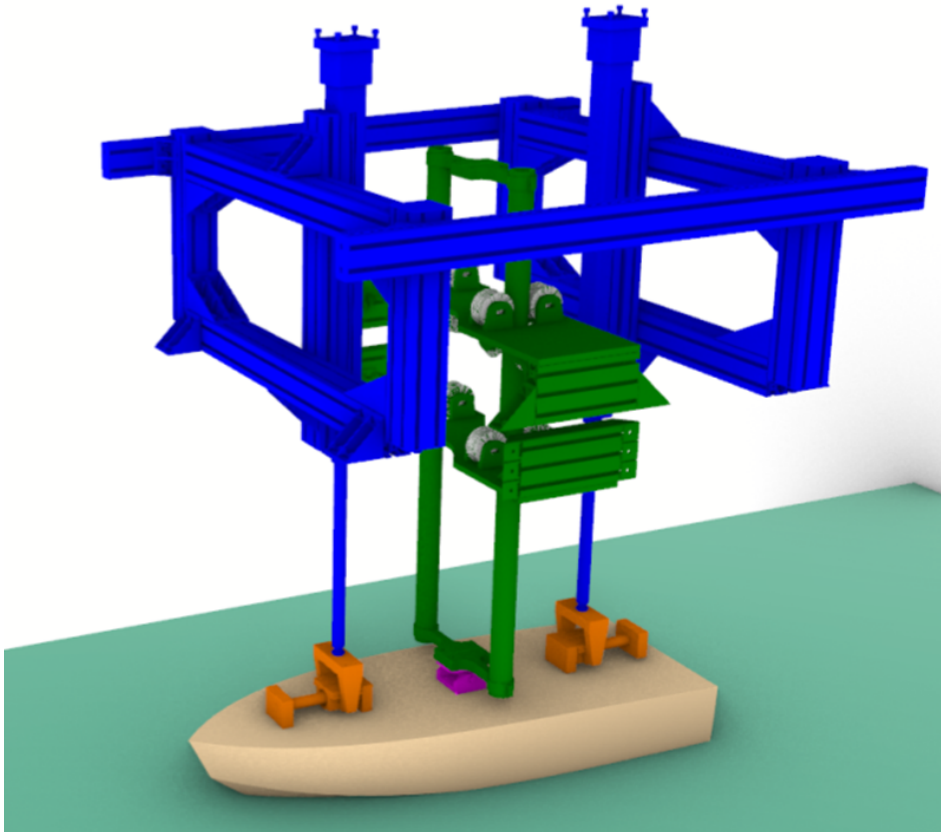

Figure 4.2: Vertical Planar Motion Mechanism CAD Drawing, Courtesy of DLBA.

m/s^2. These maximum motion values are less than the motor's maximum, making them the limiting motion parameters of the system. The combination of the linear actuators allows the attached model to attain a pitch of +/- 35.1° at a rate of 73.8 °/s in the current configuration. Changing the distance between the actuators will allow the pitch motion values to change. The actuators are each capable of producing a maximum thrust of 9300 N.

4.2.2 Linear Actuator Drive System

The linear actuators are each driven by Parker MPP-series high power and low inertia brushless servo motors. The motor has a 1.8 kW rating with encoder feedback and power brakes. The servo motors drive the linear actuators and measure position with an internal incre-

mental encoder. The incremental encoder has a configurable resolution. The manufacturer's recommended value of 1000 counts per revolution per channel was chosen for this testing. The servo motors are each controlled by servo drives. The Parker S100V2 Compax3S single axis servo drives chosen for this design are rated for continuous 20A current and an input voltage of 240 VAC. The servo drives powers the motors based on the command signal and collects feedback of the incremental encoder data from the motor. The servo drive is connected to the carriage computer with a RS232 cable. The servo drives are programmable to allow for the user to configure the control mode of the drive. This testing utilizes the velocity control mode for all testing.

4.2.3 Linear Actuator Control System

The two servo drives are simultaneously controlled by a NI 9149 cRIO chassis with an FPGA chip. The chassis is also connected to a laptop onboard the carriage with LabVIEW. The cRIO measures the current position and velocity value from the servo drive and then generates the command signal calculated in LabVIEW to be sent to the servo drive. This allows for closed loop control of the motors.

The control software for the VPMM and the Data Acquisition System (DAQ) systems is written in LabVIEW. This is a graphical programming language compatible with NI devices. The main functions that make up the control software are a motion profile generator, a UDP data packet dissector, and a PID control loop.

The motion profile generator creates the prescribed motion profile for each actuator and the carriage. The necessary delay to ensure that the model slams into the water at the middle of the tank is also calculated and added to the prescribed motion profile for the actuators. The motion profile generator accepts inputs for the total travel distance, the desired steady

state velocity, the acceleration, and the jerk the model should experience.

A local Ethernet network, explained in more detail later in this section, synchronizes all the components of the overall system with UDP data packets. The UDP data packet dissector unpacks the 16-bit UDP data packet to collect the carriage Cycle Time and measured velocity. This allows the VPMM to know the relative time and velocity of the carriage at all times.

The PID control loop function uses the closed feedback loop to constantly adjust the speed of the motor to match the prescribed motion profile. The closed feedback loop provides the measured position and velocity of the motor. The error in the system is defined as the difference between the prescribed values and the measured values. PID stands for the proportional, integral, and derivative gain parameters that can be adjusted to attain the desired controller performance. The proportional gain produces an output that is proportional to the current error. Integral gain produces an output proportional to the sum of the error over time to reduce steady state error. The derivative gain is a damping term that reduces the output when the measured motion is increasing rapidly. The PID controller calculates the control output by combining these three components. Extensive tabletop testing was conducted to tune the PID parameters to meet the performance requirements set by the VPMM designers. The combination of the towing carriage and VPMM are displayed in Figure 4.3. The graphic depicts the orientation of the controlled motion directions and the capabilities of the system.

4.2.4 Homing System

A combination of Parker Daedal P8S series electronic sensors sets the home position and usable stroke limits. The sensors directly mount on the linear actuator, enabling contactless

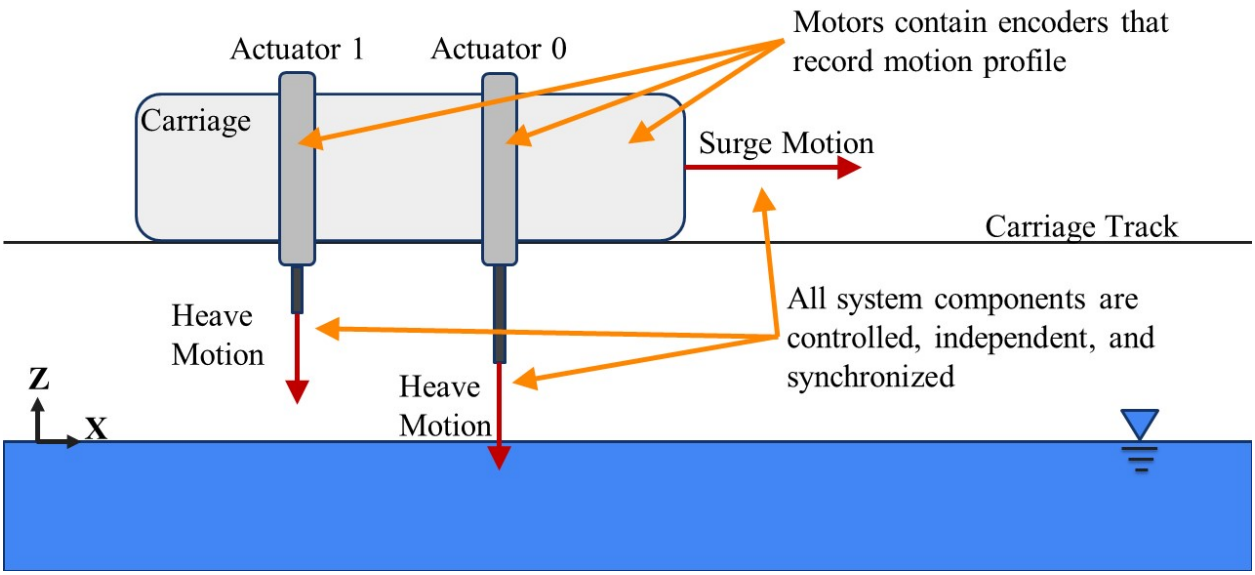

Figure 4.3: Towing Carriage and VPMM Overview Cartoon

sensing of the piston position. The home position sensor stops the actuator at the set home position during the homing algorithm in LabVIEW. The usable stroke limit sensor powers off the motor when the piston magnet position passes by the sensor.

4.2.5 Heave Staff Assembly

The heave staff assembly is a combination of mechanical components that provide sufficient reaction support to reduce the out-of-line loads on the actuators. The pivot box attached to the end of the heave staff assembly provides free pitch motion, but this can be removed if pitch reaction support is also desired. The reaction support is provided by the combination of the 3.2 mm thick aluminum pipes and the U-groove wheels. The pipes are free to move vertically, and the wheels are free to spin. This freedom allows the linear actuators to provide the controlled heave slam force and provide support as the vessel re-emerges.

4.3 Generic Prismatic Planing Hull

4.3.1 Creation of the Hullform

The Generic Prismatic Planing Hull (GPPH) model is used as the test model. This model was specially selected to provide similar results to the towing tanks experiments conducted at the USNA [5, 6, 7]. The similar results can therefore be used as a means to verify the VPMM experimental setup. To ensure this model would work in the Virginia Tech tank, which is significantly smaller than the USNA's tank, both the maximum velocity and wake reflection were taken into account. The calculations for wave reflection confirm that the bow wave will not intercept the hull of the model throughout the speed range. The VT towing tank carriage can reach a maximum speed of 7 m/s allowing for a 1.22 m model to reach a length based Froude number of Fn = 2.02. The USNA's 1.22 m GPPH was used to create a negative mold of the model, which was then used to create the final VT model. The principle characteristics and sheer body plan can be visualized in Figure 4.4. The layup schedule was based on the original USNA model's, with the addition of some additional layers for added rigidity. This model was manufactured by a previous student in the research group, Mark Shepheard. Further details of the model construction can be found in Mark's thesis [13].

Sheer Plan of the GPPH

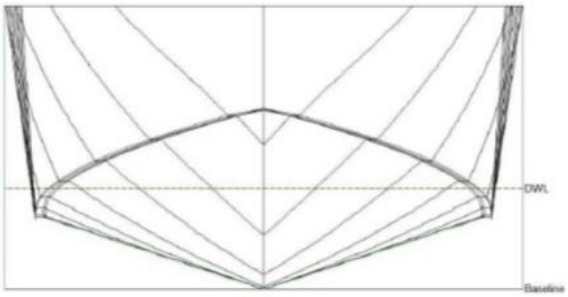

Principle Characteristics of the GPPH

Characteristic	Full-Scale	Model
Length Overall/L_{OA} (m)	13.0	1.22
Max Beam/B (m)	4.0	0.36
Draft/T (m)	0.77	0.0721
Displacement/Δ (tons)	15.9	0.013
LCG (m)	4.6	0.4298
VCG (m)	1.5	0.1372
Deadrise/β (°)	18	18

Figure 4.4: Sheer Plan and Principle Characteristics of the Generic Prismatic Planing Hull-form, (Ikeda Judge (2014), used with permission [5])

4.3.2 Model Mounting Setup

Careful consideration was taken to develop a mount system that will allow for a large range of motion without significantly influencing the physics seen by the model. Timothy Gillen and Matthew Donelson, previous students that worked on a similar research project, developed a mounting system that allowed free heave, pitch, and surge while restricting all other degrees of freedom. The mounting system has two connection points to the model to allow both forces and moments to be measured. The mounting system attaches to both linear actuators and the heave staff posts. The linear actuators are connected to pivot boxes that run along linear bearings. The linear bearings allow for a greater range of pitch angles than just pivot boxes can allow. The heave staff posts are connected to a pivot box that is only free to pitch. This connection provides reactionary support against surge, sway, roll, and yaw relative to the carriage. This mounting system was modified to fit the GPPH model. The connection points of the mounting system to the GPPH will influence the local strength of the structure and, consequently, hydroelasticity effects. A connection along the keel was chosen to minimize this impact. A small stainless steel bar was fiberglassed to the model along the keel of the

GPPH to provide a connection to the mounting system. The bar dimensions were as small as possible, and the amount of fiberglass used to connect the bar was minimal. The drawing of the mounting system can be seen below in Figure 4.5.

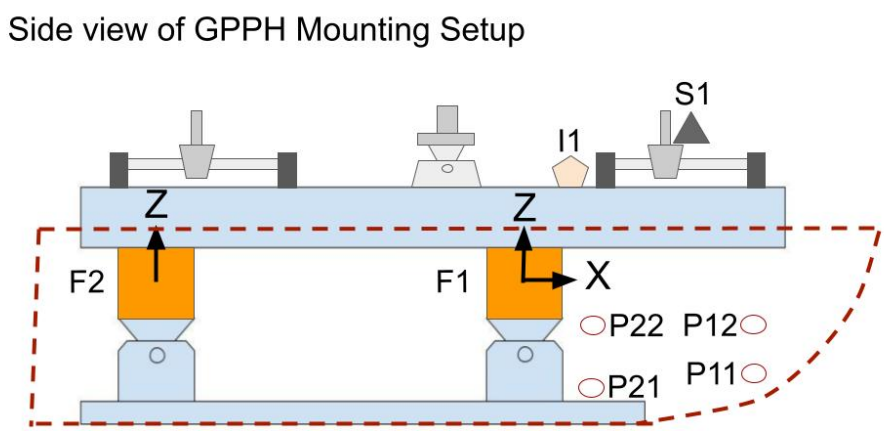

Figure 4.5: Side View of Sensor Layout and Mounting Configuration

4.4 Instrumentation

A multitude of sensors and cameras are used to capture the physical phenomena that the GPPH model experiences during a slam event. For this testing, a string potentiometer, an inclinometer, two load cells, four pressure sensors, a GoPro camera, and a high-speed camera are used. An overview of the sensor locations on the model are shown in Figure 4.6.

The load cells are represented as orange rectangles labeled "F1" and "F2." Note that the load cell near the stern, $F2$, is a single axis sensor measuring force in the Z' direction, or heave direction. The load cell located at midship, $F1$, is a triple axis load cell measuring forces in the X', Y', and Z' directions. The inclinometer is represented as a tan pentagon. The string potentiometer is represented as a gray triangle. The pressure sensors are represented

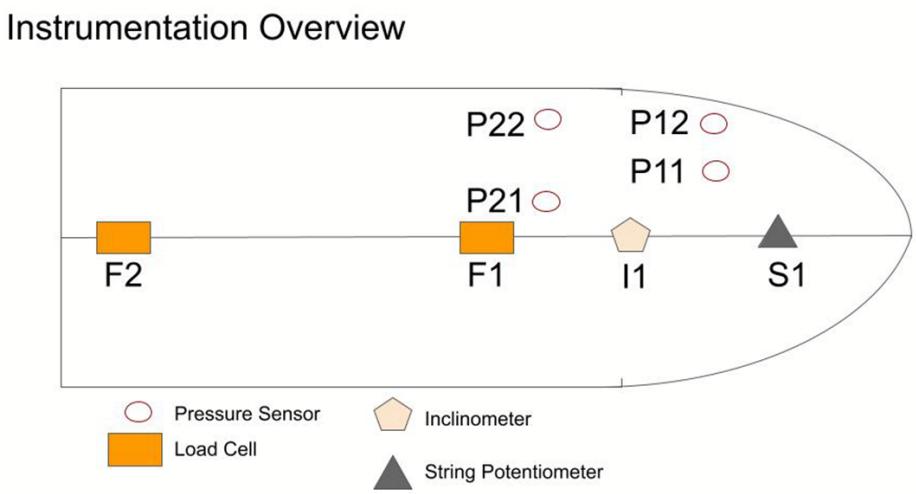

Figure 4.6: Top Down View of Sensor Layout

as red circles, with one set near the bow and one set near midship. The GoPro camera points towards the bow of the model, slightly offset from the centerline. The high-speed camera is pointed nearly isometrically to the model to gain a full view of the slamming phenomena. Each of these sensors are described in the following subsections.

4.4.1 String Potentiometer

A SGD-120-3 string potentiometer will be attached to the linear actuator pivot box located near the bow. Since the VPMM imposes prescribed motions onto the model, the potentiometer acts to verify that the actual movement pattern matches the programmed movement pattern. The potentiometer will measure the heave of the bow linear actuator to verify the position of the model with the incremental encoder measurement. The potentiometer has a maximum range of 3.048 m and is a DC instrument that gives off a continuous signal. Thus, the resolution of the potentiometer measurement is limited by the DAQ and not by the sensor. This signal was sampled at 2000 Hz, which is sufficient to capture the dynamic position of the model. The potentiometer has 0.3% full scale accuracy. In addi-

tion, the potentiometer has an IP67 rating to ensure its protection against the harsh testing environment.

4.4.2 Inclinometer

A SQ-GIX-2022 GravityGyro inclinometer was secured onto the back spine of the model mount to record the pitch of the model. The inclinometer is used to validate the encoder data and ensure that the trim angle is held constant during the slam event. The inclinometer has a range of +/- 75° in pitch and +/-180° in roll. The static tilt accuracy of the sensor is 0.1°, and the dynamic tilt accuracy is 0.5° of RMS error. The sensor also has a high shock tolerance of 1000 g ½ sin 0.1 ms 3x in any axis. This value is significantly higher than any shock expected to occur during this series of experiments. Within the expected operating conditions, the additional error due to vibration, shock, and acceleration is less than the 0.5° RMS error. The sensor has an IP67 rating to ensure its protection against the harsh testing environment. The inclinometer has a sufficient sampling frequency of 2000 Hz to capture the possible trim angle changes during impact.

4.4.3 Load Cells

The mounting system connects two load cells to fully capture the forces and moments applied to the model. A Futek MTA400 tri-axial load cell is located at midship. An Omega LC103B-250 single axis load cell is located near the stern.

The MTA400 tri-axial load cell measures forces in the X', Y', and Z' directions. The load capacity in the X' and Y' directions (Fx, Fy respectively) is 1112 N, and the load capacity in the Z' direction (Fz) is 2224 N. The sensor is sampled at 2000 Hz, which is sufficient to capture the hydrodynamic forces applied to the model. The sensor has an IP40 rating,

making it vulnerable to the wet testing environment. The sensor is covered with thin plastic to add protection against any potential water contact. The sensor has a sensitivity of 0.25% of its rated output. The rated output of the sensor is very low, on the scale of mV, compared to the max input range of +/-5 V for the NI 9234 DAQ measurement device. The Futek model IAA100 strain gauge amplifier is used to apply a gain of 1665 to the load cell signal. This gain is sufficient to bring the output of the load cell to the same magnitude as the input range of the DAQ measurement device. The IAA100 has a total error of 0.01% of its full scale reading.

The Omega LC103B-250 load cell measures forces in the Z' direction. The combination of this load cell and the Futek load cell allows for the moment to be measured through the slam event. The load capacity of the sensor is 2224 N. The sensor is sampled at 2000 Hz, which is sufficient to capture the hydrodynamic forces and also match the sampling rate of the Futek load cell. The sensor has an IP67 rating, so it is fully capable of handling the harsh testing environment. The sensor has a sensitivity of 0.035% of the rated output. In the same way as the Futek load cell, the Omega load cell has a very low output signal on the scale of mV. A Micro Measurements 2310B signal conditioning amplifier is used to amplify the signal to the same magnitude as the NI 9234 DAQ measurement device. A gain of 1000 is applied to sufficiently amplify the signal. The signal conditioner also applies a low pass filter set to 100 Hz to reduce the effect of the electrical noise caused by the motors on the signal. The signal conditioner has an error tolerance of 0.02 % of its full scale reading.

4.4.4 Pressure Sensors

PCB Model 102B18 ICP Pressure sensors are mounted along the bottom of the hull on the starboard side. The pressures measured during slamming events occur very rapidly and

generate high peak pressures. These sensors have a measurement range of 344.7 kPa, corresponding to a +/-5 V output. The sensors have a +/-15% sensitivity of 14.5 mV/kPa. The pressure sensors were sampled at 20 kHz for all trials. This high sampling rate is necessary to adequately capture the peak pressure during the slamming event. The probes require a mounting torque of 7-11 N-m. Aluminum cylinders were manufactured and epoxied to the hull to provide the threading, required thickness, and structure to achieve this mounting torque on the fiberglass hull. Every three to five trials, these sensors were surface-treated with a thermal ablative coating to mitigate any changes in temperature.

4.4.5 GoPro Camera

The GoPro Hero 11 camera is mounted onto the carriage in line with the centerline of the model. The GoPro is used to capture the entire slam event and verify the visual data captured by the high-speed camera. The Hero 11 model has a 5.312k resolution for video at 60 fps and a 5.568k resolution for photos. The model is capable of capturing video at 120 fps with a reduced 4K resolution. The camera is rugged and waterproof, making it capable of handling the harsh testing environment.

4.4.6 High-Speed Camera

The carriage mounts a Phantom VEO 710S high-speed camera to record the entire slam event of the model. The cameras can capture video at 7000 fps with a resolution of 1 megapixel, making them capable of capturing the slam event even at the highest speeds of the experimental matrix. The visual data of the slam event can be time synchronized with the other sensor data to visualize the physical phenomena that occurred. Unfortunately, high trim angle cases are not well visualized by the current angle of camera mount. Future

work should look to mount this camera at better positions to make its collected data more useful, especially for visually tracking the spray root.

4.4.7 DAQ System

The data acquisition system collects the measured signals from the many sensors. The NI 9174 cDAQ chassis contains multiple modules to comprise the data acquisition system for this testing. The string potentiometer and inclinometer are connected to the NI 9201 analog input module. The load cells are connected to the NI 9234 four channel dynamic signal acquisition module. The pressure sensors are connected to the NI 9231 simultaneous bridge modules.

4.5 Local Ethernet Network

The VPMM is synchronized with the DAQ system and the carriage through a local Ethernet network. A Cat5e star-quad Ethernet cable is routed from the carriage onshore PLC to the onboard carriage servo drives, onshore carriage desktop, and onboard VPMM laptop. Two intermediate Ethernet switches are used to connect all these systems, one onboard the carriage and one onshore. This local network creates a communication network between the carriage and the VPMM. Therefore, the real-time carriage data being read by the Pepperl and Fuchs linear code reader is accessible to the VPMM control system and DAQ system through the local network. This communication allows for synchronization between the carriage system, the VPMM system, and the DAQ system.

4.5.1 Common Origin for Time and Position

One application of the local network is the communication of a common origin time for the carriage, VPMM, and DAQ systems. The onshore PLC has a counter of the relative time since the system was powered on, labeled "Cycle Time" by the original designer. The Cycle Time is sent to the carriage desktop and VPMM laptop at a rate of 200 Hz. The VPMM and DAQ systems are set to initialize when the carriage velocity reaches 0.05 m/s. This value was selected so that the systems are triggered near the start of the carriage motion but would not be triggered by noise in the carriage velocity measurement. The common origin time is the Cycle Time when the carriage reaches a velocity of 0.05 m/s and when the VPMM and DAQ are initialized. The Cycle Time is also collected at the start of the DAQ data collection and for each iteration of the VPMM control loop and carriage control loop. This common origin time, along with the Cycle Time stamp when each system starts data collection, is used to synchronize the time of the data in post processing. The sequence of events that make up this synchronization can be visualized in Figure 4.7 below.

The time offset in the data is found by collecting the relative Cycle Time when the linear actuator encoders measured a distance equal to the distance the model needed to travel to impact the water. This relative Cycle Time value is then subtracted from the Cycle Times collected at each other data point. In a similar way, the distance the model needed to travel to impact the water is also offset from all the vertical position data collected by the encoders. This sets the value of vertical position equal to 0 when the model first enters the water.

4.5.2 Automated Delay to Start Linear Actuators

Another application of this local network is an initialization delay for the VPMM and the DAQ systems. This delay is calculated in LabVIEW based on the anticipated motion profile

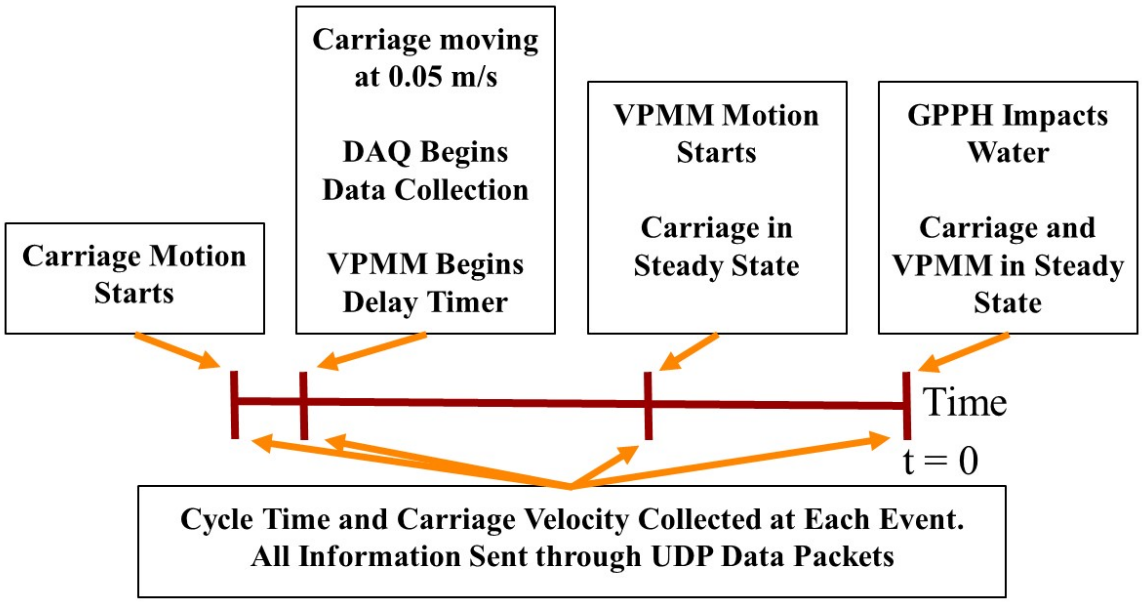

Figure 4.7: Sequence of Events For System Synchronization

of both the carriage and the VPMM system and the machine delay of the LabVIEW software. The calculated delay ensures that the model enters the water at the same time the carriage is in the middle of the towing tank. This will allow the underwater observation area in the middle of the tank to always be able to visualize the slam event. During tabletop testing, a noticeable machine delay (the time between pressing run on the LabVIEW software and the linear actuators actually starting to move) was discovered. This machine delay causes an offset between the relative time measured by the VPMM controller and the relative time measured by the carriage PLC. Through many trials, this machine delay was found to be 1.1 seconds for the LabVIEW software version used in this testing. This measured machine delay is accounted for in the initialization delay calculation to mitigate this offset between the relative times. The user is advised to adjust the total travel distance of the VPMM such that there is always a non-zero value for the initialization delay. This ensures that the total machine delay is accounted for and the carriage and VPMM are properly synchronized. The

next section of this chapter outlines both the Verification Study and the Parametric Study experimental matrices once again for clarity.

4.6 Verification Study Experimental Matrix

The derivation of the Verification Study experimental matrix was discussed in detail in Chapter 3, Section 3.3. The experimental matrix for this study is included again here in brevity.

Table 4.2: Verification Study Experimental Matrix

	Condition 1 (Run 81)	Condition 2 (Run 90)	Condition 3 (Run 97)
Surge (m/s)	6.37	6.37	6.33
Heave (m/s)	0.44	0.53	0.85
Initial Trim (°)	-3.95	-4.77	-7.60

4.7 Parametric Study Experimental Matrix

Likewise, the Parametric Study experimental matrix is included again here. The full derivation of this experimental matrix is explained in 3, Section 3.4. As previously mentioned, all combination of the table below are tested. The combinations created a total of 32 unique conditions for this study.

Table 4.3: Parametric Study Experimental Matrix

Trim (°)	Heave (m/s)	Surge (m/s)
0	0.25	5
-5	0.5	7
-10	0.75	
-15	1	

The next chapter of this thesis displays the results gathered from these experimental matrices. First the Verification Study is discussed, followed by the Parametric Study discussion. Afterwards is a discussion on the limitations of the experimental setup that were discovered during testing.

Chapter 5

Results and Discussion

5.1 Verification Study Results

The impact testing performed on the GPPH provided insight into the hydrodynamic phenomena that occur during the slamming event. In this particular experiment, a number of sensors placed throughout the GPPH model were used. A combination of load cells, pressure sensors, a string potentiometer, an inclinometer, and encoders captured various aspects of the hydrodynamic phenomena for each condition of the experimental matrix. The motion parameters for each condition was shown in Table 4.2 located in the previous chapter. The following section analyzes the data collected by these sensors and the processed results of the impact testing. In addition to looking over the data collected by the sensors, the validity of the dynamics model is also explored.

As mentioned in Chapter 4, the software synchronized the data collection system with the prescribed motion of the VPMM and the towing tank carriage. This allows a common origin for time and position in the data to be set. For all the data presented in this section, the time and position are set to zero at the start of impact.

5.1.1 Model Dynamics

The motion of the model was prescribed using a combination of the VPMM and the towing tank carriage. The prescribed motion held certain characteristics throughout the slam event for every case presented. One characteristic that was consistent was the steady-state velocity condition. For each condition, a certain heave velocity and surge velocity are prescribed to the GPPH model. At the time of impact, when $t = 0$, each of these velocities are in a steady state. This steady state velocity is held during submergence for as long as possible to develop the largest window with this condition. Figure 5.1 displays the motion profile for condition 1, which has the same typical trends as all other runs.

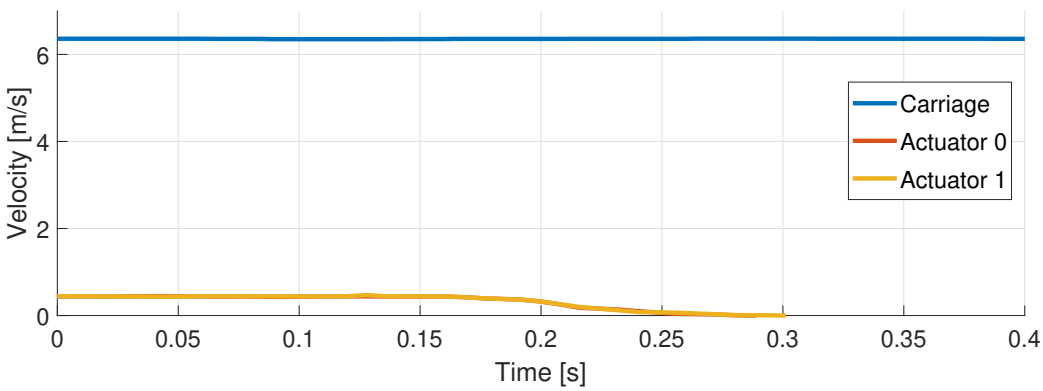

Figure 5.1: Verification of Steady State Velocity at Impact for Condition 1

Following the steady state velocity window is a period of deceleration. The towing tank carriage had a prescribed deceleration of 4 m/s^2 for every run. The deceleration of the linear actuators was prescribed to be 15 m/s^2 for every run. Figure 5.2 below displays the deceleration data from the first trial run of condition 1. The blue line represents the deceleration on the linear actuator closer to the bow, and the red line represents the linear actuator closer to the stern.

The next characteristic that was held constant between runs was a constant submergence

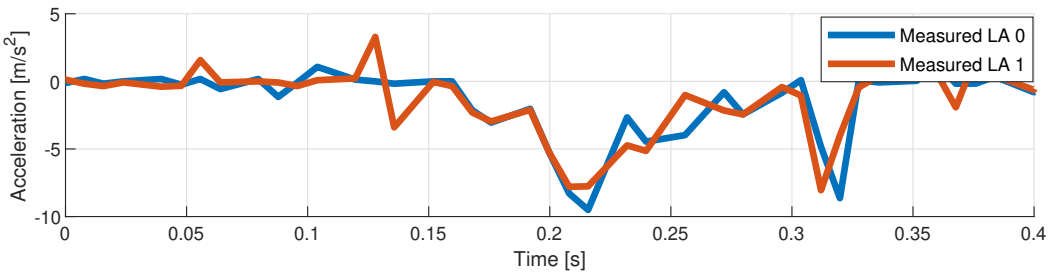

Figure 5.2: Verification of Heave Deceleration During Impact for Condition 1

depth. The limit to the amount of time in steady state velocity during submergence is the risk of flooding the model and damaging the sensors. A consistent and measured submergence was chosen to avoid this scenario. For each trim angle, the maximum allowable submergence was measured. A safety distance of 50 mm was then added to ensure the model had enough freeboard to avoid flooding. In order to keep the submergence depth constant between cases, a depth of 90 mm was chosen for all cases.

After reaching the maximum submergence depth, the model was raised out of the water for an extra level of safety. The model was prescribed to rise out of the water at a heave velocity of 0.1 m/s for 1 to 2 seconds at the conclusion of every run. This lift ensured that the model was not towed at the maximum submergence depth. This mitigated the risk of flooding and minimized the duration of high loads on the sensors and the model. An example motion profile that displays these characteristics is displayed in Figure 5.3 below.

Recall that time and position are equal to zero at the moment the model first enters the water. The method to set this origin was discussed in detail in 4.5.1.

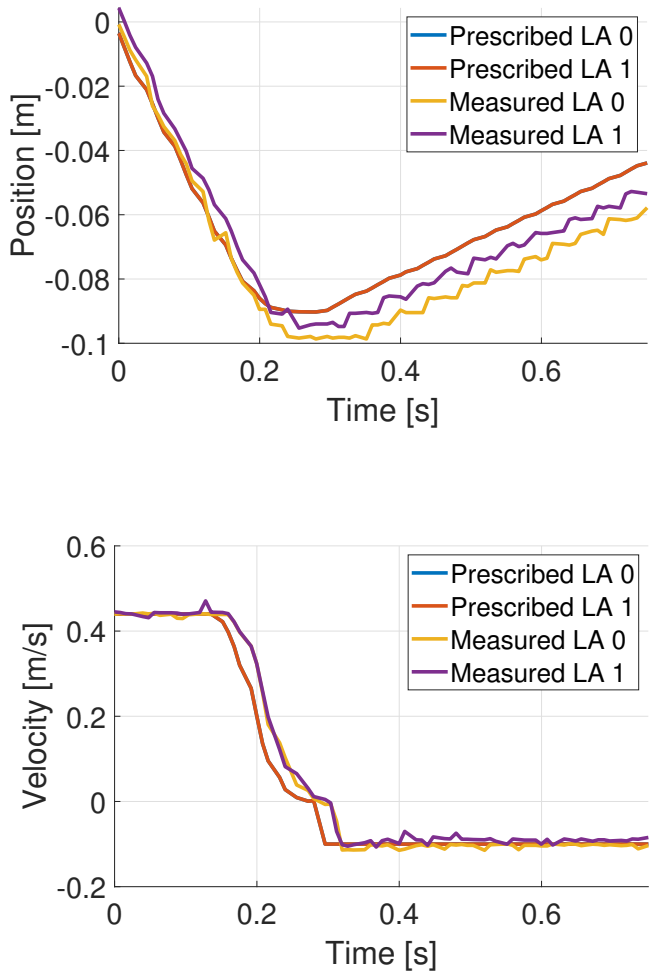

Figure 5.3: Verification of Position and Velocity of Each Actuator for Condition 1

5.1.2 Factors for Nondimensionalization

Much consideration went into the nondimensionalization of the results. Most importantly, the parameters should follow the Buckingham Pi theorem. The Buckingham Pi theorem provides multiple sets of potential nondimensionalization parameters, so additional criteria is needed to select the best set. The set of parameters should be commonly measured across different experimental setups for straight forward comparison. In addition, the set of parameters should provide some physical meaning, so as to allow intuition and experience

to provide some low fidelity validation.

For this study, the density of water and the total velocity of the vessel were chosen as the parameters to nondimensionalize the dynamic pressure. The density of water, denoted as ρ, was assumed to be 1000 kg /m^3. The total velocity (V_T) of the vessel is a function of the heave velocity (V_H) and the surge velocity (V_S) where

$$V_T = (V_H^2 + V_S^2)^{1/2}$$

The force is nondimensionalized by the same set of variables as the dynamic pressure, with the addition of the maximum wetted area, denoted as S_w. As the trim angle changes for each impact, so does the wetted area during impact. The value for wetted area for each trim angle was found using the ORCA3D Hydrostatics plugin in Rhino on a CAD model of the GPPH created by the USNA. The submergence depth for each trim angle was assumed to be equal to the prescribed submergence in the Virginia Tech trials.

The time was nondimensionalized by the time the vessel reached maximum submergence, denoted as T_{sub}. Likewise, the position was nondimensionalized by the maximum submergence depth, denoted as Pos_{sub}.

5.1.3 Dynamic Pressure Analysis

Traditional wedge drop and flat plate experiments well document the effect of spray root propagation on peak pressure. For the simplified case, when the deadrise angle is constant across the wedge and the trim angle is zero, the following trends are typical. A slightly lagging peak pressure correlates with the spray root propagating up the model. The peak pressure magnitude is greatest near the keel and progressively decreases as the spray root propagates towards the chine. In addition, the value of the deadrise angle has an influence

on the peak pressure magnitude and the velocity of the spray root propagation.

The graphs in Figure 5.4 show the pressure that the propagation of the spray root causes over time as the model impacts the water. The pressure is nondimensionalized by the dynamic pressure, where ρ is the density of freshwater and V_T is the total impact velocity equal to 6.39 m/s for all cases. The pressure distribution is also averaged over the five trials taken for each condition. With a few discussed exceptions, many trends in the data align with expectations derived from traditional wedge drop experiments. The GPPH has a more complex geometry than a typical wedge. The deadrise angle varies transversely at the bow but is constant from midship to the stern. Recall that pressure sensors P11 and P12 are transversely inline and have similar deadrise angles near the bow. Likewise, P21 and P22 are transversely inline and have the same constant deadrise angle near midships. As such, transversely inline pressure sensors should exhibit similar trends to a wedge drop experiment with a comparable deadrise angle.

The high-speed camera attempted to capture this spray root propagation visually. Figure 5.5(a) to (e) are snapshots taken from the recorded high-speed video at particular events. All snapshots are taken from the first trial of the first condition. The first snapshot displayed in Figure 5.5(a) shows the model at the start of the impact. The second snapshot in Figure 5.5(b) is taken when pressure sensor P11 reaches its peak magnitude. The next snapshot displayed in Figure 5.5(c) displays when pressure sensor P12 reaches its peak. Likewise, Figure 5.5(d) displays when pressure P22 reaches its peak. The time when P21 reaches its peak is inconclusive for this condition, so its snapshot was not included. The final snapshot displayed in Figure 5.5(e) is taken when the model reaches its full submergence.

In all three conditions, pressure sensor P11's peak pressure occurs earlier and is larger than pressure sensor P12's peak pressure. While the deadrise angle at P11 is slightly less than the deadrise angle at P12, this trend is consistent with the results of traditional wedge drop

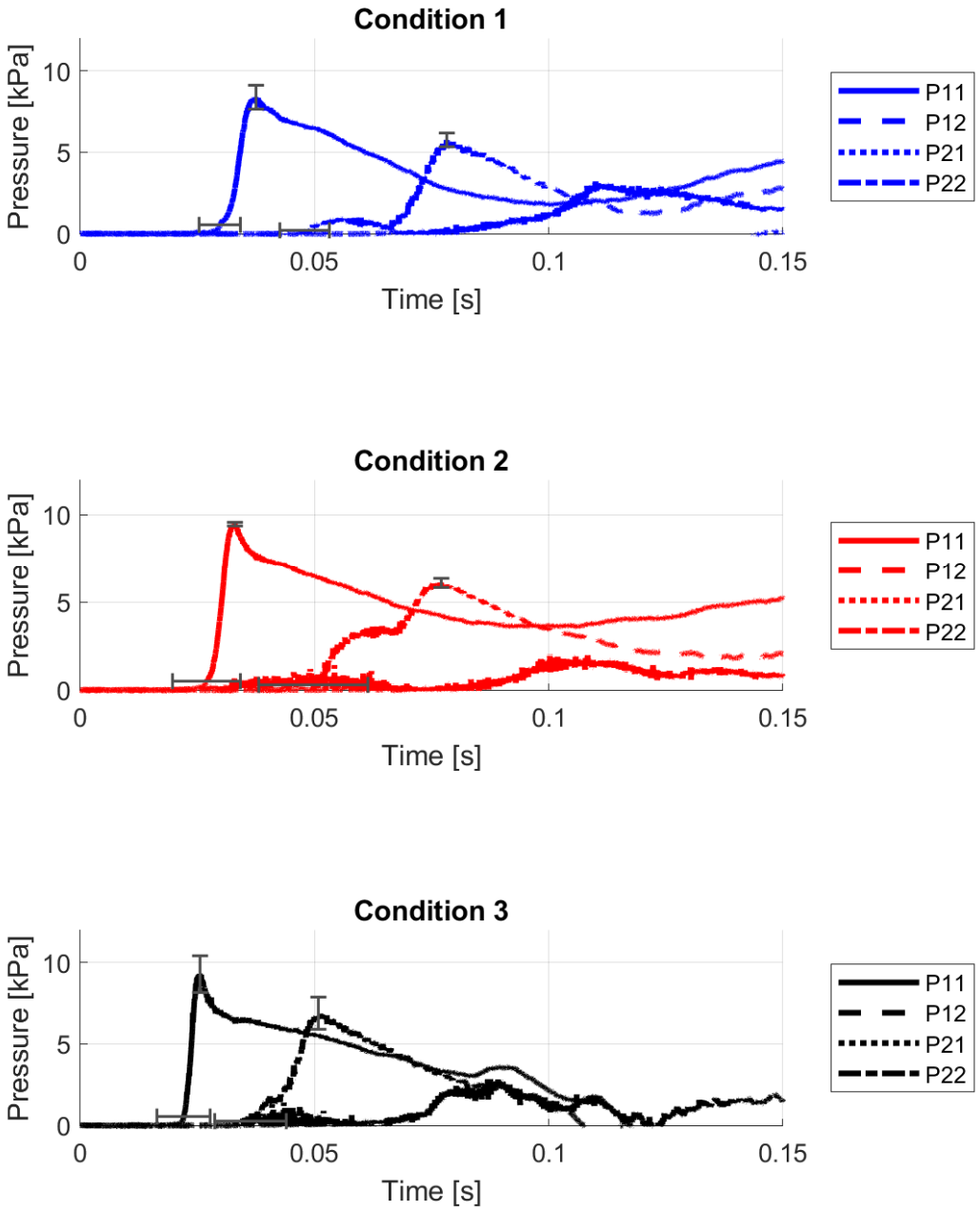

Figure 5.4: Pressure Distribution For All Conditions in the Verification Study. Error Bars Represent Standard Deviations in Pressure Rise Time Instant (Horizontal) and in Peak Pressure Magnitude (Vertical).

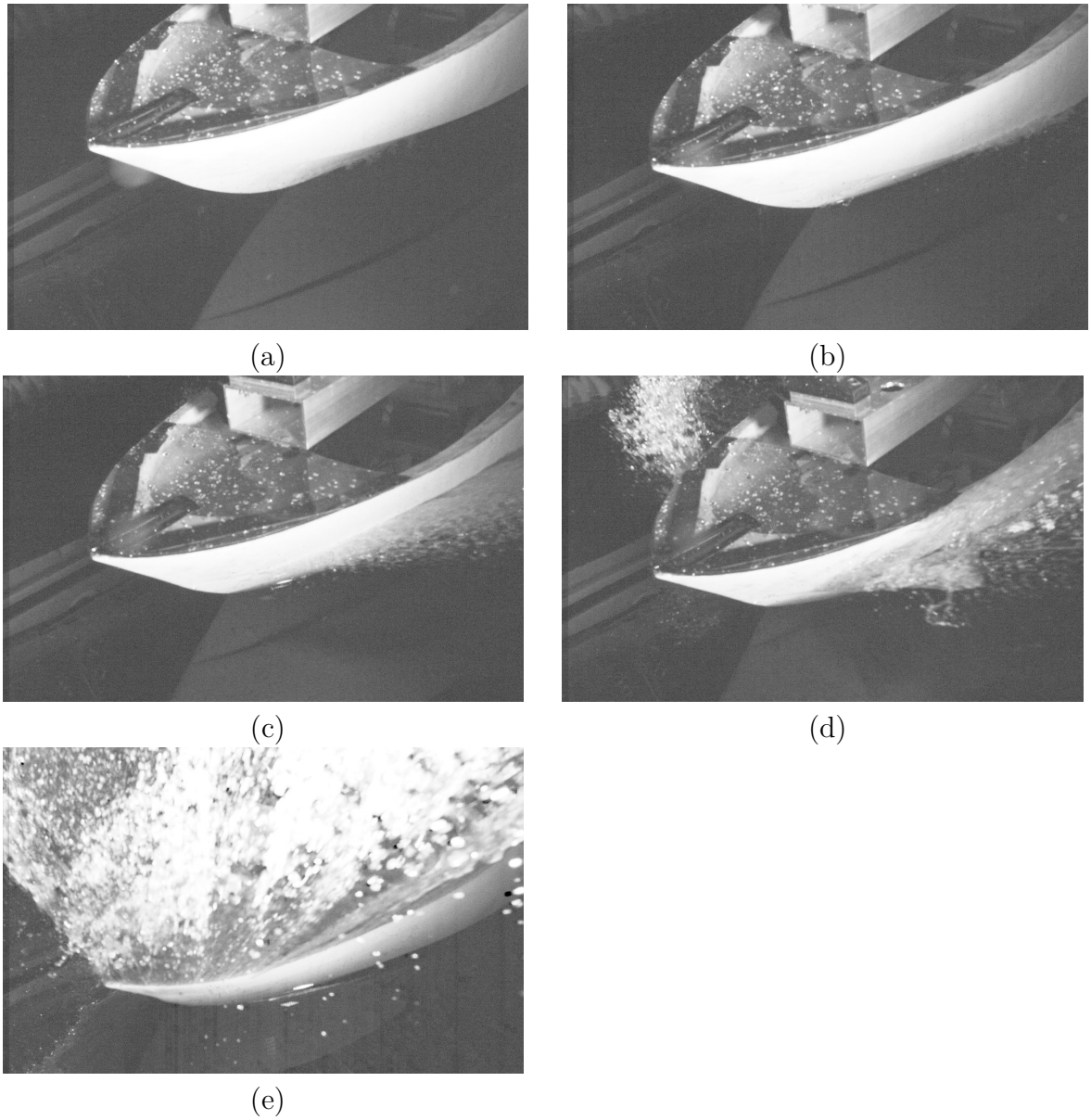

Figure 5.5: High-Speed Video Snapshots from Condition 1 Trial 1: (a) at impact start, (b) at time of P11 peak pressure, (c) at time of P12 peak pressure, (d) of time P22 peak pressure, and (e) at time of peak submergence.

experiments. The data collected by pressure sensors P21 and P22 are not consistent with the wedge drop experiments. This may be due to the difference in the experimental setup between traditional wedge drop experiments and the experiment discussed in this thesis. As mentioned in Section 5.1, Subsection 5.1.1, there was a limit to the submergence depth to avoid flooding in this experiment. This limit, driven by the significant bow down trim angle in all conditions, led to little to no spray root propagation over the P21 and P22 sensors. Testing revealed this as a limitation of the experimental setup. Future work should utilize a method to overcome this issue and make better use of these sensors when the bow down trim angle is significant. Creating a watertight deck could enable the topside near the bow to submerge, thereby increasing the allowable submergence depth for these experiments.

The Verification Study compared the data collected by Judge *et al.* to the data collected at Virginia Tech [5, 6, 7]. As previously discussed in Chapter 2, Section 2.2, Subsection 2.2.2, the GPPH model used by Judge *et al.* at the USNA towing tank is nearly identical to the GPPH model used at Virginia Tech. In addition, the point pressure sensors are in nearly identical positions on both models. These close similarities should make the results generated by both experiments comparable. Figure 5.6 displays the peak pressure over run 81 at the USNA. Notice that there is a variation in the peak pressure magnitudes. In this particular data set, the minimum peak on pressure sensor P11 was measured to be $P = 0.488$, and the max was $P = 0.597$. The range between the maximum and minimum peak pressures for each run will be represented as black dashed horizontal lines in the Virginia Tech data during comparison. The reduced repeatability was noted in the conclusion of Judge *et al.* (2020) [7]. The paper stating that the cause of this variation was due to the wave maker having issues making a consistent incoming wave. In addition, the GPPH model did not have sufficient time to return to steady state motion in between slam events. This led to the effects of one slam event to carry over to the next slam event.

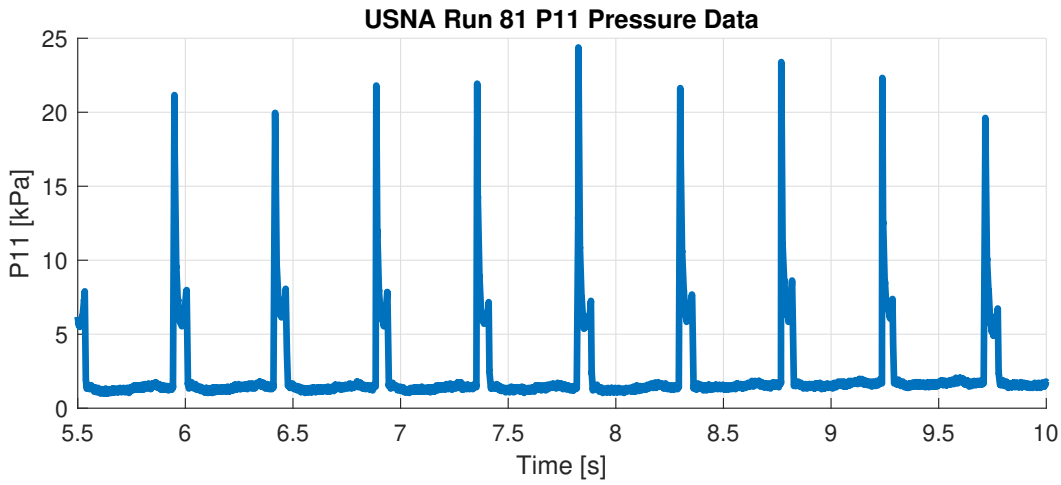

Figure 5.6: Display of Repeatability of Pressure Sensor P11 for USNA Run 81

One of the advantages of the Virginia Tech VPMM combined with the towing tank carriage is its highly consistent and controlled motion. This system led to precise testing between the experimental trials. Figure 5.7 below demonstrates this precision with an example of the data collected by P11 and P12 across the five trials conducted for condition 3. The range of peak magnitudes is very low compared to the range of peak magnitudes collected from the traditional towing tank setup at the USNA.

Figure 5.8 displays the peak pressure over time recorded by sensors P11 and P12 for all three conditions conducted at Virginia Tech. Figure 5.9 displays the same data, now overlaid and nondimensionalized. The first condition is colored blue. The second and third conditions are colored red and black, respectively. The horizontal black dashed lines in the figure represent the range of peak pressure magnitudes measured at the same sensor location during the Judge *et al.* experiments. In all three conditions, pressure sensor P11 is less than expected. In contrast, pressure sensor P12 is within the range of values measured at the USNA for conditions 1 and 3. For condition 2, the value that P12 measures is higher than the range.

The lower than expected values measured by P11 across all the conditions may be due to the reduced relative velocity imposed on the GPPH. Recall that the system limitations of the

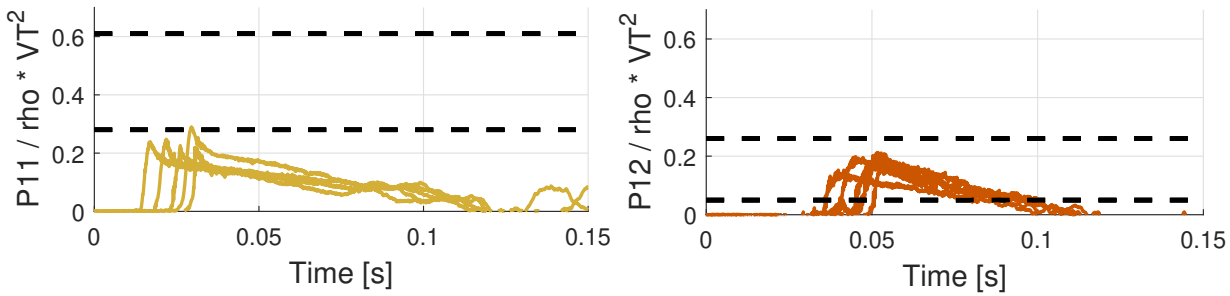

Figure 5.7: Display of Repeatability with Five Repeated Trials Overlaid on Graph, Black Dashed Lines Represent USNA Range

Virginia Tech carriage meant that the celerity of the USNA waves could not be accounted for in experimentation. Either slower speeds at the USNA or upgrades at Virginia Tech are required to validate the Virginia Tech slamming experimental setup with the USNA.

5.1.4 Force Analysis

The data presented in Figure 5.11 displays the average total force measured along the Z' axis over the time of the slam. Overlaid onto these graphs is the average vertical position of the GPPH as the model was submerged into the water over time. Recall that the time and position of impact correspond to when time and position are equal to zero, respectively. The yellow dashed vertical line corresponds to the end of the steady state velocity window. For each of the three conditions, the force gradually increases at the start of the impact. As the model is submerged further, the measured force increases rapidly. The peak force occurs around the same time as the peak submergence, when the buoyancy force is at its greatest. After the peak submergence, the model begins to rise until it exits the water. The inertial forces provided by the linear actuators and the carriage are included in this data. In the

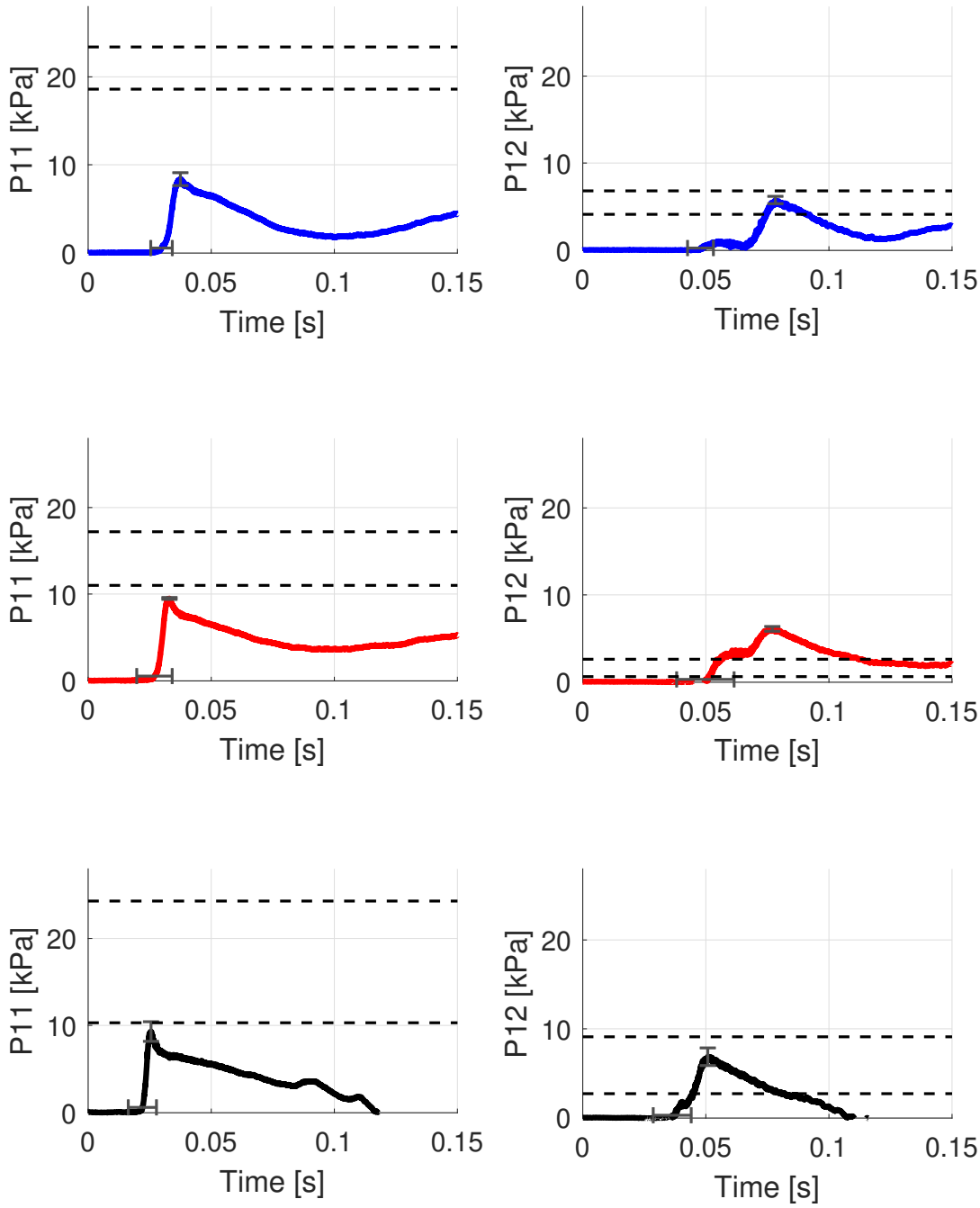

Figure 5.8: Bow Pressure Distribution For All Conditions in the Verification Study. Error Bars Represent Standard Deviations in Pressure Rise Time Instant (Horizontal) and in Peak Pressure Magnitude (Vertical).

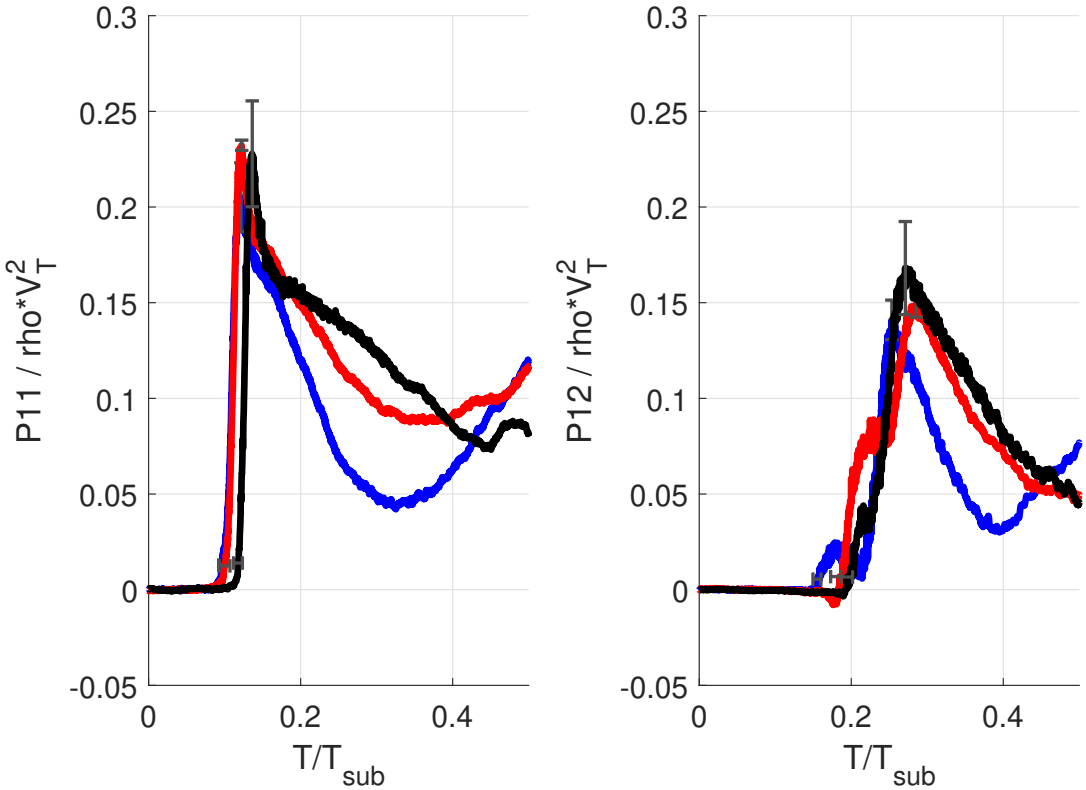

Figure 5.9: Dimensionless Bow Pressure Distribution For All Conditions in the Verification Study. Black Dashed Lines Represent USNA Range, Error Bars Represent Standard Deviations in Pressure Rise Time Instant (Horizontal) and in Peak Pressure Magnitude (Vertical).

future, a dry run of all the conditions should be conducted and subtracted from the data set to isolate the forces solely due to water impact.

At this time, no load cell data from the USNA testing is available for comparison. Any future force comparison between the Virginia Tech experiment and the USNA experiment should only occur during the steady state velocity window, where the relative dynamics model discussed in Chapter 3 is valid. As such, the analysis of the physical phenomena that occur after the steady state velocity window is not within the scope of this thesis. The behavior of the forces measured after the steady state window does appear qualitatively interesting. The current capabilities of the Virginia Tech Impact Basin allow for future work to study the deceleration period and the water exit after the slam.

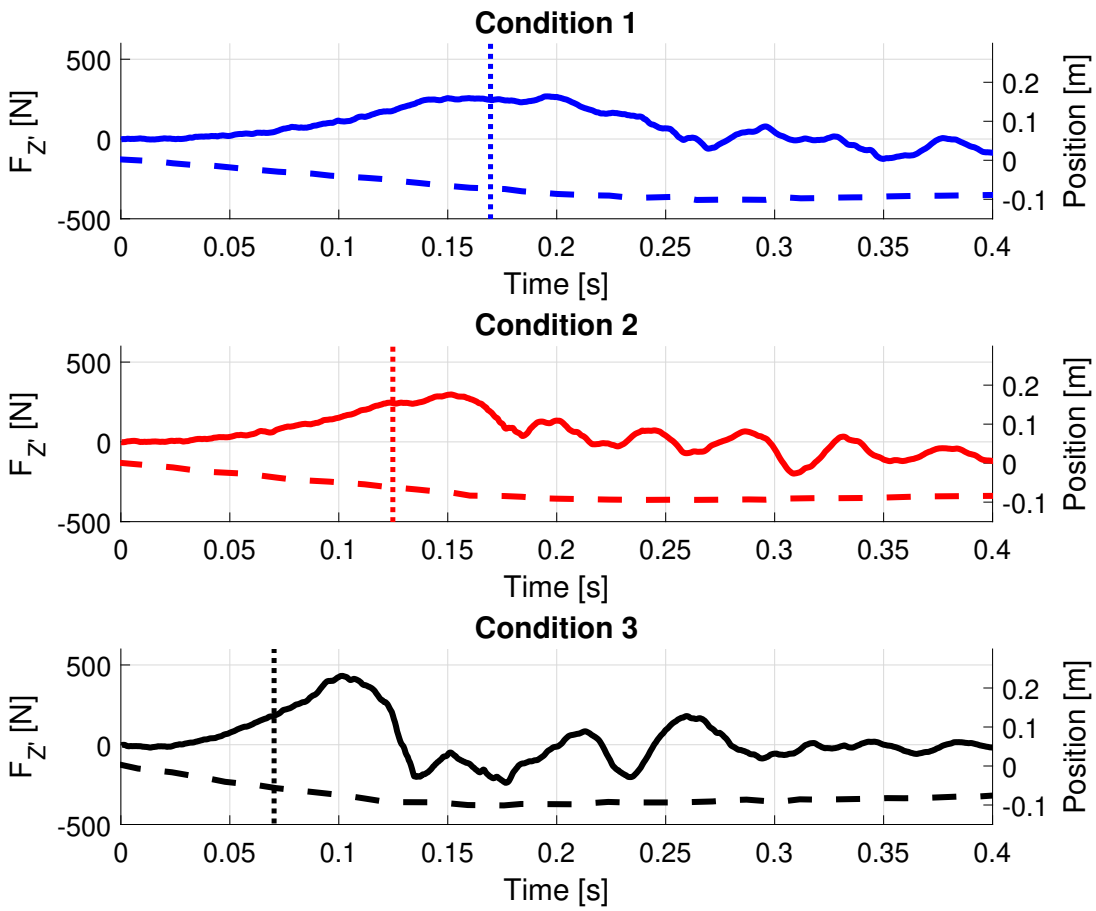

Figure 5.10: Force and Position Distribution For All Conditions in the Verification Study. Dashed Line Represents Position. Vertical Line Represents the End of Steady State Window.

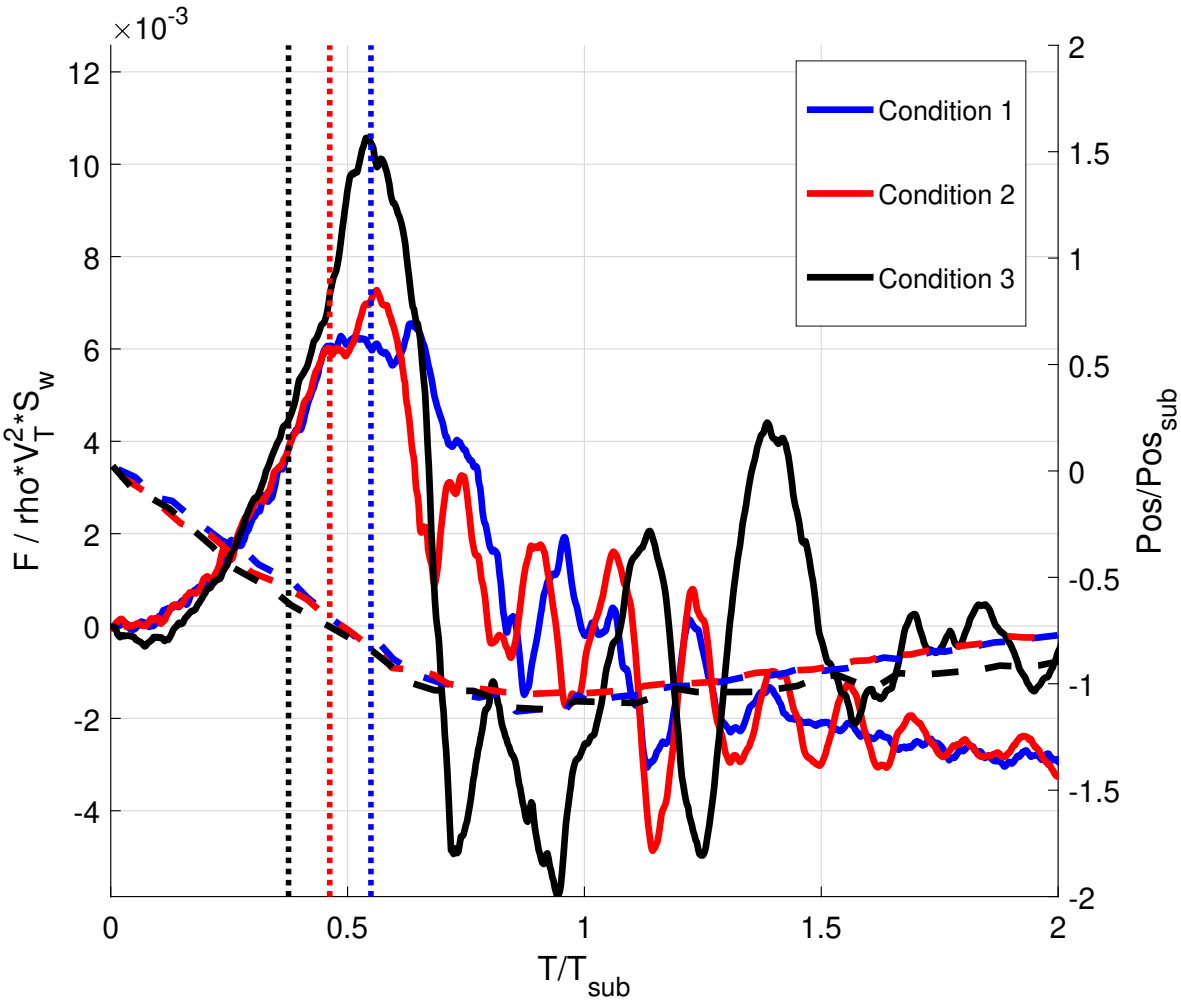

Figure 5.11: Dimensionless Force and Position Distribution For All Conditions in the Verification Study. Dashed Line Represents Position. Vertical Line Represents the End of Steady State Window.

5.2 Parametric Study Results

While the Verification Study's experimental matrix sought to validate the experimental setup, the Parametric Study's experimental matrix was conducted to study the effects of the controllable parameters. There were 32 total conditions that were repeated three times each to develop the data presented below. The detailed information is available for all 32 conditions in Table A.1. This section focuses on a select set of representative cases that demonstrate the edges of the data and the overall trends. Condition 13 and 29 are used for the varying surge velocity case. Condition 1, 5, 9, and 13 are used for the varying heave velocity case. Condition 29, 30, 31, and 32 are used for the varying trim angle case.

5.2.1 Model Dynamics

The Parametric Study had much of the same model motion requirements as the Verification Study, with a few differences. The steady state velocity at impact conditions was held for all trials of the Parametric Study. The deceleration period following the steady state velocity was consistent for most cases as well, except for the slowest heave velocity case. For the slowest heave velocity of 0.25 m/s, a deceleration of 5 m/s^2 was prescribed. For all other faster heave velocities, a deceleration of 15 m/s^2 was prescribed. The consistent submergence depth condition needed to be altered for the limiting case when the trim angle was -15°. Throughout the Parametric Study, the submergence depth stayed at 90 mm for the 0°, -5°, and -10° cases. The -15° case had a significantly lower allowable submergence, therefore, it could not safely avoid flooding at 90 mm of depth. As a result, a depth of 60 mm was chosen for the -15° case. Just as with the Verification Study, when the maximum submergence depth was reached, the model was lifted out of the water at 0.1 m/s for 1 to 2 seconds, depending on the case.

Condition	Trim (deg)	S_w (m2)	V_S (m/s)	V_H (m/s)	V_T (m/s)
1	0.000	0.419	5.000	0.250	5.006
2	-5.000	0.323	5.000	0.250	5.006
3	-10.000	0.196	5.000	0.250	5.006
4	-15.000	0.067	5.000	0.250	5.006
5	0.000	0.419	5.000	0.500	5.025
6	-5.000	0.323	5.000	0.500	5.025
7	-10.000	0.196	5.000	0.500	5.025
8	-15.000	0.067	5.000	0.500	5.025
9	0.000	0.419	5.000	0.750	5.056
10	-5.000	0.323	5.000	0.750	5.056
11	-10.000	0.196	5.000	0.750	5.056
12	-15.000	0.067	5.000	0.750	5.056
13	0.000	0.419	5.000	1.000	5.099
14	-5.000	0.323	5.000	1.000	5.099
15	-10.000	0.196	5.000	1.000	5.099
16	-15.000	0.067	5.000	1.000	5.099
17	0.000	0.419	7.000	0.250	7.004
18	-5.000	0.323	7.000	0.250	7.004
19	-10.000	0.196	7.000	0.250	7.004
20	-15.000	0.067	7.000	0.250	7.004
21	0.000	0.419	7.000	0.500	7.018
22	-5.000	0.323	7.000	0.500	7.018
23	-10.000	0.196	7.000	0.500	7.018
24	-15.000	0.067	7.000	0.500	7.018
25	0.000	0.419	7.000	0.750	7.040
26	-5.000	0.323	7.000	0.750	7.040
27	-10.000	0.196	7.000	0.750	7.040
28	-15.000	0.067	7.000	0.750	7.040
29	0.000	0.419	7.000	1.000	7.071
30	-5.000	0.323	7.000	1.000	7.071
31	-10.000	0.196	7.000	1.000	7.071
32	-15.000	0.067	7.000	1.000	7.071

Table 5.1: Full Table of Parametric Study Parameters

5.2.2 Dynamic Pressure Analysis

This section analyzes the relationship between controllable parameter changes and the dynamic pressure distribution. The three controllable parameters in this study are the surge velocity, heave velocity, and trim angle at impact. The results and discussion presented below focus on the effect of changing one of these controllable parameters at a time while keeping all other parameters constant. The effect of the surge velocity on the nondimensional pressure distribution can be visualized by comparing conditions 13 and 29. These conditions both have a trim angle of 0° and a heave velocity of 1 m/s. Individually, condition 13 has a surge velocity of 5 m/s and condition 29 has a surge velocity of 7 m/s. Figure 5.12, shown below displays the effect of this changing surge velocity. The nondimensional pressure distribution for condition 13 has a greater magnitude compared to condition 29 across all four pressure sensors. Note that there is only a small increase in the peak pressure magnitude for condition 13 compared to condition 29. This implies that the surge velocity has a minimal effect on the peak pressure magnitude when the trim angle is 0° and heave velocity is 1 m/s. Condition 13 having a greater nondimensional peak pressure while also having a slower surge velocity suggests that a significant increase in surge velocity only provides a minimal increase in peak pressure when the trim angle is 0° and heave velocity is 1 m/s.

Another controllable parameter in this study is heave velocity at impact. Figure 5.14 below displays the effect that changing the heave velocity has on the nondimensional pressure distribution. The representative cases chosen to represent this effect are conditions 1, 5, 9, and 13. For all of these conditions, the surge velocity is 5 m/s and the trim angle is 0° throughout the impact. Each pressure sensor shown below has a different trend, yielding no obvious global trends. Pressure sensor P11 measured the nondimensional peak pressure to be proportional to the heave velocity.

Surge Velocity (m/s)	Condition	Line
5	13	
7	29	

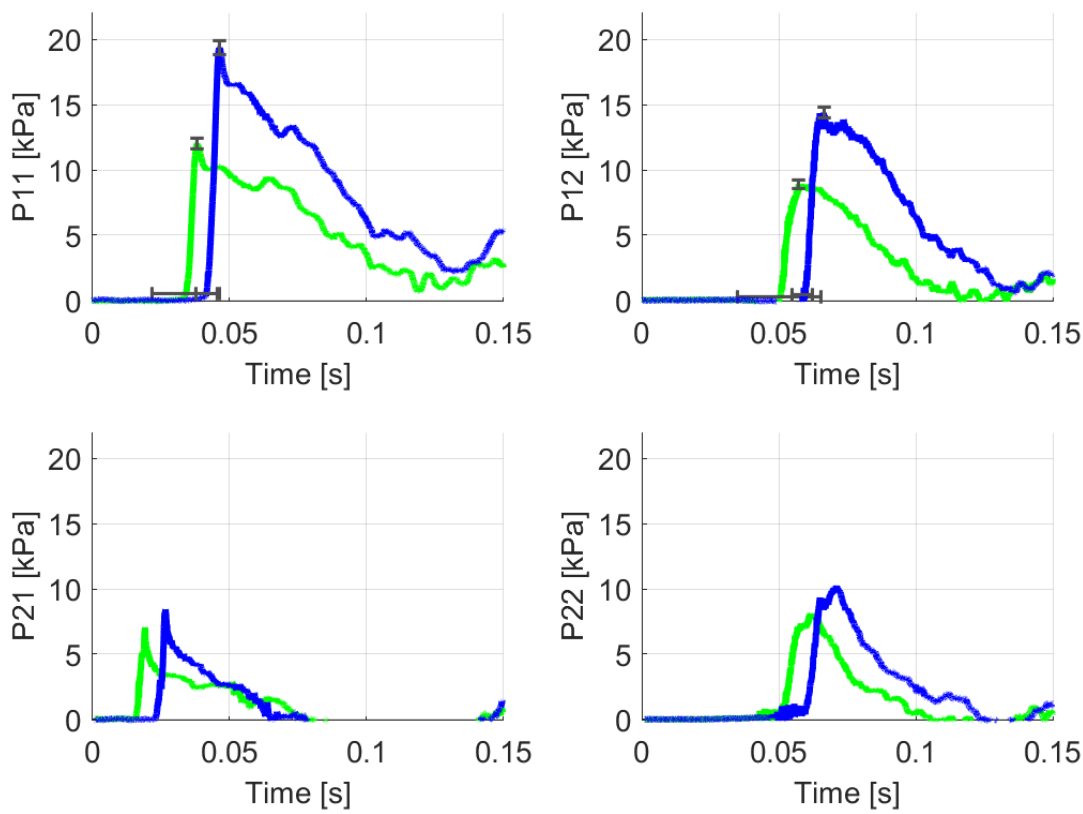

Figure 5.12: Pressure Distribution When Varying Surge Velocity. Trim angle is 0° and Heave Velocity is 1 m/s

Surge Velocity (m/s)	Condition	Line
5	13	
7	29	

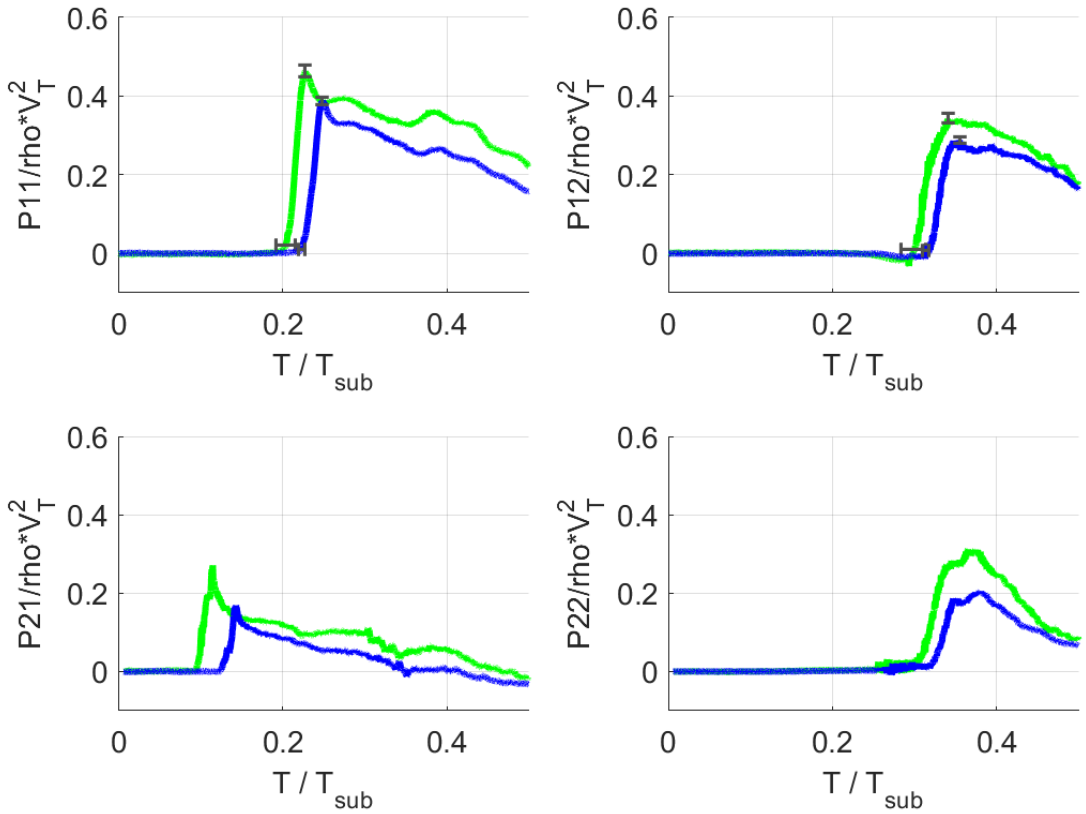

Figure 5.13: Dimensionless Pressure Distribution When Varying Surge Velocity. Trim angle is 0° and Heave Velocity is 1 m/s

As the heave velocity increased, so did the peak magnitude. Interestingly, the peak pressure occurred for the 0.75 m/s case before the peak occurred for the 1 m/s case. Pressure sensor P21 had similar results, but less decisively. The peak pressure magnitude was greatest for the fastest heave velocity, and lowest for the slowest heave velocity. The time that the magnitudes occurred was also tied to the heave velocity, but in the opposite form than expected. The peak occurred soonest for the slowest heave velocity and latest for the fastest heave velocity. Pressure sensors P12 and P22 shared similar trends with each other, albeit different trends than seen on P11 and P21. Both P12 and P22 measured nearly identical pressure distributions for the 0.75 m/s case and the 1 m/s case. These distributions had the greatest peak magnitudes and occurred soonest. The 0.5 m/s case varied slightly between P12 and P22, with P22 measuring a higher peak magnitude. Both sensors saw little to no pressure measured for the 0.25 m/s case.

The third controllable parameter was the trim angle during impact. Figure 5.16 below displays the effect that changing the trim angle has on the nondimensional pressure distribution. The representative cases chosen to represent this effect are conditions 29, 30, 31, and 32. For all of these conditions, the surge velocity is 7 m/s and the heave velocity is 1 m/s throughout the impact. A few global trends could be identified for this parameter change. The magnitude of the peak pressure was inversely proportional to the trim angle across all the pressure sensors. As the trim angle increased, the magnitude of the peak pressure decreased. On the pressure sensors closest to the keel, P11 and P21, the peak magnitude occurred in the same order. The soonest peak occurred for the -10° case, followed by the -15° case, then the -5° case, and lastly the 0° case.

This order was not apparent for the pressure sensors farther from the keel, P21 and P22. The pressure sensor P21 only had a discernible pressure distribution in the 0° case. All other cases measured negligible distributions. Pressure sensor P22 had discernible peaks for the

Heave Velocity (m/s)	Condition	Line
0.25	1	
0.5	5	
0.75	9	
1	13	

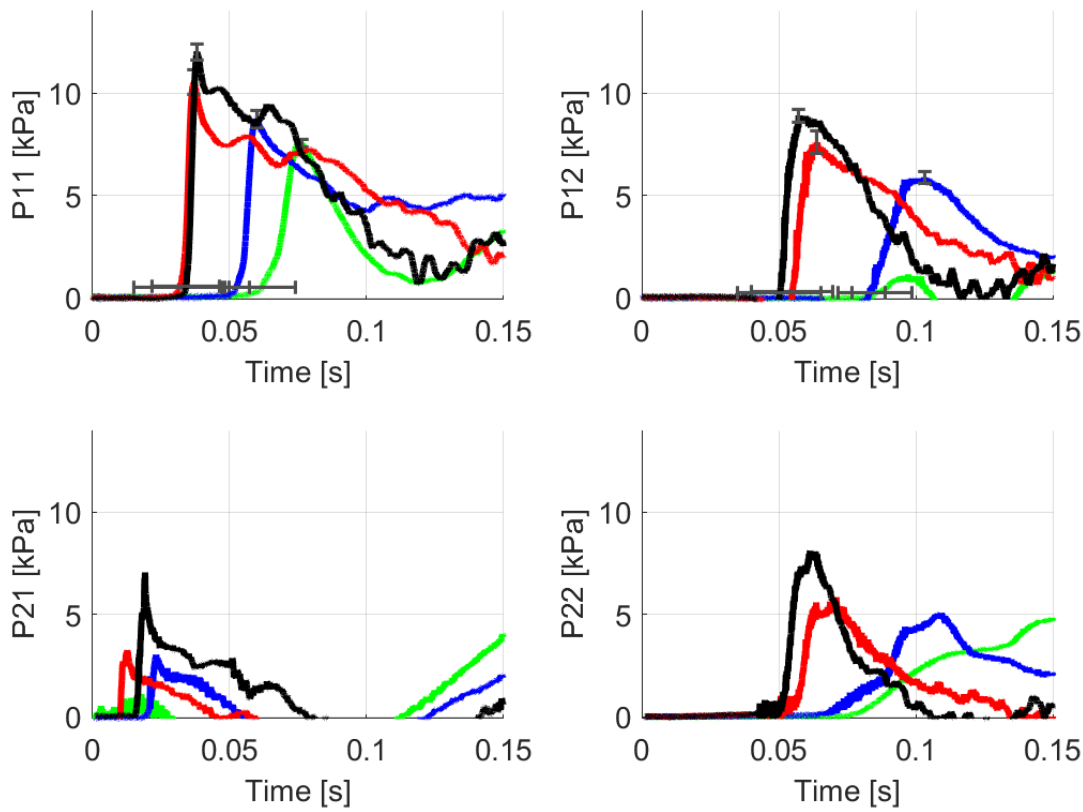

Figure 5.14: Pressure Distribution When Varying Heave Velocity. Trim Angle is 0° and Surge Velocity is 7 m/s

Heave Velocity (m/s)	Condition	Line
0.25	1	
0.5	5	
0.75	9	
1	13	

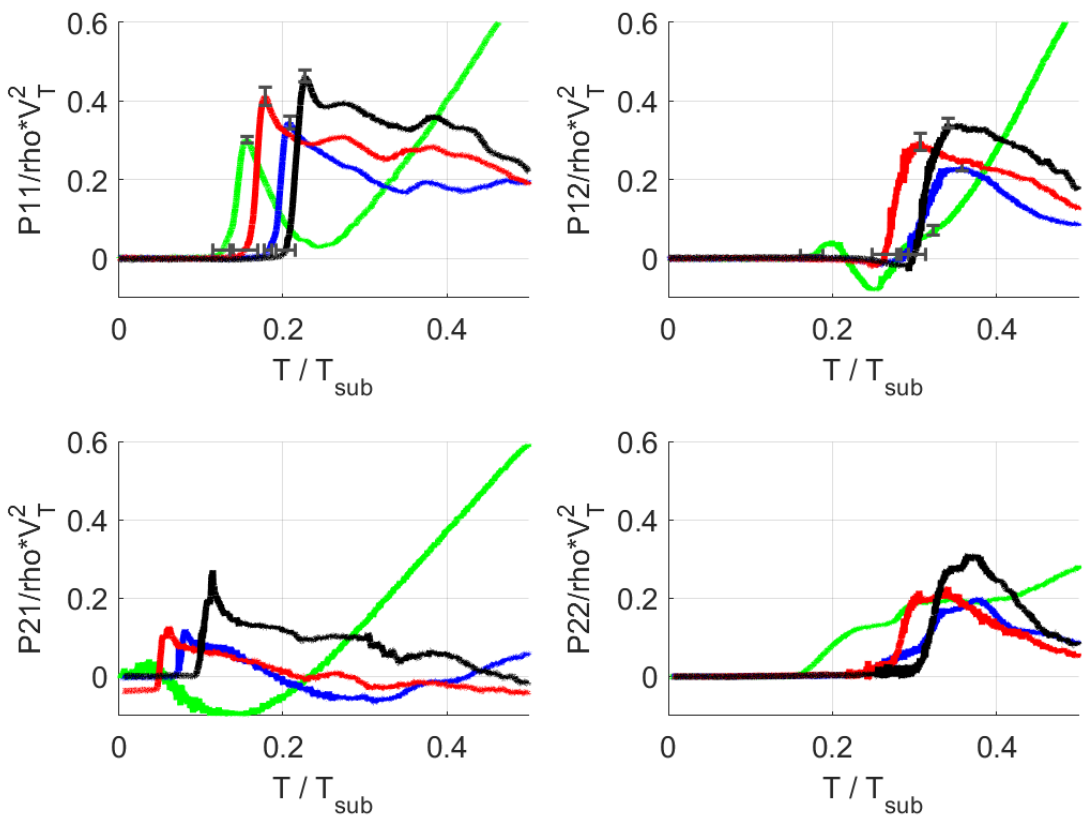

Figure 5.15: Dimensionless Pressure Distribution When Varying Heave Velocity. Trim Angle is 0° and Surge Velocity is 7 m/s

Trim Angle (°)	Condition	Line
0	29	
-5	30	
-10	31	
-15	32	

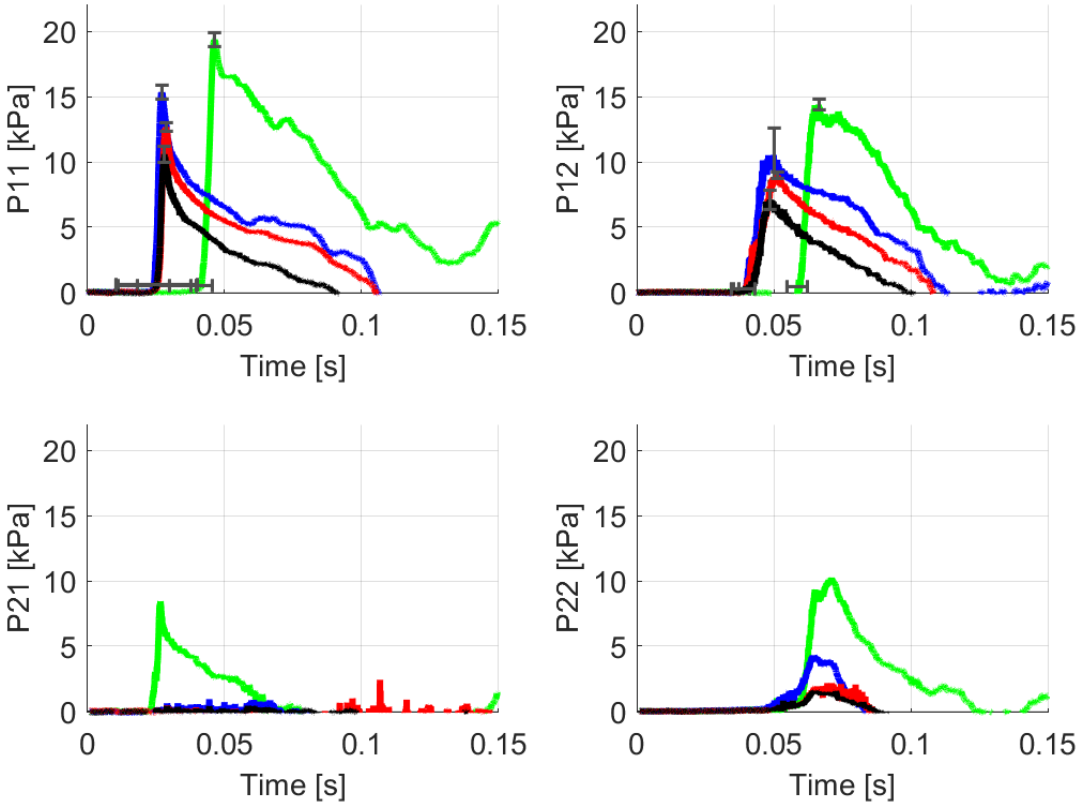

Figure 5.16: Pressure Distribution When Varying Trim Angle at Impact. Surge Velocity is 7 m/s and Heave Velocity is 1 m/s

Trim Angle (°)	Condition	Line
0	29	
-5	30	
-10	31	
-15	32	

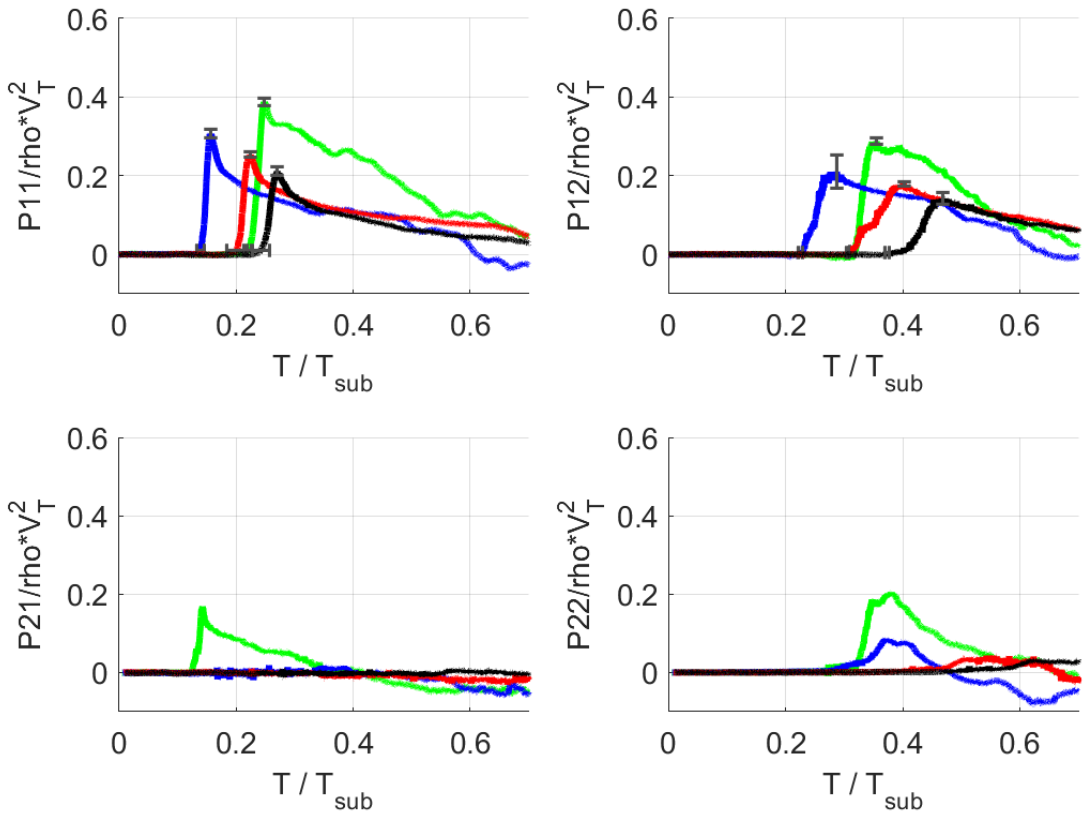

Figure 5.17: Dimensionless Pressure Distribution When Varying Trim Angle at Impact. Surge Velocity is 7 m/s and Heave Velocity is 1 m/s

0° and -5° cases; however, the -10° and -15° cases had negligible values. The 0° case had a larger peak that occurred sooner than the -5° case for this pressure sensor.

The previously mentioned figures display only a select few representative cases to highlight the effects of changing one parameter at a time. The averaged, nondimensionalized, peak pressure for all the conditions is displayed below in Figure 5.18 and Figure 5.19. More analysis on these results will provide further insight.

5.2.3 Force Analysis

This section analyzes the relationship between controllable parameter changes and the average total force distribution measured along the Z' axis. As previously mentioned, this study focused on varying the three controllable parameters individually to isolate their effect on the total force. For each of the trend plots discussed below, one controllable parameter is changing while the other controllable parameters remain constant.

The first controllable parameter that is analyzed is the surge velocity. The representative cases selected to demonstrate this trend are condition 13 and condition 29. Here the heave velocity is 1 m/s and the trim angle is 0°. Individually, condition 13 has a surge velocity of 5 m/s and condition 29 has a surge velocity of 7 m/s. Figure 5.20 below displays the effect that changing the surge velocity has on the force distribution. Each case is represented by a different color, where the force distribution is represented by a solid line, the position profile is represented by a dashed line, and the end of the steady state velocity window is represented by a dotted vertical line. As expected, the faster 7 m/s case generated a greater measured force than the slower 5 m/s case. As was previously seen in the analysis of the forces in the Verification Study, the peak force value occurred beyond the steady state velocity window.

The next controllable parameter that was varied was the heave velocity at impact. Figure

Trim Angle (°)	Surge Velocity (m/s)	Symbol
0	5	●
	7	●
-5	5	◆
	7	◆
-10	5	■
	7	■
-15	5	▲
	7	▲

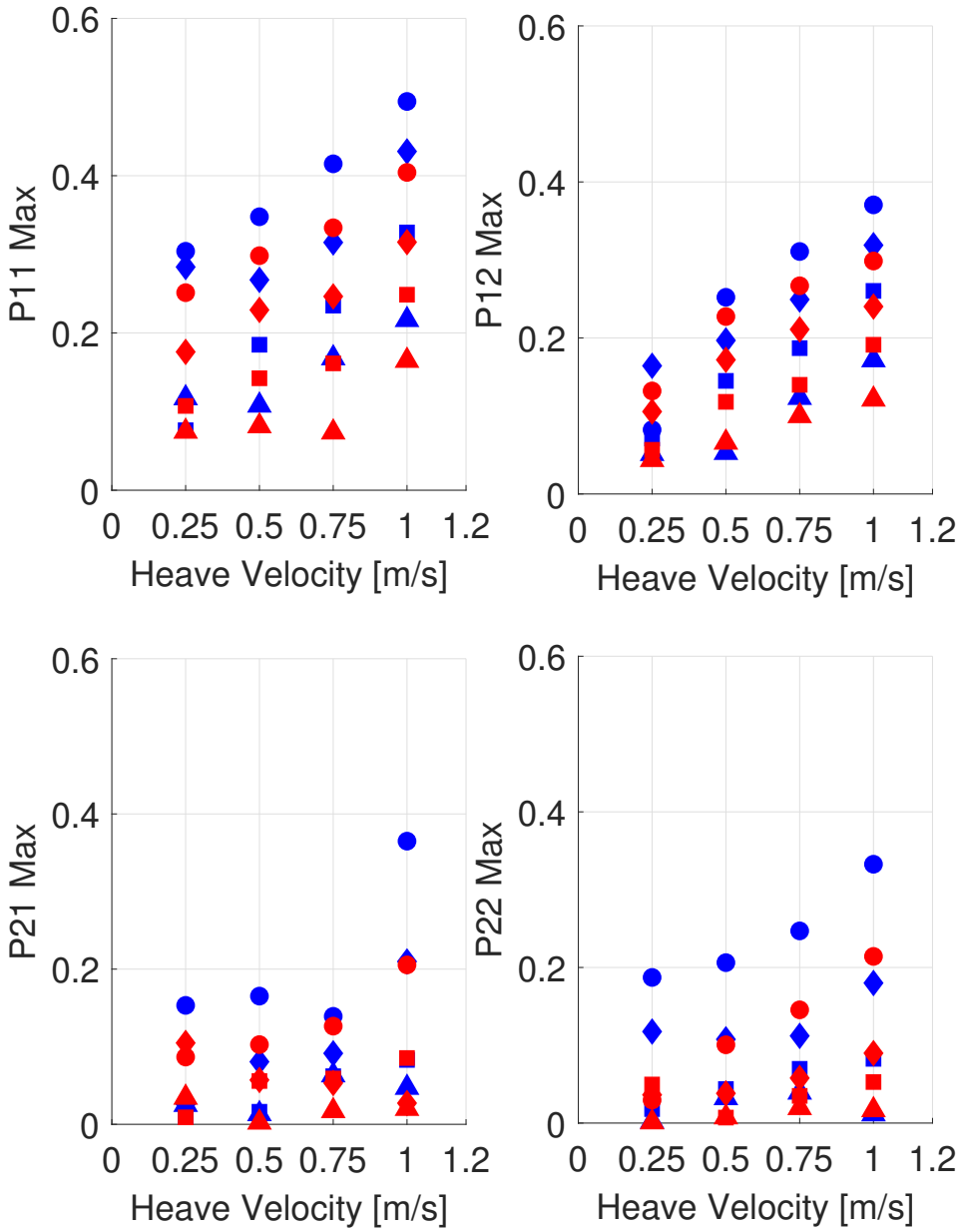

Figure 5.18: Peak Pressure Summary Plot - Varying Heave Velocity

Heave Velocity (m/s)	Surge Velocity (m/s)	Symbol
0.25	5	●
	7	●
0.5	5	◆
	7	◆
0.75	5	■
	7	■
1	5	▲
	7	▲

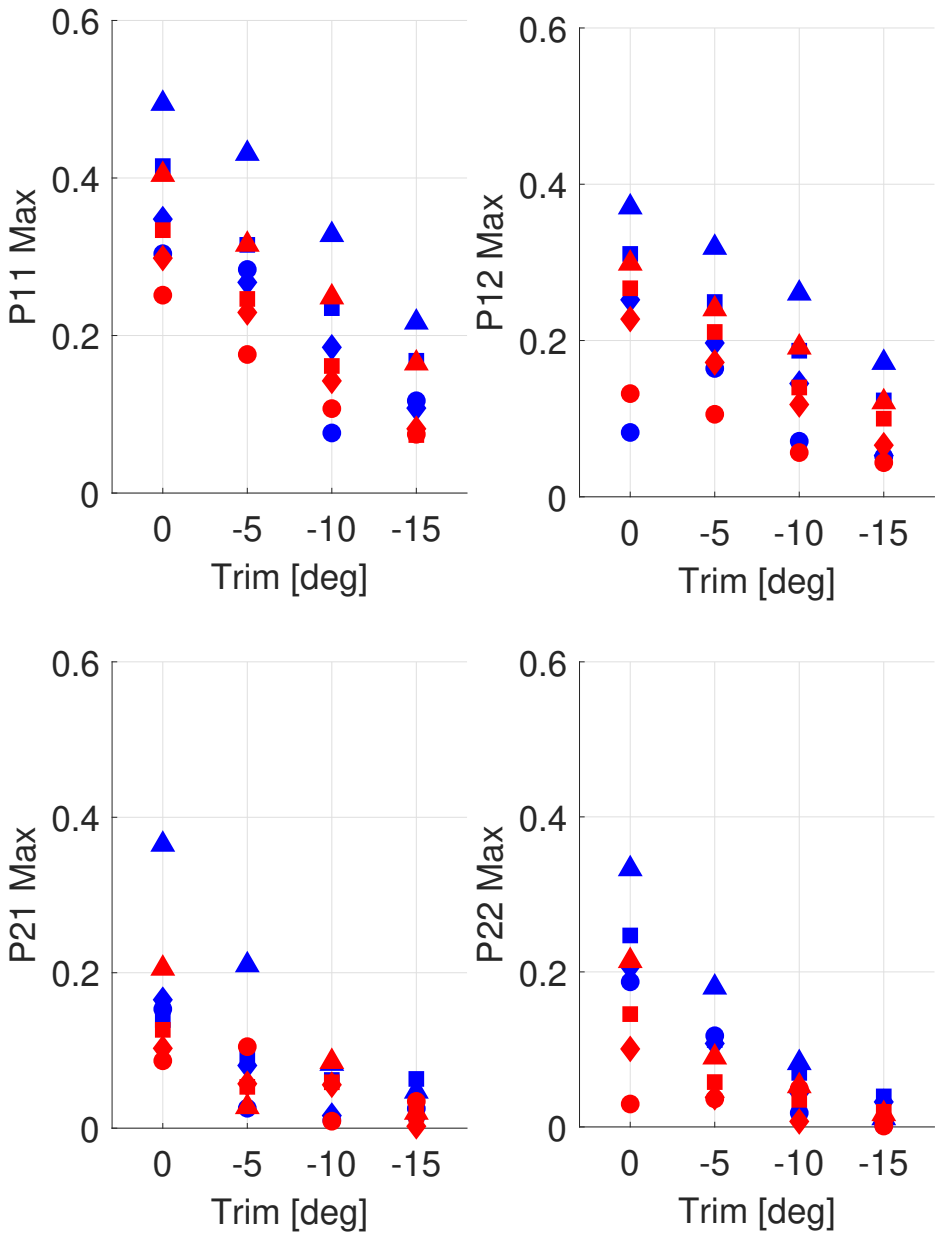

Figure 5.19: Peak Pressure Summary Plot - Varying Trim Angle

Surge Velocity (m/s)	Condition	Variable	Line
5	13	Force	
		Position	
		End Steady State	
7	29	Force	
		Position	
		End Steady State	

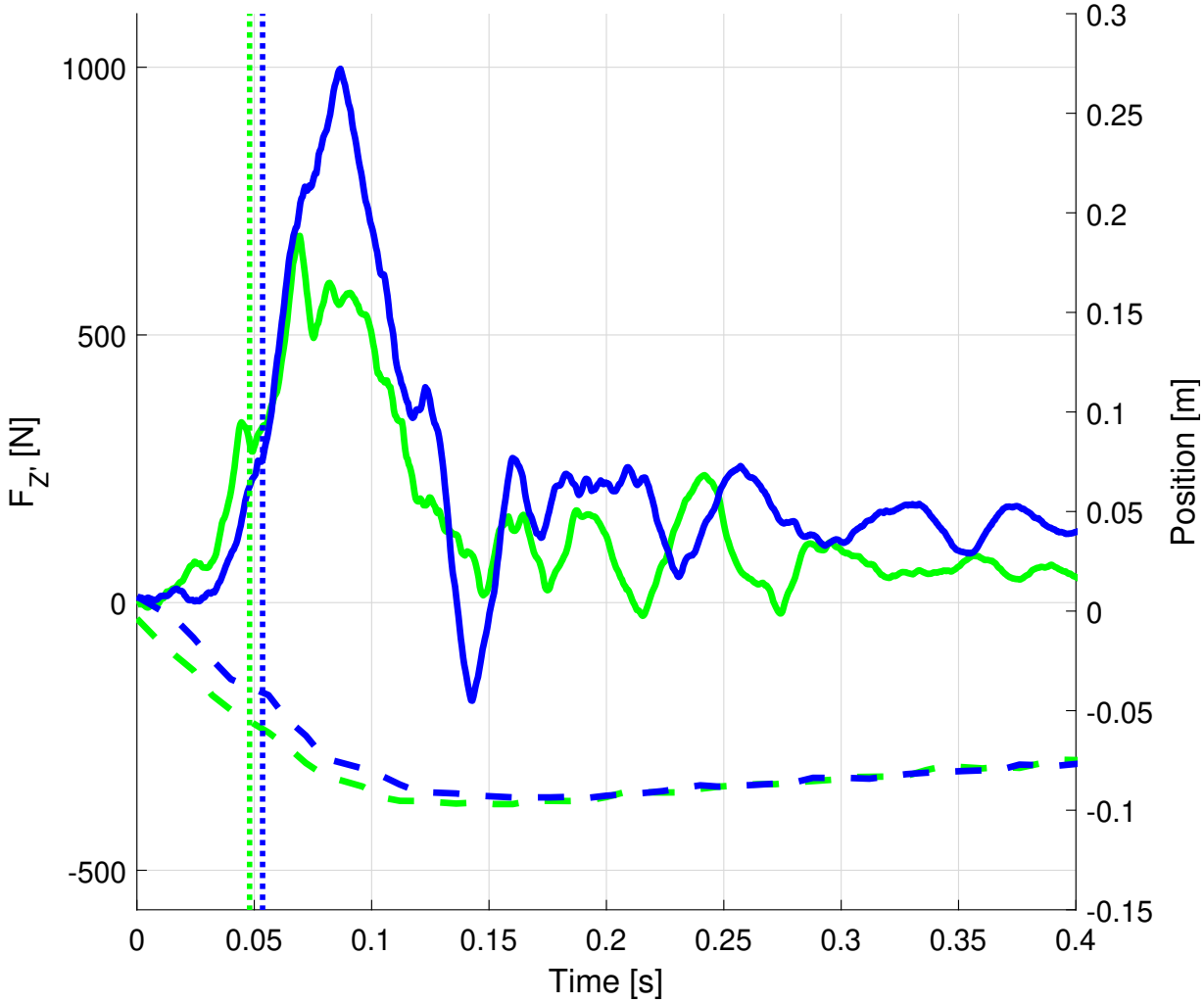

Figure 5.20: Force Distribution When Varying Surge Velocity. Trim Angle is 0° and Heave Velocity is 1 m/s

Surge Velocity (m/s)	Condition	Variable	Line
5	13	Force	
		Position	
		End Steady State	
7	29	Force	
		Position	
		End Steady State	

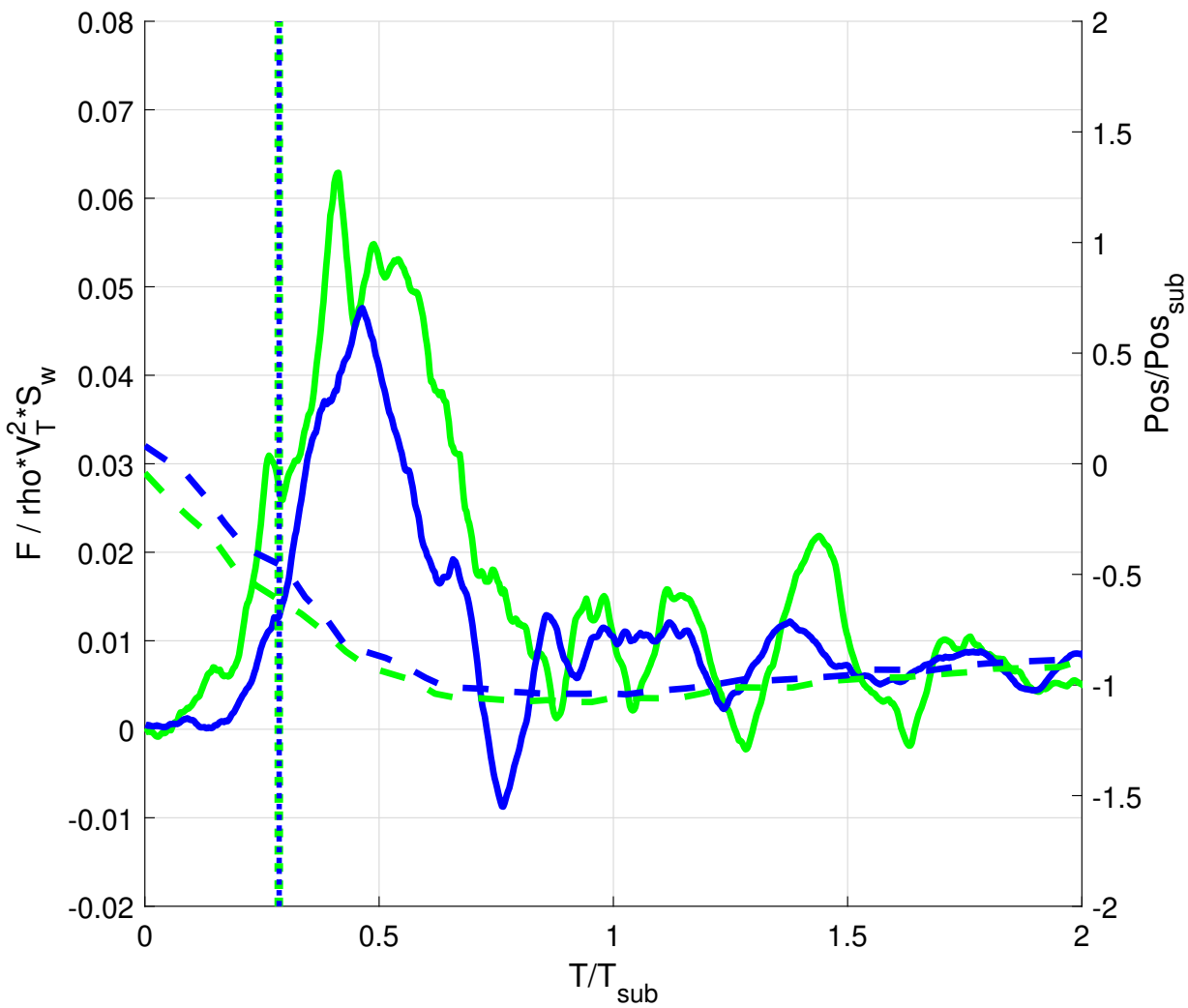

Figure 5.21: Dimensionless Force Distribution When Varying Surge Velocity. Trim Angle is 0° and Heave Velocity is 1 m/s

5.22 below displays the effect of the heave velocity on the force distribution. The representative cases selected were conditions 1, 5, 9, and 13. For each of these conditions, the surge velocity was 5 m/s and the trim angle was 0° throughout the impact. The selected representative cases have the slowest surge velocity and the lowest trim angle. This makes the trends caused by the heave velocity most distinguished. Figure 5.22 has the force distribution, position over time, and end of the steady state velocity window for each condition. As expected, the peak magnitude of the force is proportional to the heave velocity. The fastest heave velocity case measured the greatest peak force, and the slowest heave velocity measured the lowest peak force. Notice that the peak force occurs sooner as the heave velocity increases. This indicates that increasing the heave velocity may increase the rate of force growth. At the faster heave velocities, 0.75 m/s and 1 m/s, the peak force occurs later than the steady state velocity window. This trend is not as distinguished in the lower heave velocity cases of 0.25 m/s and 0.5 m/s. This is likely due to the slower speed cases having an extended steady state velocity window since they do not need the extra time to decelerate to a stop.

The final controllable parameter to be varied in this study is the trim angle during impact. Figure 5.24 below displays the effect that changing the impact trim angle has on the force distribution. The greatest total velocity cases were chosen as the representative group. This is because the trends are most pronounced in the highest velocity cases. The representative conditions are 29, 30, 31, and 32. Analyzing the results reveals that the peak force is inversely proportional to the trim angle. This is likely due to the orientation of the experimental setup. As the trim angle is increased, the submerged volume of the model is decreased. This leads to a reduced buoyancy force throughout the slam event. The previously mentioned figures display only a select few representative cases to highlight the effects of changing one parameter at a time. The averaged peak total Z' force within the steady state velocity window for all conditions is displayed in Figure 5.26.

Heave Velocity (m/s)	Condition	Variable	Line
0.25	1	Force	
		Position	
		End Steady State	
0.5	5	Force	
		Position	
		End Steady State	
0.75	9	Force	
		Position	
		End Steady State	
1	13	Force	
		Position	
		End Steady State	

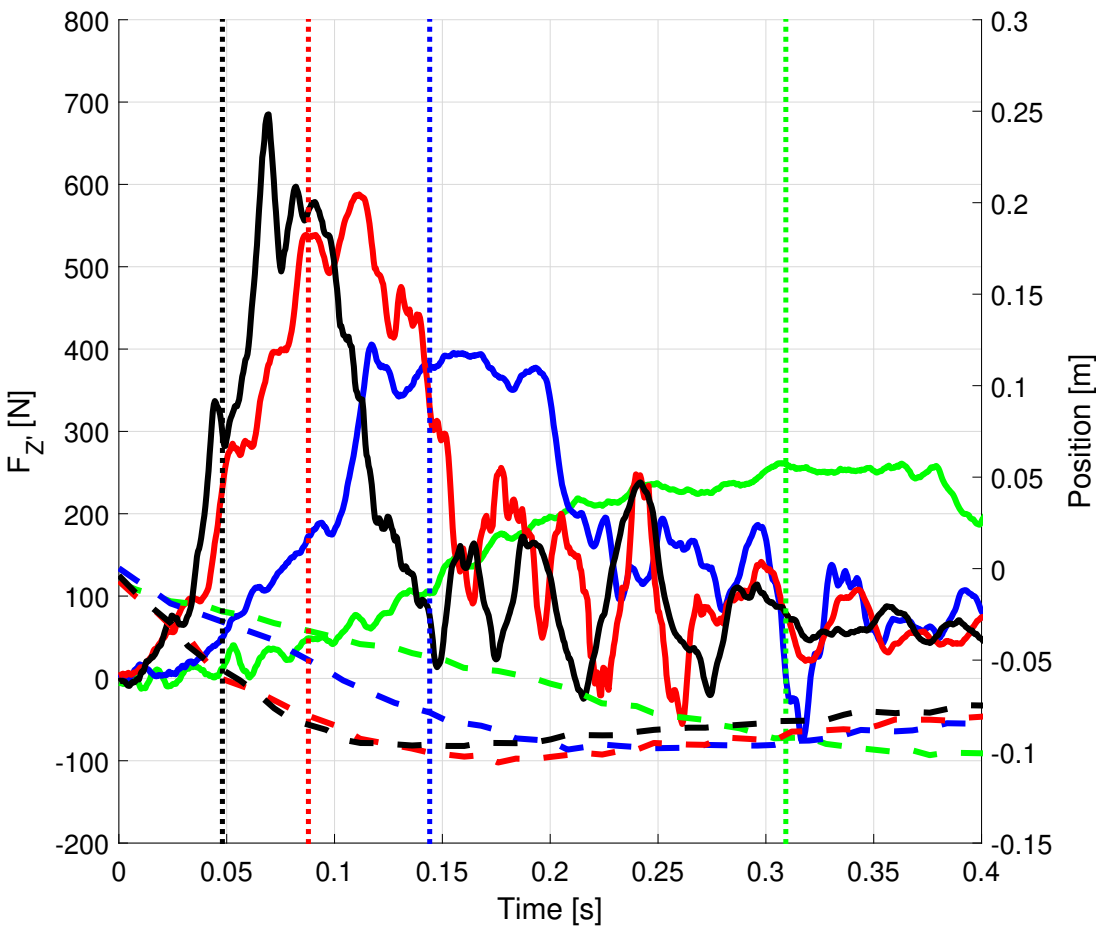

Figure 5.22: Force Distribution When Varying Heave Velocity. Trim Angle is 0° and Surge Velocity is 7 m/s

Heave Velocity (m/s)	Condition	Variable	Line
0.25	1	Force	
		Position	
		End Steady State	
0.5	5	Force	
		Position	
		End Steady State	
0.75	9	Force	
		Position	
		End Steady State	
1	13	Force	
		Position	
		End Steady State	

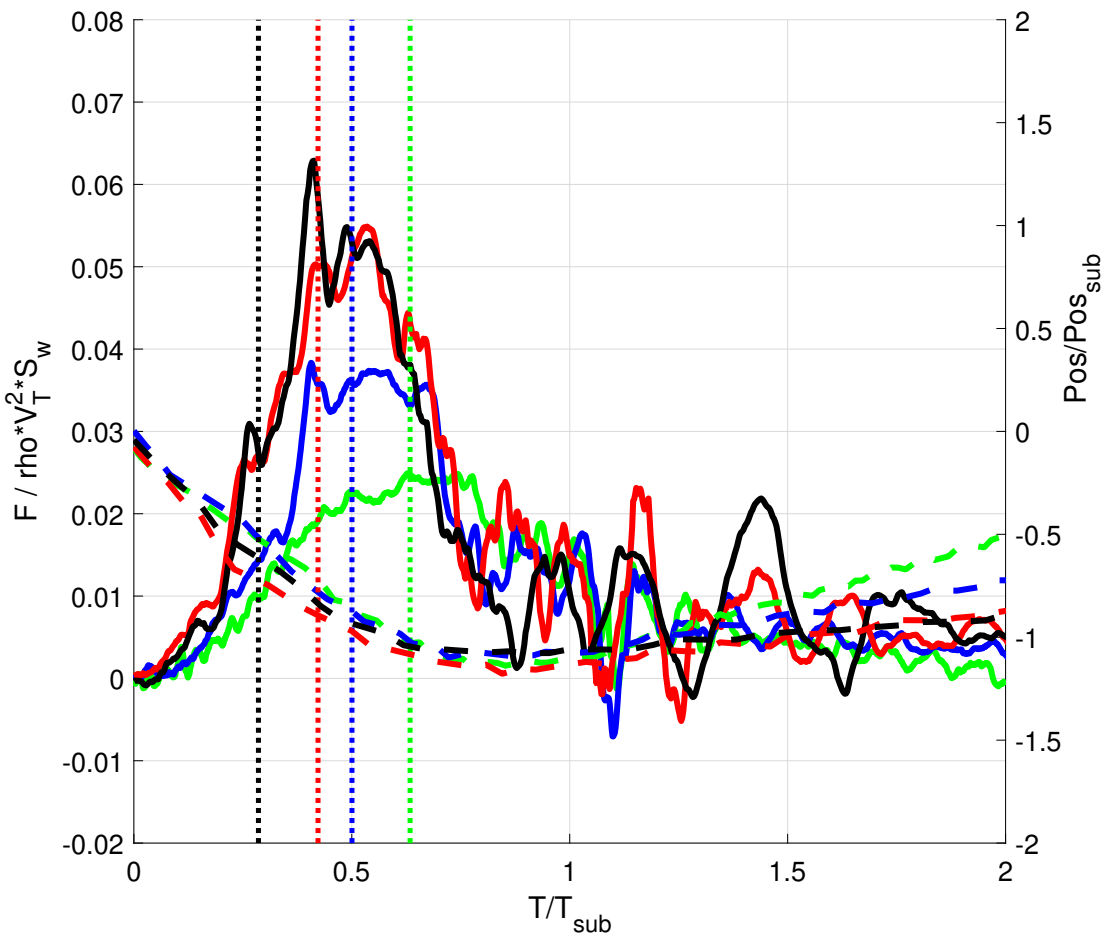

Figure 5.23: Dimensionless Force Distribution When Varying Heave Velocity. Trim Angle is 0° and Surge Velocity is 7 m/s

Trim Angle (°)	Condition	Variable	Line
0	1	Force	
		Position	
		End Steady State	
-5	5	Force	
		Position	
		End Steady State	
-10	9	Force	
		Position	
		End Steady State	
-15	13	Force	
		Position	
		End Steady State	

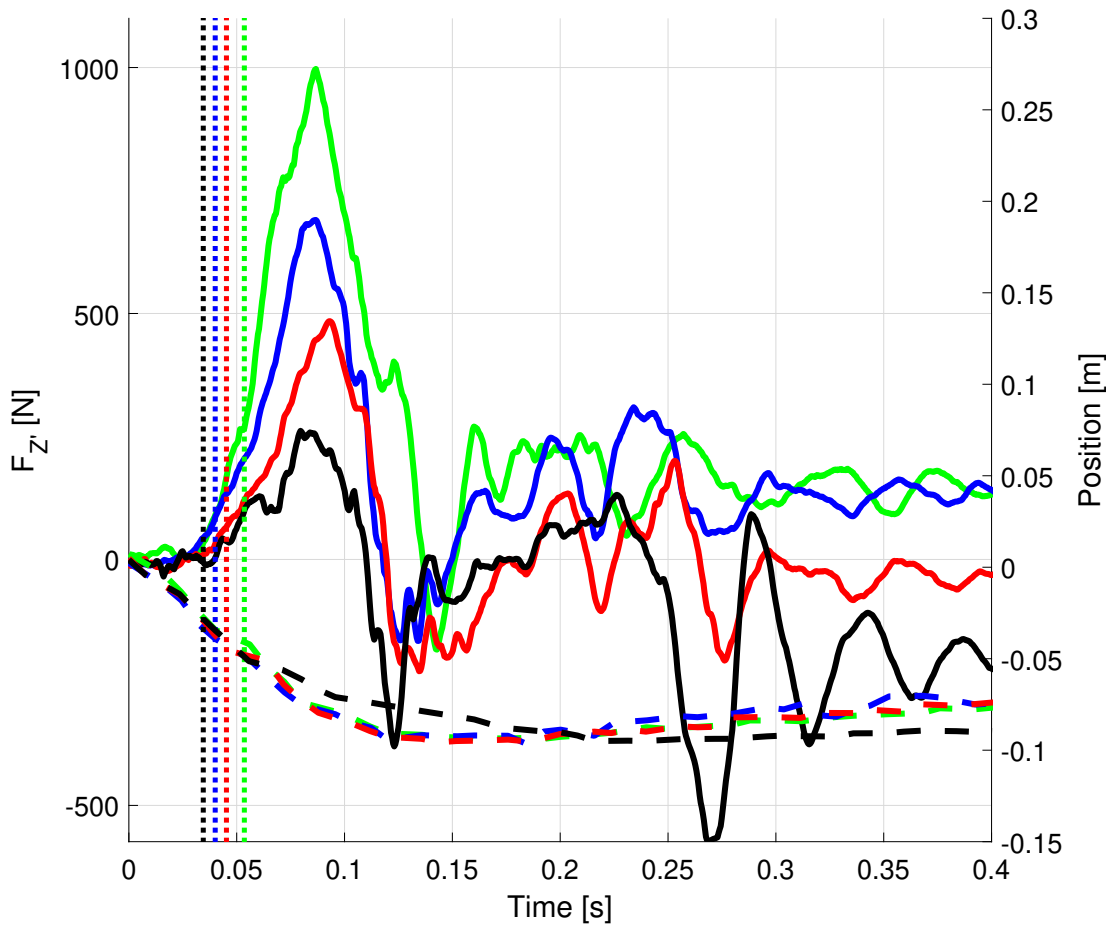

Figure 5.24: Force Distribution When Varying Trim Angle. Surge Velocity is 7 m/s and Heave Velocity is 1 m/s

Trim Angle (°)	Condition	Variable	Line
0	1	Force	
		Position	
		End Steady State	
-5	5	Force	
		Position	
		End Steady State	
-10	9	Force	
		Position	
		End Steady State	
-15	13	Force	
		Position	
		End Steady State	

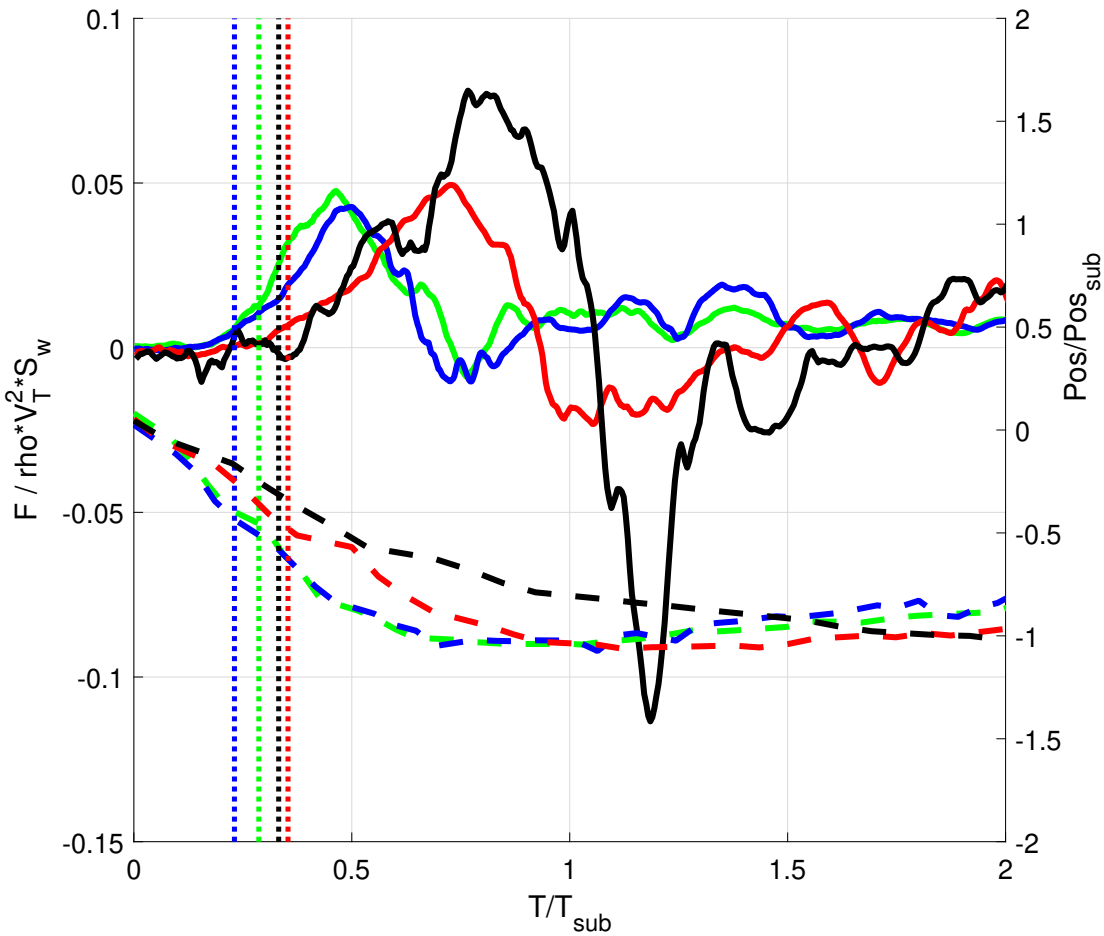

Figure 5.25: Dimensionless Force Distribution When Varying Trim Angle. Surge Velocity is 7 m/s and Heave Velocity is 1 m/s

Trim Angle (°)	Surge Velocity (m/s)	Symbol
0	5	●
	7	●
-5	5	◆
	7	◆
-10	5	■
	7	■
-15	5	▲
	7	▲

Heave Velocity (m/s)	Surge Velocity (m/s)	Symbol
0.25	5	●
	7	●
0.5	5	◆
	7	◆
0.75	5	■
	7	■
1	5	▲
	7	▲

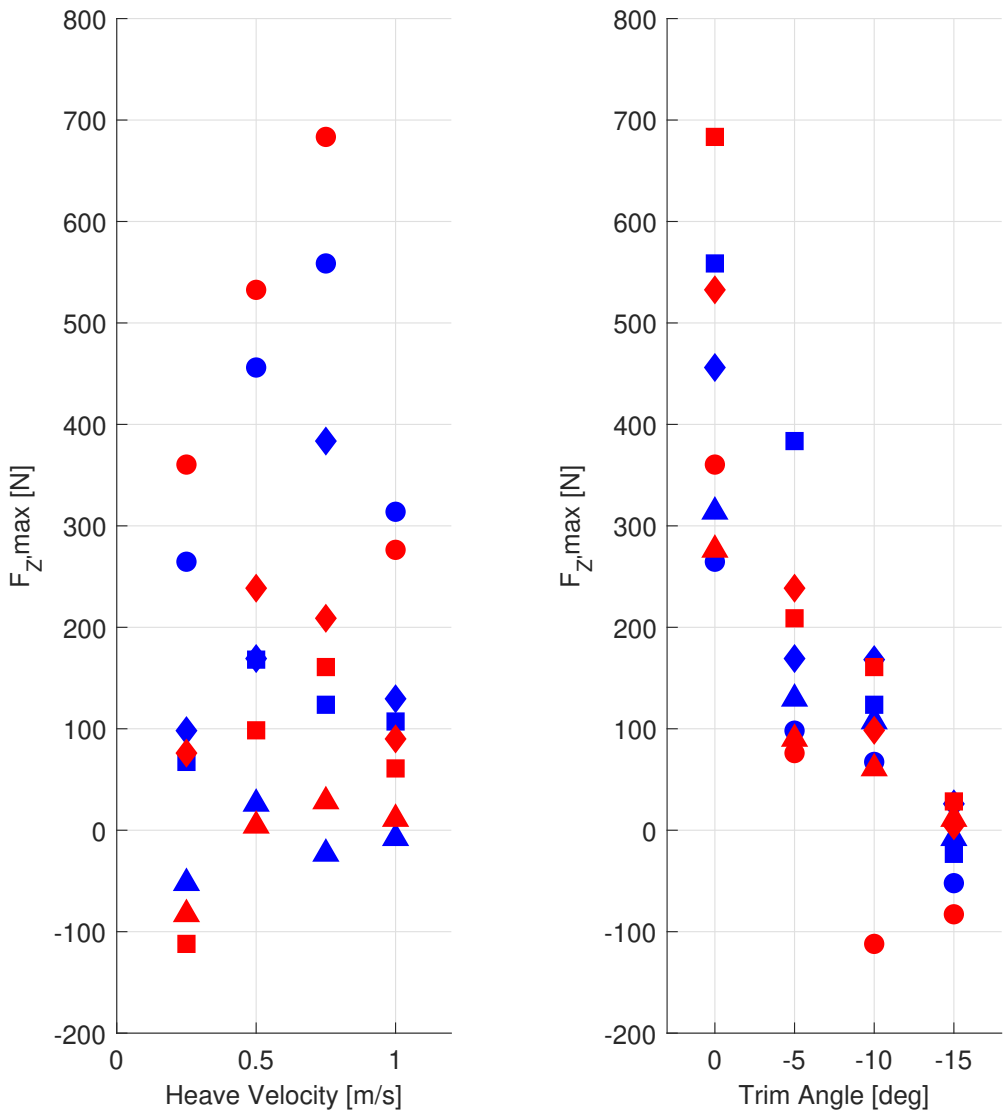

Figure 5.26: Peak Force Summary Plots: Varying Heave Velocity (Left) and Varying Trim Angle (Right).

5.3 System Limitations

Testing for the Verification Study and the Parametric Study revealed system limitations that this analysis and future experiments should take into account. The dynamic model and the current experimental configuration are the sources of these limitations.

The relative dynamic model is valid when the velocities and forces are consistent between the inertial reference frame and the body reference frame. The prescribed motion profiles used in this testing did not account for the changing acceleration observed during the USNA testing. As a result, the force balance between the reference frames is only valid at the time of impact. The proper acceleration profile to justify the body reference frame during submergence needs to be calculated to better retain the physics between Virginia Tech and the USNA.

The dynamic model also assumes that the impacted wave has a constant slope. In reality, waves have a highly variable slope. This model does not account for the complex submergence profile that results from this variability. The simplified submergence profile leads to a different buoyancy force over the slam event.

Since the wave is the point of reference in the body reference frame, all the motion in the system needs to be imposed onto the model by the VPMM and towing tank carriage. In extreme cases, when both the wave celerity and the model heading velocity are high in the inertial frame, the body reference frame requires very high model velocities to maintain the system dynamics. Therefore, a limiting factor for high-speed cases is the velocity capabilities of the VPMM and carriage. The velocity capabilities of the VPMM are further limited by the model weight. Heavier models will require greater torque to accelerate and decelerate at the maximum rate. The current GPPH model required too much torque to properly decelerate for the highest heave velocity conditions, resulting in overvoltage errors on the

motors and model position overshoot.

The Virginia Tech GPPH model was made to be as similar as possible to the USNA GPPH model. This included mirroring the location of the pressure sensors between the two models. The USNA GPPH model was made for traditional towing tank testing that assumed the model would be floating on the surface of the water throughout the test. Therefore, the testing would engage all the pressure sensors along the bottom of the hull. The experimental setup at Virginia Tech suspends the GPPH model above the water surface and only submerges the bow for the high trim cases. As a result, the pressure sensors far from the bow are often not engaged for high trim tests.

Currently, the load measured along the Z' axis is dominated by the hydrostatic component of the total force. This is because the velocity component along the Z' axis is very low when the trim angle is 5-10° for the range of heave and surge velocities used in these experimental matrices. The Z' velocity is low due to the orientation of the GPPH in the body frame. The current orientation causes the Z' velocity contributed by the heave velocity and surge velocity to subtract from one another. This makes sense given the current assumptions, as you expect a surface vessel operating in a steady state to have a low heave velocity in the inertial frame. A surface vessel is not flying up into the sky or sinking into the ocean. In a more complex dynamic model, the GPPH could be considered a rigid body with a rotational component. A rigid body model could allow future users to calculate the forces seen at a particular location on the model. This would allow a greater focus on the hydrodynamic component near the bow.

The advantages of this work are its ability to serve as validation data for numerical simulations as well as provide information on how different parameters affect slamming pressures and loads.

In this chapter the Verification Study results for 3 conditions were compared to USNA experiments. Results of the Parametric Study were analyzed for cases when one motion parameter was varied. The first representative case varied surge velocity, with trim angle and heave velocity held constant. The second case varied heave velocity, with trim angle and surge velocity held constant. The third case varied trim angle, with surge and heave velocity held constant.

Chapter 6

Conclusions

6.1 Summary

6.1.1 Vertical Planar Motion Mechanism and Carriage

This thesis presents a novel testing method to analyze the physical phenomena that occur when a surface vessel slams into a wave. The Vertical Planar Motion Mechanism was designed and constructed to carry out this particular test and other similar experiments. The VPMM was combined with the newly redesigned Virginia Tech towing tank carriage to provide controlled heave, pitch, and surge motion. Each linear actuator system in the VPMM is capable of imposing a velocity of 1.3 m/s and an acceleration of 15 m/s^2. The combination of the linear actuators allows for controlled pitch position, velocity, and acceleration. The Virginia Tech towing tank carriage is capable of imposing a velocity of 7 m/s and an acceleration of 5 m/s^2. The VPMM was controlled and synchronized with the carriage by a control software developed in house.

6.1.2 Generic Prismatic Planing Hull

All of the presented tests used the Generic Prismatic Planing Hull as the model. The GPPH has typical characteristics of full scale planing hullforms. The controlled motion being

prescribed to the GPPH provided a means to reliably simulate a wide range of slamming events. A robust mounting setup was designed and constructed to allow a wide range of motions. The mounting setup was also designed for minimal impact on the key physical phenomena studied, especially hydroelasticity effects. The mold for the Virginia Tech GPPH was made from the USNA GPPH to minimize model variation between the two facilities.

6.1.3 Relative Dynamic Model

The Virginia Tech facility does not have an operable wavemaker. The relative dynamic model was created to eliminate the need for a wave to be generated without changing the physics of the slam event. In essence, the relative dynamic model shifts the traditional towing tank test from an inertial reference frame to a body reference frame. The location where the surface vessel impacts the wave is the point of reference in the body reference frame. This particular point of reference sets the velocity of the wave to zero in the body reference frame. In addition, the model approximates the wave as having a constant slope. This approximation means that the wave in the body reference frame has both zero velocity and a constant slope. A reference frame rotation is applied such that the slope of the wave is equal to zero in the body reference frame. This allows the calm water surface to represent the wave in the body reference frame. As a result of these reference frame manipulations, all the motion in the system is applied to the surface vessel. The VPMM and the towing tank carriage together prescribed the necessary heave, pitch, and surge motion onto the surface vessel to maintain the system's physics.

6.1.4 Verification Study Conclusions

The United States Naval Academy ran extensive wave slamming tests on their GPPH model. The testing was conducted at the USNA facility which has a high-speed towing tank carriage and an operable wavemaker. The slamming tests were conducted by towing the GPPH model at a constant surge velocity through a prescribed set of waves. This experiment was chosen as the validation case for the novel testing method developed in this thesis. The Verification Study was conducted to compare the sensor data collected at the USNA to the data collected at Virginia Tech for dynamically equivalent runs. The Virginia Tech GPPH model was made from a mold created by the USNA GPPH model to minimize variation between the tested models. Key dynamic parameters were extracted from the USNA tests and input into the relative dynamic model. Initial calculations found that the Virginia Tech facility did not have the necessary velocity capabilities to conduct dynamically equivalent tests. The wave celerity of the USNA waves was assumed to be zero to reduce the velocity needed to be produced at Virginia Tech to be within system capability. The output of the relative dynamics model calculations, with all the listed assumptions, made the Verification Study experimental matrix tested at Virginia Tech.

The assumptions used in the dynamic model, particularly setting the wave celerity equal to zero, limit the validity of any comparison between the two facilities. Future work should aim to quantify these assumptions' effects to account for them or eliminate them entirely through more complex modeling. The results of the Verification Study were analyzed and discussed, knowing these limitations, to give a baseline for this future work. The measurement of the dynamic peak pressure at the USNA showed significant variation between the runs. Judge *et al.* (2020) commented on the issue of repeatability in the testing [7]. As such, the range of the peak pressure magnitudes measured at USNA were used to compare against Virginia Tech's facility. Two point pressure sensors located near the bow that have equivalent locations on

the USNA GPPH and the Virginia Tech GPPH were selected for comparison. The pressure sensor closer to the baseline consistently measured peak pressures lower than the range. The pressure sensor located closer to the chine measured peak pressures within the range for conditions 1 and 3. For condition 2, the measured peak near the chine exceeded the range.

The USNA experimental setup did not incorporate a load cell into the testing. Therefore, the forces generated during the Virginia Tech testing could not be compared to any USNA data. Hopefully, the USNA will consider adding a load cell to their setup for future experiments to allow further comparison of these two facilities.

The differences between the two facilities is significant at this time. Therefore, the results generated from the USNA testing is not comparable to the Virginia Tech testing. Only one sensor, pressure sensor P12, measured comparable results between the two facilities. None of the other sensors measured supportive data between the two facilities. More development will need to done in order to sufficiently compare the results between these two facilities.

6.1.5 Parametric Study Conclusions

The Parametric Study was conducted to better understand the influence of controllable parameters on measured data across 32 unique conditions. The experimental matrix for this study was derived from the physical limits of the Virginia Tech experimental setup. The controllable parameters were steady state heave velocity, steady state surge velocity, and trim angle during impact. Each condition was conducted three times to strengthen the reliability of the trends. The study varied one parameter at a time while keeping others constant to isolate the effects on peak pressure magnitudes and total force along the Z' axis.

The study suggests that surge velocity has a minimal impact on peak pressure magnitude. The representative cases 13 and 29 showed that slower surge velocities can result in higher

nondimensional peak pressures when the trim angle is 0°. This suggests a minimal effect of surge velocity on dynamic pressure increase. Varying the heave velocity showed inconsistent trends across different sensors. In the dimensionless data, increasing the heave velocity led to the peak pressures occurring later. Increasing the heave velocity also led to greater peak pressures in the dimensionless data for across all four sensors. Increasing the trim angle had an inversely proportional relationship with peak pressure magnitudes. This suggests that increasing the trim angle decreases the peak pressure. The experimental setup limited the dynamic pressure seen on the sensors located near midship at large trim angles.

The study also examined the total force measured along the Z' axis. The results showed a correlation between increased impact velocity and greater peak force magnitudes. Varying the surge velocity once again showed a minimal effect in the dimensionless data when the trim angle was 0°. Varying the trim angle had the inverse effect, where increased trim angles led to decreased peak forces in the dimensional data. This is likely due to the experimental setup. Increasing the trim angle reduced the submerged volume of the model and, consequently, the buoyancy force. The decrease in buoyancy force leads to a decrease in the overall measured force. This effect was seen in the dimensionless force data where the wetted area was accounted for. In the dimensionless data, the largest peak was seen by the -15° trim case. The dimensionless peaks for all other trim angles were similar in value. Overall, the Parametric Study found that the heave velocity and trim angle at impact play a dominant role in the slam event.

6.1.6 System Limitations Summary

The verification and parametric studies identified system limitations due to the dynamic model and experimental setup. The Virginia Tech experiments only mirror the USNA testing

physics at the moment of impact due to unaccounted acceleration profiles and wave slope variability. The Virginia Tech experiments were limited by VPMM and the towing tank carriage's velocity capabilities, especially for high-speed conditions. The experimental setup at Virginia Tech led to certain pressures being unaffected by the spray root at the higher trim cases. The current orientation of the GPPH and its sensors leads to very low velocities in the Z' direction for the 5° and 10° trim cases. This leads to the total force being measured along the Z' axis for these cases to be dominated by the hydrostatic component.

6.2 Future Work

This thesis presented one small step taken to better test and analyze high-speed slamming events. These events remain a broad and complex problem that has yet to be solved. The novel test method presented in this thesis provides a new angle to analyze the slamming problem. Given that this is one of the first experiments of its kind, its full potential is likely unrealized. To help reach this potential, all the systems discussed in this thesis were designed to be robust, scalable, and modular. This should allow seamless integration of future work. The next section presents a few suggestions that the next researchers can implement to meaningfully improve this novel test method.

As previously discussed, the relative dynamics model relies on the accelerations of the inertial reference frame to be justified in the body reference frame. Future work should include a method to determine the necessary accelerations prescribed by the VPMM and the towing tank carriage to keep the accelerations consistent throughout the slam event. Existing equipment can be used to make this inexpensive improvement.

If more funding is available, an operable wavemaker would be a worthwhile purchase. Controlled slams into waves would allow for a more accurate simulation of the buoyancy force

profile during submergence. A wavemaker would also decrease the velocity that needs to be imposed onto GPPH model to maintain system dynamics. This would enable Virginia Tech to test a wider range of motion profiles.

Beyond the scope of dynamics, future work should measure and analyze the structural deformation that occurs during the slam event. Stereoscopic digital image correlation (S-DIC), Li-DAR, strain gauges, or a combination of these methods can accomplish this. A better understanding of the deformation profile as motion parameters are varied would be of great use to the planing vessel designer. This information would allow future designs to leverage hydroelasticity effects for lighter weight hullforms with better performance.

In the far future, machine learning models can use this controlled experiment to predict vessel dynamics during the slam event, given the pre-impact motion parameters of the system. Proper training could allow the machine learning model to suggest maneuvers that mitigate the severity of the slamming event. This would be a great tool for pilots operating at high speeds in heavy sea states.

High-speed surface vessel continue to be limited by wave slamming. More research is needed both experimentally and computationally to gain a better understanding of the physics of the slam event. This knowledge can be used by designer to create lighter weight vessels with favorable materials and architecture to mitigate the severity of slamming. This knowledge can also be beneficial to operators, allowing them to better understand their vessel's limitations. Quality research in this field will continue to benefit the wide range of stakeholders, and lead to greater improvements in high-speed craft.

Bibliography

[1] Theodore H. Von Karman. The impact on seaplane floats during landing, October 1929. URL https://ntrs.nasa.gov/citations/19930081174. NTRS Author Affiliations: Aerodynamical Institute of the Technical High School, Aachen NTRS Report/Patent Number: NACA-TN-321 NTRS Document ID: 19930081174 NTRS Research Center: Legacy CDMS (CDMS).

[2] Herbert Wagner. Landing of Seaplanes, May 1931. URL https://digital.library.unt.edu/ark:/67531/metadc63624/. Number: NACA-TM-622.

[3] William S. Vorus. A Flat Cylinder Theory for Vessel Impact and Steady Planing Resistance. *Journal of Ship Research*, 40(02):89–106, June 1996. ISSN 0022-4502. doi: 10.5957/jsr.1996.40.2.89. URL https://doi.org/10.5957/jsr.1996.40.2.89.

[4] Gerald Fridsma. A SYSTEMATIC STUDY OF THE ROUGH-WATER PERFORMANCE OF PLANING BOATS:. Technical report, Defense Technical Information Center, Fort Belvoir, VA, November 1969. URL http://www.dtic.mil/docs/citations/AD0708694.

[5] Christine M. Ikeda and Carolyn Q. Judge. Slamming Impacts of Hydrodynamically–Supported Craft. In *Volume 8A: Ocean Engineering*, page V08AT06A035, San Francisco, California, USA, June 2014. American Society of Mechanical Engineers. ISBN 978-0-7918-4550-9. doi: 10.1115/OMAE2014-23387. URL https://asmedigitalcollection.asme.org/OMAE/proceedings/OMAE2014/45509/San%20Francisco,%20California,%20USA/279064.

[6] Carolyn Q. Judge, John A. Judge, and Christine M. Ikeda. Impact Pressures

on the Bottom of a Prismatic Planing Hull During Water Impact. In *Day 2 Thu, September 03, 2015*, page D021S007R002, Washington, DC, September 2015. SNAME. doi: 10.5957/FAST-2015-033. URL https://onepetro.org/snamefast/proceedings/FAST15/2-FAST15/D021S007R002/461522.

[7] Carolyn Q. Judge, Maysam Mousaviraad, Frederick Stern, Evan Lee, Anne Fullerton, Jayson Geiser, Christine Schleicher, Craig Merrill, Charles Weil, Jason Morin, Minyee Jiang, and Christine Ikeda. Experiments and CFD of a high-speed deep-V planing hull – part II: Slamming in waves. *Applied Ocean Research*, 97:132–45, April 2020. ISSN 0141-1187. doi: 10.1016/j.apor.2020.102059. Place: Netherlands Publisher: Elsevier B.V.

[8] An Wang and James H. Duncan. The controlled vertical impact of an inclined flat plate on a quiescent water surface. *Journal of Fluid Mechanics*, 879:468–511, November 2019. ISSN 0022-1120, 1469-7645. doi: 10.1017/jfm.2019.630. URL https://www.cambridge.org/core/product/identifier/S002211201900630X/type/journal_article.

[9] An Wang, Kit Pan Wong, Miao Yu, Kenneth T. Kiger, and James H. Duncan. The controlled impact of elastic plates on a quiescent water surface. *Journal of Fluid Mechanics*, 939:A4, May 2022. ISSN 0022-1120, 1469-7645. doi: 10.1017/jfm.2022.154. URL https://www.cambridge.org/core/product/identifier/S0022112022001549/type/journal_article.

[10] M. Javad Javaherian, Zhongshu Ren, and Christine Gilbert. Reconstructed Kinematics and Hydrodynamic Loading Using Spray Root Propagation in Wedge Water Entry. OnePetro, September 2020. URL https://dx.doi.org/.

[11] Mohammad Javad Javaherian, Zhongshu Ren, and Christine Gilbert. Flow Visualiza-

tion, Hydrodynamics, and Structural Response of a Flexible Wedge in Water Entry Experiments. *Journal of Ship Research*, 67:1–13, April 2022. doi: 10.5957/JOSR.12200060.

[12] Michael R. Riley and Timothy Coats. Lessons Learned from Full-Scale Seakeeping Trial Acceleration Data for High-Speed Planing Craft and Implications for Scale Model Testing. In *SNAME 30th American Towing Tank Conference, ATTC 2017, October 4, 2017*, SNAME 30th American Towing Tank Conference, ATTC 2017, West Bethesda, MD, United states, 2017. Society of Naval Architects and Marine Engineers. doi: 10.5957/ATTC-2017-0011.

[13] Mark W Shepheard. Slamming of High-Speed Craft: A Machine Learning & Parametric Study of Slamming Events.

Appendices

Appendix A

All Verification Study Trials Graphed

Condition	Trim (deg)	S_w (m2)	V_S (m/s)	V_H (m/s)	V_T (m/s)
1	0.000	0.419	5.000	0.250	5.006
2	-5.000	0.323	5.000	0.250	5.006
3	-10.000	0.196	5.000	0.250	5.006
4	-15.000	0.067	5.000	0.250	5.006
5	0.000	0.419	5.000	0.500	5.025
6	-5.000	0.323	5.000	0.500	5.025
7	-10.000	0.196	5.000	0.500	5.025
8	-15.000	0.067	5.000	0.500	5.025
9	0.000	0.419	5.000	0.750	5.056
10	-5.000	0.323	5.000	0.750	5.056
11	-10.000	0.196	5.000	0.750	5.056
12	-15.000	0.067	5.000	0.750	5.056
13	0.000	0.419	5.000	1.000	5.099
14	-5.000	0.323	5.000	1.000	5.099
15	-10.000	0.196	5.000	1.000	5.099
16	-15.000	0.067	5.000	1.000	5.099
17	0.000	0.419	7.000	0.250	7.004
18	-5.000	0.323	7.000	0.250	7.004
19	-10.000	0.196	7.000	0.250	7.004
20	-15.000	0.067	7.000	0.250	7.004
21	0.000	0.419	7.000	0.500	7.018
22	-5.000	0.323	7.000	0.500	7.018
23	-10.000	0.196	7.000	0.500	7.018
24	-15.000	0.067	7.000	0.500	7.018
25	0.000	0.419	7.000	0.750	7.040
26	-5.000	0.323	7.000	0.750	7.040
27	-10.000	0.196	7.000	0.750	7.040
28	-15.000	0.067	7.000	0.750	7.040
29	0.000	0.419	7.000	1.000	7.071
30	-5.000	0.323	7.000	1.000	7.071
31	-10.000	0.196	7.000	1.000	7.071
32	-15.000	0.067	7.000	1.000	7.071

Table A.1: Full Table of Parametric Study Parameters

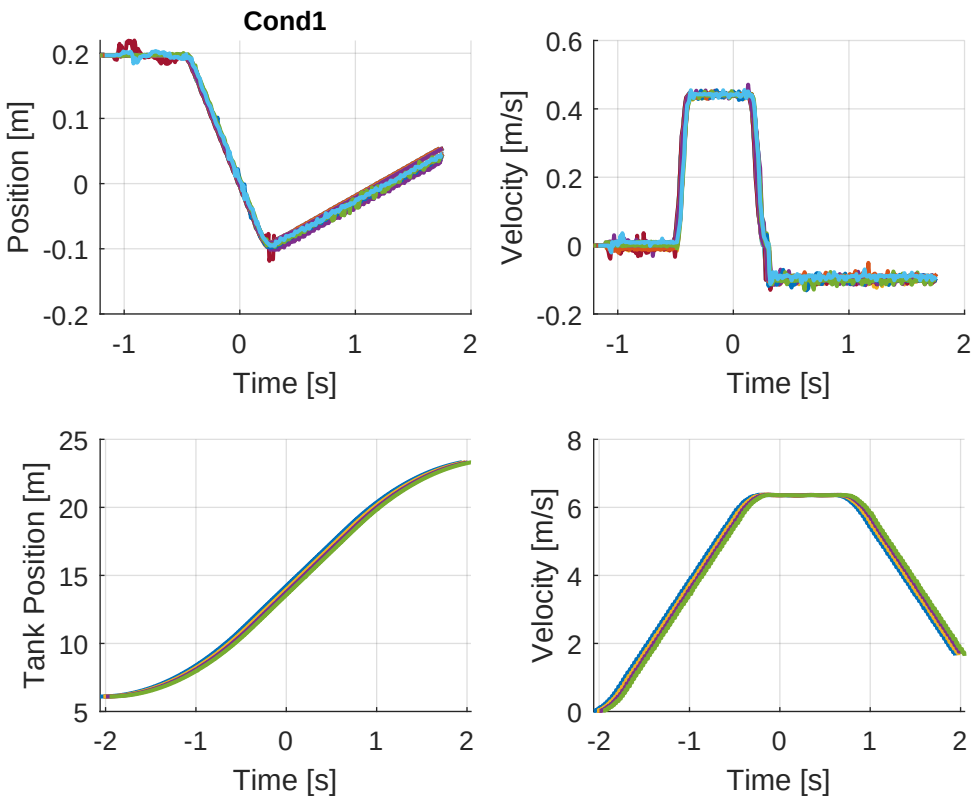
Cond1
Position [m]
Time [s]
Velocity [m/s]
Time [s]
Tank Position [m]
Time [s]
Velocity [m/s]
Time [s]

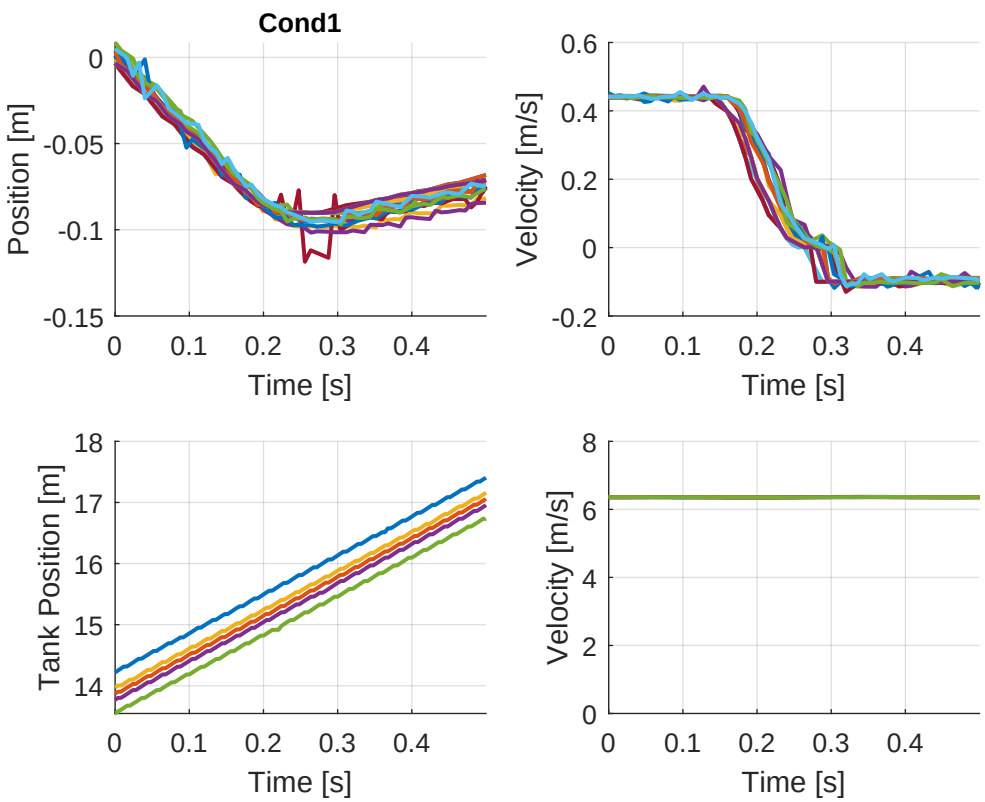
Cond1
Position [m]
0
-0.05
-0.1
-0.15
0
0.1
0.2
0.3
0.4
Time [s]
Velocity [m/s]
0.6
0.4
0.2
0
-0.2
0
0.1
0.2
0.3
0.4
Time [s]
Tank Position [m]
18
17
16
15
14
0
0.1
0.2
0.3
0.4
Time [s]
Velocity [m/s]
8
6
4
2
0
0
0.1
0.2
0.3
0.4
Time [s]

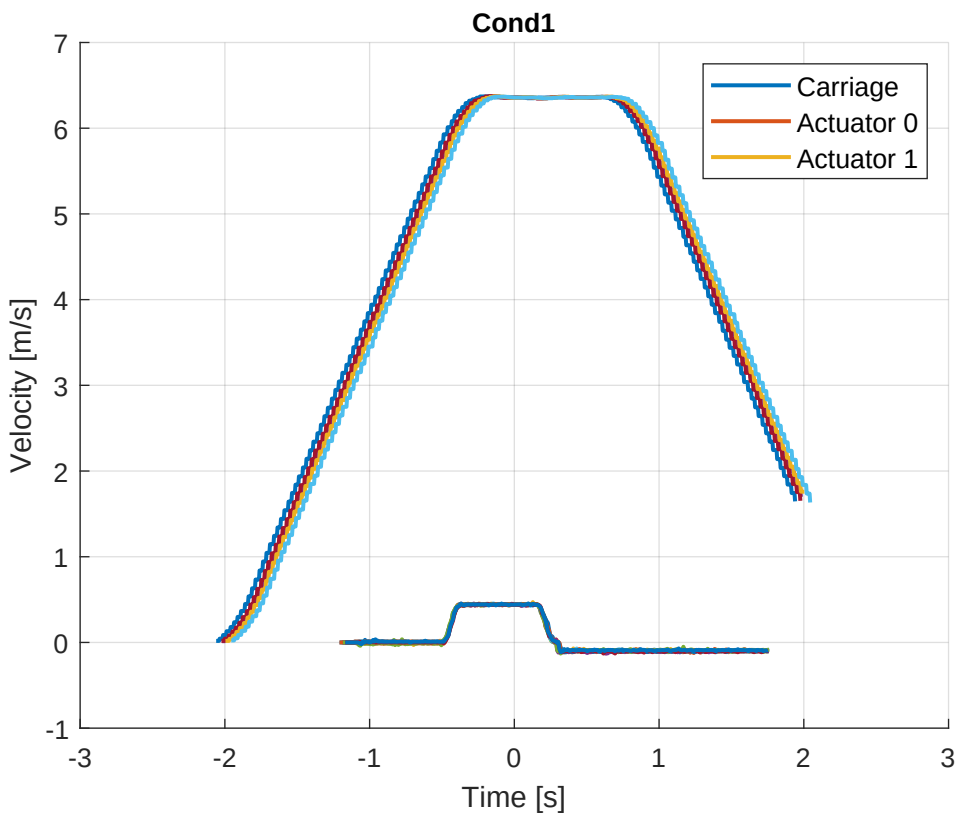
Cond1
Carriage
Actuator 0
Actuator 1
Velocity [m/s]
Time [s]
7
6
5
4
3
2
1
0
-1
-3
-2
-1
0
1
2
3

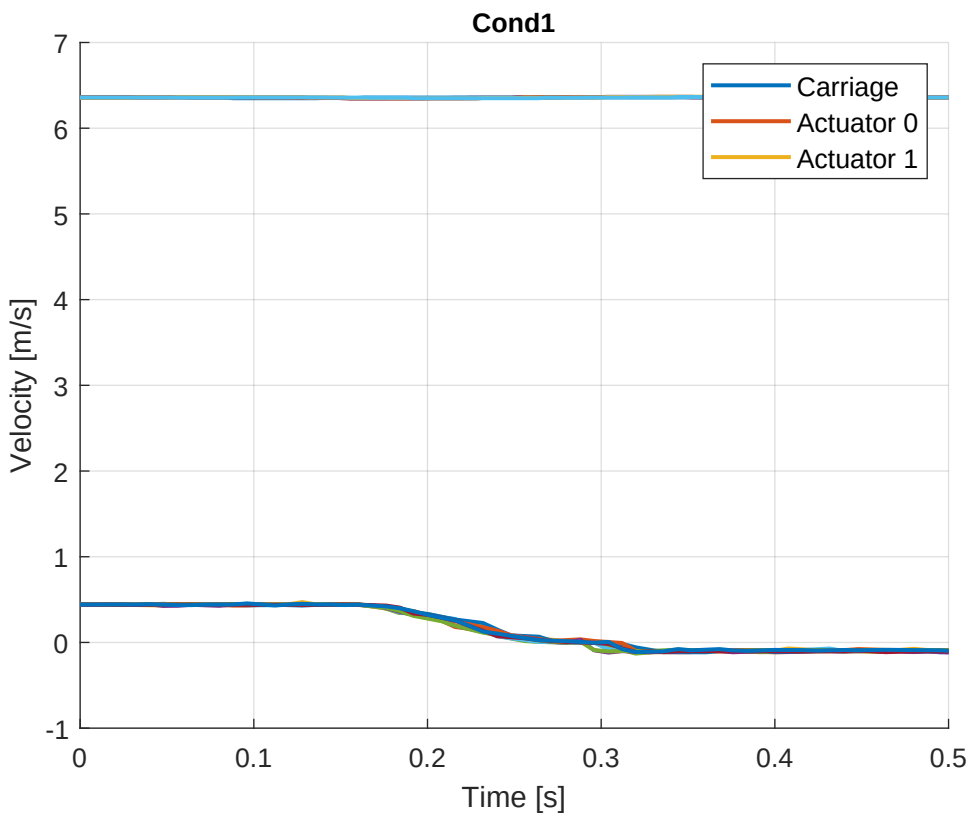
Cond1
Carriage
Actuator 0
Actuator 1
Velocity [m/s]
Time [s]
7
6
5
4
3
2
1
0
-1
0
0.1
0.2
0.3
0.4
0.5

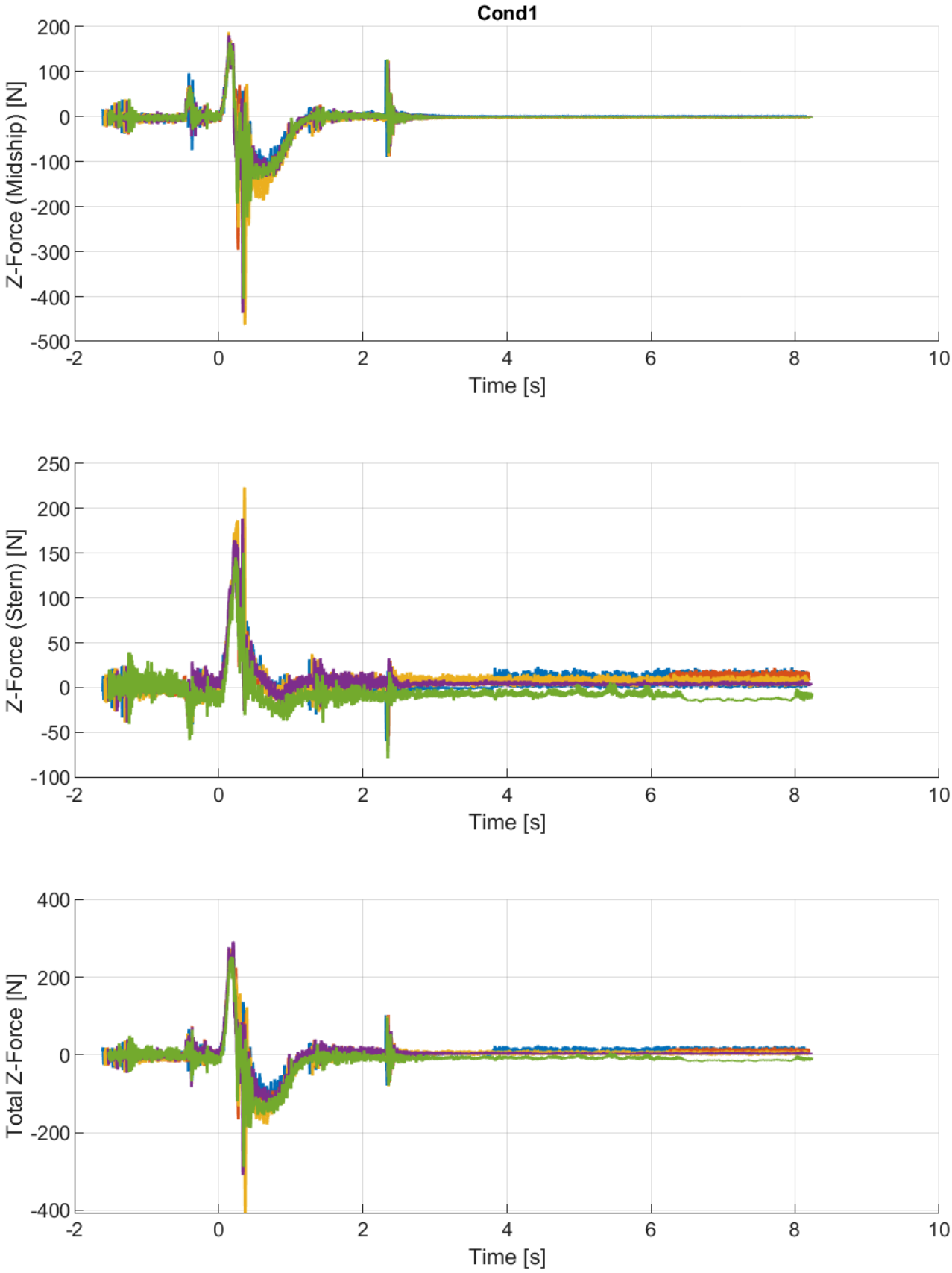
Cond1
Z-Force (Midship) [N]
200
100
0
-100
-200
-300
-400
-500
-2
0
2
4
6
8
10
Time [s]
Z-Force (Stern) [N]
250
200
150
100
50
0
-50
-100
-2
0
2
4
6
8
10
Time [s]
Total Z-Force [N]
400
200
0
-200
-400
-2
0
2
4
6
8
10
Time [s]

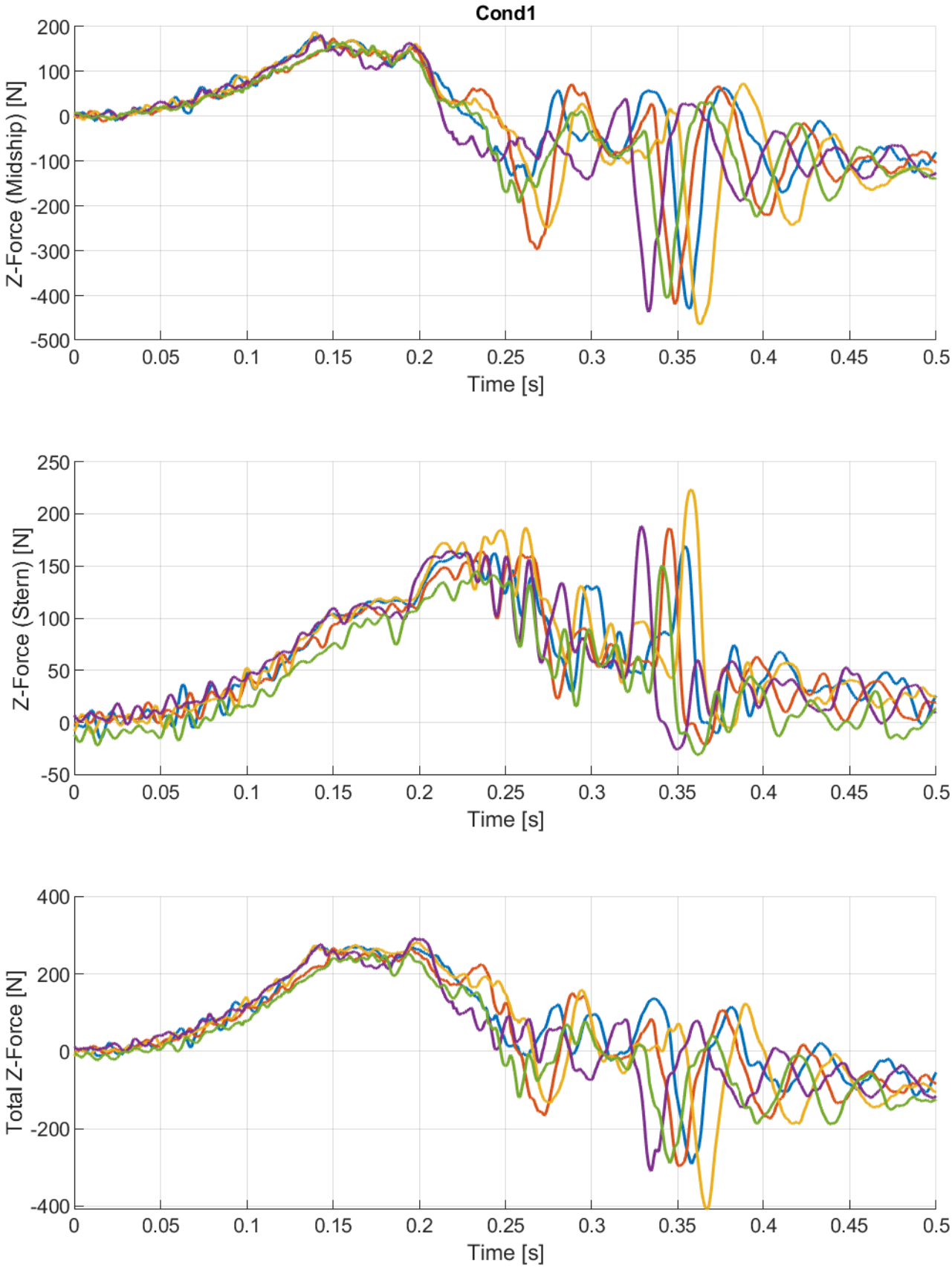
Cond1
Z-Force (Midship) [N]
200
100
0
-100
-200
-300
-400
-500
0
0.05
0.1
0.15
0.2
0.25
0.3
0.35
0.4
0.45
0.5
Time [s]
Z-Force (Stern) [N]
250
200
150
100
50
0
-50
Time [s]
Total Z-Force [N]
400
200
0
-200
-400
Time [s]

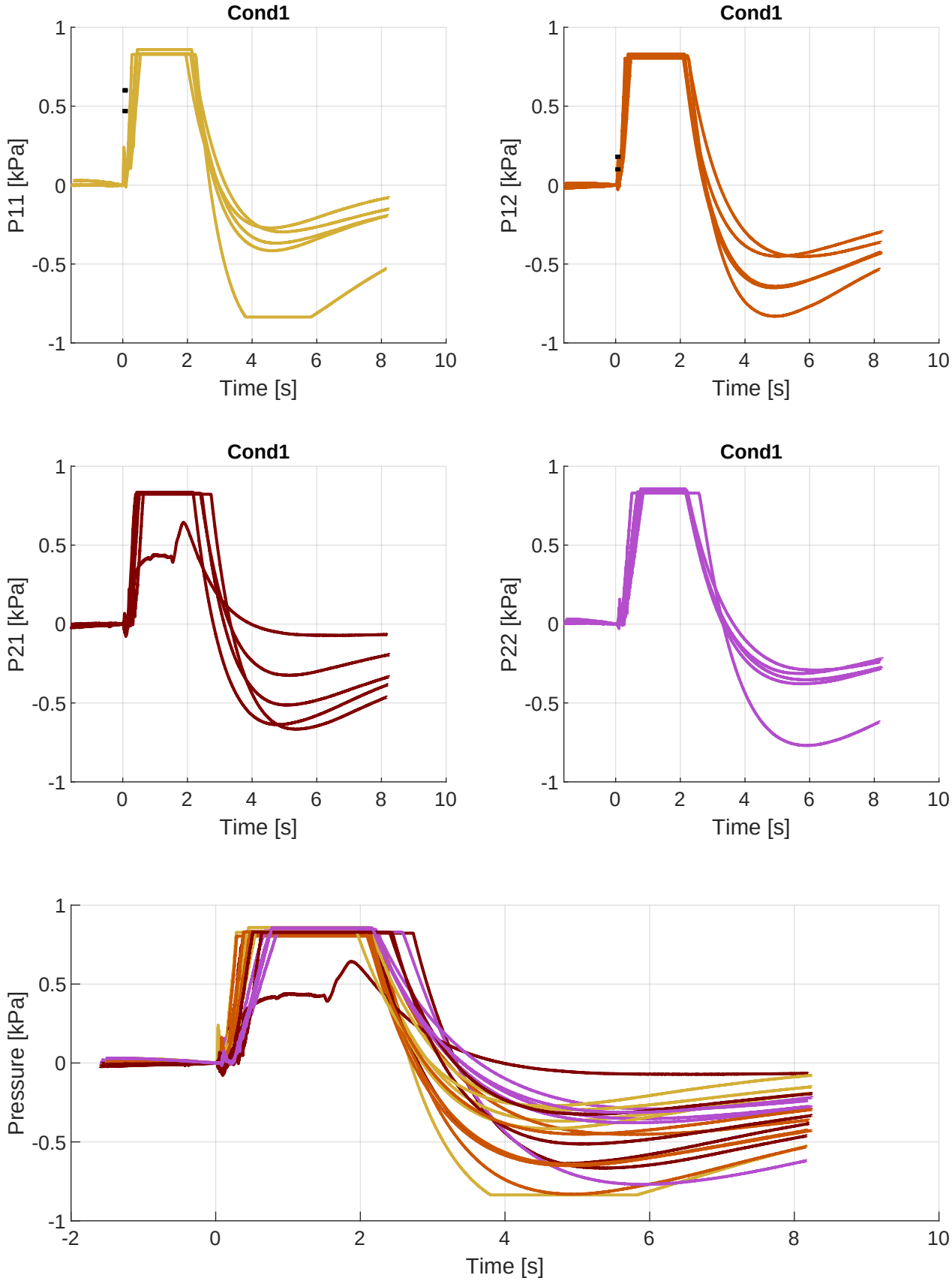
Cond1
P11 [kPa]
Time [s]
Cond1
P12 [kPa]
Time [s]
Cond1
P21 [kPa]
Time [s]
Cond1
P22 [kPa]
Time [s]
Pressure [kPa]
Time [s]

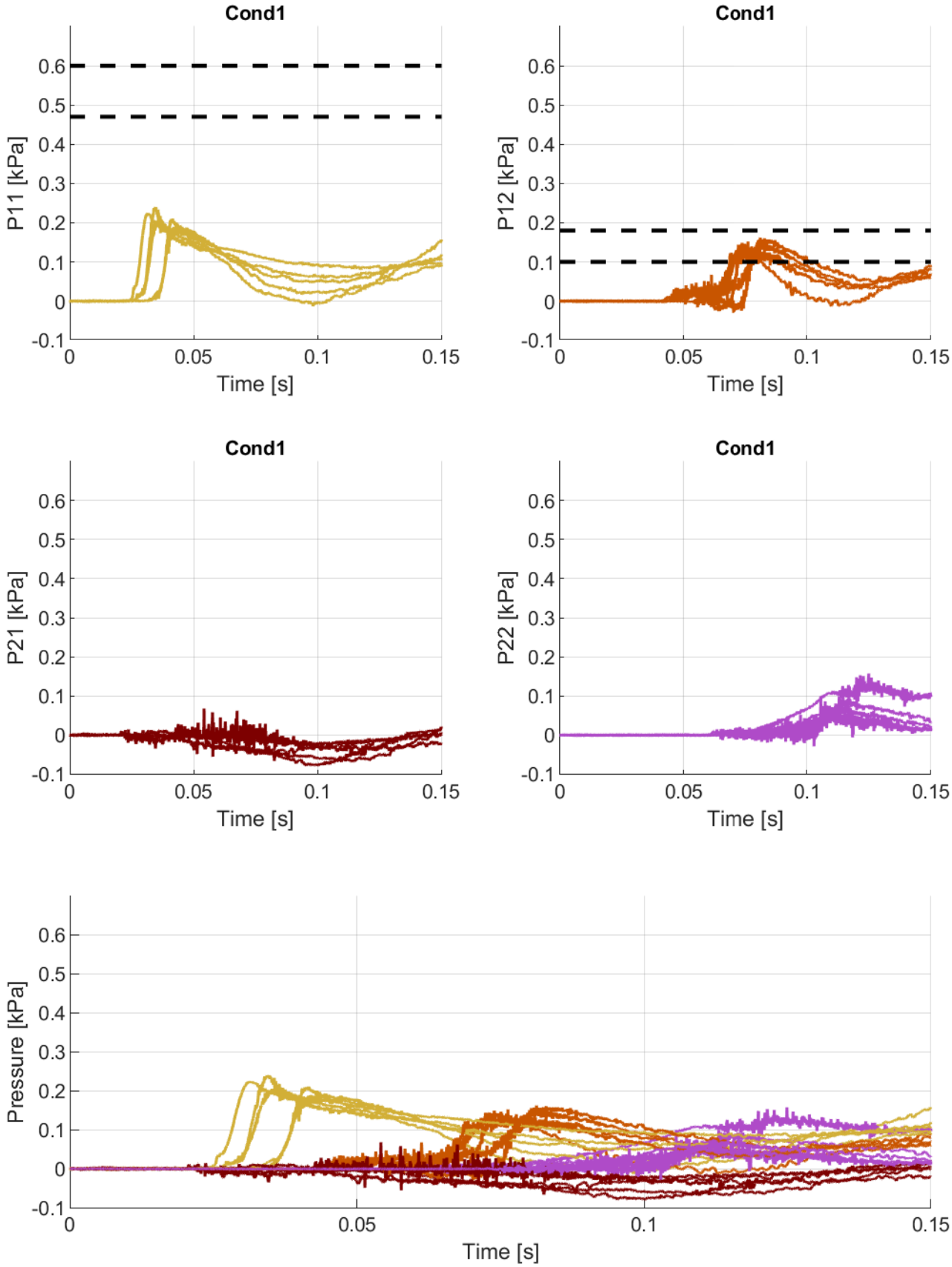
Cond1
P11 [kPa]
Time [s]
Cond1
P12 [kPa]
Time [s]
Cond1
P21 [kPa]
Time [s]
Cond1
P22 [kPa]
Time [s]
Pressure [kPa]
Time [s]

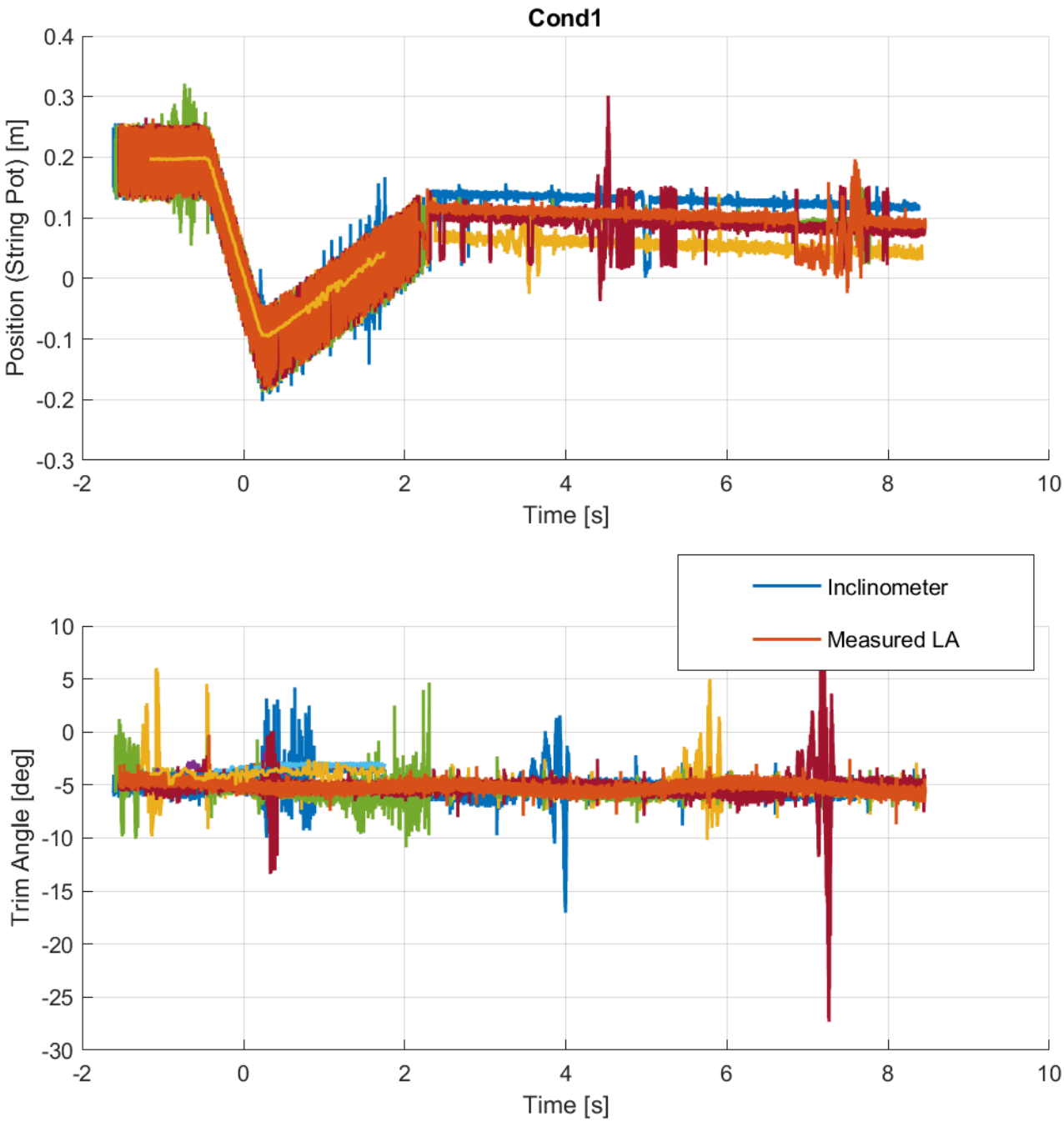
Cond1
Position (String Pot) [m]
0.4
0.3
0.2
0.1
0
-0.1
-0.2
-0.3
-2
0
2
4
6
8
10
Time [s]
Inclinometer
Measured LA
Trim Angle [deg]
10
5
0
-5
-10
-15
-20
-25
-30
-2
0
2
4
6
8
10
Time [s]

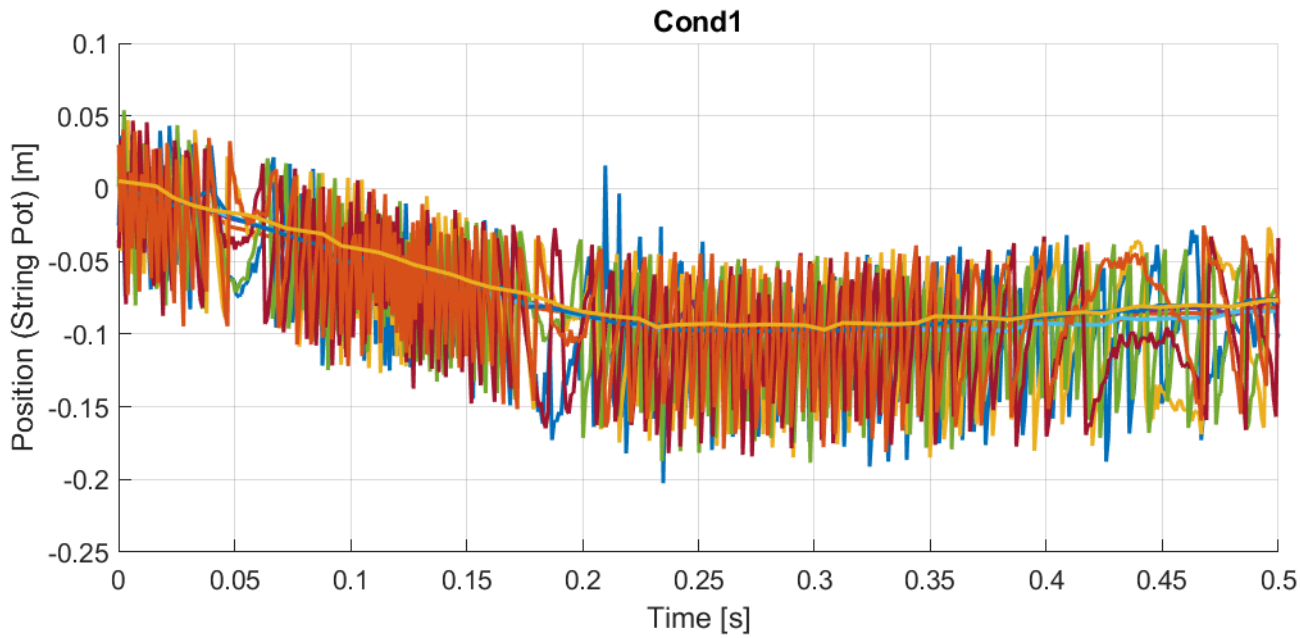
Cond1
Position (String Pot) [m]
0.1
0.05
0
-0.05
-0.1
-0.15
-0.2
-0.25
0
0.05
0.1
0.15
0.2
0.25
0.3
0.35
0.4
0.45
0.5
Time [s]

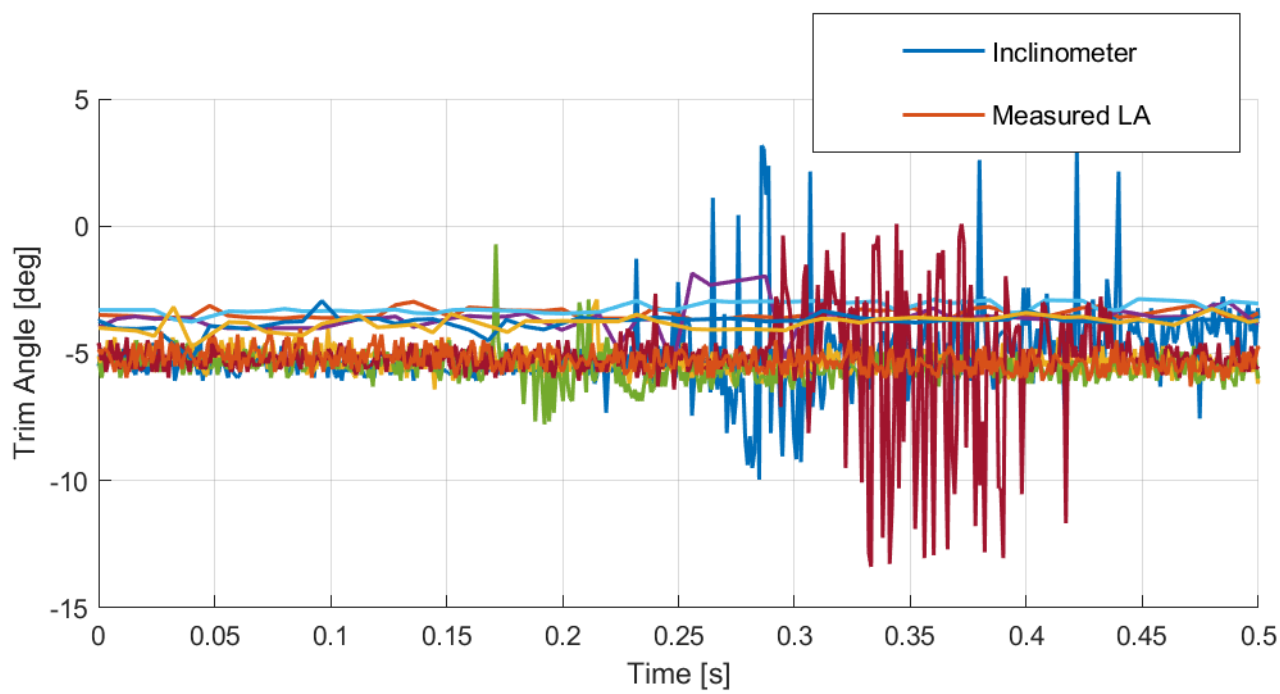
Inclinometer
Measured LA
Trim Angle [deg]
5
0
-5
-10
-15
0
0.05
0.1
0.15
0.2
0.25
0.3
0.35
0.4
0.45
0.5
Time [s]

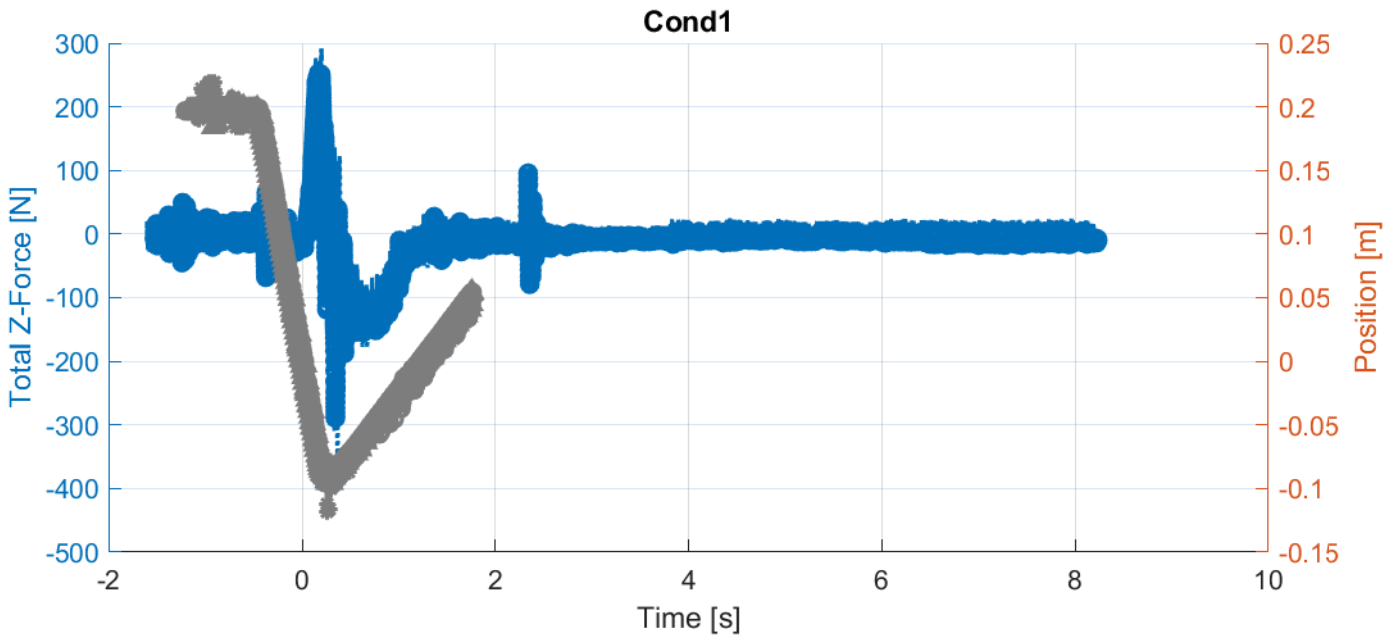
Cond1
Total Z-Force [N]
Position [m]
Time [s]
300
200
100
0
-100
-200
-300
-400
-500
0.25
0.2
0.15
0.1
0.05
0
-0.05
-0.1
-0.15
-2
0
2
4
6
8
10

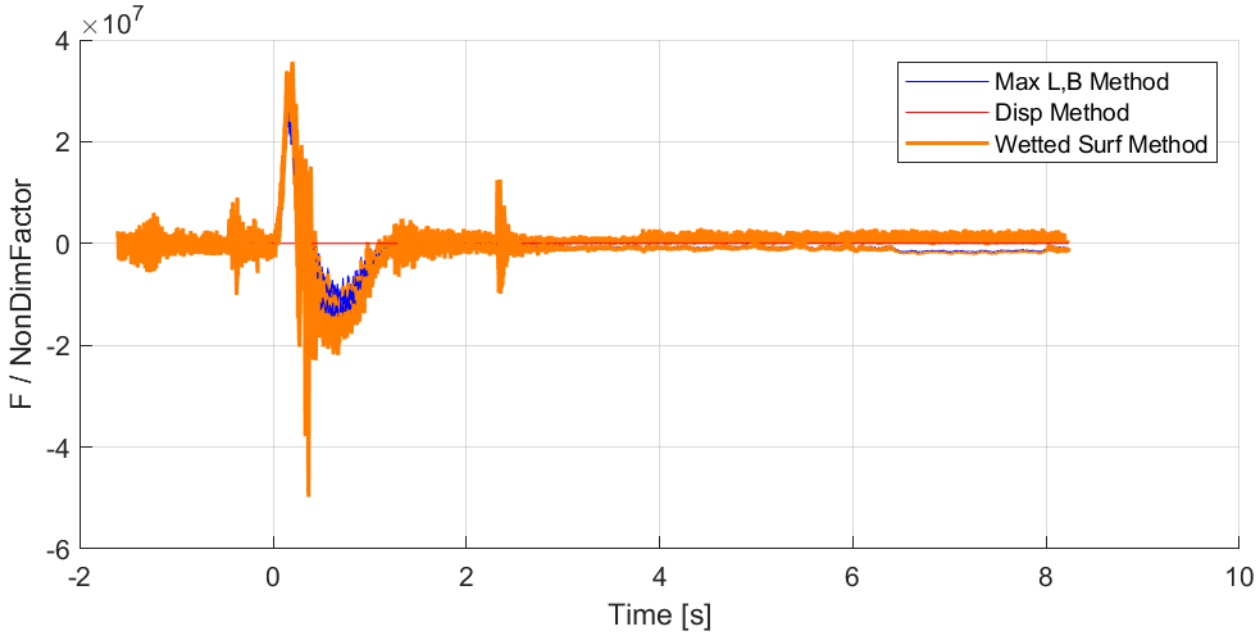
×10^7
F / NonDimFactor
Time [s]
Max L,B Method
Disp Method
Wetted Surf Method
4
2
0
-2
-4
-6
-2
0
2
4
6
8
10

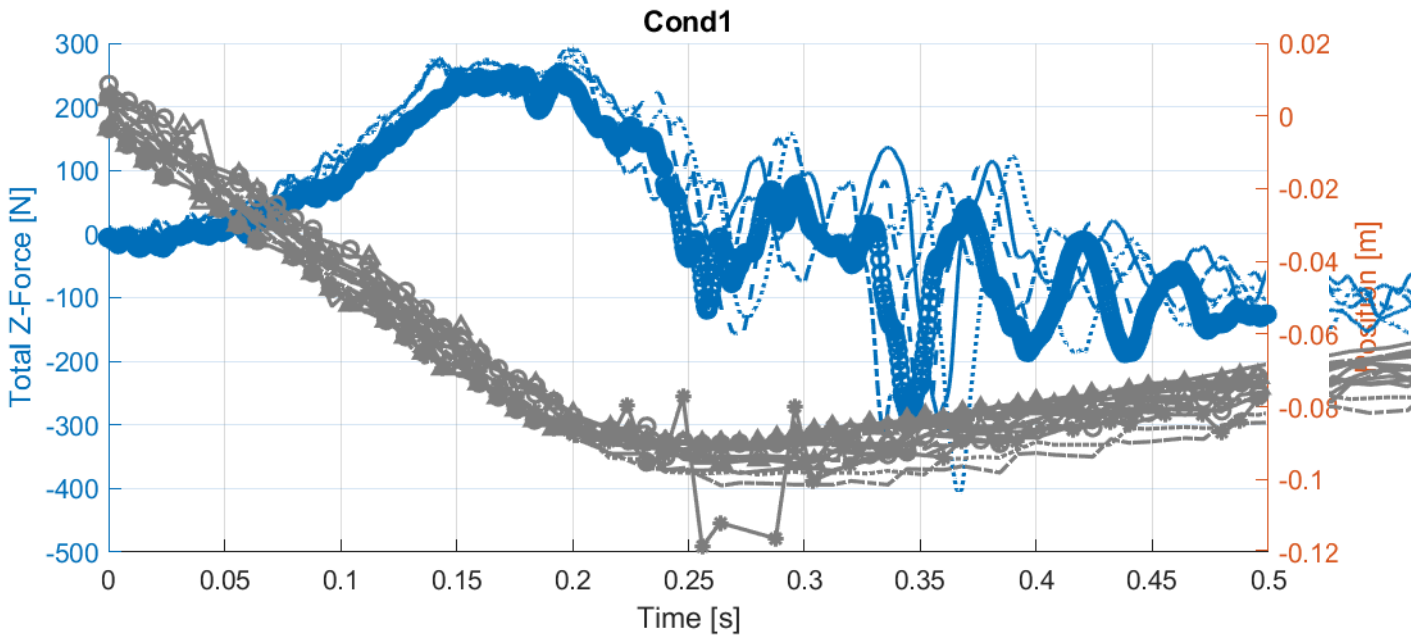
Cond1
Total Z-Force [N]
Position [m]
Time [s]
300
200
100
0
-100
-200
-300
-400
-500
0.02
0
-0.02
-0.04
-0.06
-0.08
-0.1
-0.12
0
0.05
0.1
0.15
0.2
0.25
0.3
0.35
0.4
0.45
0.5

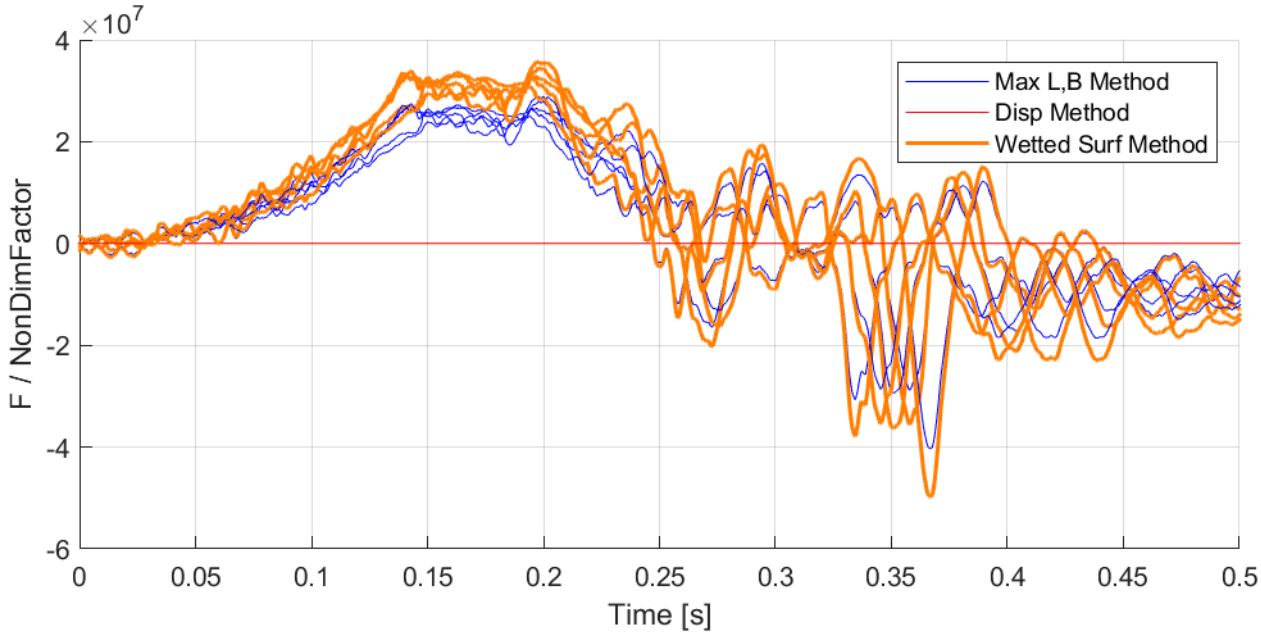
×10^7
F / NonDimFactor
Time [s]
Max L,B Method
Disp Method
Wetted Surf Method
4
2
0
-2
-4
-6
0
0.05
0.1
0.15
0.2
0.25
0.3
0.35
0.4
0.45
0.5

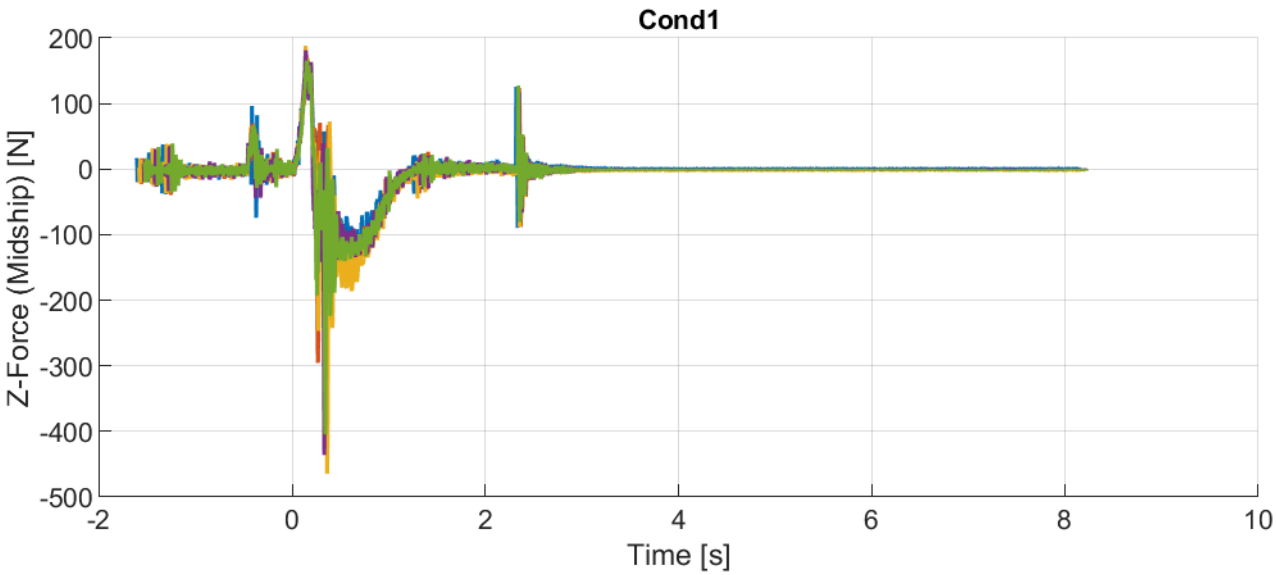
Cond1
Z-Force (Midship) [N]
200
100
0
-100
-200
-300
-400
-500
-2
0
2
4
6
8
10
Time [s]

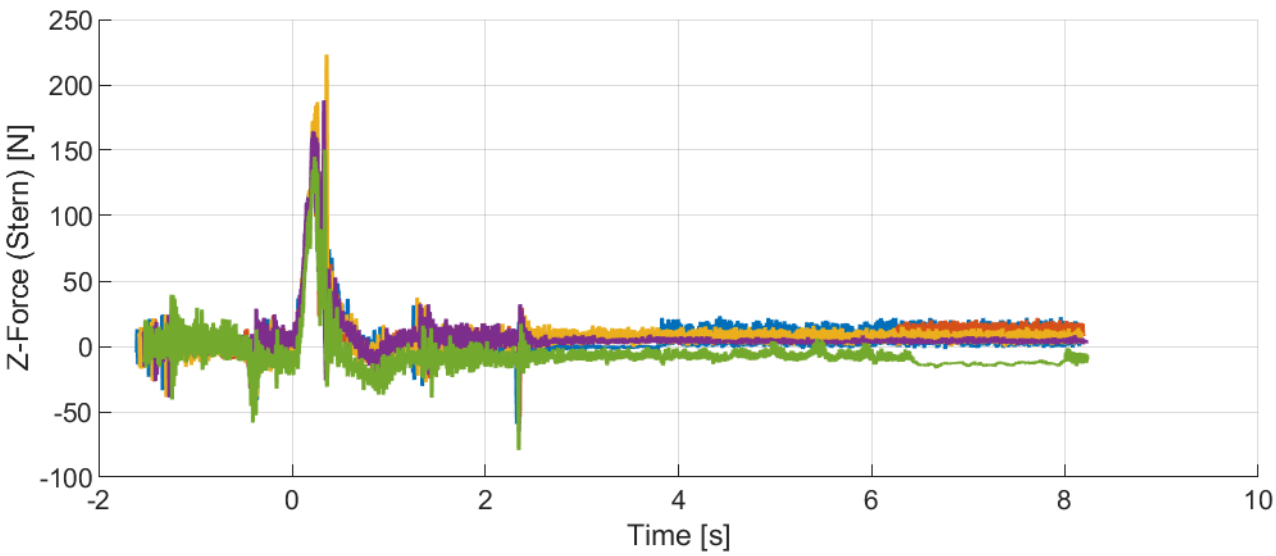
Z-Force (Stern) [N]
250
200
150
100
50
0
-50
-100
-2
0
2
4
6
8
10
Time [s]

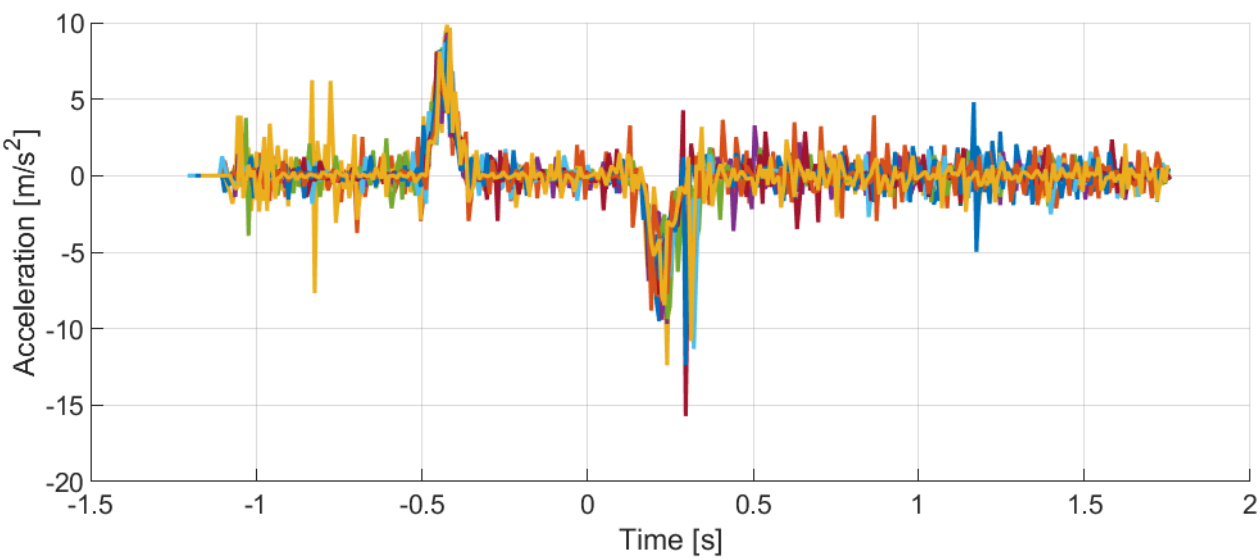
Acceleration [m/s^2]
10
5
0
-5
-10
-15
-20
-1.5
-1
-0.5
0
0.5
1
1.5
2
Time [s]

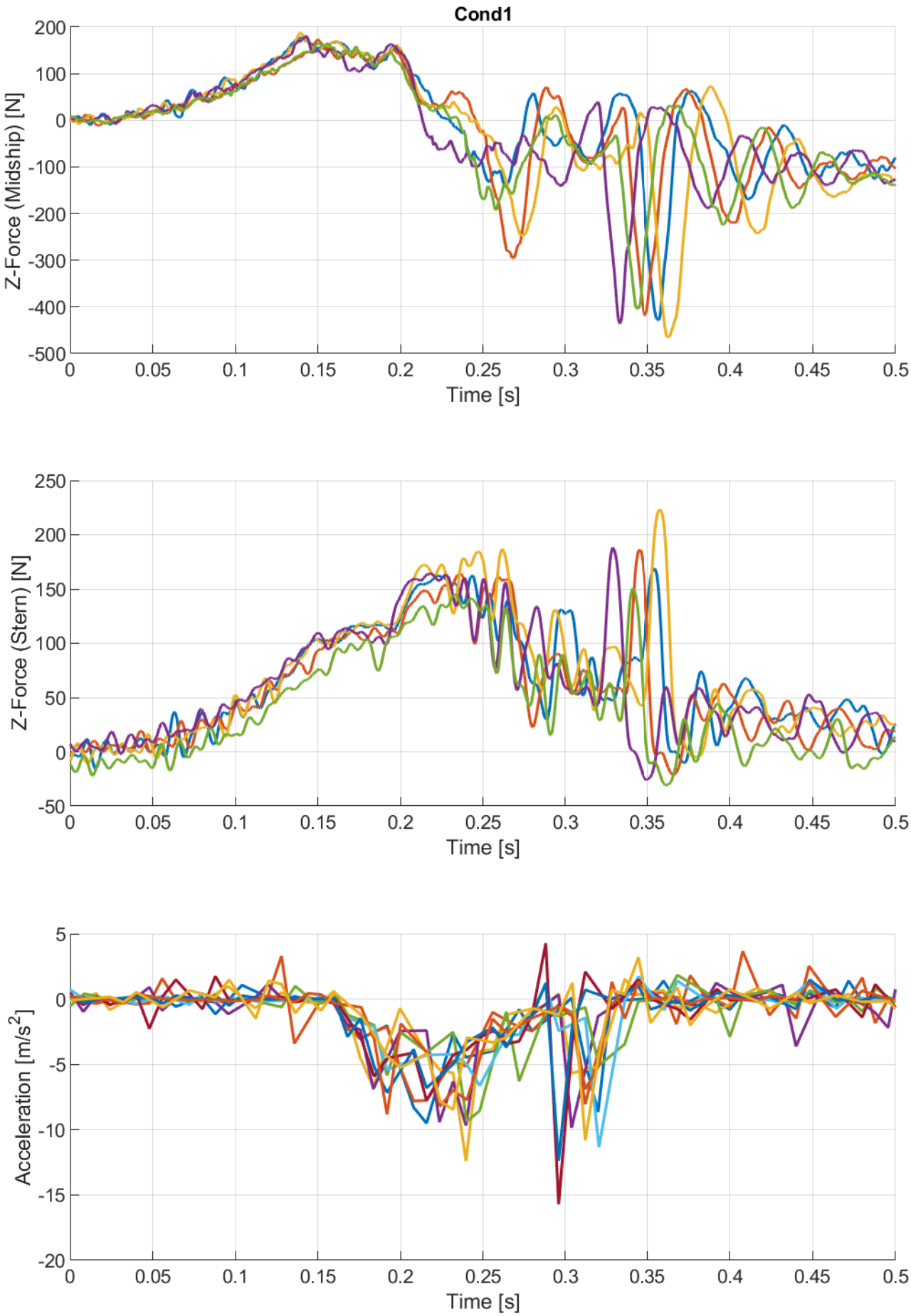
Cond1
Z-Force (Midship) [N]
Time [s]
Z-Force (Stern) [N]
Time [s]
Acceleration [m/s^2]
Time [s]

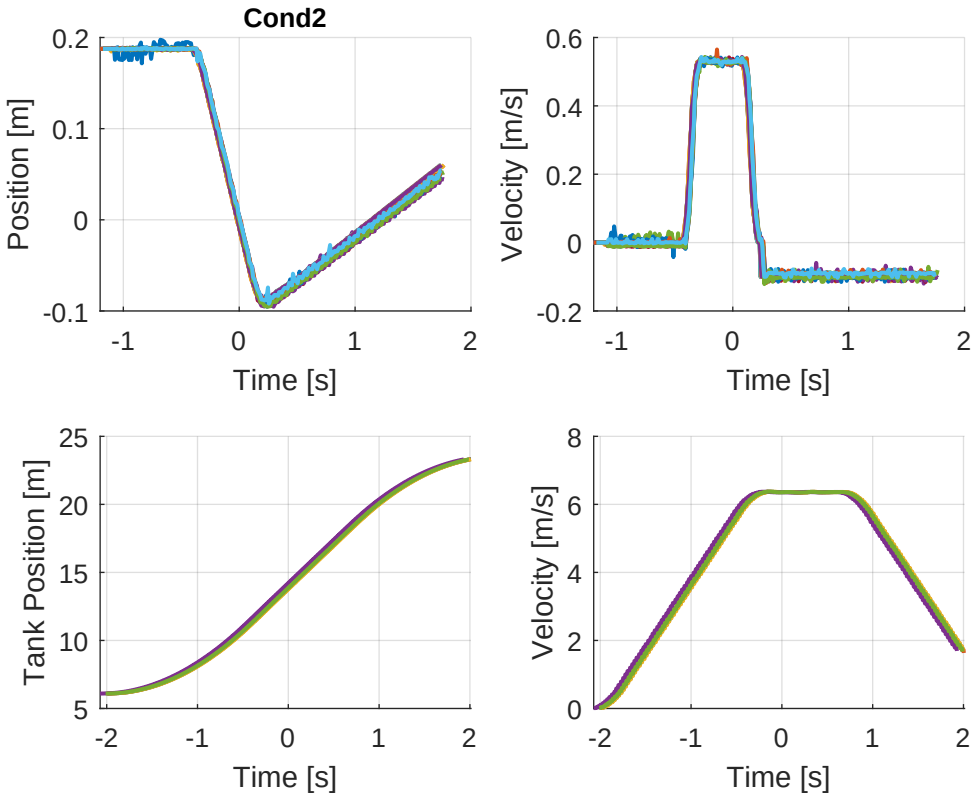
Cond2
Position [m]
Time [s]
Velocity [m/s]
Time [s]
Tank Position [m]
Time [s]
Velocity [m/s]
Time [s]

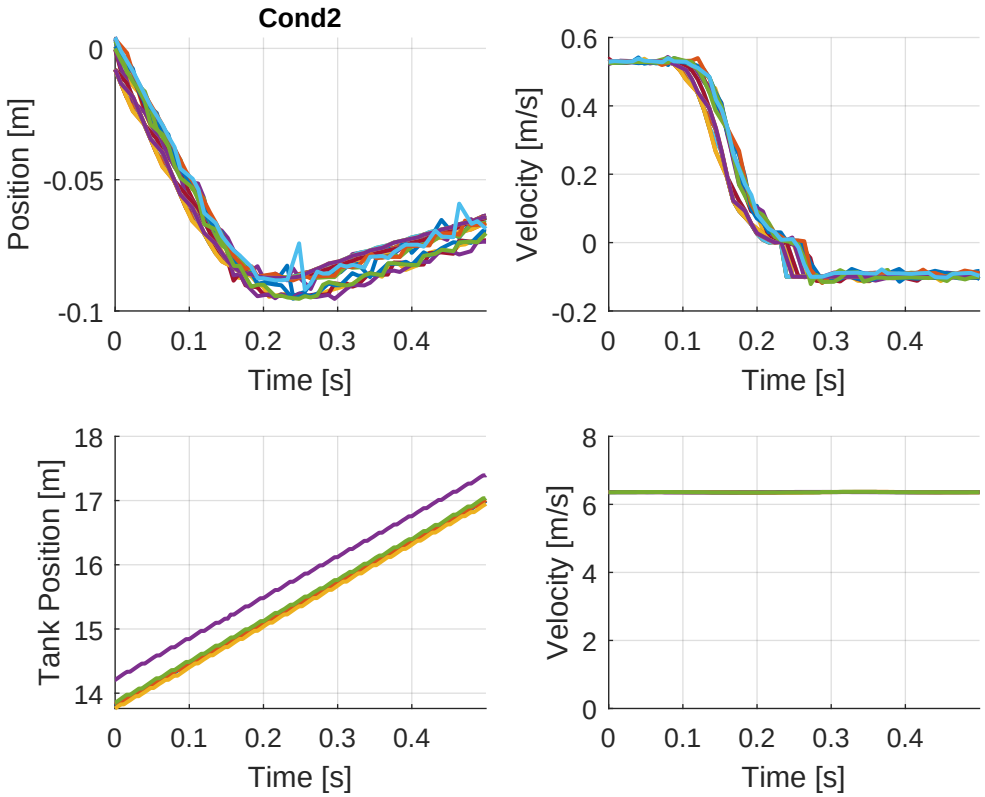
Cond2
Position [m]
0
-0.05
-0.1
0
0.1
0.2
0.3
0.4
Time [s]
Velocity [m/s]
0.6
0.4
0.2
0
-0.2
Time [s]
Tank Position [m]
18
17
16
15
14
Time [s]
Velocity [m/s]
8
6
4
2
0
Time [s]

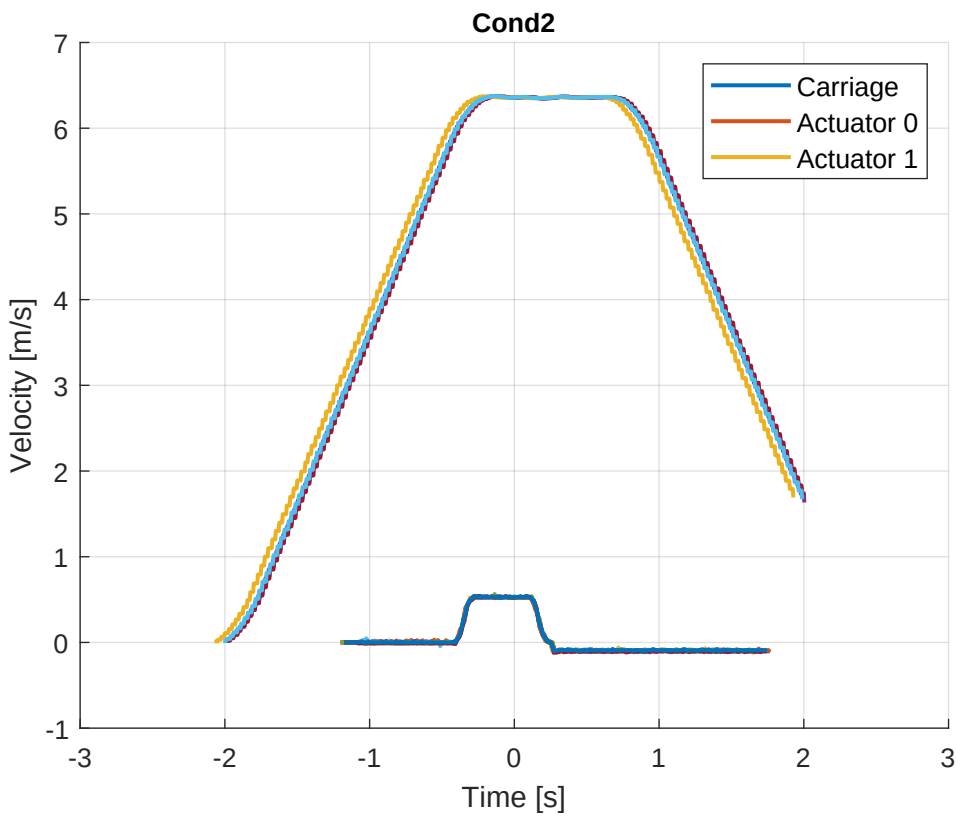
Cond2
Carriage
Actuator 0
Actuator 1
Velocity [m/s]
Time [s]
7
6
5
4
3
2
1
0
-1
-3
-2
-1
0
1
2
3

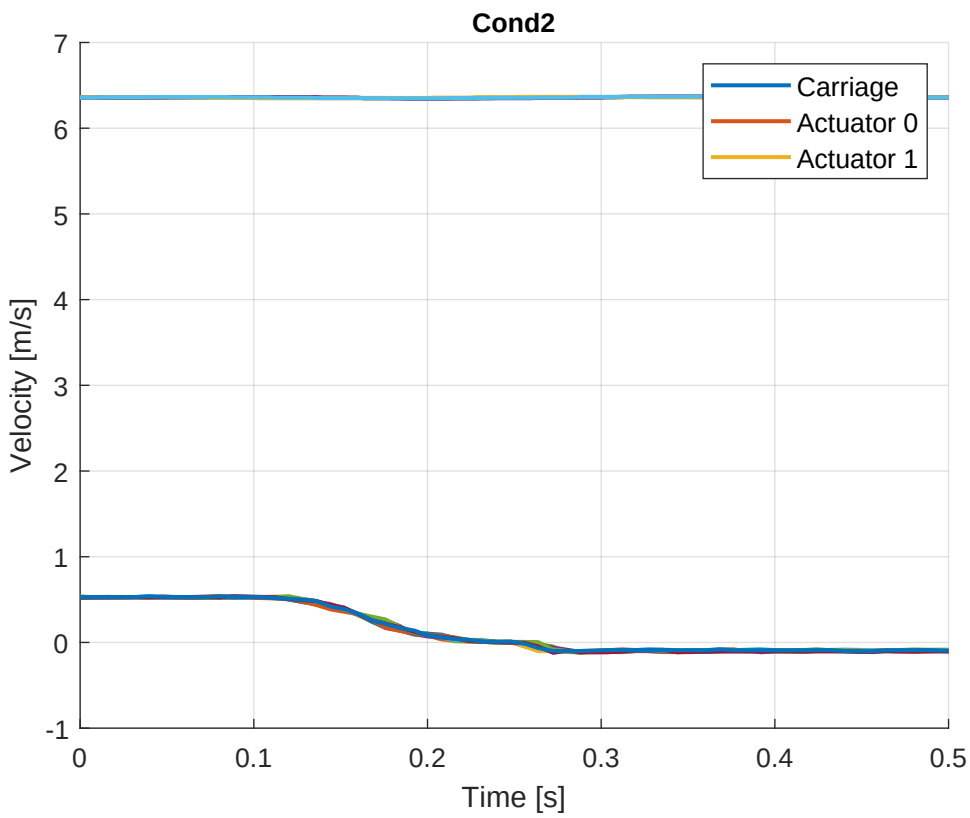
Cond2
Carriage
Actuator 0
Actuator 1
Velocity [m/s]
Time [s]
7
6
5
4
3
2
1
0
-1
0
0.1
0.2
0.3
0.4
0.5

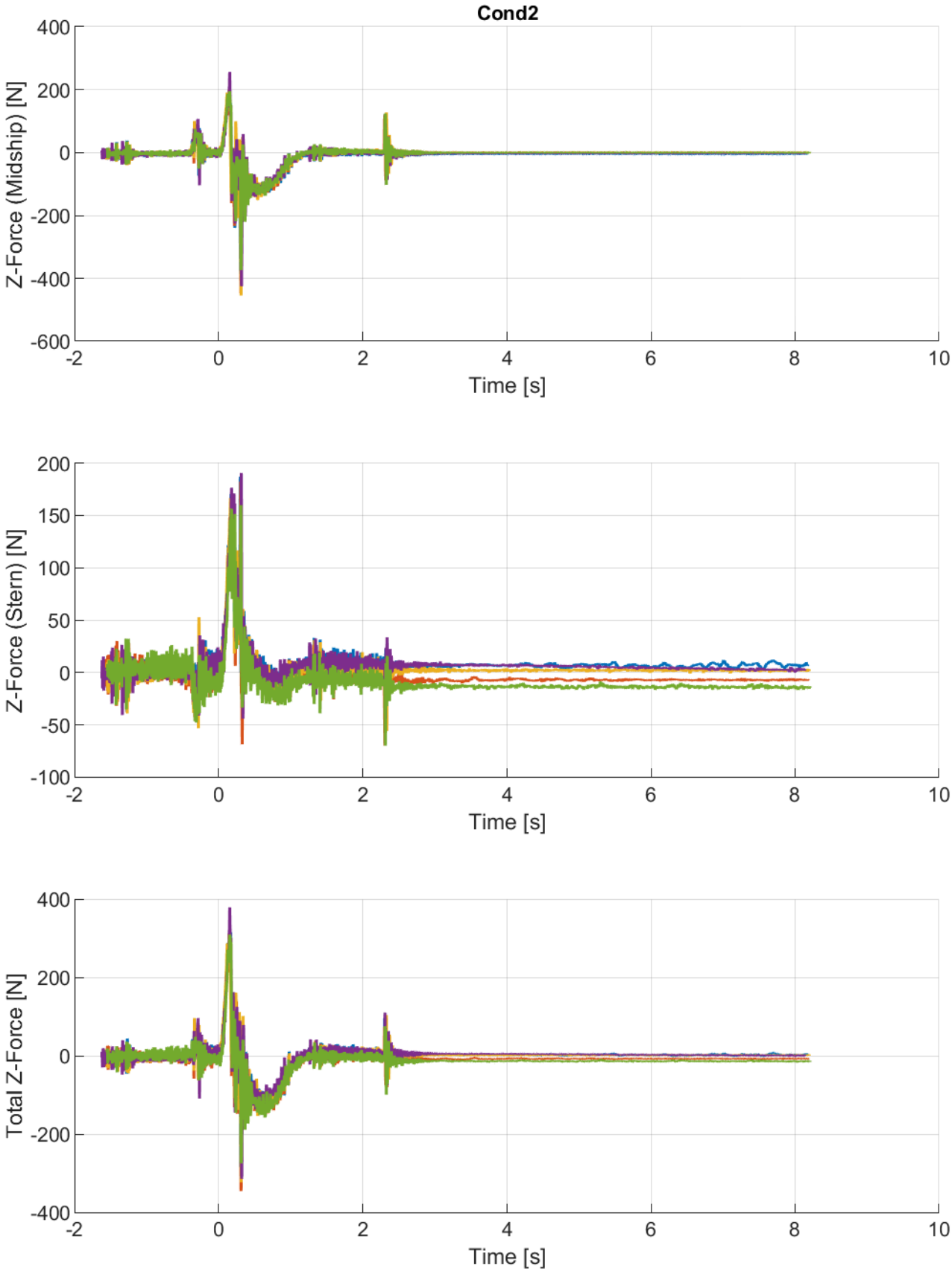
Cond2
Z-Force (Midship) [N]
400
200
0
-200
-400
-600
-2
0
2
4
6
8
10
Time [s]
Z-Force (Stern) [N]
200
150
100
50
0
-50
-100
-2
0
2
4
6
8
10
Time [s]
Total Z-Force [N]
400
200
0
-200
-400
-2
0
2
4
6
8
10
Time [s]

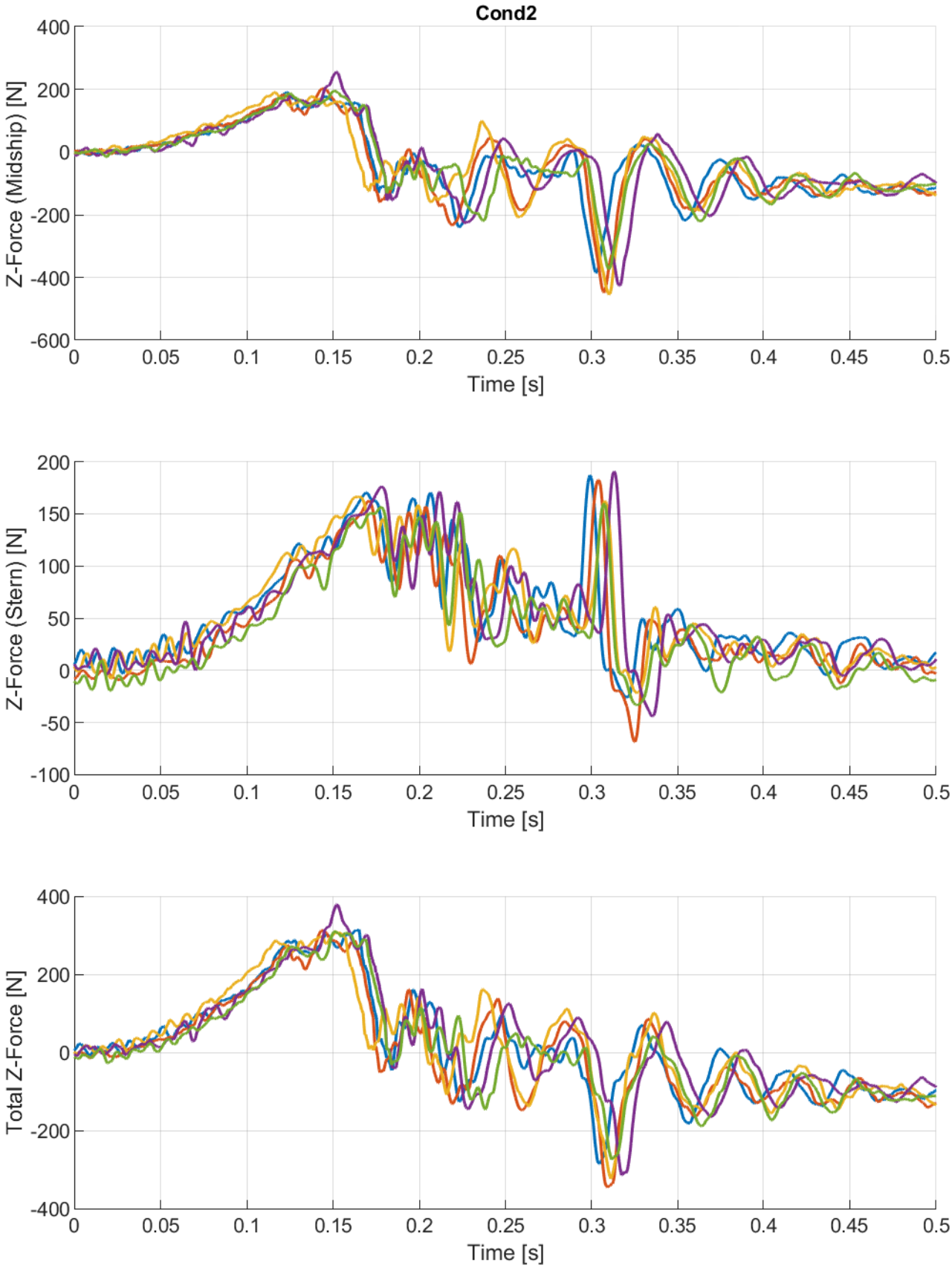
Cond2
Z-Force (Midship) [N]
400
200
0
-200
-400
-600
0
0.05
0.1
0.15
0.2
0.25
0.3
0.35
0.4
0.45
0.5
Time [s]
Z-Force (Stern) [N]
200
150
100
50
0
-50
-100
Time [s]
Total Z-Force [N]
400
200
0
-200
-400
Time [s]

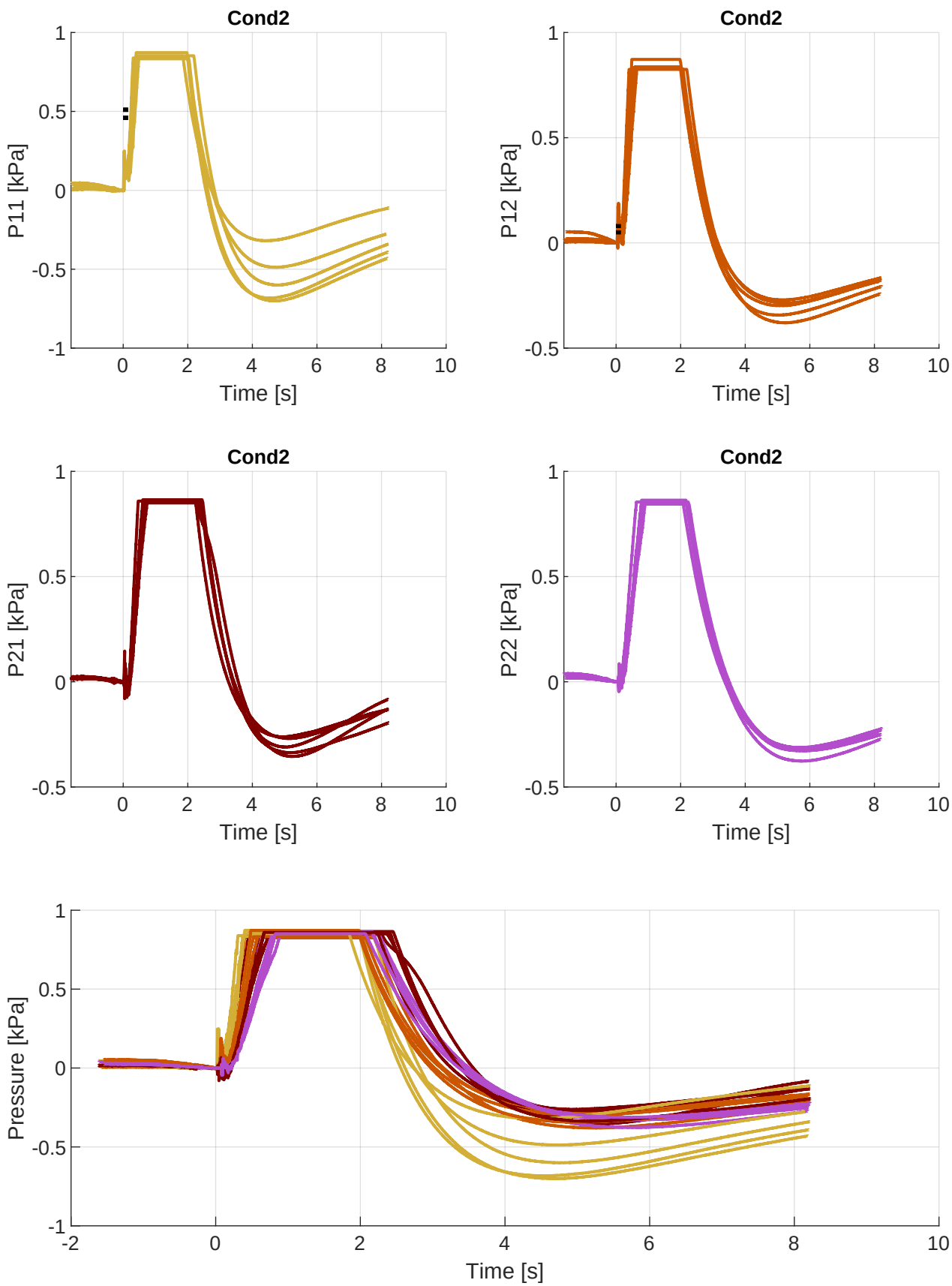
Cond2
P11 [kPa]
Time [s]
Cond2
P12 [kPa]
Time [s]
Cond2
P21 [kPa]
Time [s]
Cond2
P22 [kPa]
Time [s]
Pressure [kPa]
Time [s]

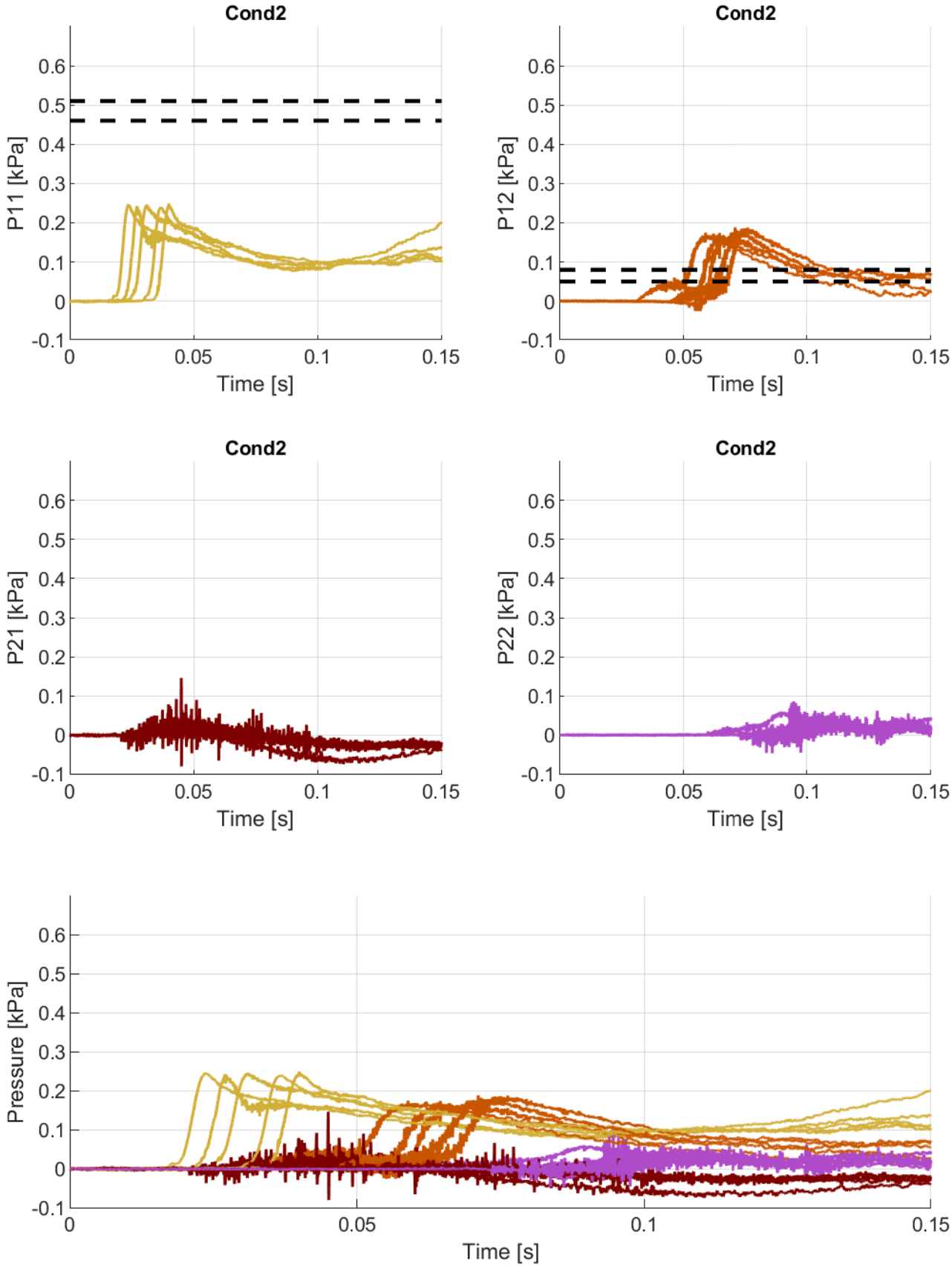
Cond2
P11 [kPa]
Time [s]
Cond2
P12 [kPa]
Time [s]
Cond2
P21 [kPa]
Time [s]
Cond2
P22 [kPa]
Time [s]
Pressure [kPa]
Time [s]

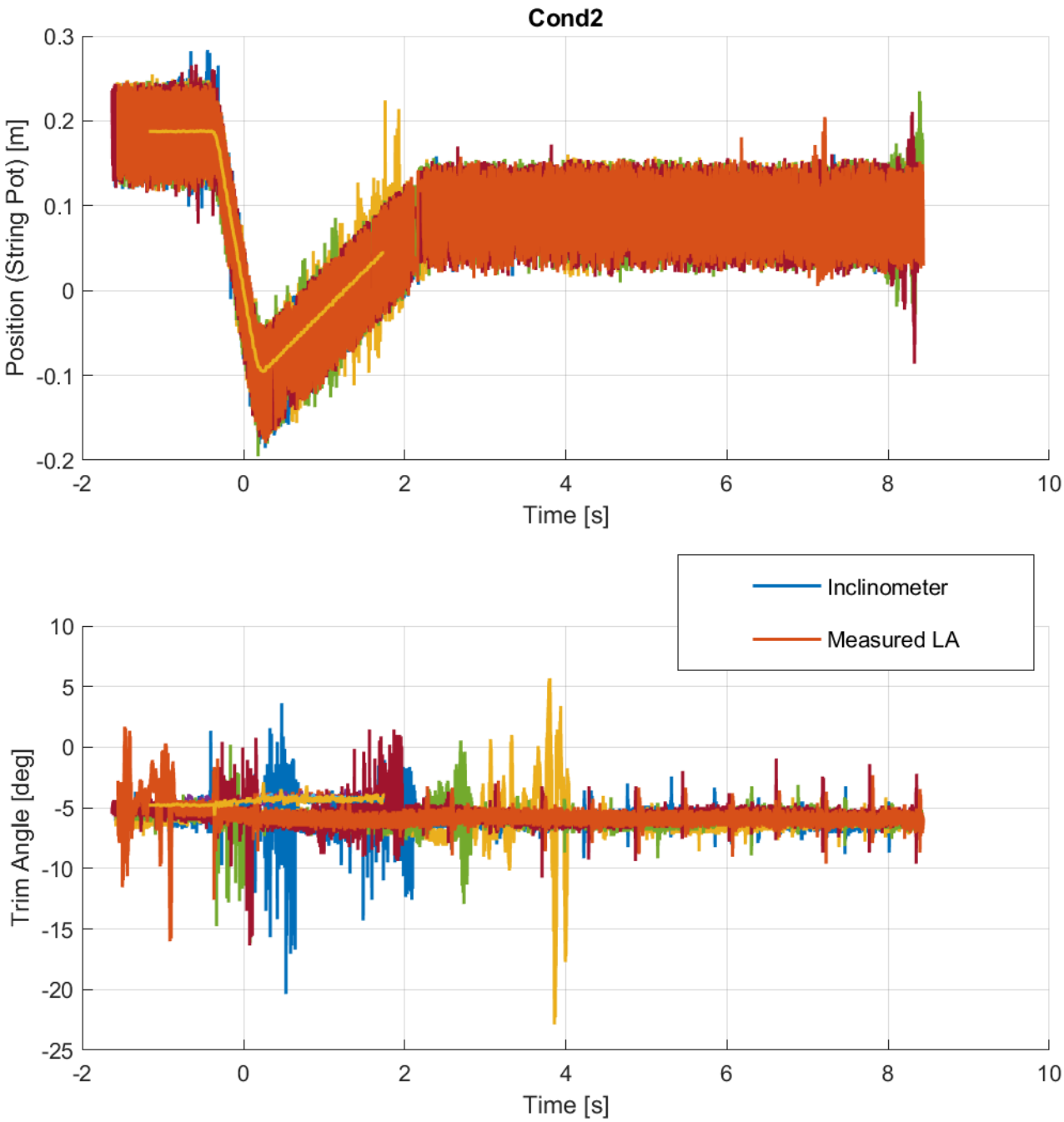
Cond2
Position (String Pot) [m]
0.3
0.2
0.1
0
-0.1
-0.2
-2
0
2
4
6
8
10
Time [s]
Inclinometer
Measured LA
Trim Angle [deg]
10
5
0
-5
-10
-15
-20
-25
-2
0
2
4
6
8
10
Time [s]

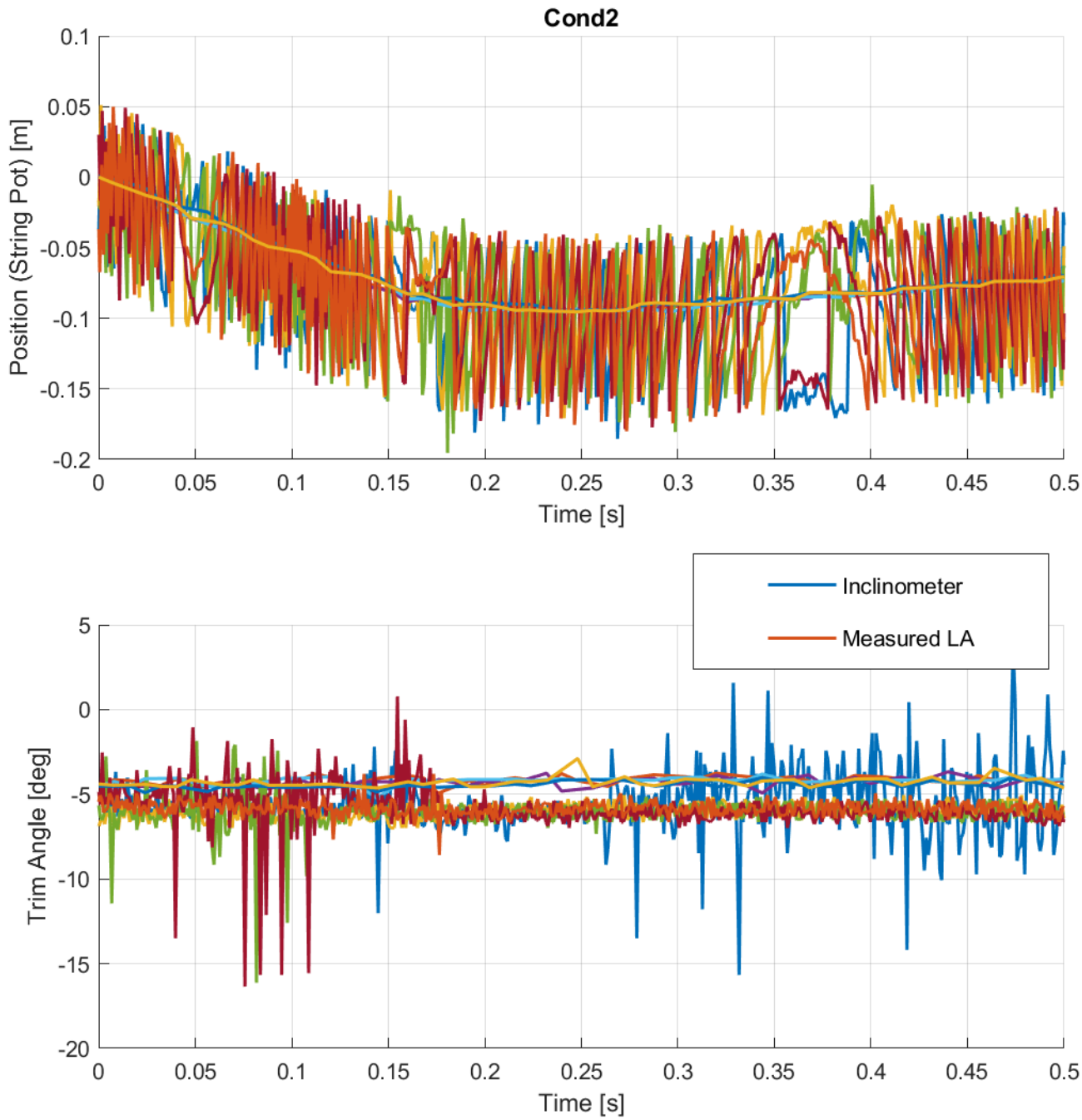
Cond2
Position (String Pot) [m]
0.1
0.05
0
-0.05
-0.1
-0.15
-0.2
0
0.05
0.1
0.15
0.2
0.25
0.3
0.35
0.4
0.45
0.5
Time [s]
Inclinometer
Measured LA
Trim Angle [deg]
5
0
-5
-10
-15
-20
0
0.05
0.1
0.15
0.2
0.25
0.3
0.35
0.4
0.45
0.5
Time [s]

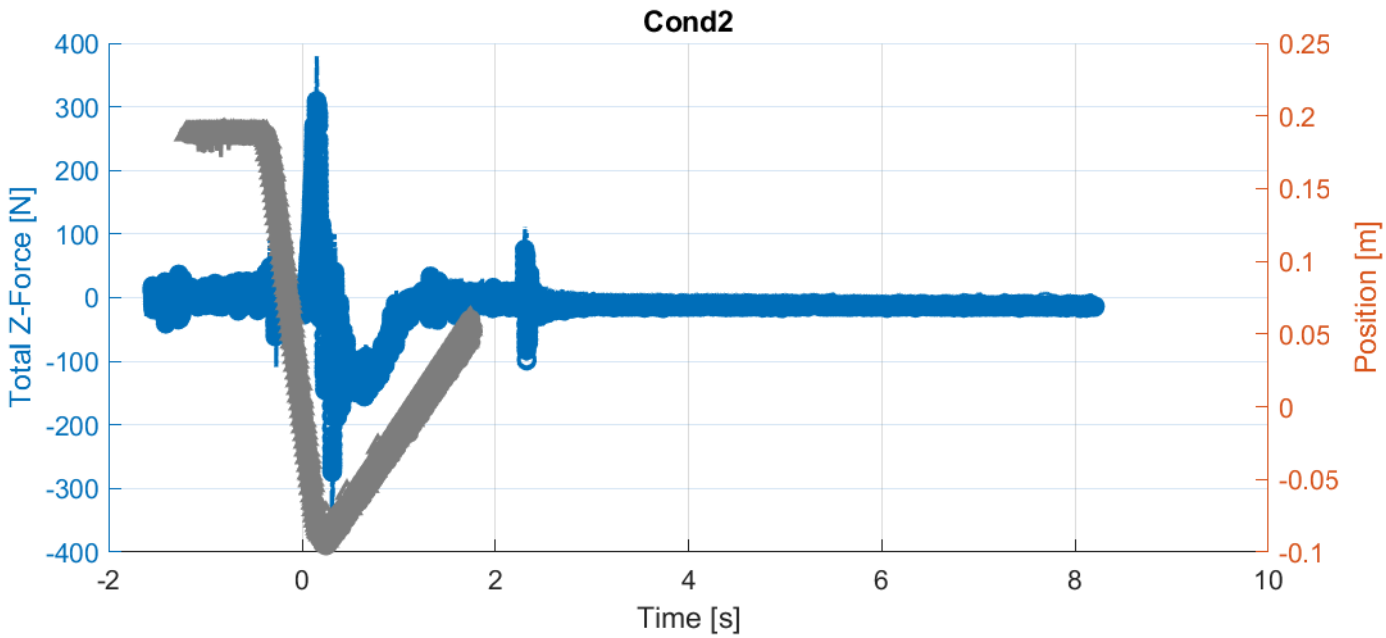
Cond2
Total Z-Force [N]
Position [m]
Time [s]
400
300
200
100
0
-100
-200
-300
-400
0.25
0.2
0.15
0.1
0.05
0
-0.05
-0.1
-2
0
2
4
6
8
10

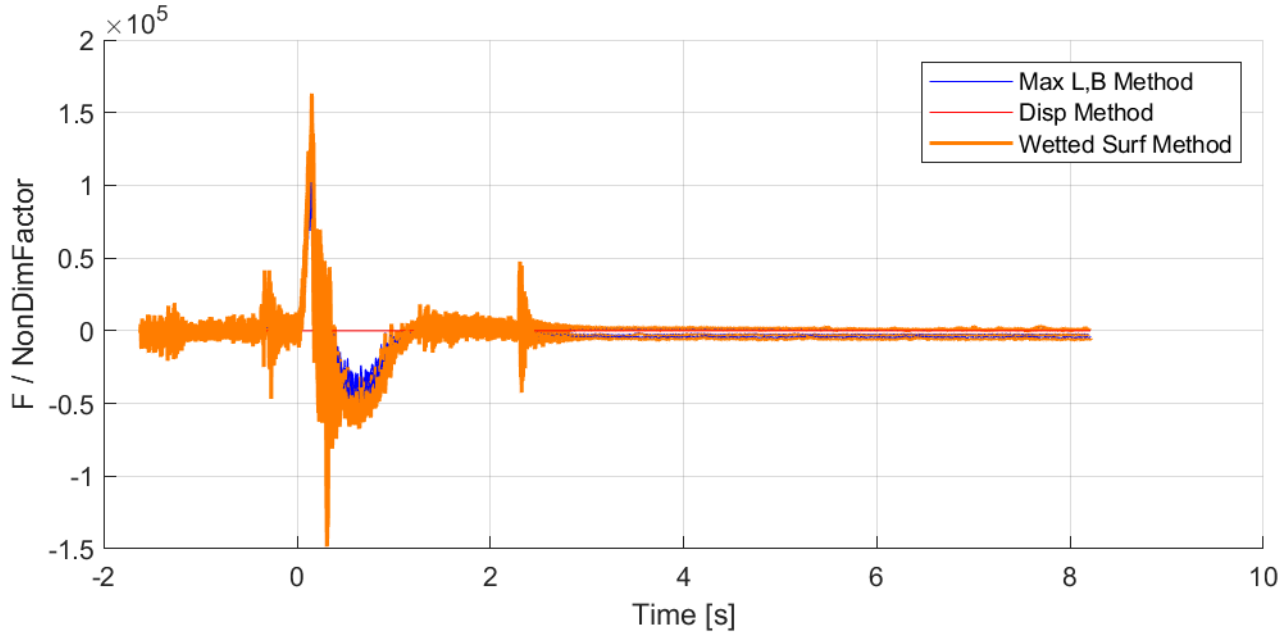
×10^5
F / NonDimFactor
Time [s]
Max L,B Method
Disp Method
Wetted Surf Method
2
1.5
1
0.5
0
-0.5
-1
-1.5
-2
0
2
4
6
8
10

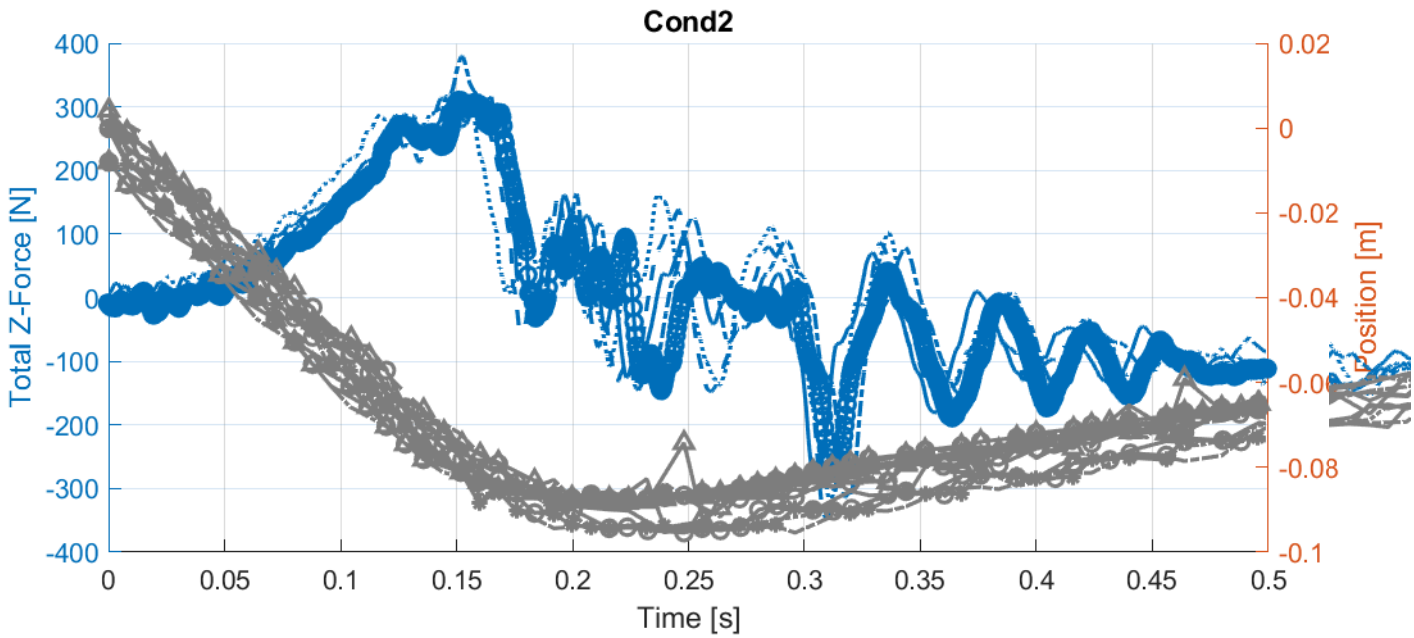
Cond2
Total Z-Force [N]
Position [m]
Time [s]
400
300
200
100
0
-100
-200
-300
-400
0.02
0
-0.02
-0.04
-0.08
-0.1
0
0.05
0.1
0.15
0.2
0.25
0.3
0.35
0.4
0.45
0.5

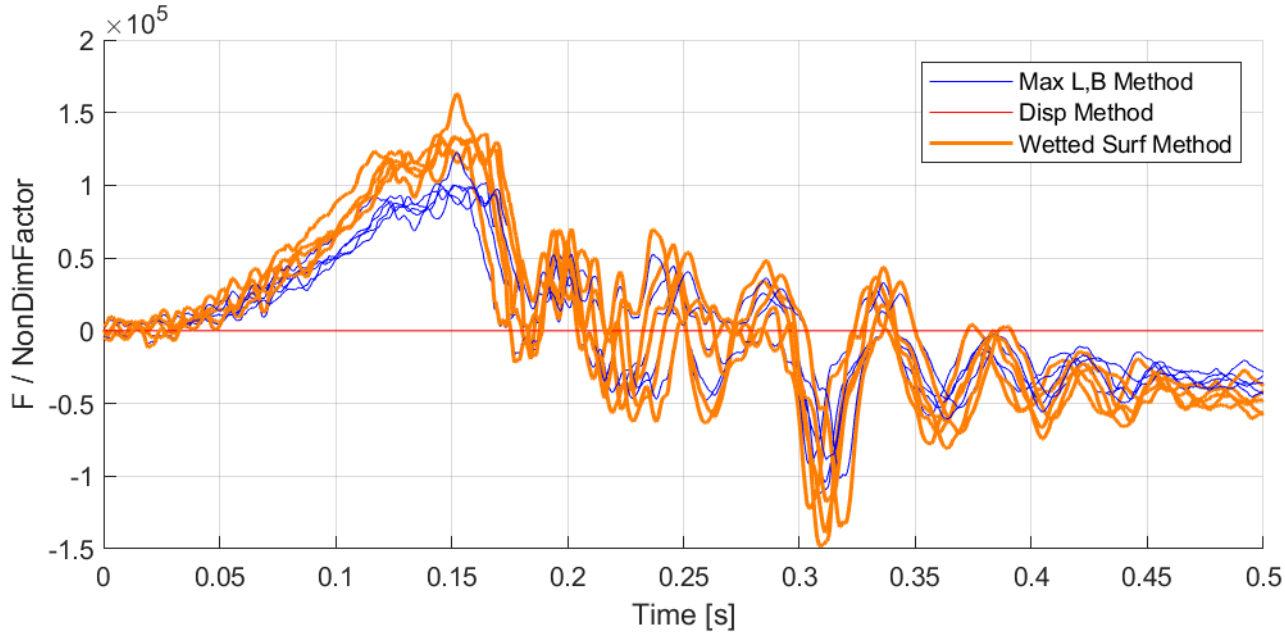
×10^5
F / NonDimFactor
Time [s]
Max L,B Method
Disp Method
Wetted Surf Method
2
1.5
1
0.5
0
-0.5
-1
-1.5
0
0.05
0.1
0.15
0.2
0.25
0.3
0.35
0.4
0.45
0.5

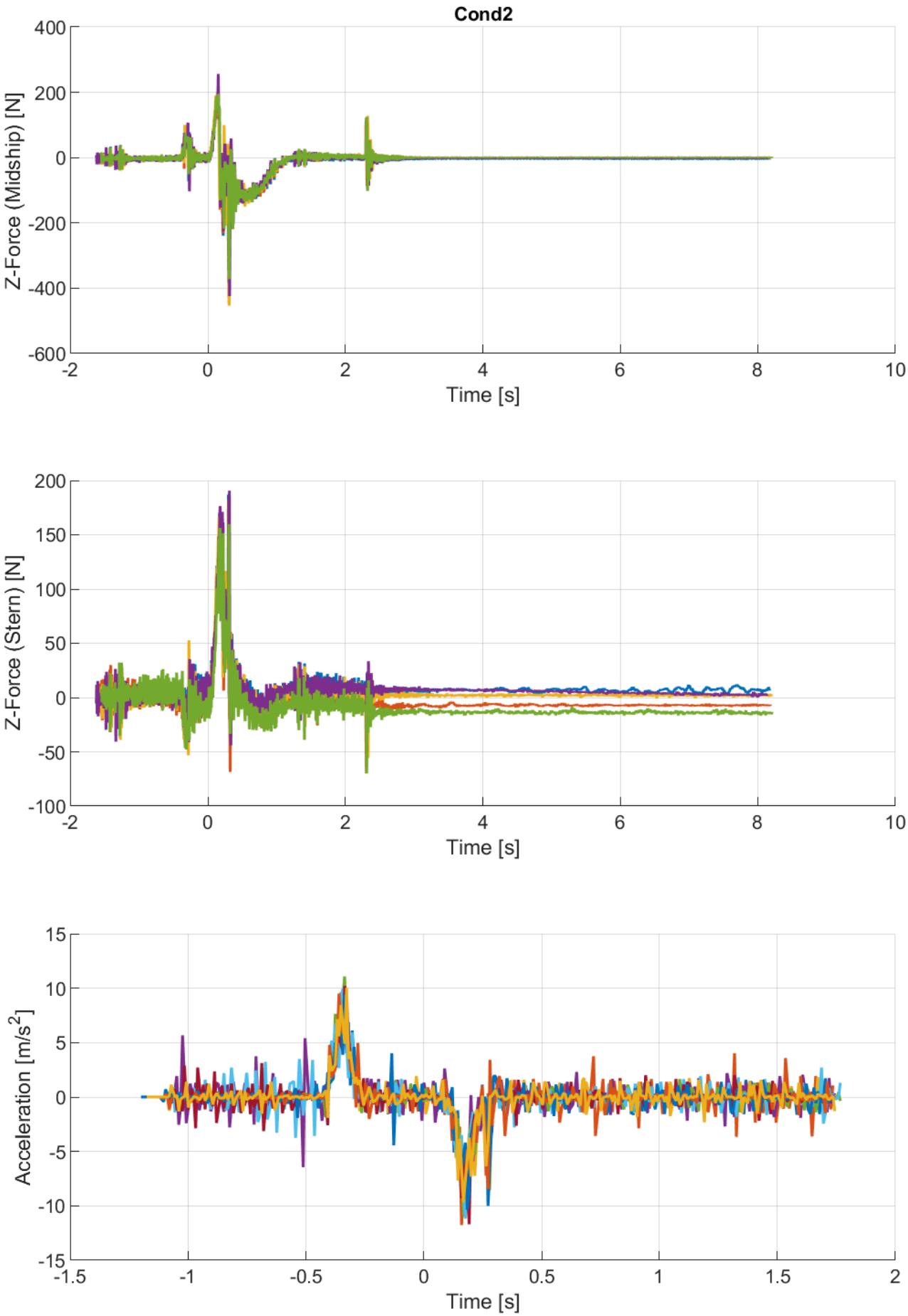
Cond2
Z-Force (Midship) [N]
400
200
0
-200
-400
-600
-2
0
2
4
6
8
10
Time [s]
Z-Force (Stern) [N]
200
150
100
50
0
-50
-100
-2
0
2
4
6
8
10
Time [s]
Acceleration [m/s^2]
15
10
5
0
-5
-10
-15
-1.5
-1
-0.5
0
0.5
1
1.5
2
Time [s]

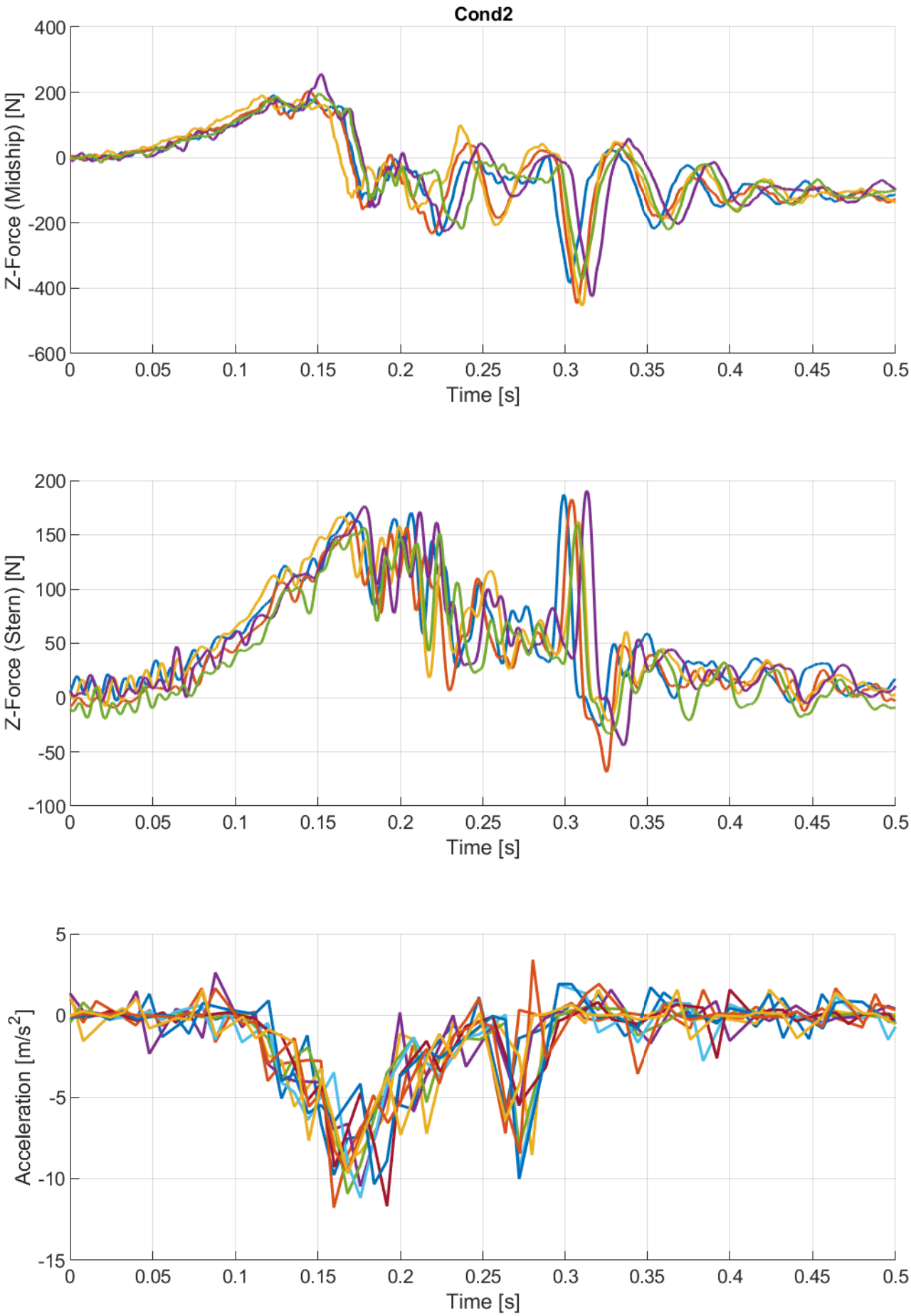
Cond2
Z-Force (Midship) [N]
400
200
0
-200
-400
-600
0
0.05
0.1
0.15
0.2
0.25
0.3
0.35
0.4
0.45
0.5
Time [s]
Z-Force (Stern) [N]
200
150
100
50
0
-50
-100
Time [s]
Acceleration [m/s^2]
5
0
-5
-10
-15
Time [s]

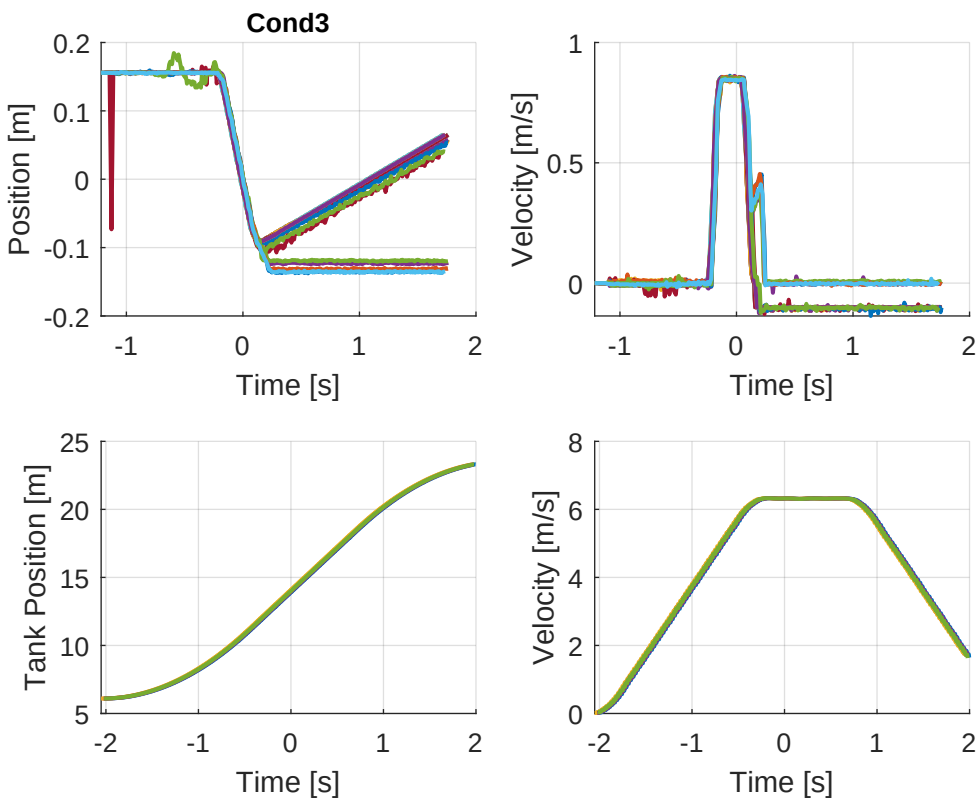
Cond3
Position [m]
Time [s]
Velocity [m/s]
Time [s]
Tank Position [m]
Time [s]
Velocity [m/s]
Time [s]

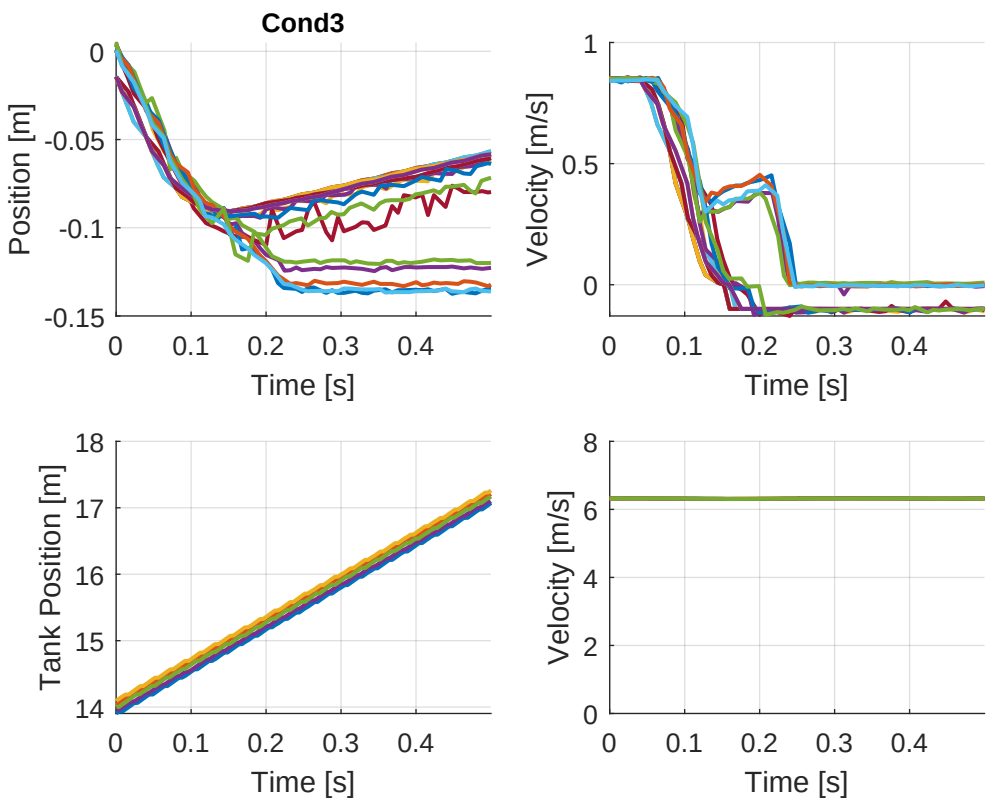
Cond3
Position [m]
0
-0.05
-0.1
-0.15
0
0.1
0.2
0.3
0.4
Time [s]
Velocity [m/s]
1
0.5
0
0
0.1
0.2
0.3
0.4
Time [s]
Tank Position [m]
18
17
16
15
14
0
0.1
0.2
0.3
0.4
Time [s]
Velocity [m/s]
8
6
4
2
0
0
0.1
0.2
0.3
0.4
Time [s]

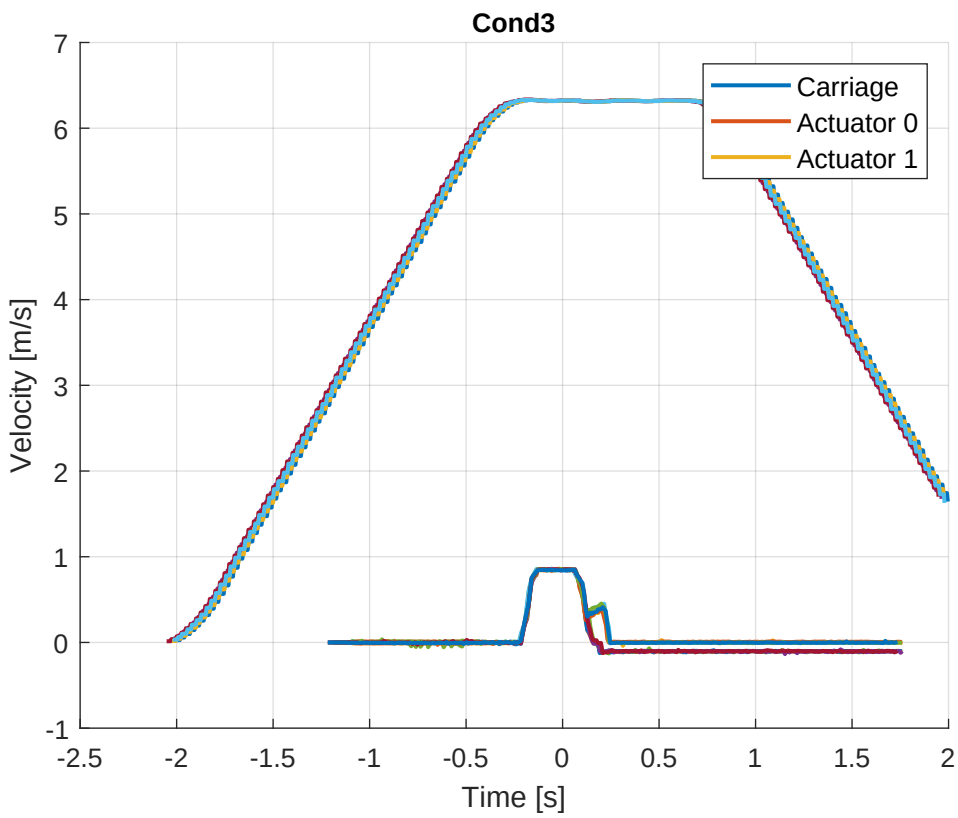
Cond3
Carriage
Actuator 0
Actuator 1
Velocity [m/s]
Time [s]
7
6
5
4
3
2
1
0
-1
-2.5
-2
-1.5
-1
-0.5
0
0.5
1
1.5
2

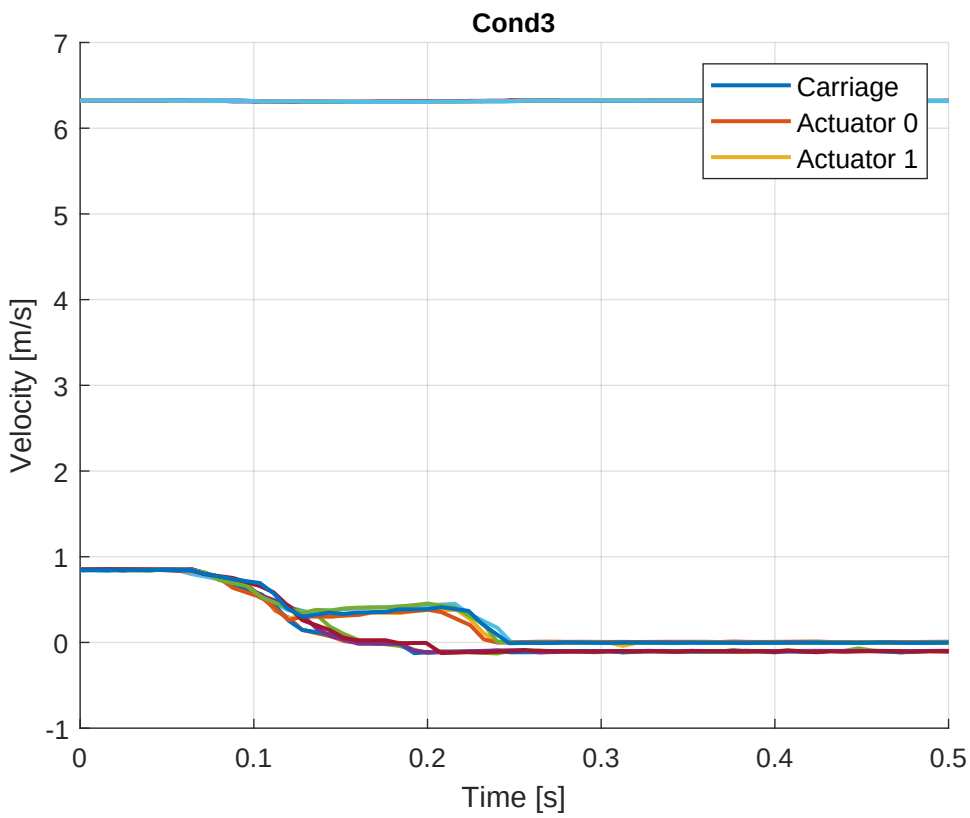
Cond3
Carriage
Actuator 0
Actuator 1
Velocity [m/s]
Time [s]
7
6
5
4
3
2
1
0
-1
0
0.1
0.2
0.3
0.4
0.5

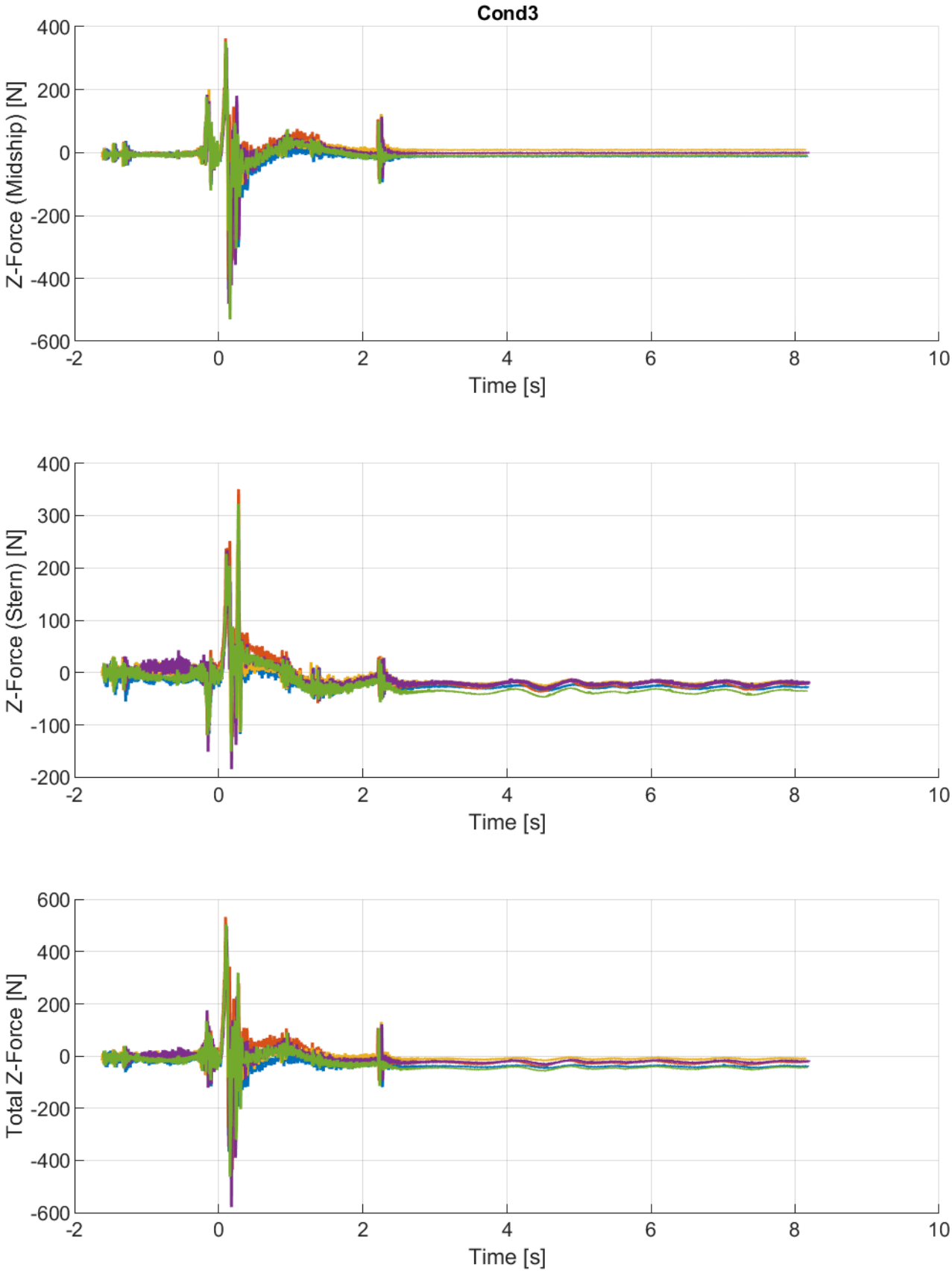
Cond3
Z-Force (Midship) [N]
400
200
0
-200
-400
-600
-2
0
2
4
6
8
10
Time [s]
Z-Force (Stern) [N]
400
300
200
100
0
-100
-200
-2
0
2
4
6
8
10
Time [s]
Total Z-Force [N]
600
400
200
0
-200
-400
-600
-2
0
2
4
6
8
10
Time [s]

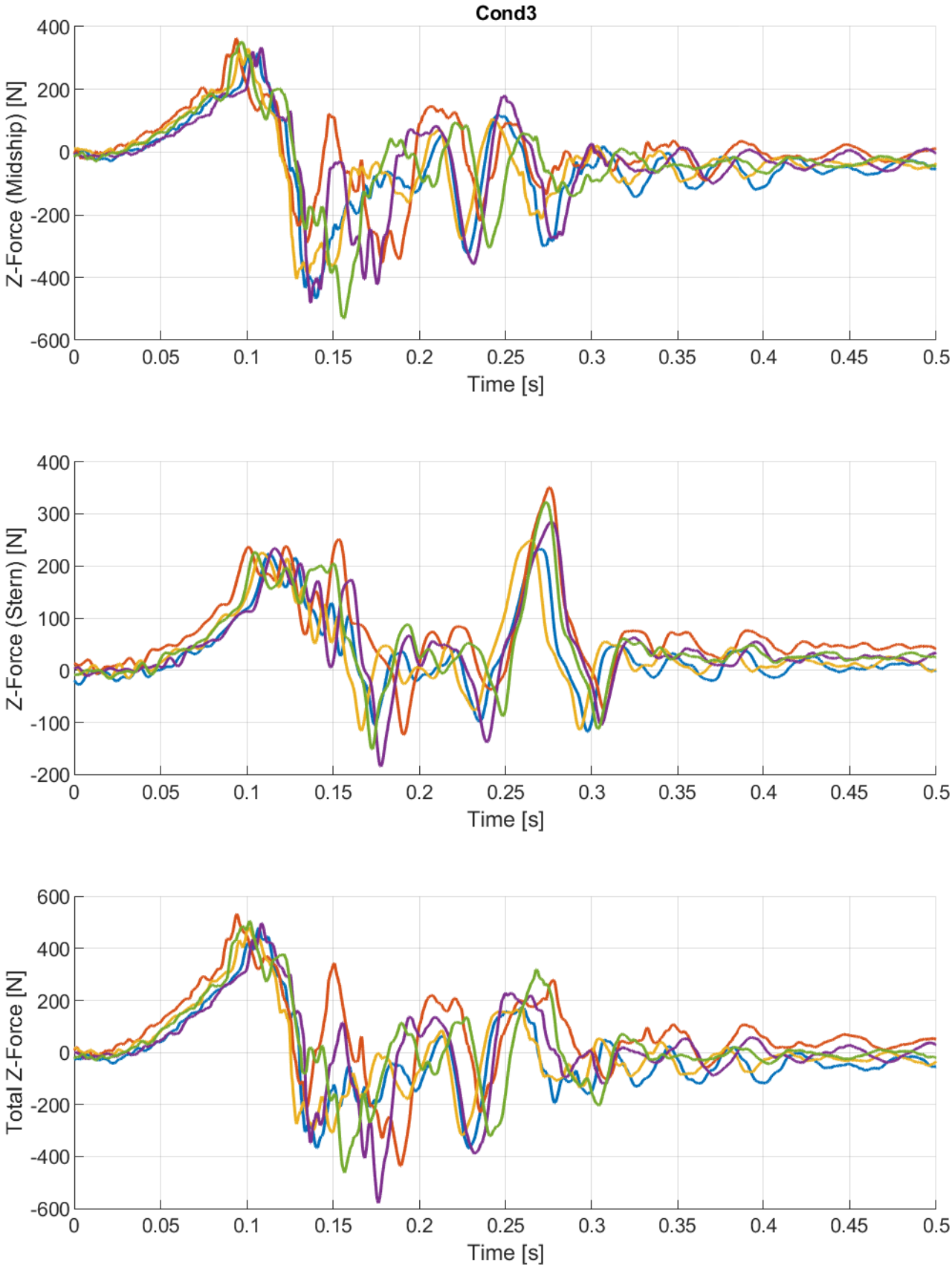
Cond3
Z-Force (Midship) [N]
400
200
0
-200
-400
-600
0
0.05
0.1
0.15
0.2
0.25
0.3
0.35
0.4
0.45
0.5
Time [s]
Z-Force (Stern) [N]
400
300
200
100
0
-100
-200
Time [s]
Total Z-Force [N]
600
400
200
0
-200
-400
-600
Time [s]

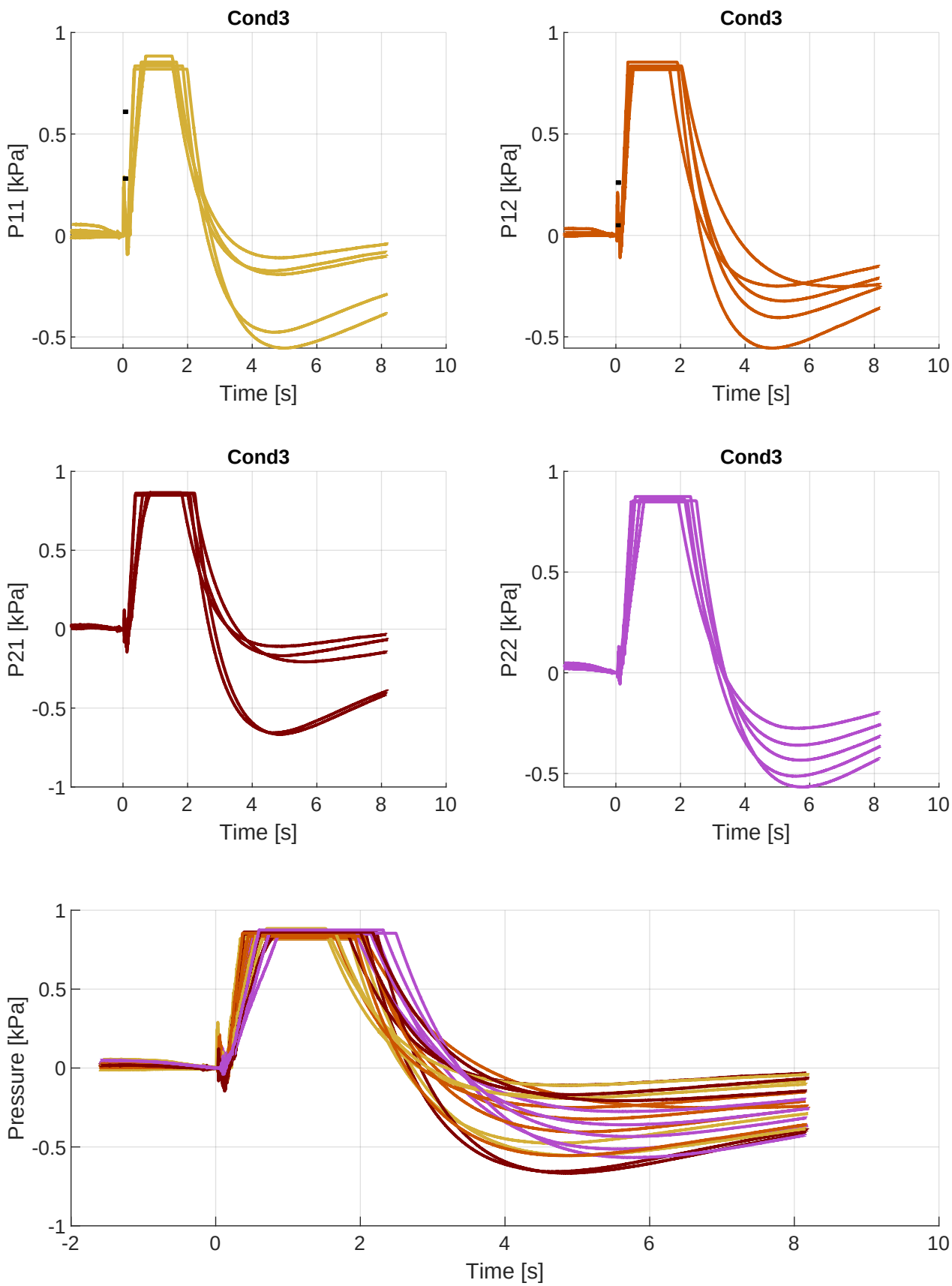
Cond3
P11 [kPa]
Time [s]
Cond3
P12 [kPa]
Time [s]
Cond3
P21 [kPa]
Time [s]
Cond3
P22 [kPa]
Time [s]
Pressure [kPa]
Time [s]

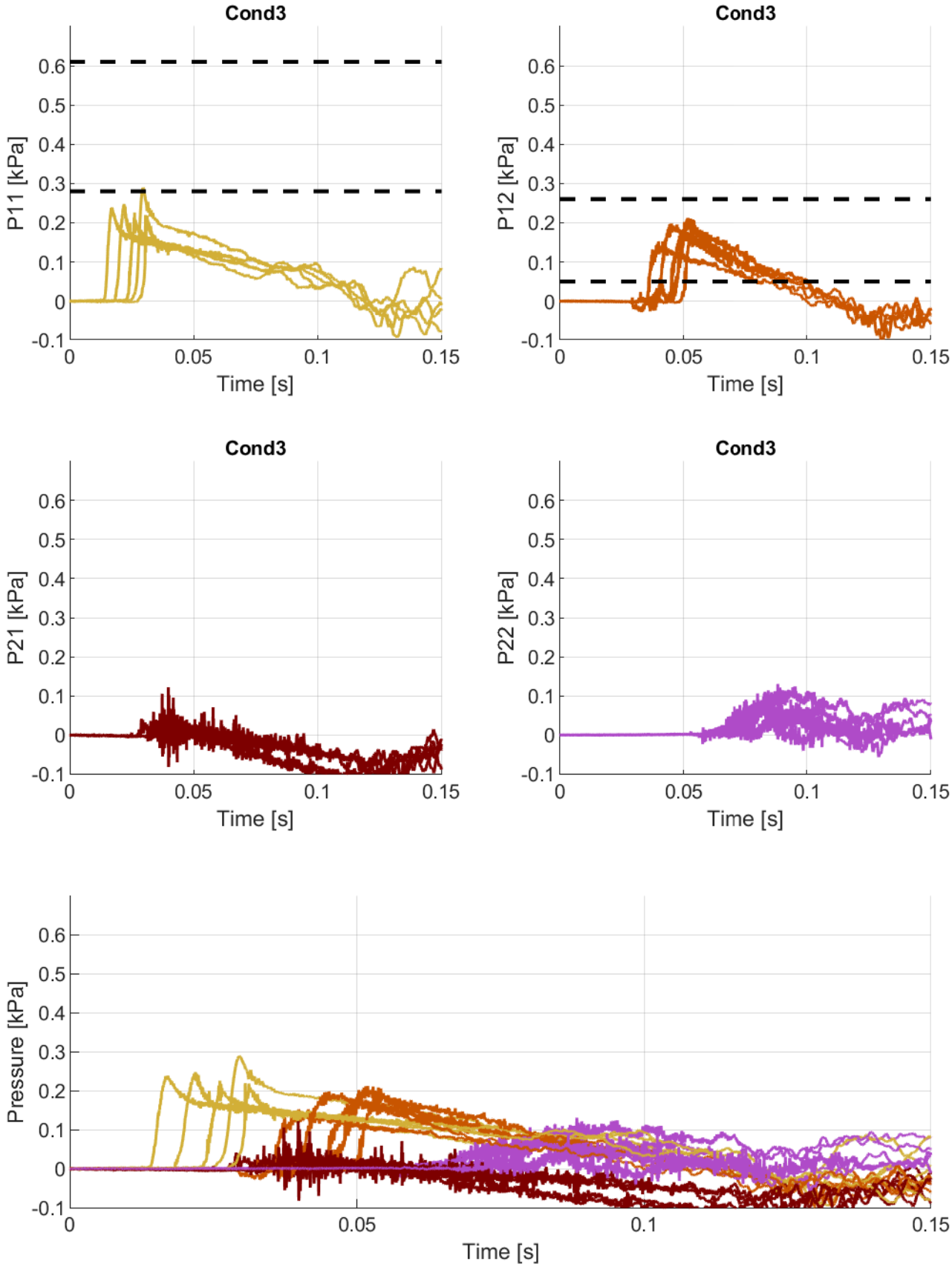
Cond3
P11 [kPa]
Time [s]
Cond3
P12 [kPa]
Time [s]
Cond3
P21 [kPa]
Time [s]
Cond3
P22 [kPa]
Time [s]
Pressure [kPa]
Time [s]

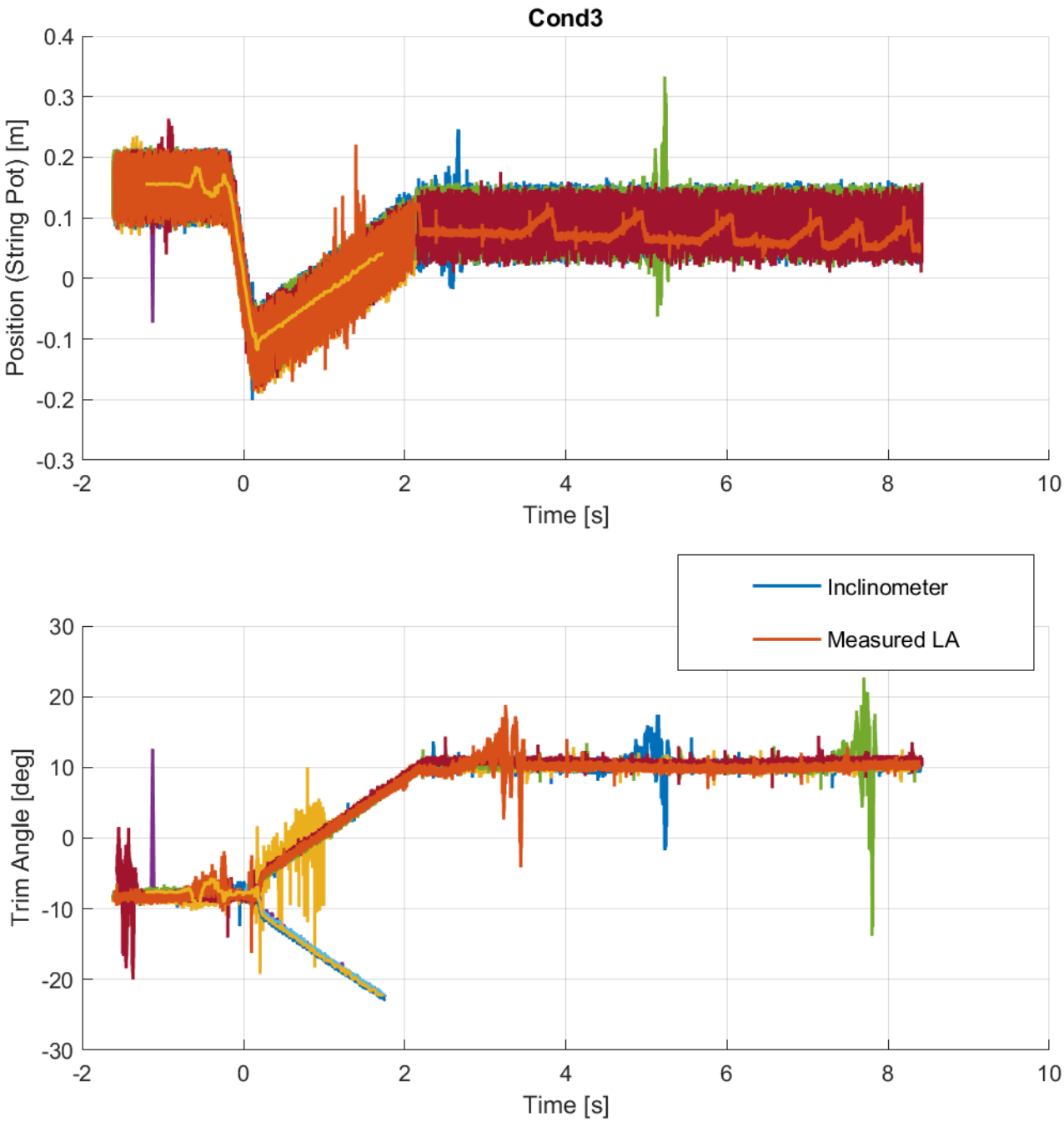
Cond3
Position (String Pot) [m]
0.4
0.3
0.2
0.1
0
-0.1
-0.2
-0.3
-2
0
2
4
6
8
10
Time [s]
Inclinometer
Measured LA
Trim Angle [deg]
30
20
10
0
-10
-20
-30
-2
0
2
4
6
8
10
Time [s]

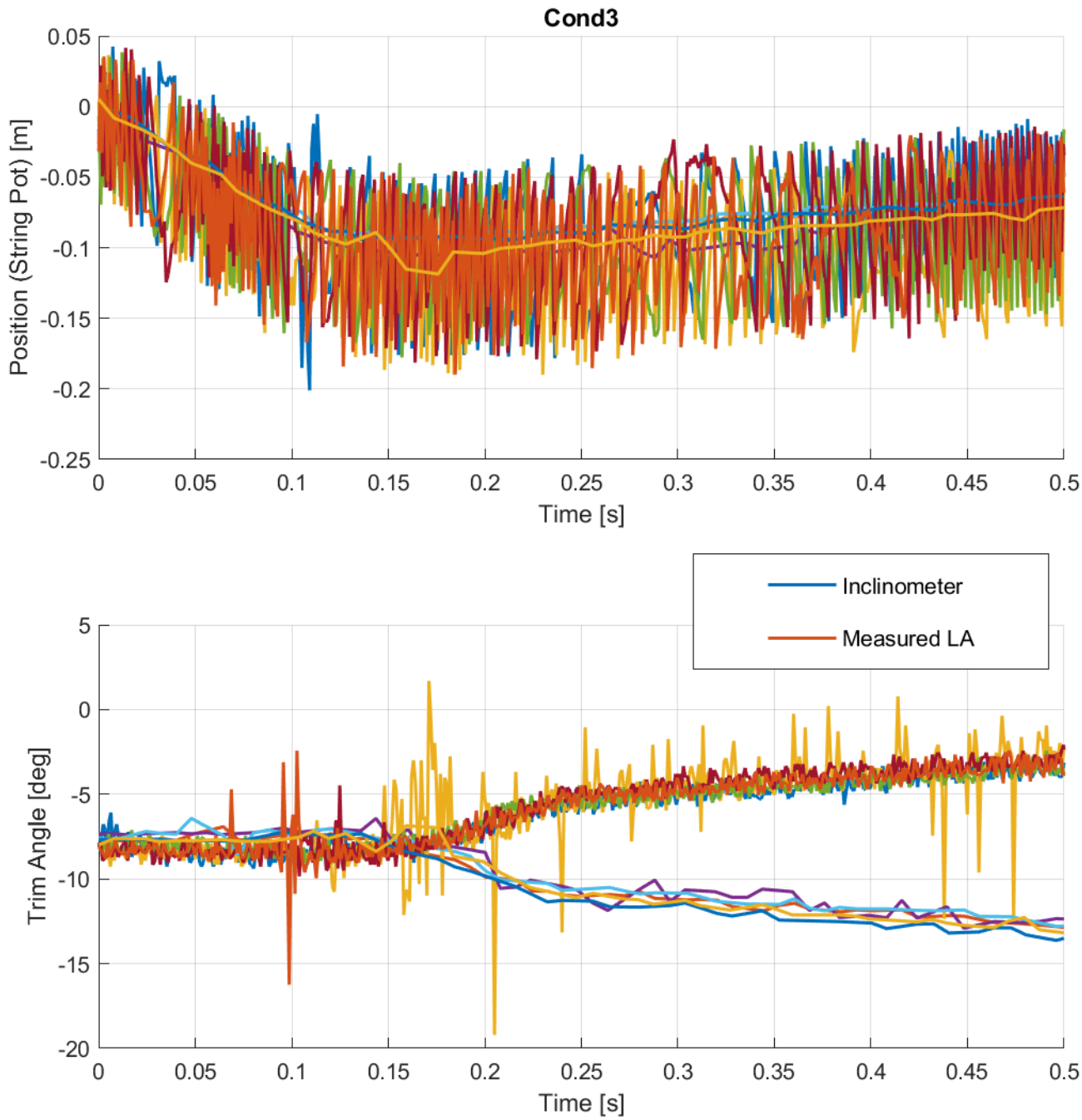
Cond3
Position (String Pot) [m]
0.05
0
-0.05
-0.1
-0.15
-0.2
-0.25
0
0.05
0.1
0.15
0.2
0.25
0.3
0.35
0.4
0.45
0.5
Time [s]
Inclinometer
Measured LA
Trim Angle [deg]
5
0
-5
-10
-15
-20
0
0.05
0.1
0.15
0.2
0.25
0.3
0.35
0.4
0.45
0.5
Time [s]

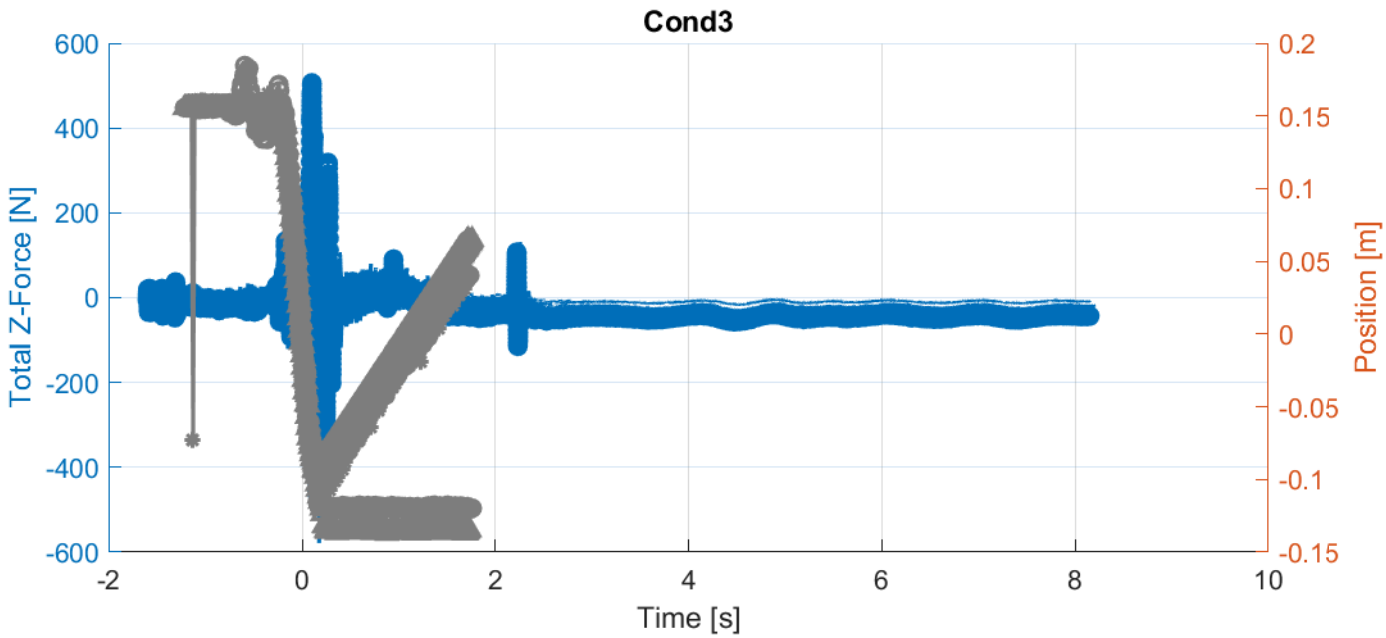
Cond3
Total Z-Force [N]
Position [m]
Time [s]
600
400
200
0
-200
-400
-600
0.2
0.15
0.1
0.05
0
-0.05
-0.1
-0.15
-2
0
2
4
6
8
10

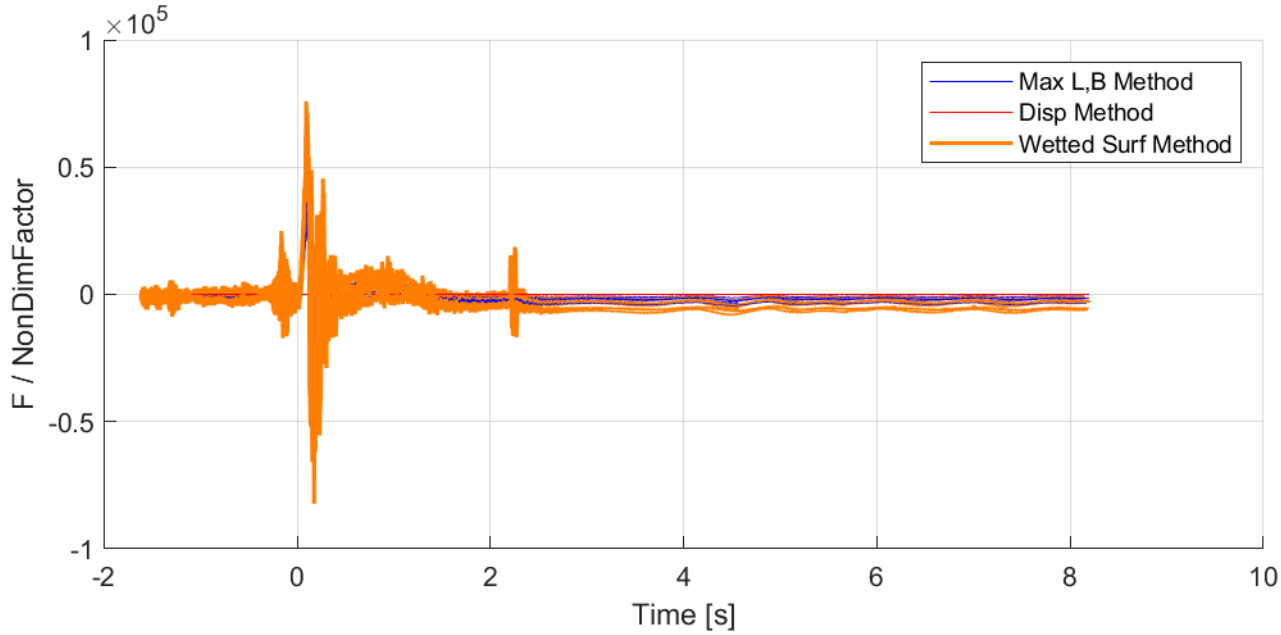
×10^5
F / NonDimFactor
Time [s]
Max L,B Method
Disp Method
Wetted Surf Method
1
0.5
0
-0.5
-1
-2
0
2
4
6
8
10

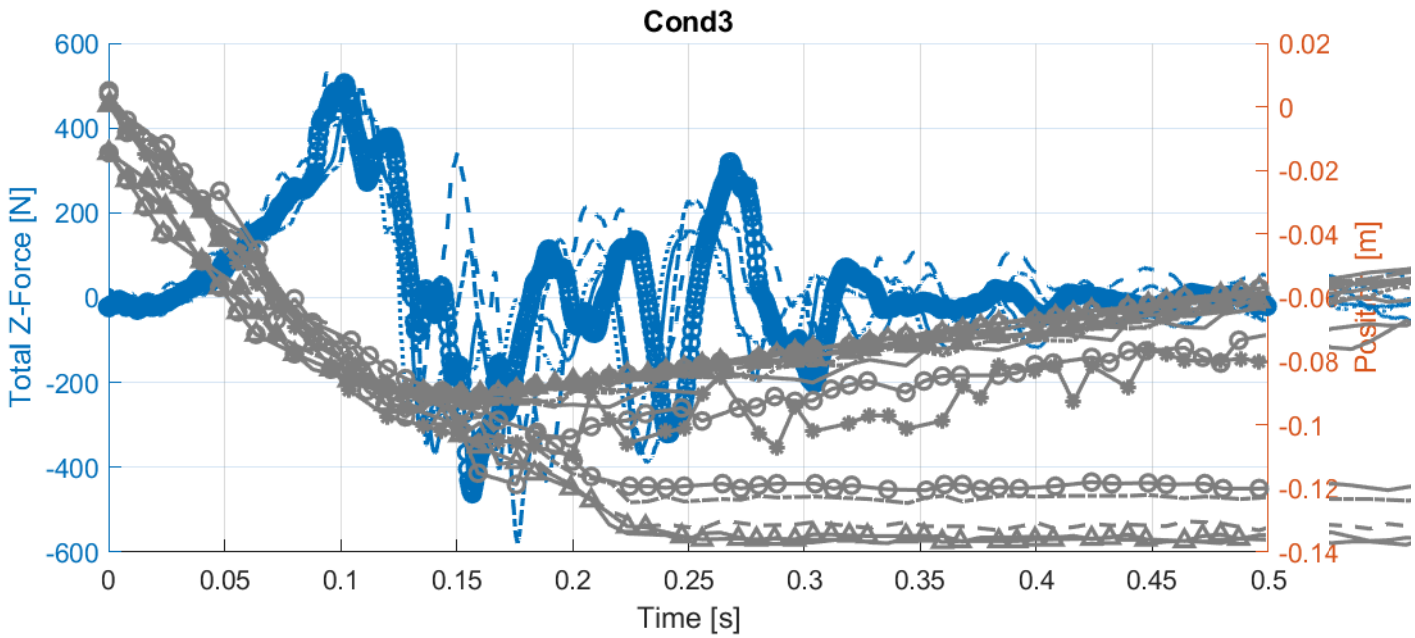
Cond3
Total Z-Force [N]
Time [s]
600
400
200
0
-200
-400
-600
0.02
0
-0.02
-0.04
-0.08
-0.1
-0.12
-0.14
0
0.05
0.1
0.15
0.2
0.25
0.3
0.35
0.4
0.45
0.5

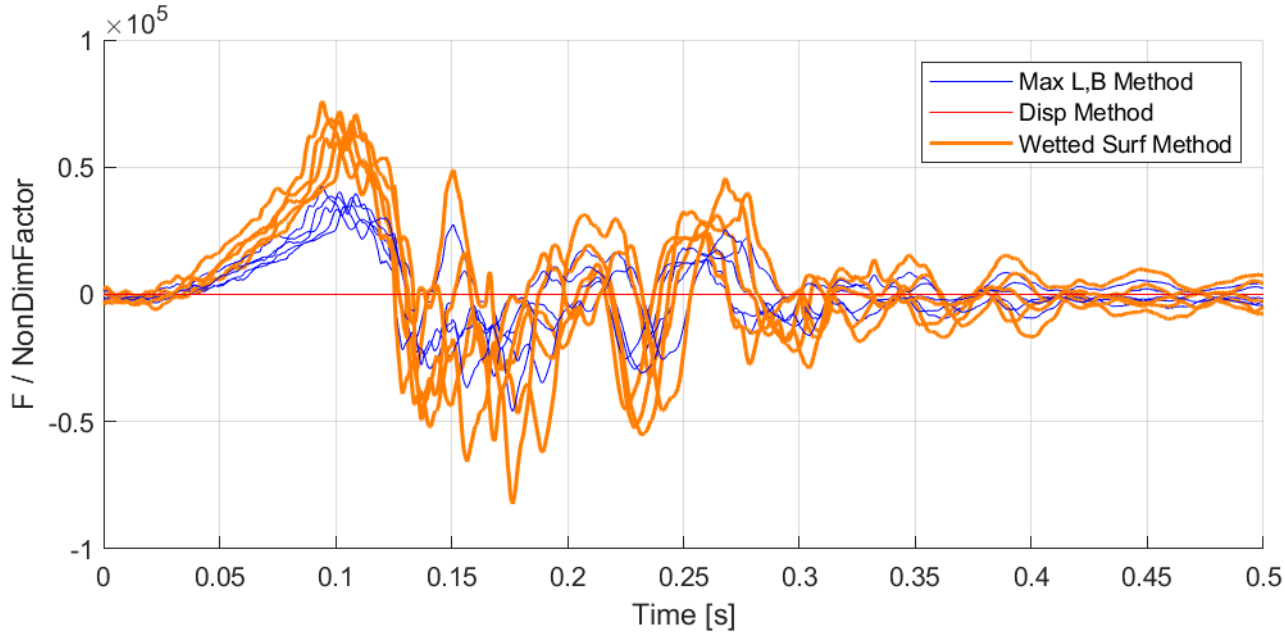
×10^5
1
0.5
0
-0.5
-1
F / NonDimFactor
Time [s]
Max L,B Method
Disp Method
Wetted Surf Method
0
0.05
0.1
0.15
0.2
0.25
0.3
0.35
0.4
0.45
0.5

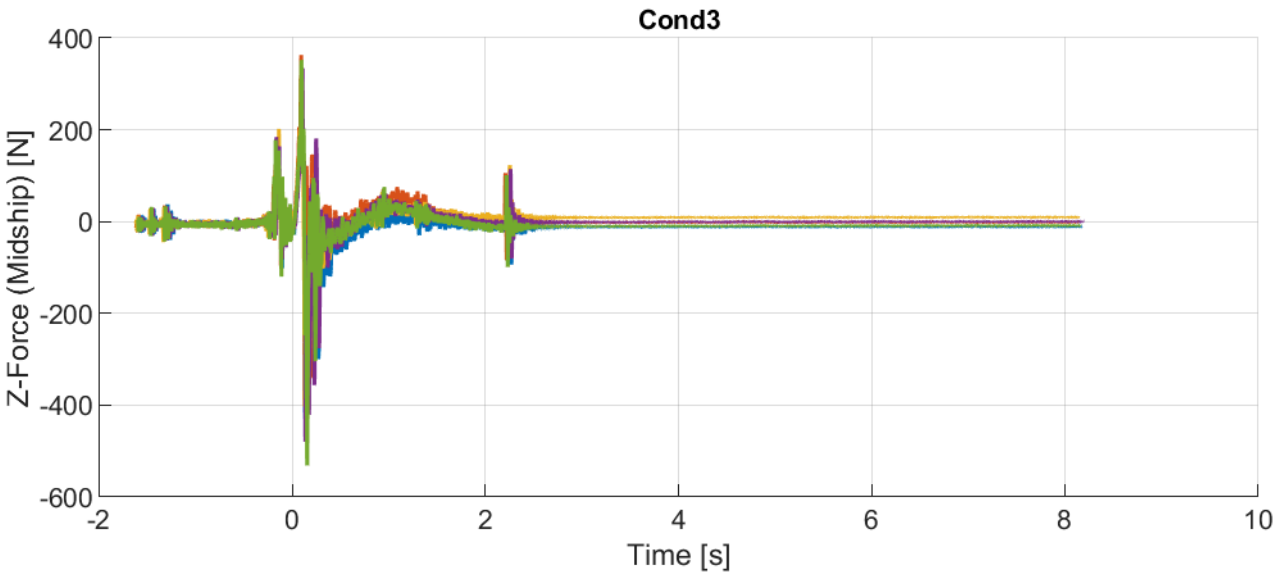
Cond3
Z-Force (Midship) [N]
400
200
0
-200
-400
-600
-2
0
2
4
6
8
10
Time [s]

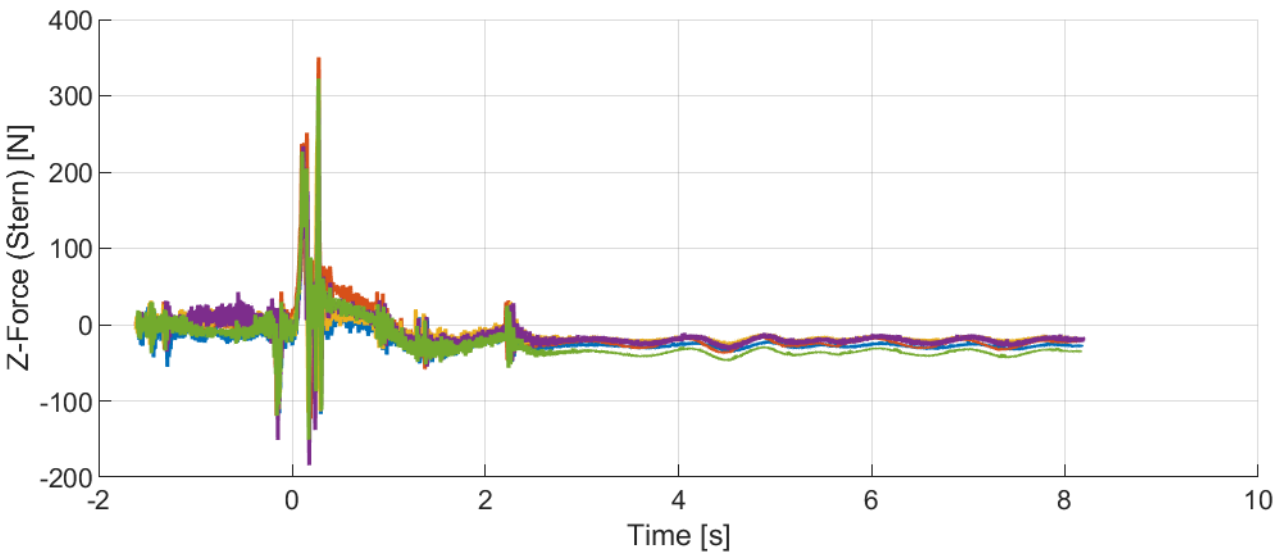
Z-Force (Stern) [N]
400
300
200
100
0
-100
-200
-2
0
2
4
6
8
10
Time [s]

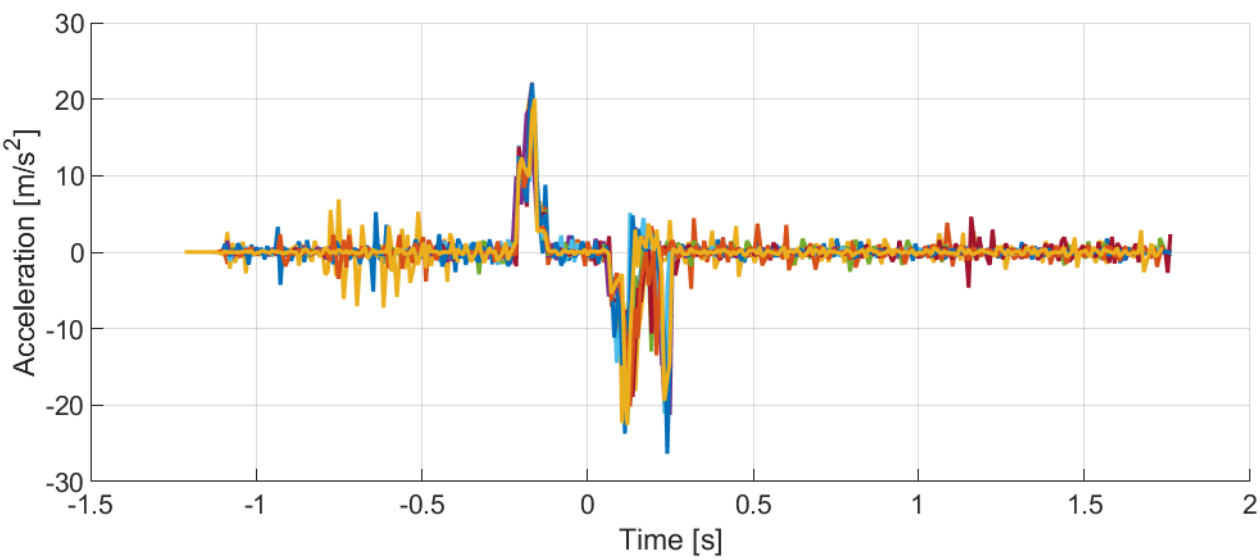
Acceleration [m/s2]
30
20
10
0
-10
-20
-30
-1.5
-1
-0.5
0
0.5
1
1.5
2
Time [s]

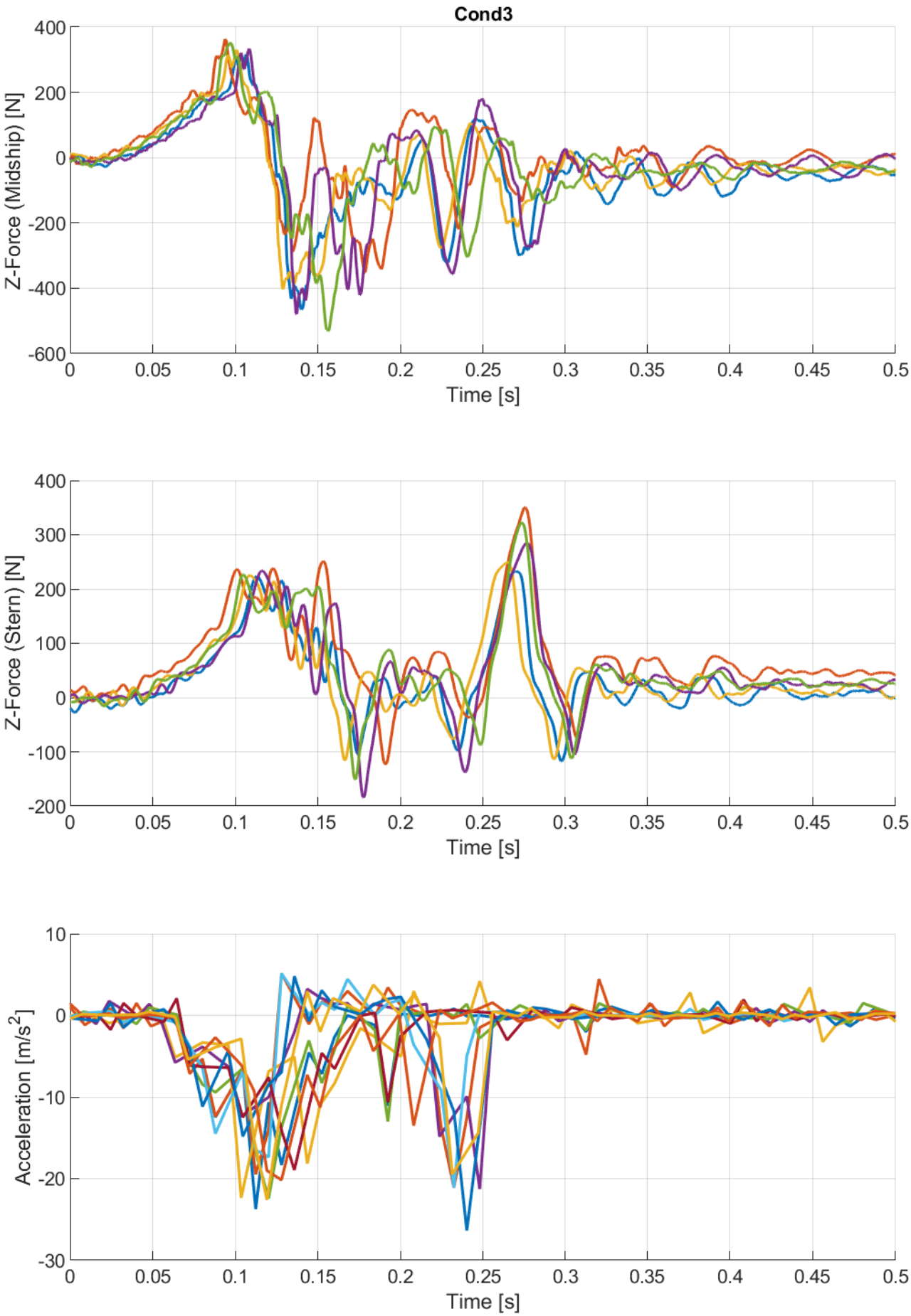
Cond3
Z-Force (Midship) [N]
400
200
0
-200
-400
-600
0
0.05
0.1
0.15
0.2
0.25
0.3
0.35
0.4
0.45
0.5
Time [s]
Z-Force (Stern) [N]
400
300
200
100
0
-100
-200
Time [s]
Acceleration [m/s^2]
10
0
-10
-20
-30
Time [s]

Appendix B

VPMM Control and Data Acquisition Software

VPMMControlHighSpeed_v2.vi
C:\Users\towtankuser\Documents\LabVIEWMC\examples\CompactRIO\FPGA Fundamentals\FPGA Math and Analysis\Floating-point PID\Multi-Rate PID\VPMMControlHighSpeed_v2.vi
Last modified on 4/3/2024 at 6:09 PM
Printed on 4/3/2024 at 6:12 PM

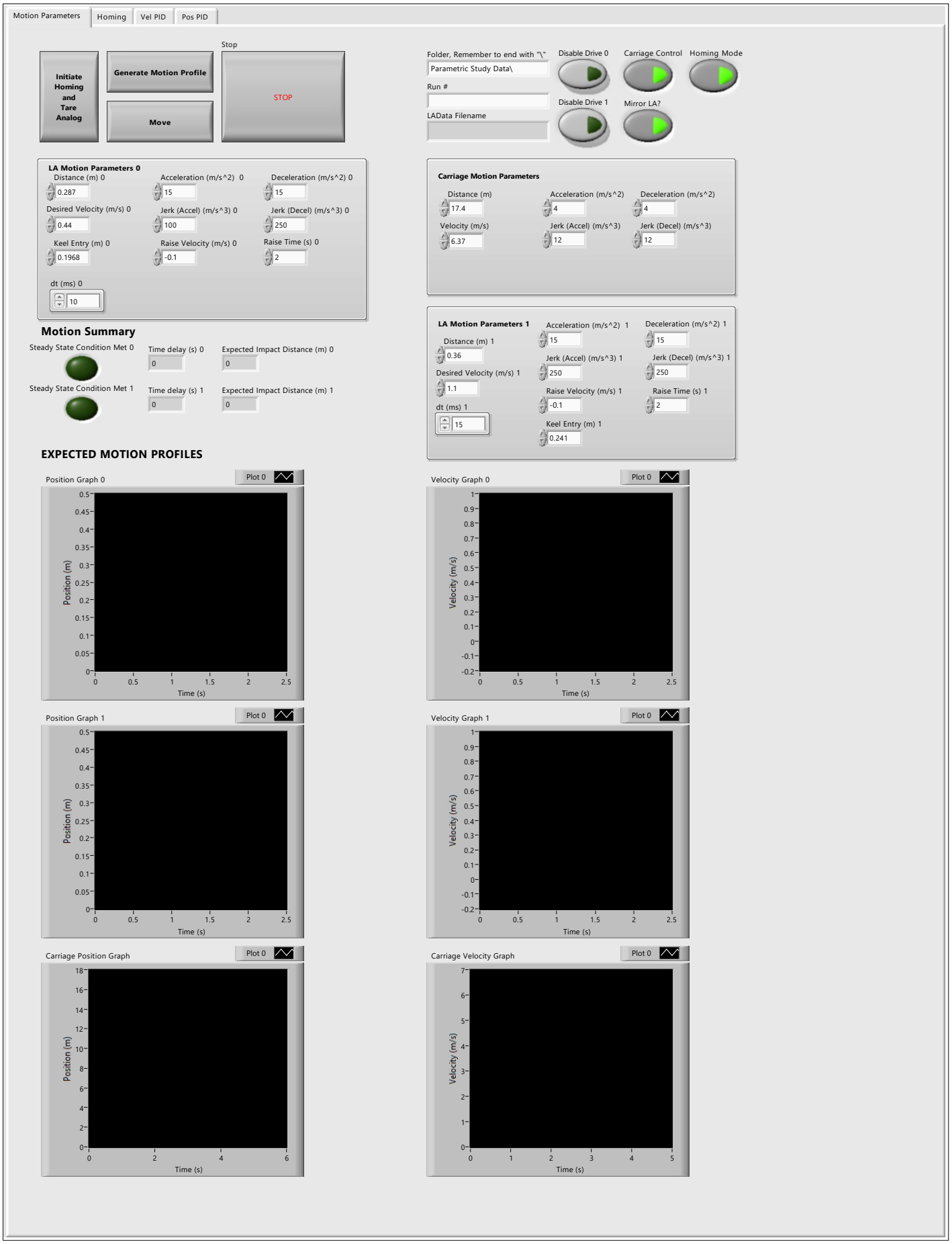

VPMMControlHighSpeed_v2.vi
C:\Users\towtankuser\Documents\LabVIEWMC\examples\CompactRIO\FPGA Fundamentals\FPGA Math and Analysis\Floating-point PID\Multi-Rate PID\VPMMControlHighSpeed_v2.vi
Last modified on 4/4/2024 at 10:50 AM
Printed on 4/4/2024 at 10:51 AM

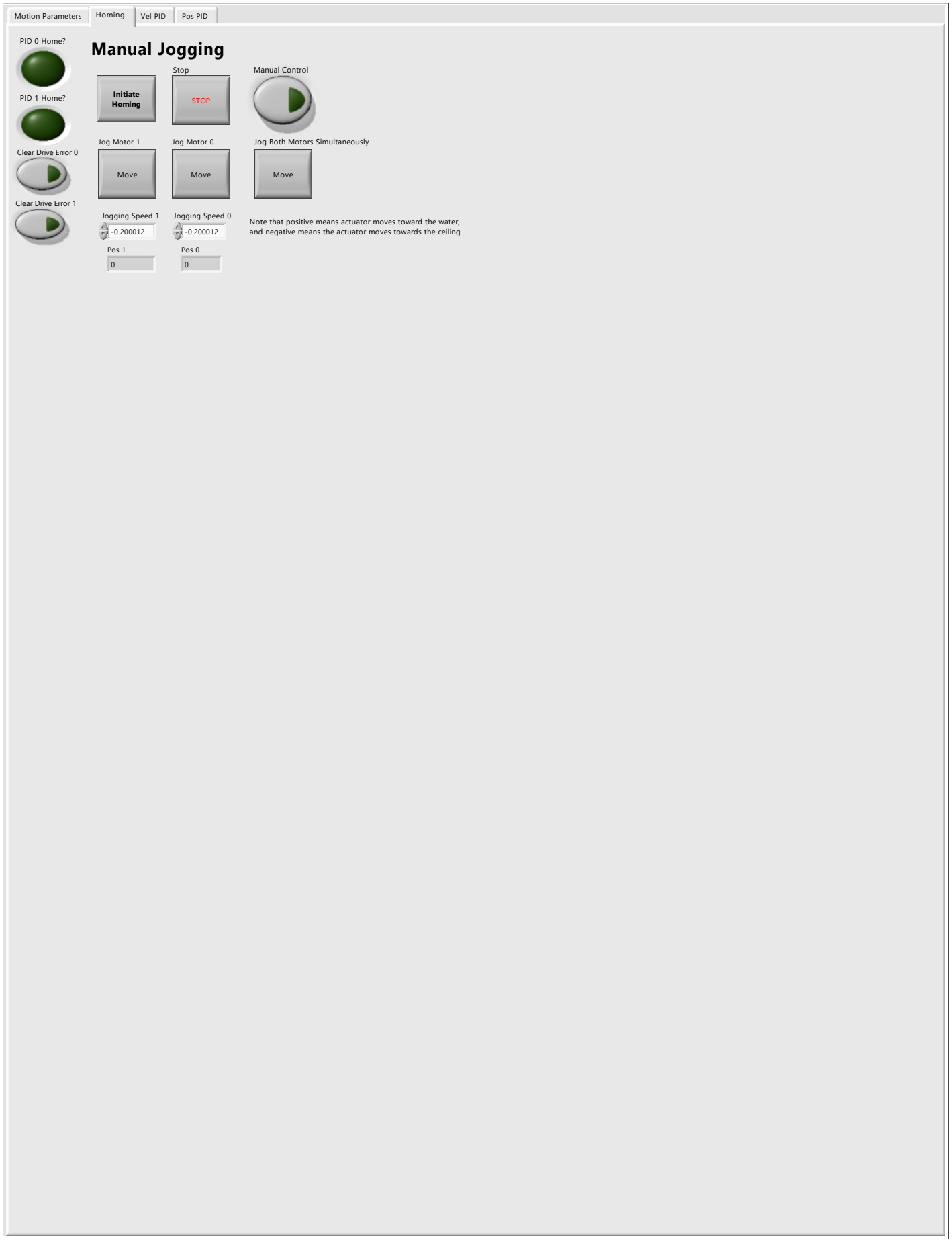

VPMMControlHighSpeed_v2.vi
C:\Users\towtankuser\Documents\LabVIEWMC\examples\CompactRIO\FPGA Fundamentals\FPGA Math and Analysis\Floating-point PID\Multi-Rate PID\VPMMControlHighSpeed_v2.vi
Last modified on 4/4/2024 at 10:50 AM
Printed on 4/4/2024 at 10:52 AM

VPMMControlHighSpeed_v2.vi
C:\Users\towtankuser\Documents\LabVIEWMC\examples\CompactRIO\FPGA Fundamentals\FPGA Math and Analysis\Floating-point PID\Multi-Rate PID\VPMMControlHighSpeed_v2.vi
Last modified on 4/4/2024 at 10:50 AM
Printed on 4/4/2024 at 10:52 AM

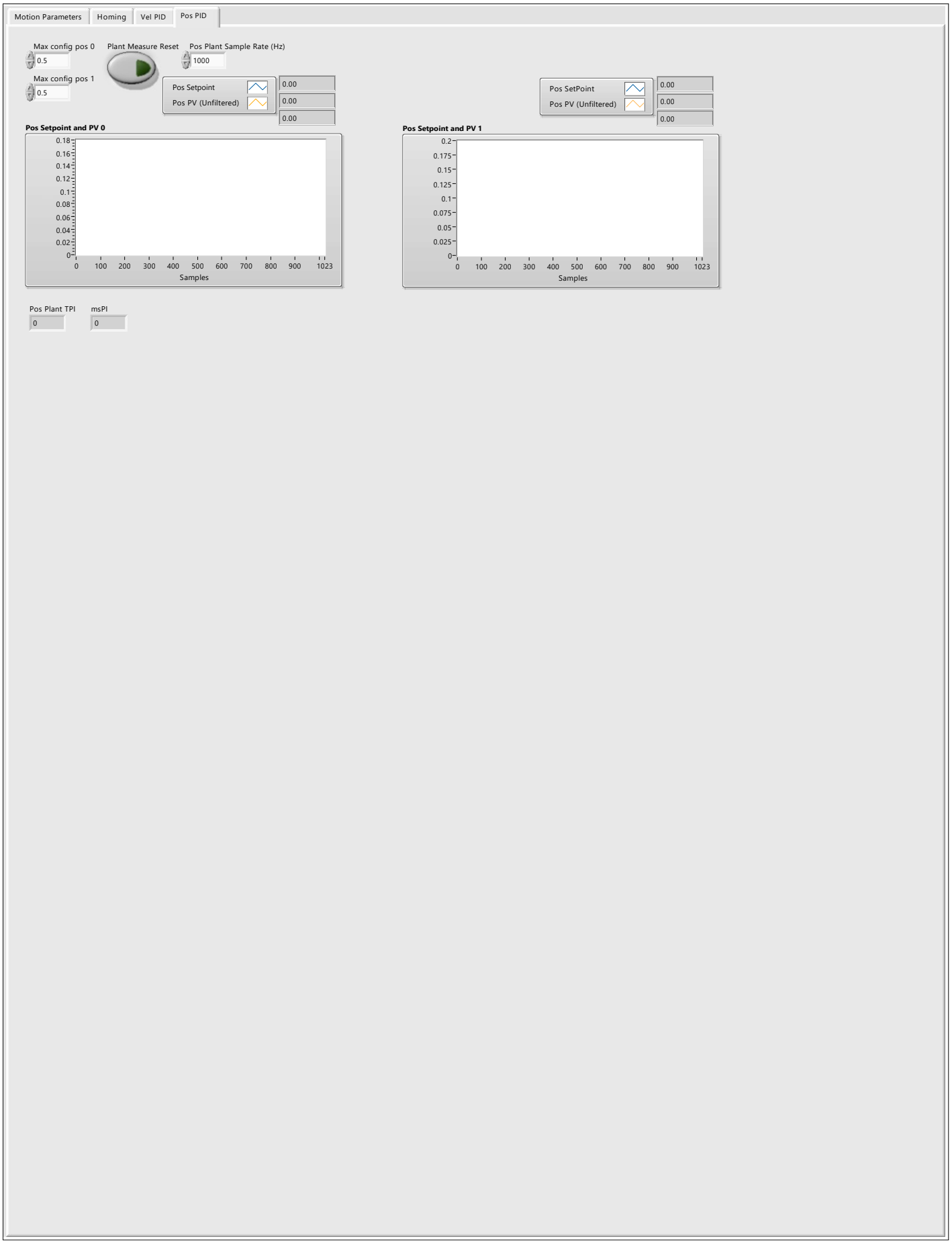

VPMMControlHighSpeed_v2.vi
C:\Users\towtankuser\Documents\LabVIEWMC\examples\CompactRIO\FPGA Fundamentals\FPGA Math and Analysis\Floating-point PID\Multi-Rate PID\VPMMControlHighSpeed_v2.vi
Last modified on 4/3/2024 at 6:09 PM
Printed on 4/3/2024 at 6:12 PM

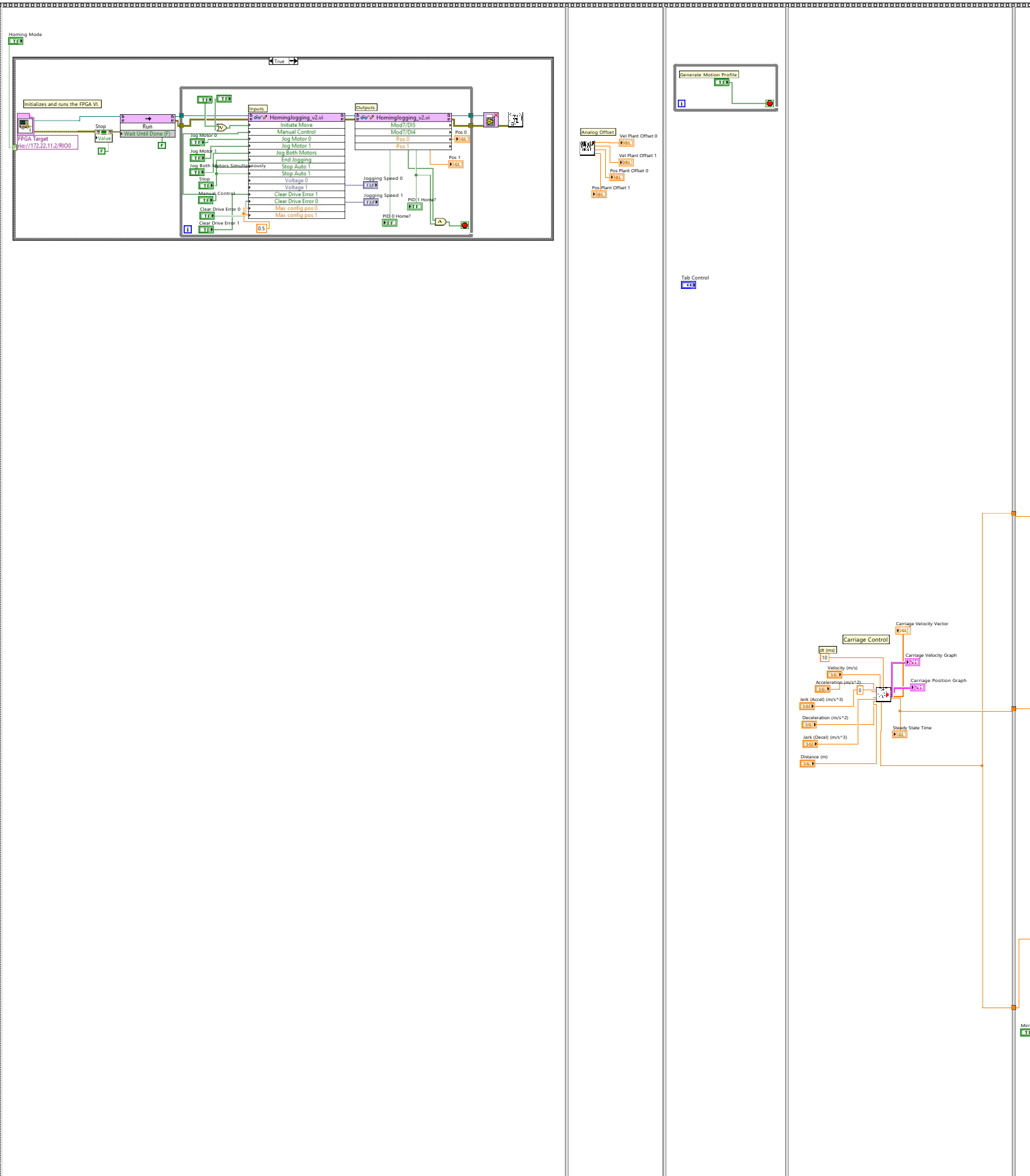

VPMMControlHighSpeed_v2.vi
C:\Users\towtankuser\Documents\LabVIEWMC\examples\CompactRIO\FPGA Fundamentals\FPGA Math and Analysis\Floating-point PID\Multi-Rate PID\VPMMControlHighSpeed_v2.vi
Last modified on 4/3/2024 at 6:09 PM
Printed on 4/3/2024 at 6:12 PM

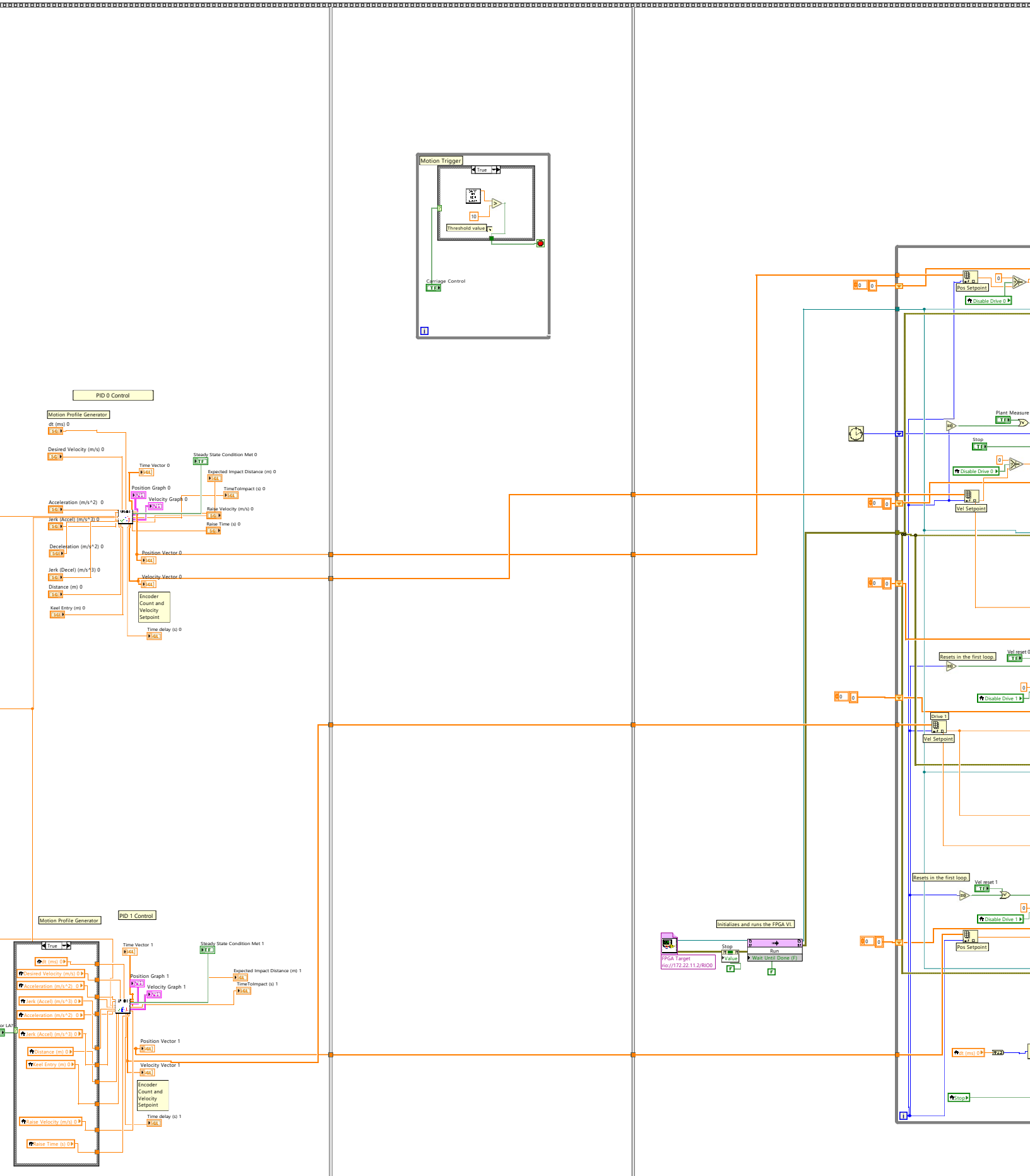

VPMMControlHighSpeed_v2.vi
C:\Users\towtankuser\Documents\LabVIEWMC\examples\CompactRIO\FPGA Fundamentals\FPGA Math and Analysis\Floating-point PID\Multi-Rate PID\VPMMControlHighSpeed_v2.vi
Last modified on 4/3/2024 at 6:09 PM
Printed on 4/3/2024 at 6:12 PM

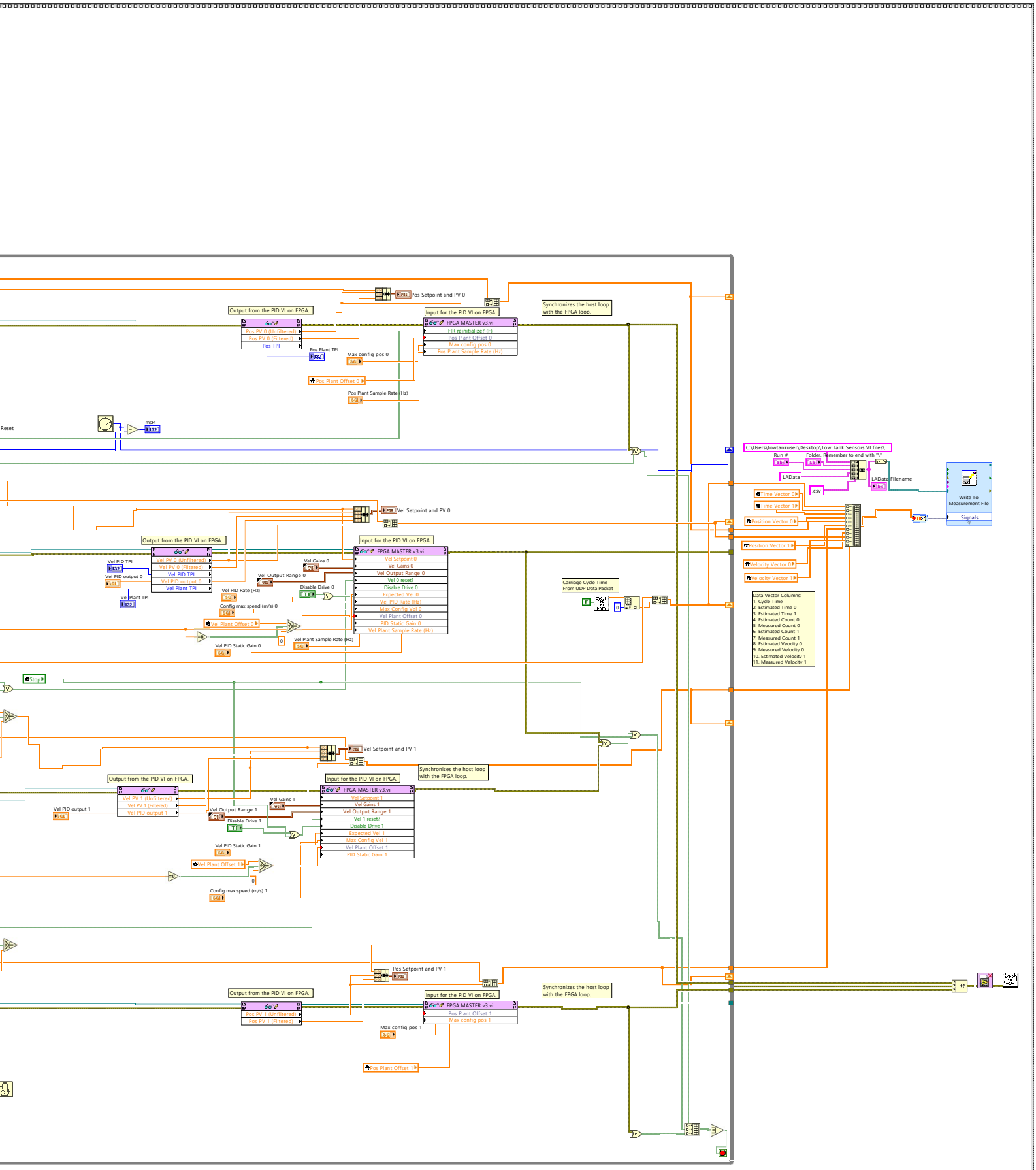

VPMMControlHighSpeed_v2.vi
C:\Users\towtankuser\Documents\LabVIEWMC\examples\CompactRIO\FPGA Fundamentals\FPGA Math and Analysis\Floating-point PID\Multi-Rate PID\VPMMControlHighSpeed_v2.vi
Last modified on 4/3/2024 at 6:09 PM
Printed on 4/3/2024 at 6:12 PM

ex_subFileWrite.vi
C:\Program Files (x86)\National Instruments\LabVIEW 2020\vi.lib\express\express output\ExFileWriteBlock.llb\ex_subFileWrite.vi

usiDataType.ctl
C:\Program Files (x86)\National Instruments\LabVIEW 2020\vi.lib\express\express shared\ex_EditUserDefinedProperties\usiDataType.ctl

ex_userDefProperty.ctl
C:\Program Files (x86)\National Instruments\LabVIEW 2020\vi.lib\express\express shared\ExFile.llb\ex_userDefProperty.ctl

ex_propertySource.ctl
C:\Program Files (x86)\National Instruments\LabVIEW 2020\vi.lib\express\express shared\ExFile.llb\ex_propertySource.ctl

ex_FileFormats.ctl
C:\Program Files (x86)\National Instruments\LabVIEW 2020\vi.lib\express\express shared\ExFile.llb\ex_FileFormats.ctl

Waveform Array To Dynamic.vi
C:\Program Files (x86)\National Instruments\LabVIEW 2020\vi.lib\express\express shared\transition.llb\Waveform Array To Dynamic.vi

Cycle Time test packet dissector.vi
C:\Users\towtankuser\Downloads\EdesignLabVIEW\LabVIEW\Cycle Time test packet dissector.vi

Velocity test packet dissector.vi
C:\Users\towtankuser\Downloads\EdesignLabVIEW\LabVIEW\Velocity test packet dissector.vi

MotionProfileGenerator_v4.vi
C:\Users\towtankuser\Documents\LabVIEWMC\examples\CompactRIO\FPGA Fundamentals\FPGA Math and Analysis\Floating-point PID\Multi-Rate PID\MotionProfileGenerator_v4.vi

VPMMControlHighSpeed_v2.vi
C:\Users\towtankuser\Documents\LabVIEWMC\examples\CompactRIO\FPGA Fundamentals\FPGA Math and Analysis\Floating-point PID\Multi-Rate PID\VPMMControlHighSpeed_v2.vi
Last modified on 4/3/2024 at 6:09 PM
Printed on 4/3/2024 at 6:12 PM

MotionProfileGenerator_v2.vi
C:\Users\towtankuser\Documents\LabVIEWMC\examples\CompactRIO\FPGA Fundamentals\FPGA Math and Analysis\Floating-point PID\Multi-Rate PID\MotionProfileGenerator_v2.vi

Analog Offset Host.vi
C:\Users\towtankuser\Documents\LabVIEWMC\examples\CompactRIO\FPGA Fundamentals\FPGA Math and Analysis\Floating-point PID\Multi-Rate PID\Analog Offset Host.vi

Error Cluster From Error Code.vi
C:\Program Files (x86)\National Instruments\LabVIEW 2020\vi.lib\Utility\error.llb\Error Cluster From Error Code.vi

Simple Error Handler.vi
C:\Program Files (x86)\National Instruments\LabVIEW 2020\vi.lib\Utility\error.llb\Simple Error Handler.vi

MotionProfileGenerator_v4.vi
C:\Users\towtankuser\Documents\LabVIEWMC\examples\CompactRIO\FPGA Fundamentals\FPGA Math and Analysis\Floating-point PID\Multi-Rate PID\MotionProfileGenerator_v4.vi
Last modified on 2/6/2024 at 10:07 AM
Printed on 4/4/2024 at 12:03 PM

MotionProfileGenerator_v4.vi
C:\Users\towtankuser\Documents\LabVIEWMC\examples\CompactRIO\FPGA Fundamentals\FPGA Math and Analysis\Floating-point PID\Multi-Rate PID\MotionProfileGenerator_v4.vi
Last modified on 2/6/2024 at 10:07 AM
Printed on 4/4/2024 at 12:05 PM

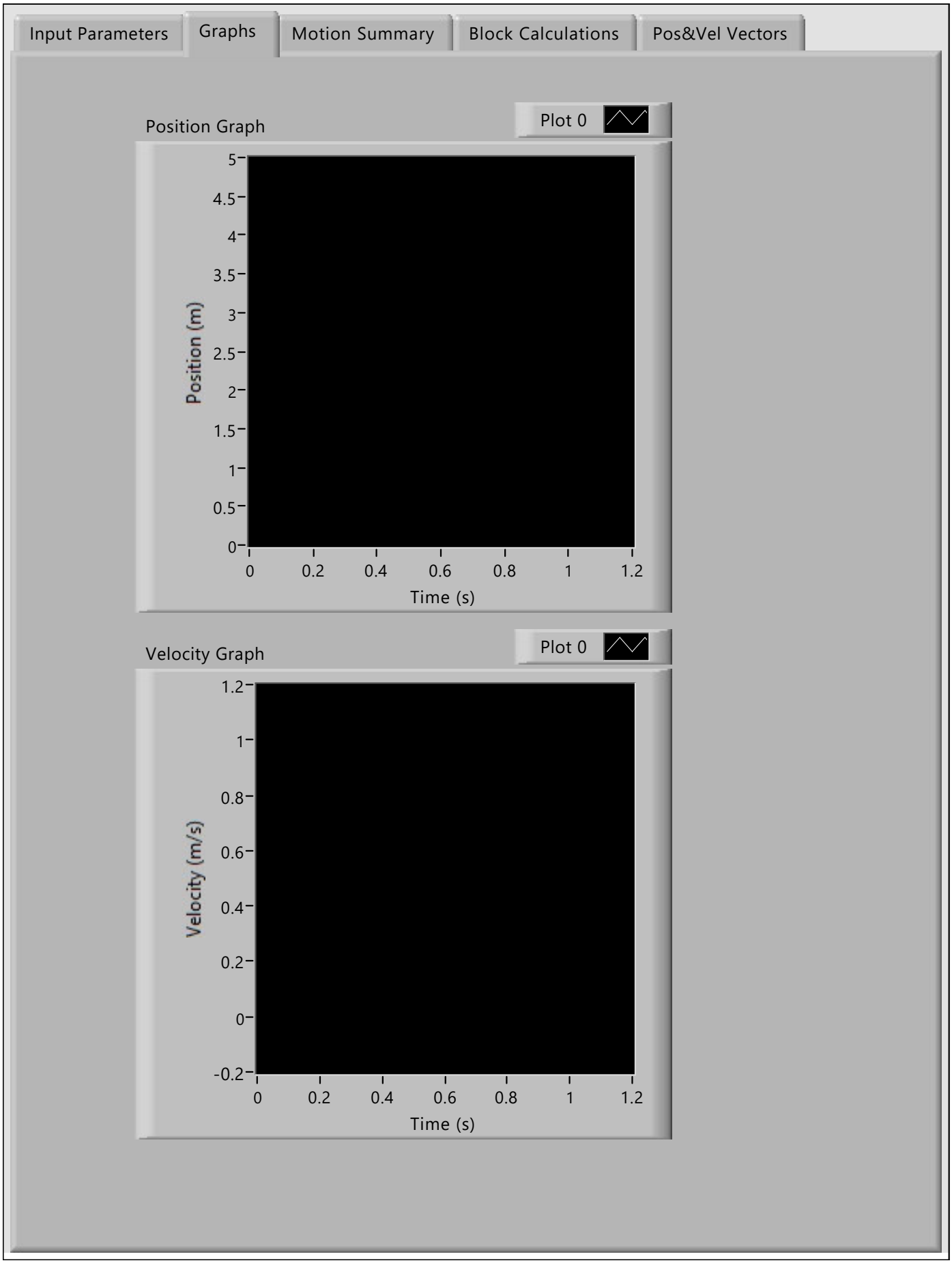

MotionProfileGenerator_v4.vi
C:\Users\towtankuser\Documents\LabVIEWMC\examples\CompactRIO\FPGA Fundamentals\FPGA Math and Analysis\Floating-point PID\Multi-Rate PID\MotionProfileGenerator_v4.vi
Last modified on 2/6/2024 at 10:07 AM
Printed on 4/4/2024 at 12:06 PM

Input Parameters | Graphs | Motion Summary | Block Calculations | Pos&Vel Vectors

Motion Summary

Overall	Steady State	Acceleration Summary	Deceleration Summary
Overall Time	Steady State Time	Accel Ramp Time	Decel Ramp Time
0	0	0	0
Overall Distance	Steady State Distance	Accel Ramp Distance	Decel Ramp Distance
0	0	0	0

Time delay (s)
0

TimetoMidTank (s)
0

TimeToImpact (s)
0

Expected Impact Duration (s)
0

Expected Impact Distance (m)
0

Max Pos
0

Max count
0

Steady State Condition Met

MotionProfileGenerator_v4.vi
C:\Users\towtankuser\Documents\LabVIEWMC\examples\CompactRIO\FPGA Fundamentals\FPGA Math and Analysis\Floating-point PID\Multi-Rate PID\MotionProfileGenerator_v4.vi
Last modified on 2/6/2024 at 10:07 AM
Printed on 4/4/2024 at 12:06 PM

Input Parameters | Graphs | Motion Summary | Block Calculations | Pos&Vel Vectors

Block 1 Check

delta_t1	0
V1	0
A1	0
a2 1	0
delta_d1	0

Block 2 Check

delta_t2	0
a0 2	0
V2	0
a1 2	0
A2	0
delta_d2	0

Block 3 Check

delta_t3	0
a0 3	0
V3	0
a1 3	0
A3	0
a2 3	0
delta_d3	0

Block 4 Check

delta_t4	0
V4	0
A4	0
delta_d4	0

Block 5 Check

delta_t5	0
a0 5	0
V5	0
A5	0
a2 5	0
delta_d5	0

Block 6 Check

delta_t6	0
a0 6	0
V6	0
a1 6	0
A6	0
delta_d6	0

Block 7 Check

delta_t7	0
a0 7	0
V7	0
a1 7	0
A7	0
a2 7	0
delta_d7	0

MotionProfileGenerator_v4.vi
C:\Users\towtankuser\Documents\LabVIEWMC\examples\CompactRIO\FPGA Fundamentals\FPGA Math and Analysis\Floating-point PID\Multi-Rate PID\MotionProfileGenerator_v4.vi
Last modified on 2/6/2024 at 10:07 AM
Printed on 4/3/2024 at 6:12 PM

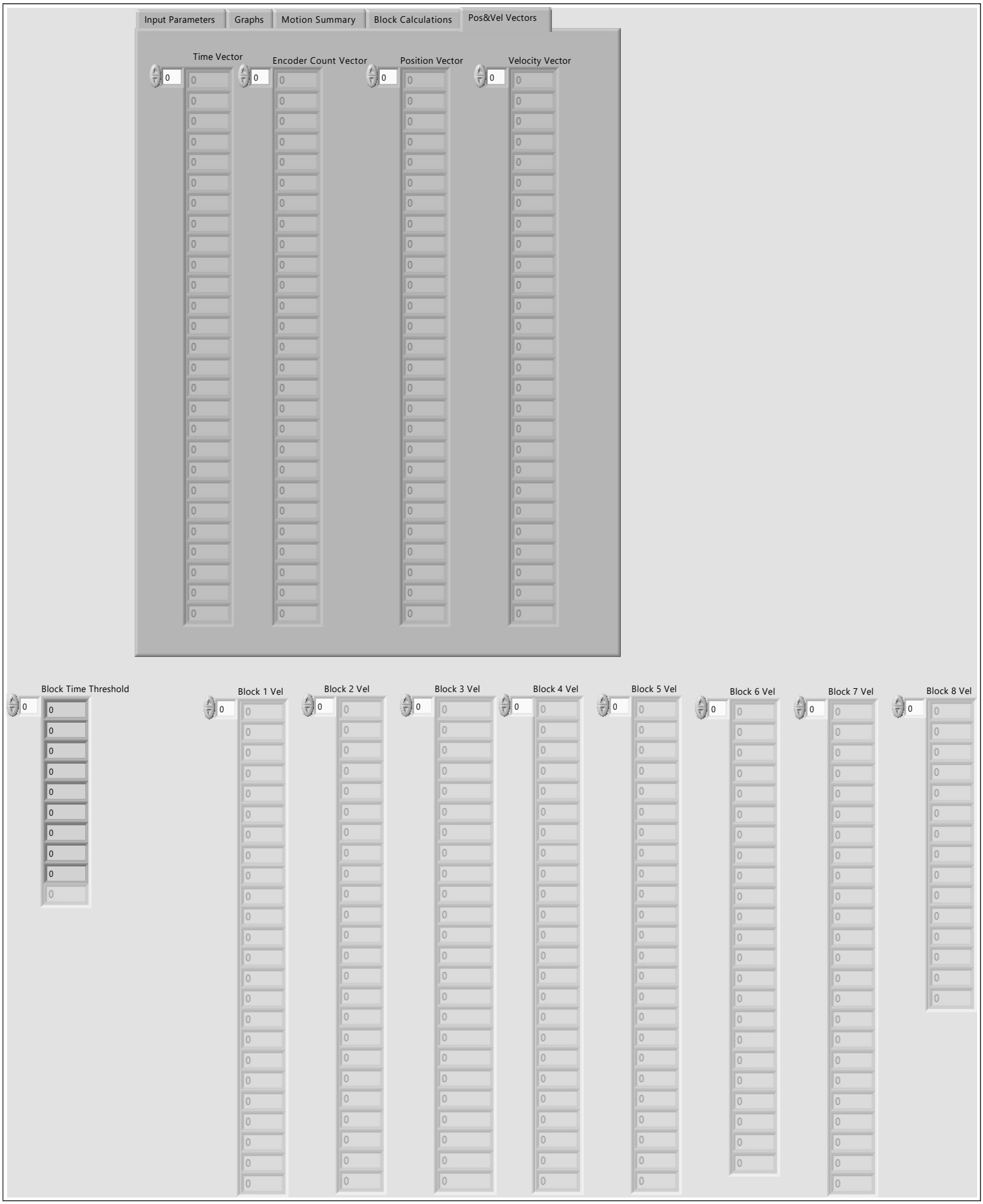

MotionProfileGenerator_v4.vi
C:\Users\towtankuser\Documents\LabVIEWMC\examples\CompactRIO\FPGA Fundamentals\FPGA Math and Analysis\Floating-point PID\Multi-Rate PID\MotionProfileGenerator_v4.vi
Last modified on 2/6/2024 at 10:07 AM
Printed on 4/3/2024 at 6:12 PM

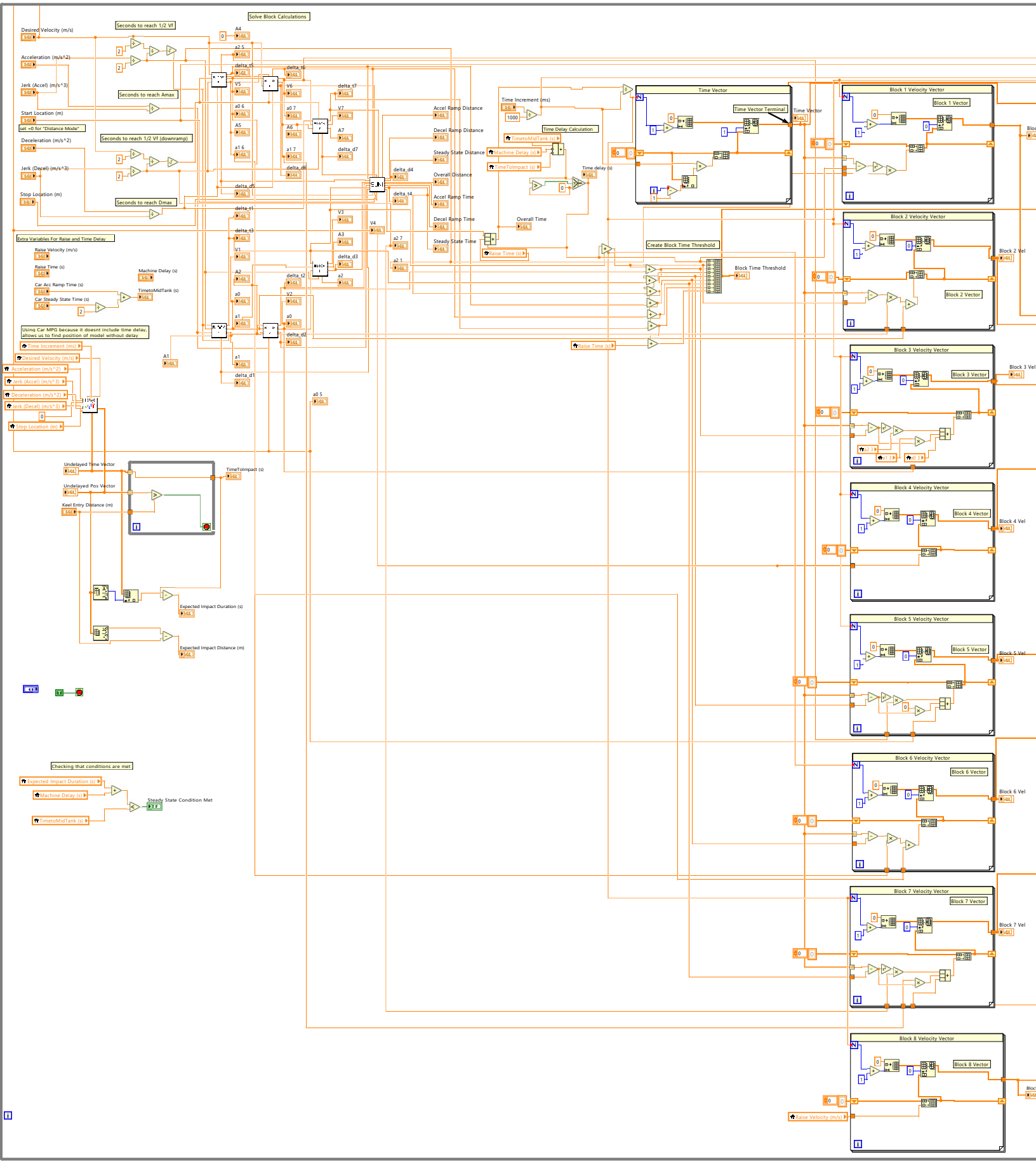

MotionProfileGenerator_v4.vi
C:\Users\towtankuser\Documents\LabVIEWMC\examples\CompactRIO\FPGA Fundamentals\FPGA Math and Analysis\Floating-point PID\Multi-Rate PID\MotionProfileGenerator_v4.vi
Last modified on 2/6/2024 at 10:07 AM
Printed on 4/3/2024 at 6:12 PM

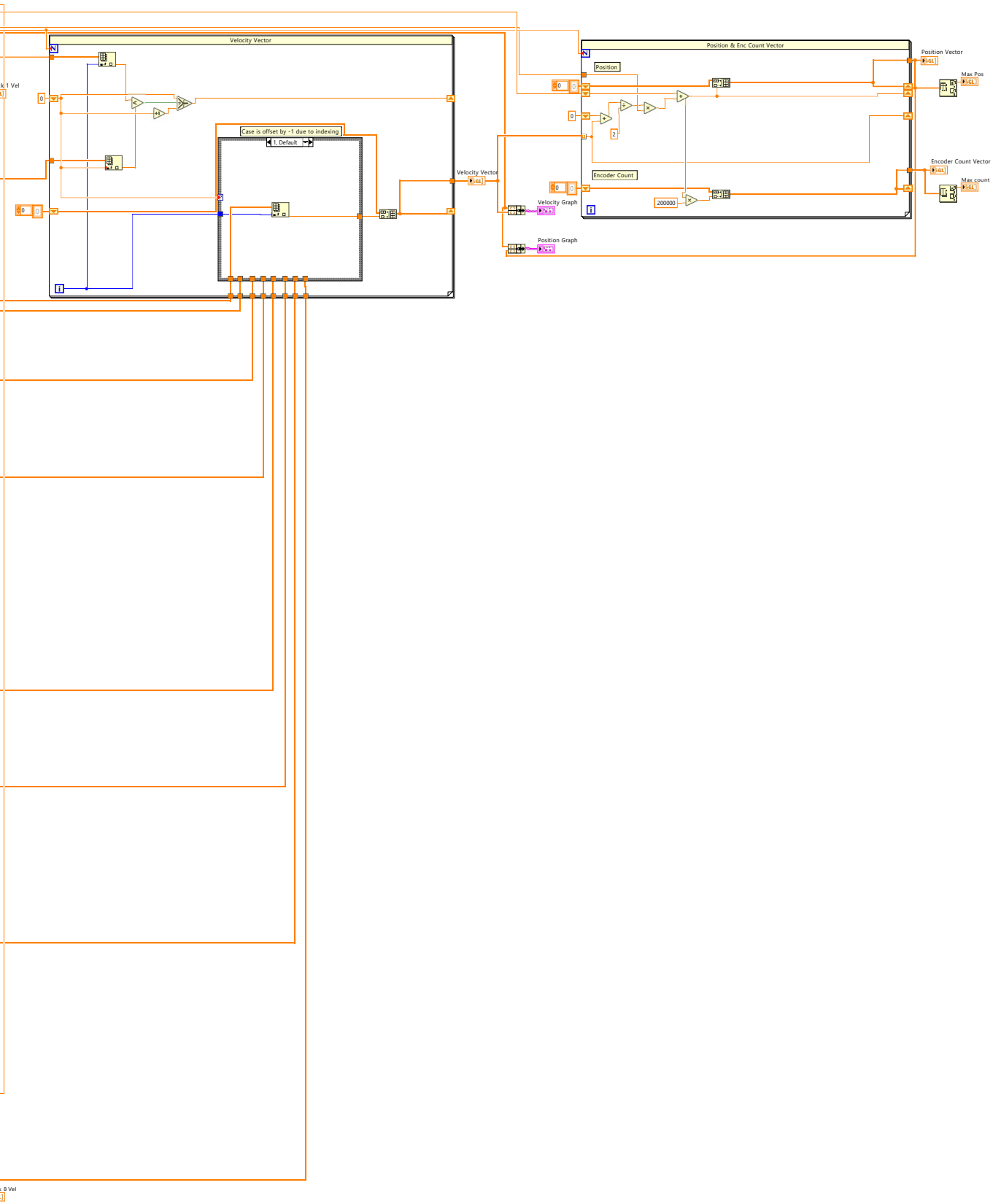

MotionProfileGenerator_v4.vi
C:\Users\towtankuser\Documents\LabVIEWMC\examples\CompactRIO\FPGA Fundamentals\FPGA Math and Analysis\Floating-point PID\Multi-Rate PID\MotionProfileGenerator_v4.vi
Last modified on 2/6/2024 at 10:07 AM
Printed on 4/3/2024 at 6:12 PM

MotionProfileGenerator_v2.vi
C:\Users\towtankuser\Documents\LabVIEWMC\examples\CompactRIO\FPGA Fundamentals\FPGA Math and Analysis\Floating-point PID\Multi-Rate PID\MotionProfileGenerator_v2.vi

Summary_subMPG.vi
C:\Users\towtankuser\Documents\LabVIEWMC\examples\CompactRIO\FPGA Fundamentals\FPGA Math and Analysis\Floating-point PID\Multi-Rate PID\Summary_subMPG.vi

Block7_subMPG.vi
C:\Users\towtankuser\Documents\LabVIEWMC\examples\CompactRIO\FPGA Fundamentals\FPGA Math and Analysis\Floating-point PID\Multi-Rate PID\Block7_subMPG.vi

Block6_subMPG.vi
C:\Users\towtankuser\Documents\LabVIEWMC\examples\CompactRIO\FPGA Fundamentals\FPGA Math and Analysis\Floating-point PID\Multi-Rate PID\Block6_subMPG.vi

Block5_subMPG.vi
C:\Users\towtankuser\Documents\LabVIEWMC\examples\CompactRIO\FPGA Fundamentals\FPGA Math and Analysis\Floating-point PID\Multi-Rate PID\Block5_subMPG.vi

Block3_subMPG.vi
C:\Users\towtankuser\Documents\LabVIEWMC\examples\CompactRIO\FPGA Fundamentals\FPGA Math and Analysis\Floating-point PID\Multi-Rate PID\Block3_subMPG.vi

Block2_subMPG.vi
C:\Users\towtankuser\Documents\LabVIEWMC\examples\CompactRIO\FPGA Fundamentals\FPGA Math and Analysis\Floating-point PID\Multi-Rate PID\Block2_subMPG.vi

Block1_subMPG.vi
C:\Users\towtankuser\Documents\LabVIEWMC\examples\CompactRIO\FPGA Fundamentals\FPGA Math and Analysis\Floating-point PID\Multi-Rate PID\Block1_subMPG.vi

Block1_subMPG.vi
C:\Users\towtankuser\Documents\LabVIEWMC\examples\CompactRIO\FPGA Fundamentals\FPGA Math and Analysis\Floating-point PID\Multi-Rate PID\Block1_subMPG.vi
Last modified on 7/10/2023 at 10:36 AM
Printed on 4/4/2024 at 11:54 AM

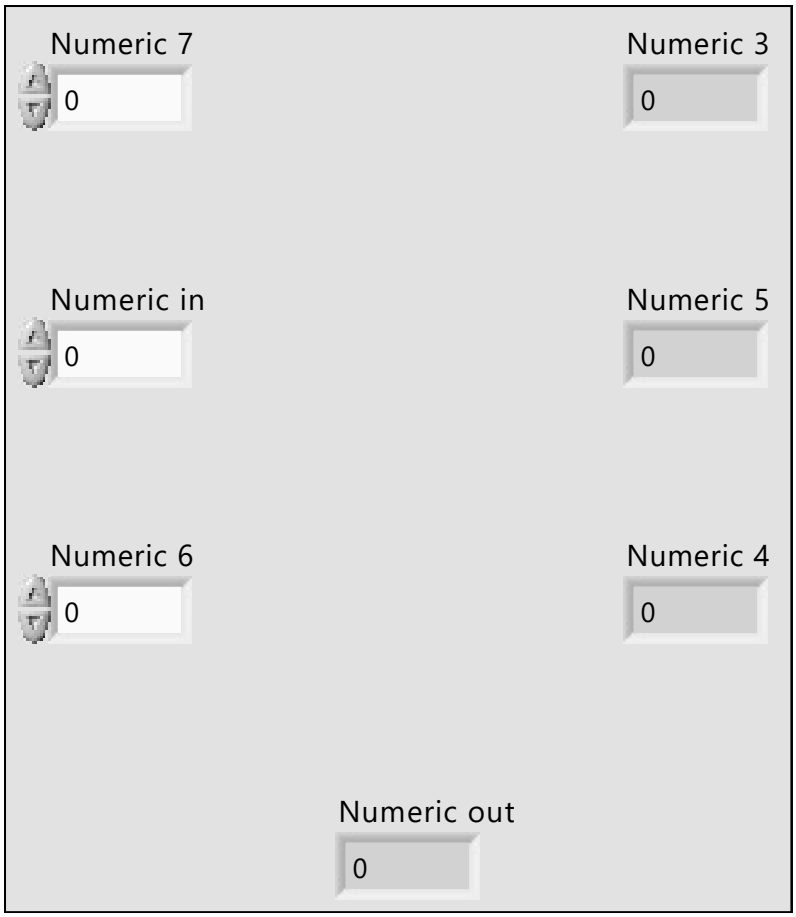

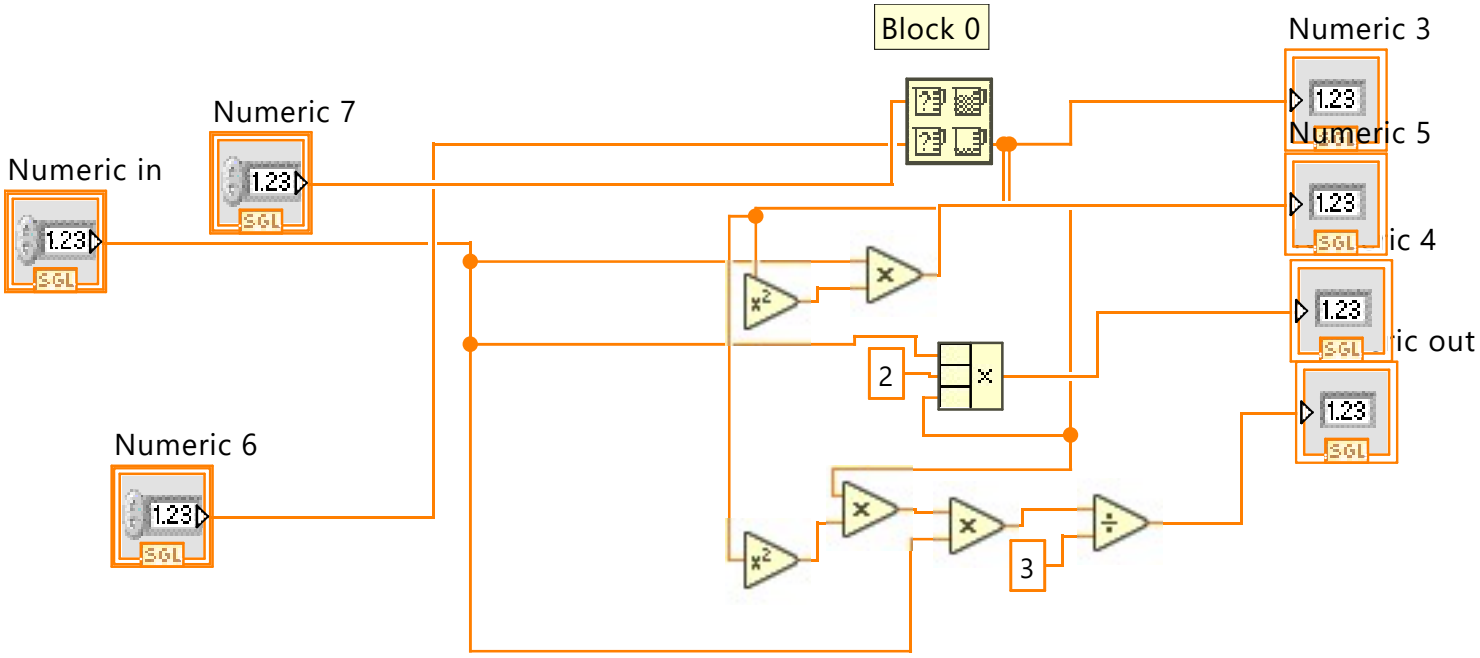

BLOCK 2

Block2_subMPG.vi
C:\Users\towtankuser\Documents\LabVIEWMC\examples\CompactRIO\FPGA Fundamentals\FPGA Math and Analysis\Floating-point PID\Multi-Rate PID\Block2_subMPG.vi
Last modified on 7/10/2023 at 10:36 AM
Printed on 4/4/2024 at 11:54 AM

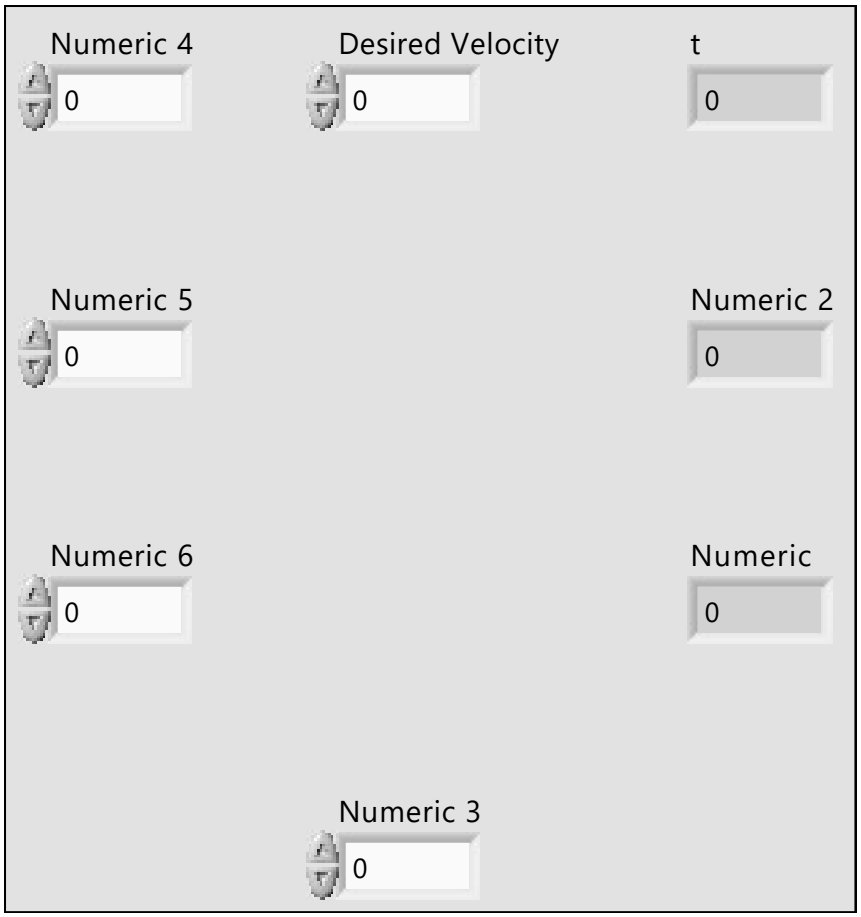

BLOCK 2

Block2_subMPG.vi
C:\Users\towtankuser\Documents\LabVIEWMC\examples\CompactRIO\FPGA Fundamentals\FPGA Math and Analysis\Floating-point PID\Multi-Rate PID\Block2_subMPG.vi
Last modified on 7/10/2023 at 10:36 AM
Printed on 4/4/2024 at 11:54 AM

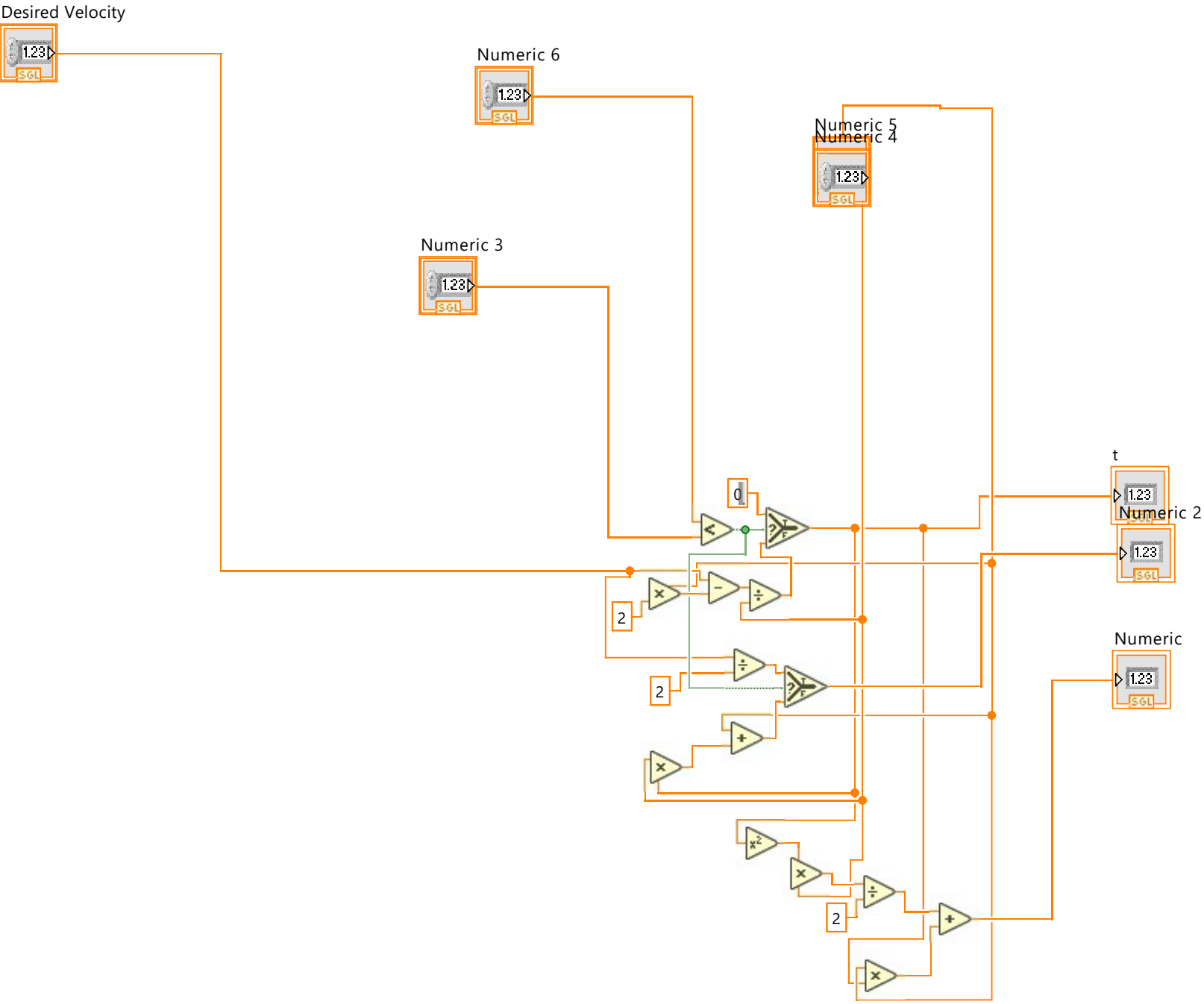

BLOCK 3

Block3_subMPG.vi
C:\Users\towtankuser\Documents\LabVIEWMC\examples\CompactRIO\FPGA Fundamentals\FPGA Math and Analysis\Floating-point PID\Multi-Rate PID\Block3_subMPG.vi
Last modified on 7/10/2023 at 2:56 PM
Printed on 4/4/2024 at 11:54 AM

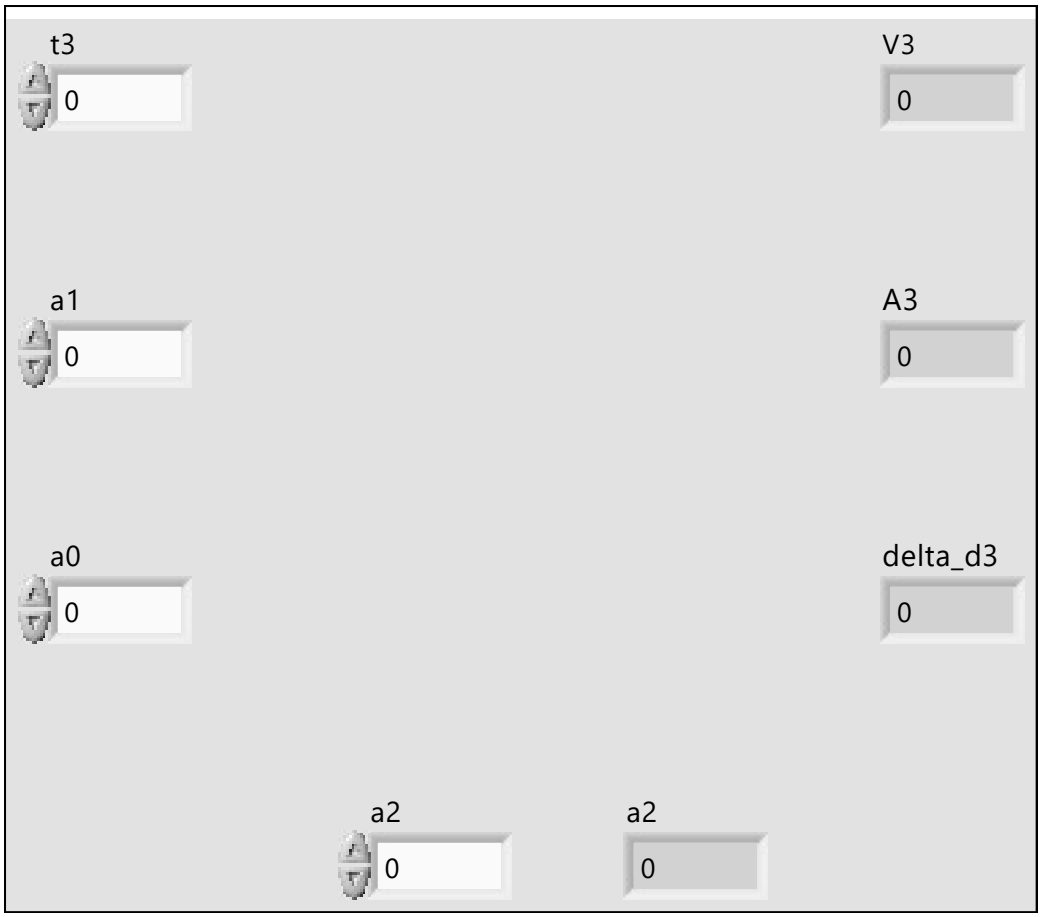

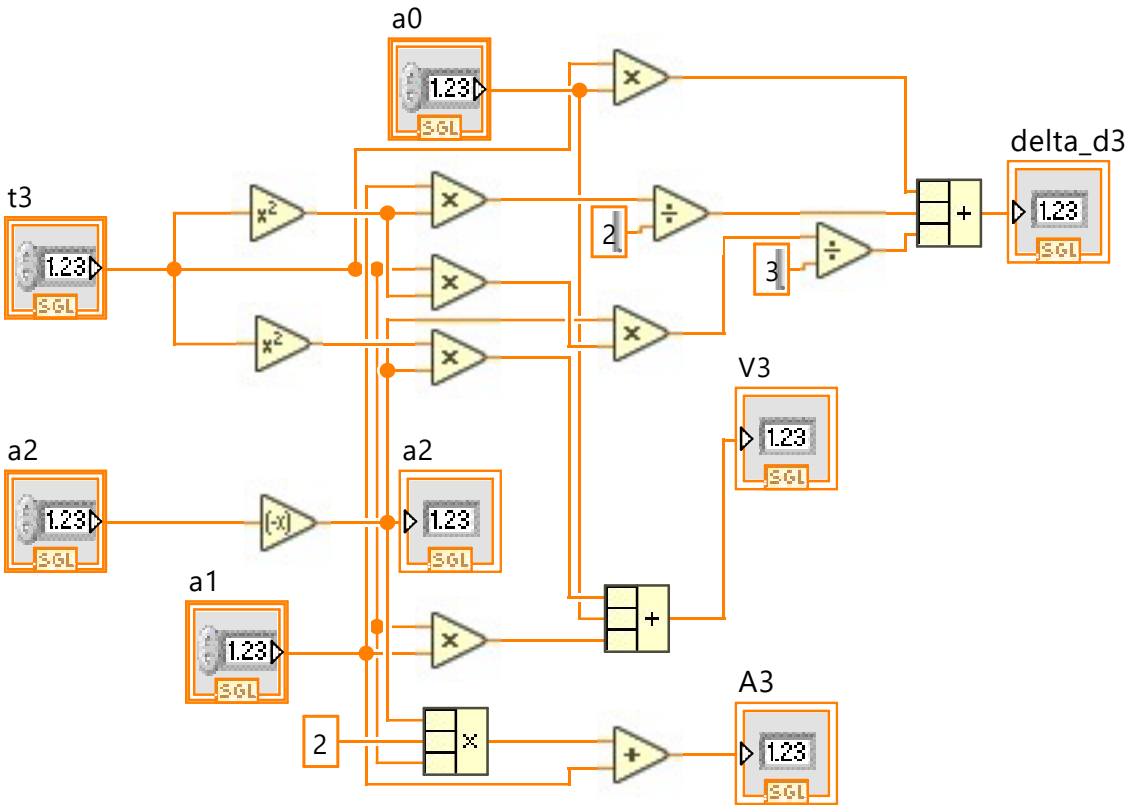

BLOCK 5

Block5_subMPG.vi
C:\Users\towtankuser\Documents\LabVIEWMC\examples\CompactRIO\FPGA Fundamentals\FPGA Math and Analysis\Floating-point PID\Multi-Rate PID\Block5_subMPG.vi
Last modified on 7/10/2023 at 10:36 AM
Printed on 4/4/2024 at 11:55 AM

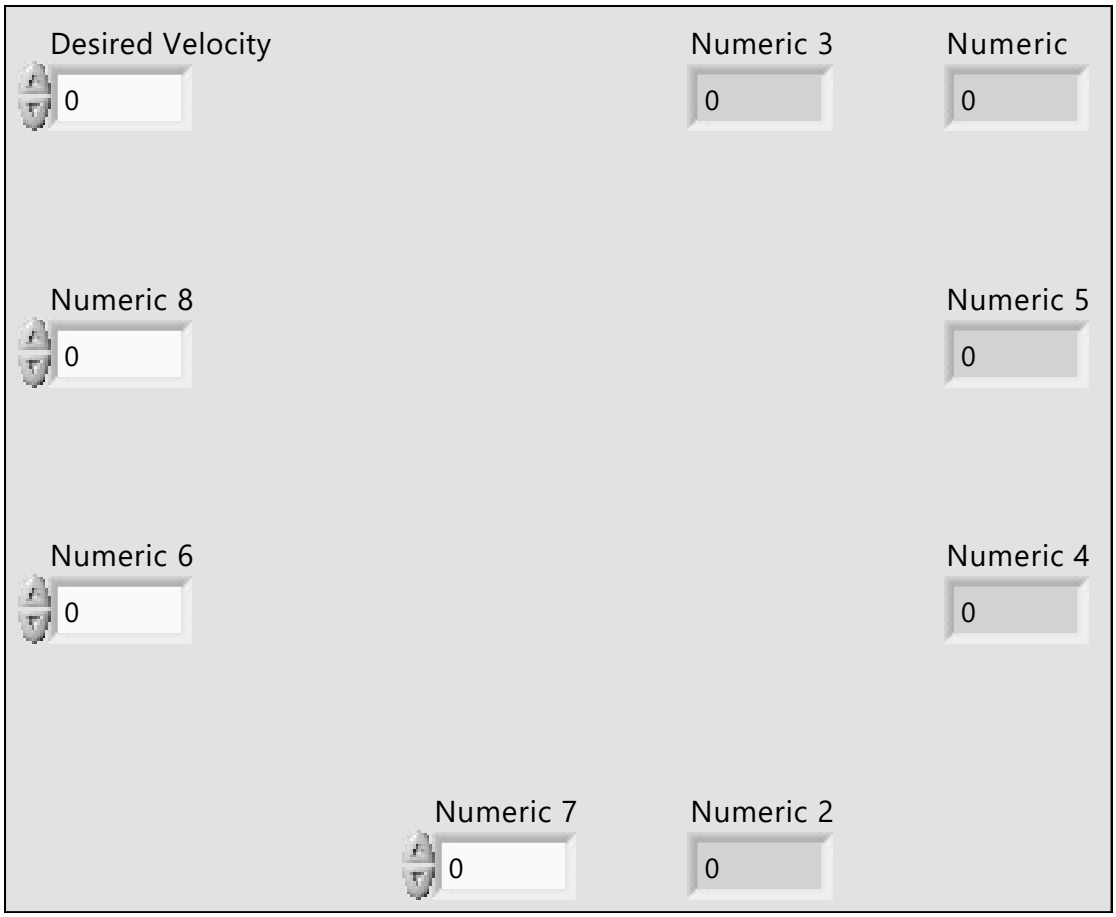

BLOCK 5

Block5_subMPG.vi
C:\Users\towtankuser\Documents\LabVIEWMC\examples\CompactRIO\FPGA Fundamentals\FPGA Math and Analysis\Floating-point PID\Multi-Rate PID\Block5_subMPG.vi
Last modified on 7/10/2023 at 10:36 AM
Printed on 4/4/2024 at 11:55 AM

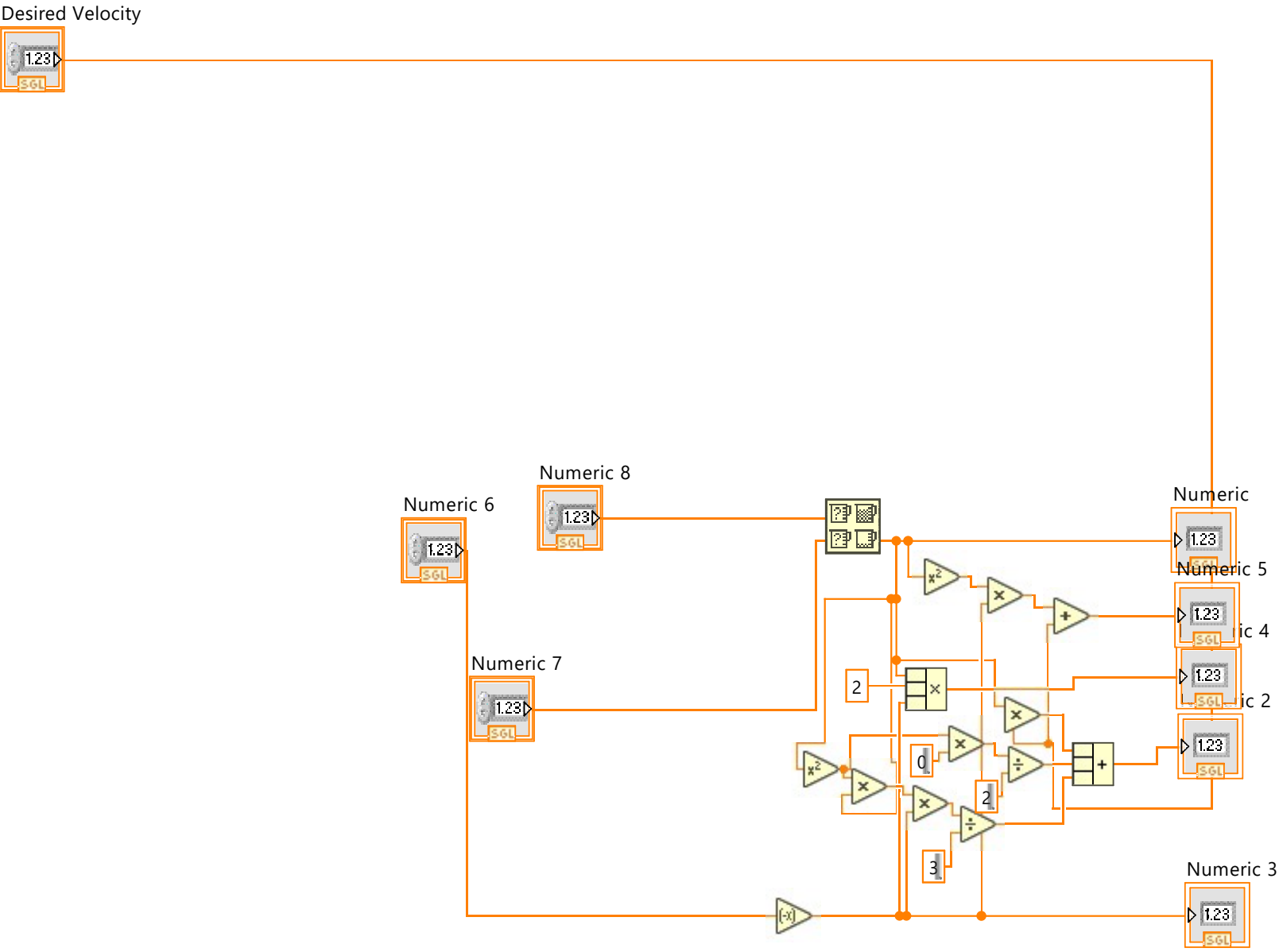

BLOCK 6

Block6_subMPG.vi
C:\Users\towtankuser\Documents\LabVIEWMC\examples\CompactRIO\FPGA Fundamentals\FPGA Math and Analysis\Floating-point PID\Multi-Rate PID\Block6_subMPG.vi
Last modified on 7/10/2023 at 5:20 PM
Printed on 4/4/2024 at 11:55 AM

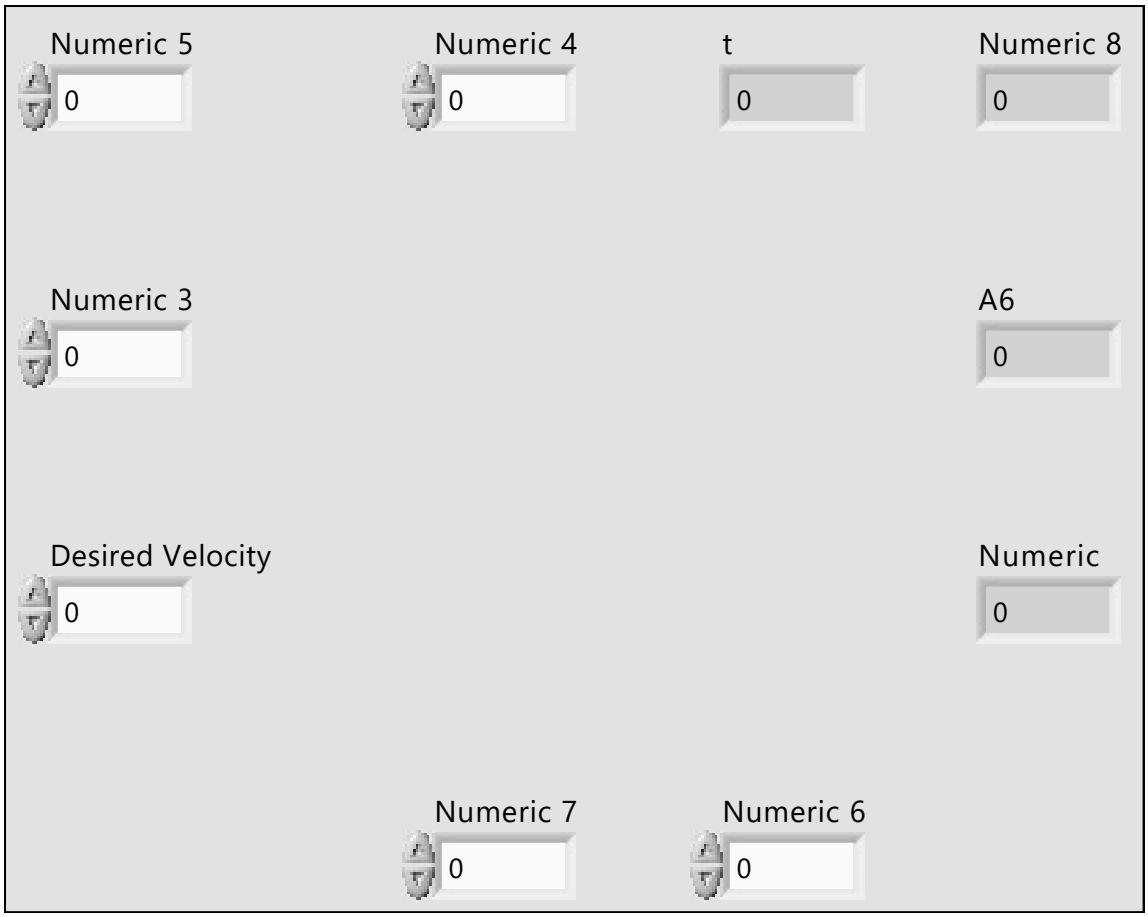

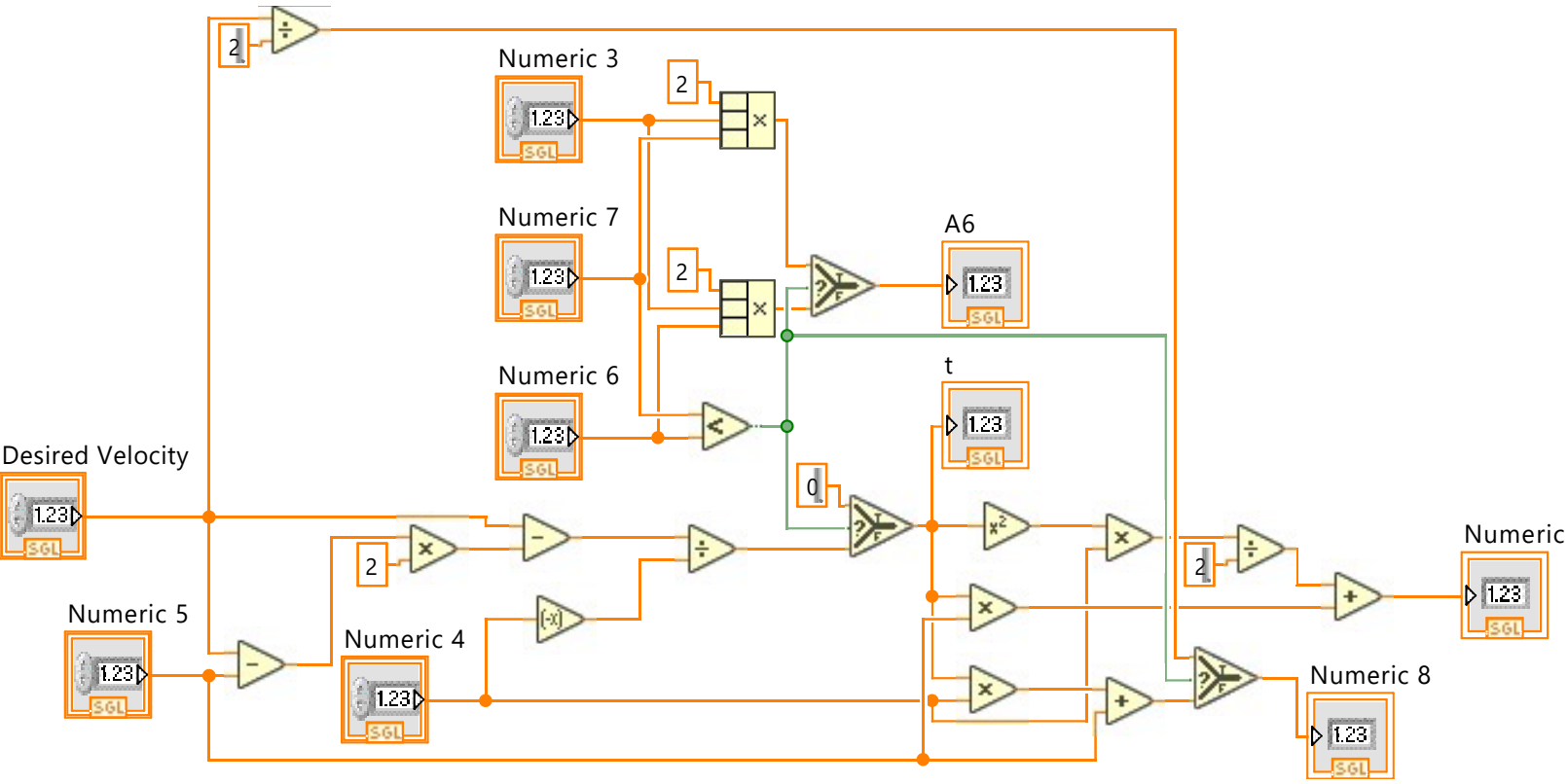

BLOCK 7

Block7_subMPG.vi
C:\Users\towtankuser\Documents\LabVIEWMC\examples\CompactRIO\FPGA Fundamentals\FPGA Math and Analysis\Floating-point PID\Multi-Rate PID\Block7_subMPG.vi
Last modified on 7/10/2023 at 5:45 PM
Printed on 4/4/2024 at 11:55 AM

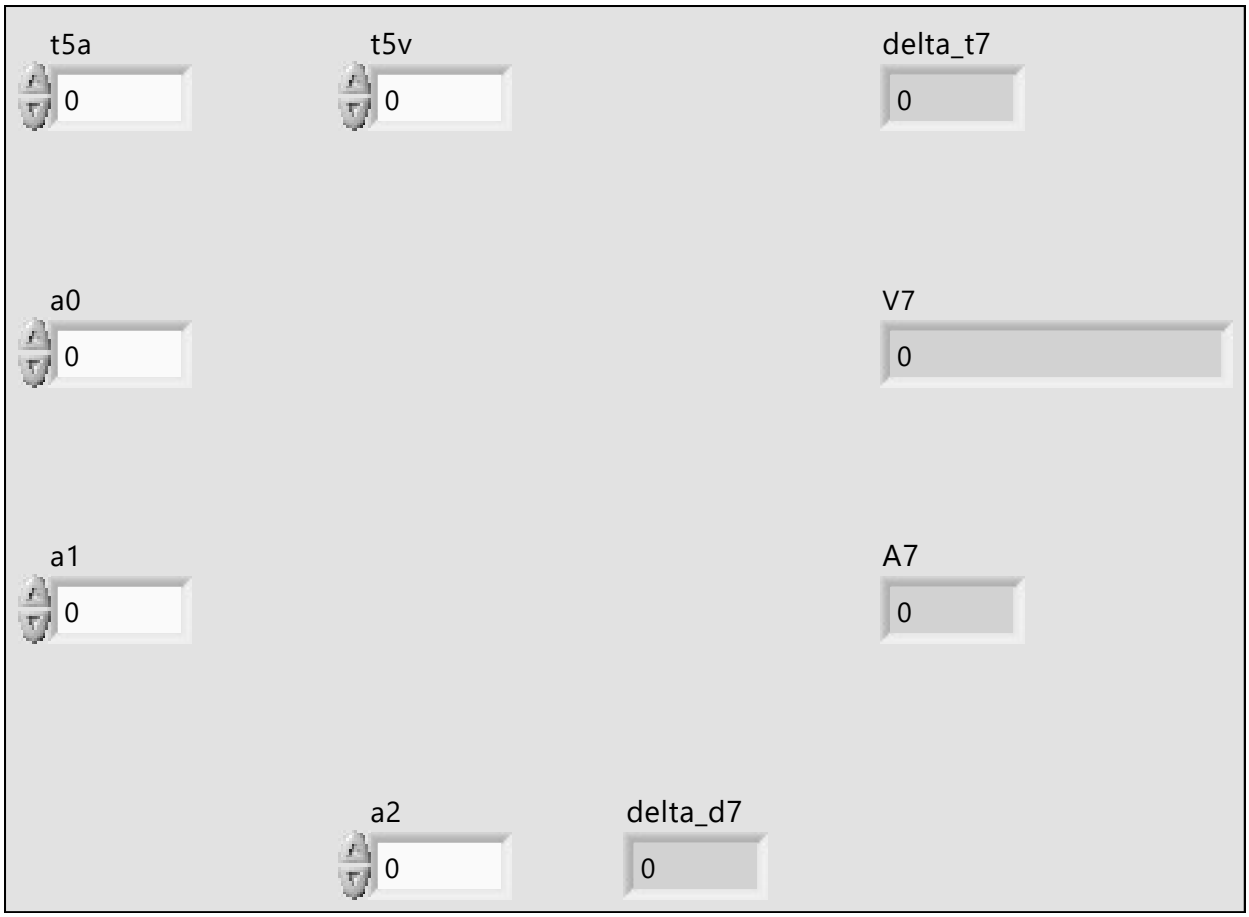

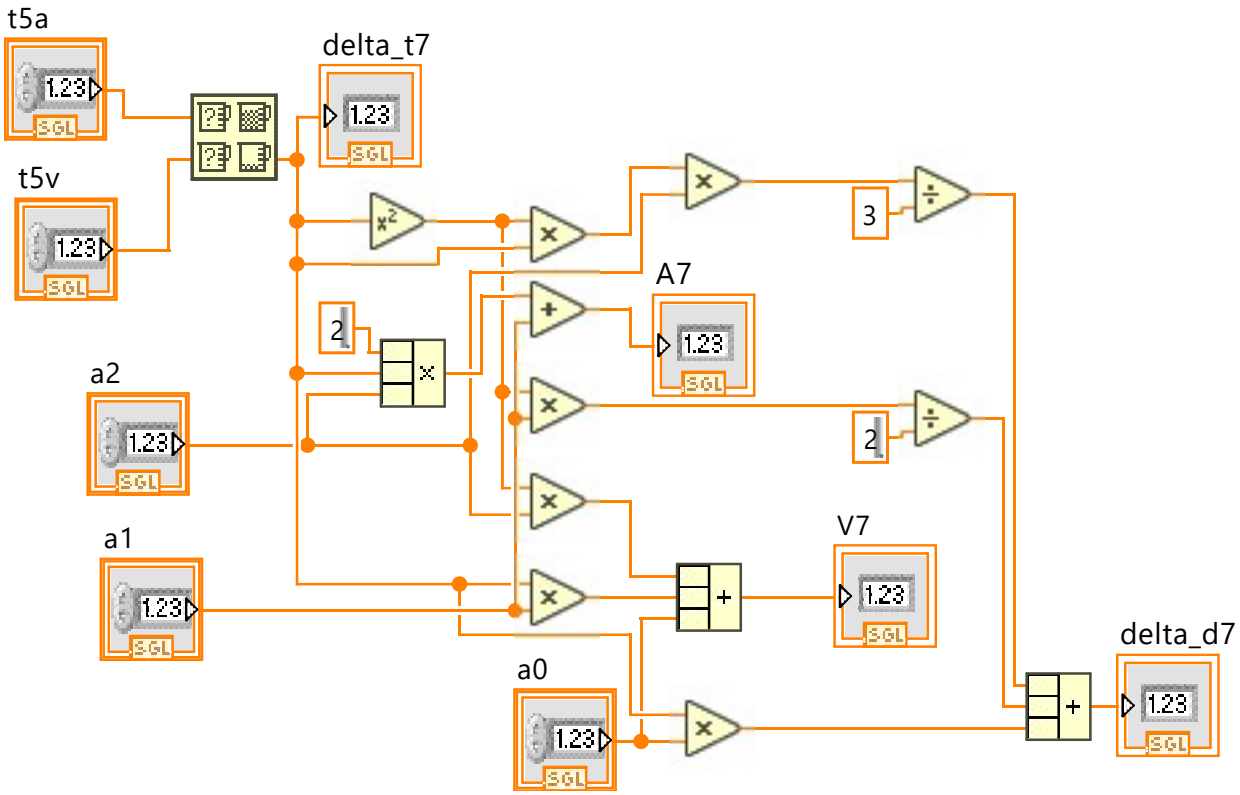

Summary_subMPG.vi
C:\Users\towtankuser\Documents\LabVIEWMC\examples\CompactRIO\FPGA Fundamentals\FPGA Math and Analysis\Floating-point PID\Multi-Rate PID\Summary_subMPG.vi
Last modified on 7/10/2023 at 2:49 PM
Printed on 4/4/2024 at 11:55 AM

SUM

Summary_subMPG.vi
C:\Users\towtankuser\Documents\LabVIEWMC\examples\CompactRIO\FPGA Fundamentals\FPGA Math and Analysis\Floating-point PID\Multi-Rate PID\Summary_subMPG.vi
Last modified on 7/10/2023 at 2:49 PM
Printed on 4/4/2024 at 11:55 AM

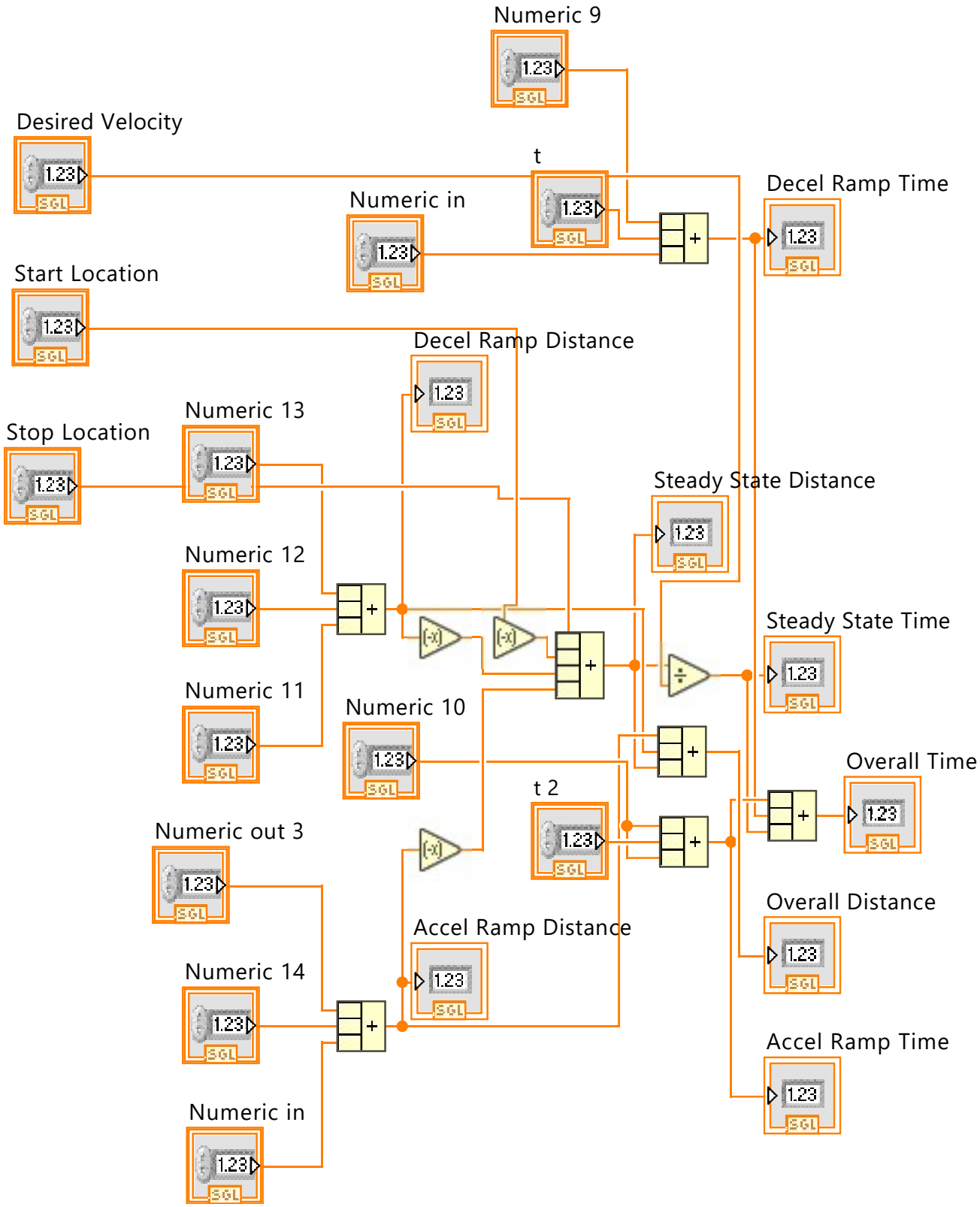

CYCLE TIME UDP DATA

Cycle Time test packet dissector.vi
C:\Users\towtankuser\Downloads\EdesignLabVIEW\LabVIEW\Cycle Time test packet dissector.vi
Last modified on 4/4/2024 at 10:45 AM
Printed on 4/4/2024 at 10:45 AM

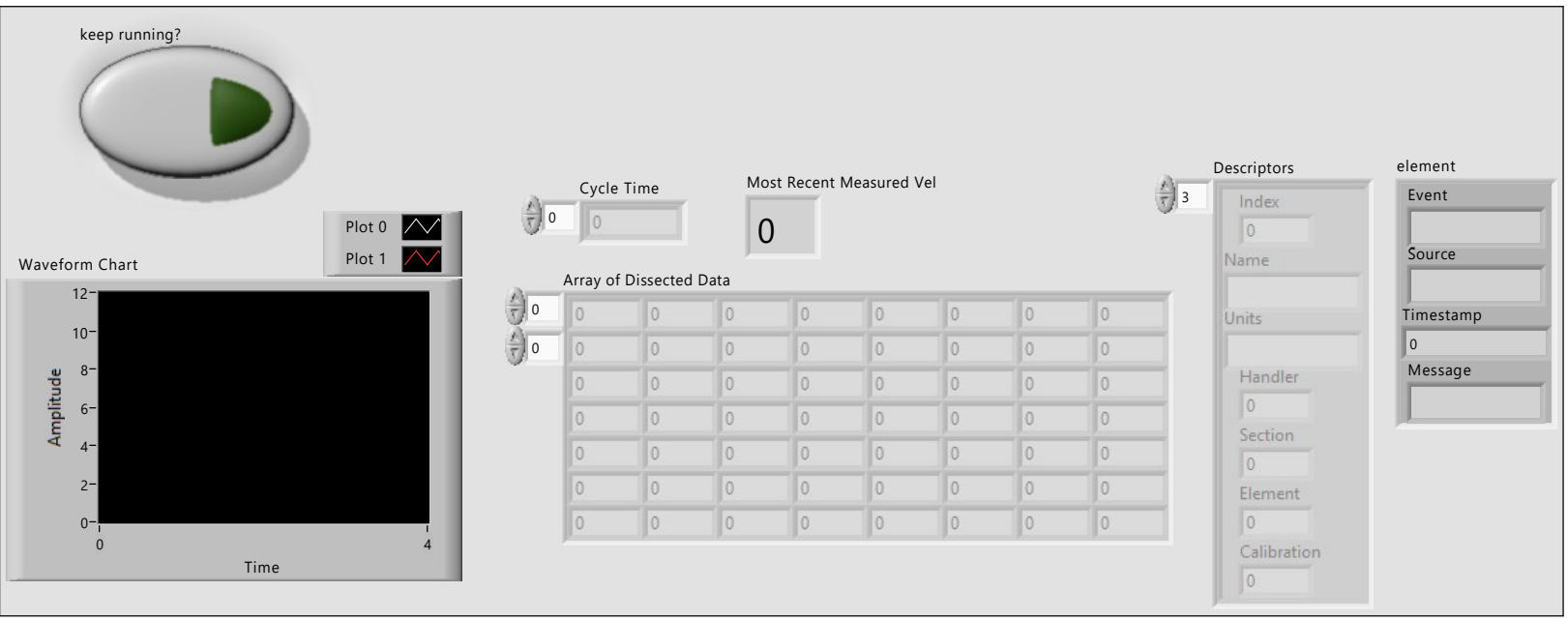

CYCLE TIME UDP DATA

Cycle Time test packet dissector.vi
C:\Users\towtankuser\Downloads\EdesignLabVIEW\LabVIEW\Cycle Time test packet dissector.vi
Last modified on 4/4/2024 at 10:45 AM
Printed on 4/4/2024 at 10:45 AM

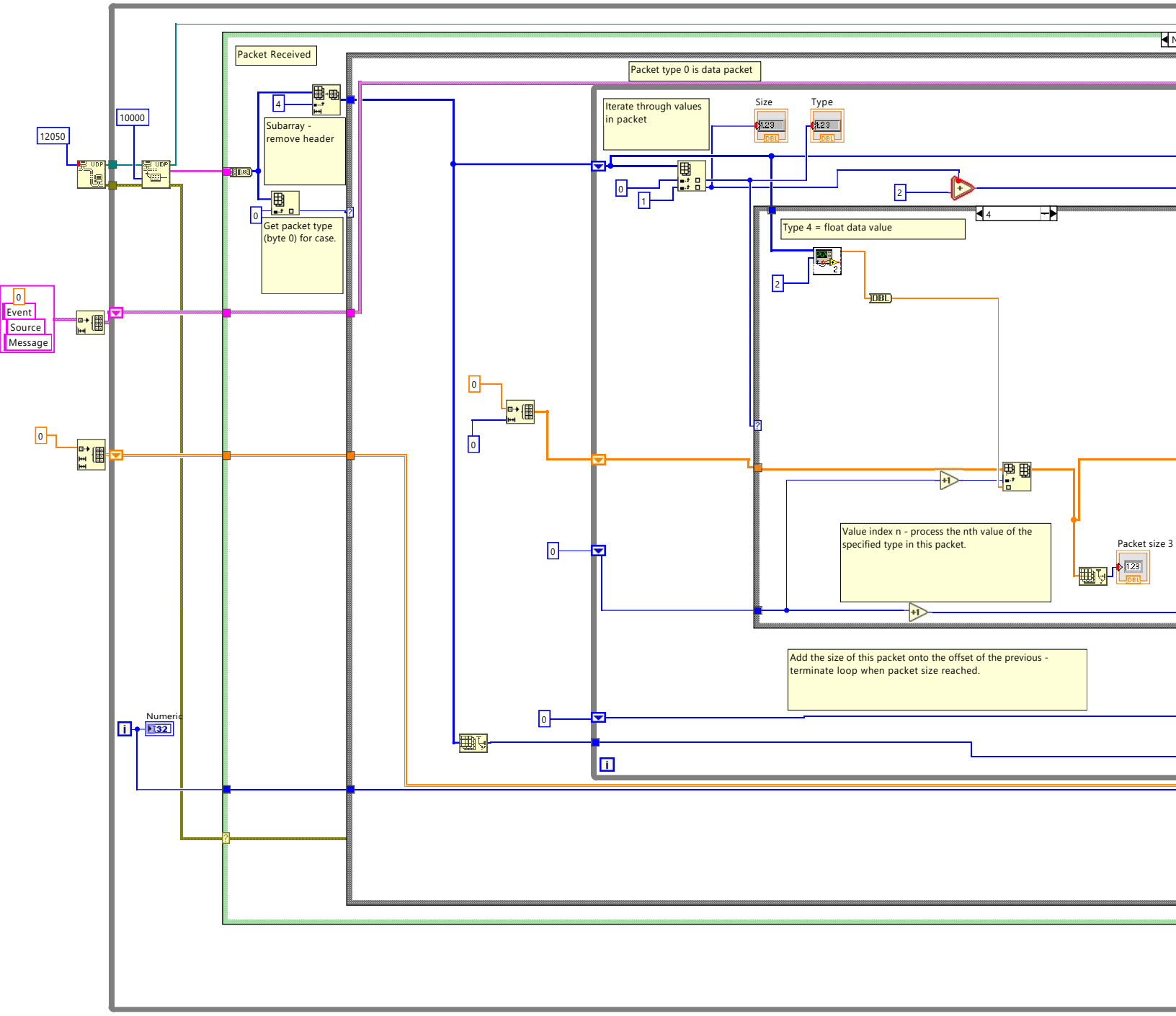

ExtractString.vi
C:\Users\towtankuser\Downloads\EdesignLabVIEW\LabVIEW\ExtractString.vi

ExtractIndex.vi
C:\Users\towtankuser\Downloads\EdesignLabVIEW\LabVIEW\ExtractIndex.vi

ExtractUInt.vi
C:\Users\towtankuser\Downloads\EdesignLabVIEW\LabVIEW\ExtractUInt.vi

ExtractFloat.vi
C:\Users\towtankuser\Downloads\EdesignLabVIEW\LabVIEW\ExtractFloat.vi

ExtractDouble.vi
C:\Users\towtankuser\Downloads\EdesignLabVIEW\LabVIEW\ExtractDouble.vi

CYCLE TIME UDP DATA

Cycle Time test packet dissector.vi
C:\Users\towtankuser\Downloads\EdesignLabVIEW\LabVIEW\Cycle Time test packet dissector.vi
Last modified on 4/4/2024 at 10:45 AM
Printed on 4/4/2024 at 10:46 AM

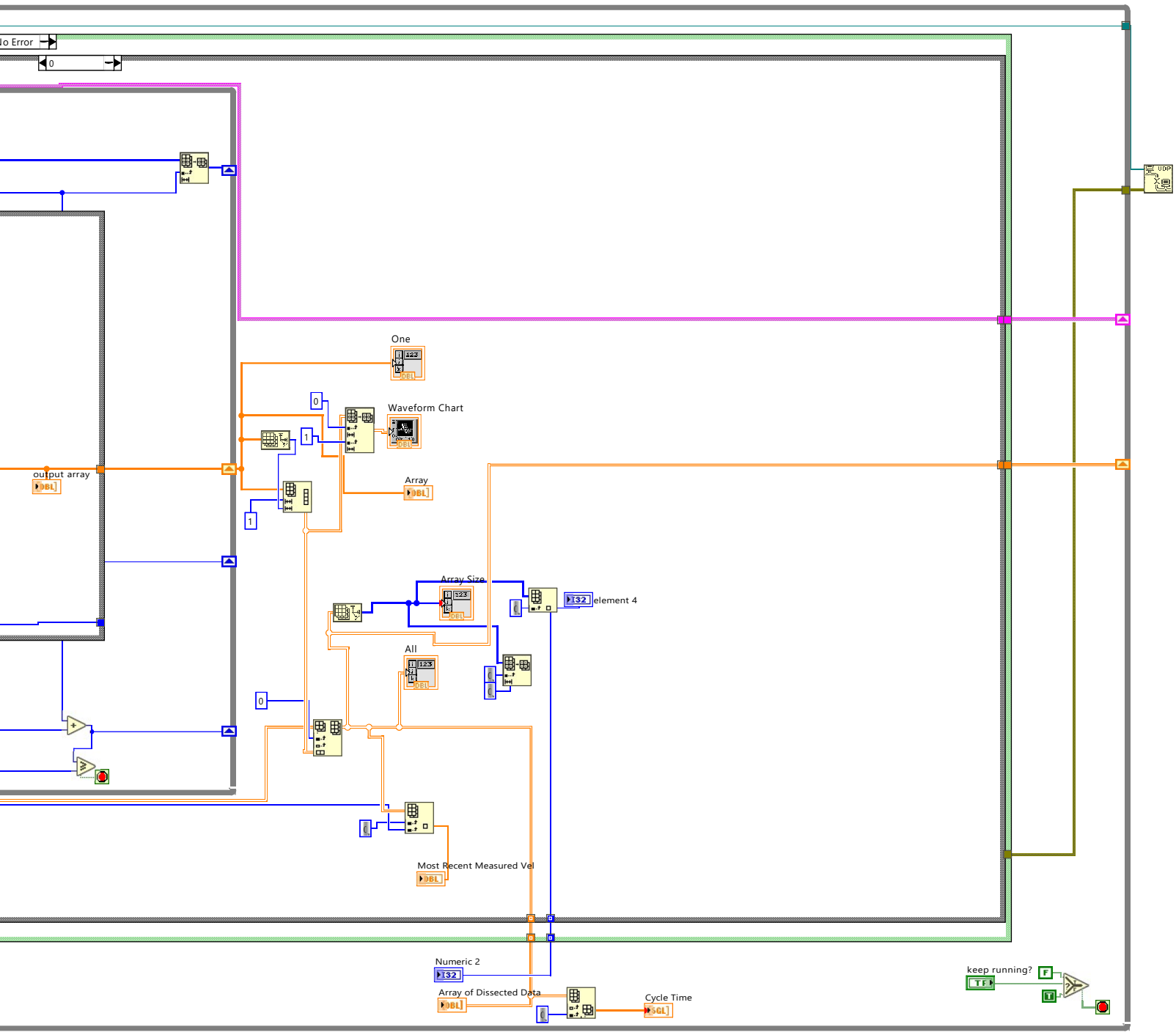

Analog Offset Host.vi
C:\Users\towtankuser\Documents\LabVIEWMC\examples\CompactRIO\FPGA Fundamentals\FPGA Math and Analysis\Floating-point PID\Multi-Rate PID\Analog Offset Host.vi
Last modified on 4/3/2024 at 5:08 PM
Printed on 4/4/2024 at 10:49 AM

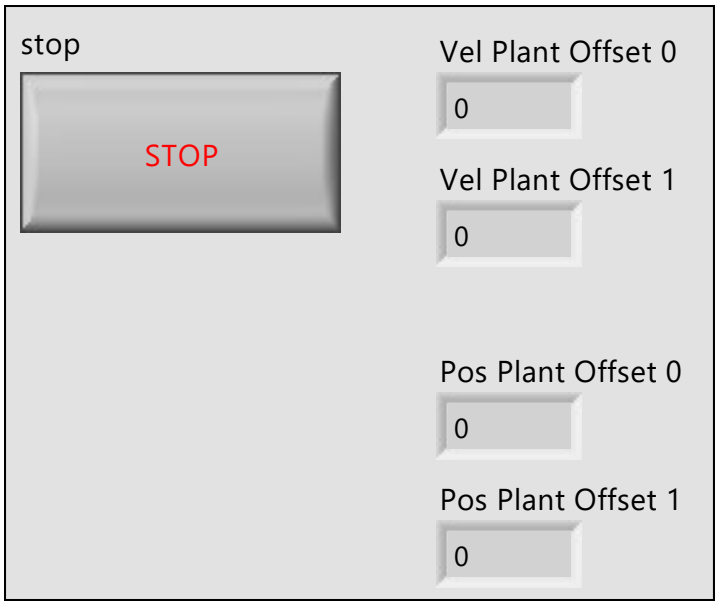

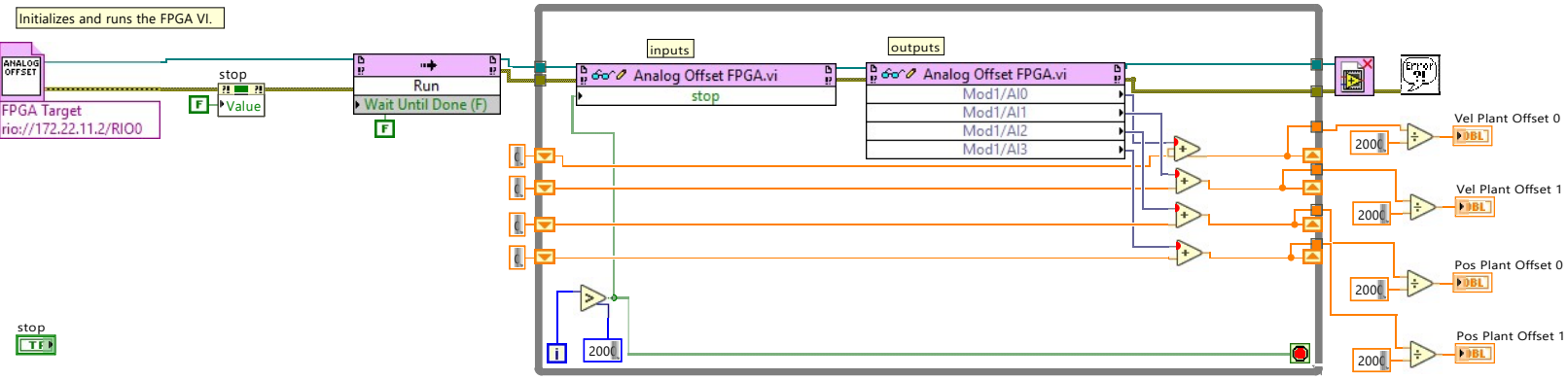

Error Cluster From Error Code.vi
C:\Program Files (x86)\National Instruments\LabVIEW 2020\vi.lib\Utility\error.llb\Error Cluster From Error Code.vi

Simple Error Handler.vi
C:\Program Files (x86)\National Instruments\LabVIEW 2020\vi.lib\Utility\error.llb\Simple Error Handler.vi

SENSOR DATA

GPPH_Sensor_Data_v4.vi
C:\Users\towtankuser\Desktop\Tow Tank Sensors VI files\GPPH_Sensor_Data_v4.vi
Last modified on 3/18/2024 at 4:00 PM
Printed on 4/4/2024 at 10:35 AM

Folder
Parametric Study Data\
Remember to keep "\" slash after name

Run #

Save Data

Carriage Control

Manually Collect Data

Saving Data

PotandInc
PotandInc

Module 1 Filename

Filename Out

error out
status
code 0
source

String Pot and Inclinometer

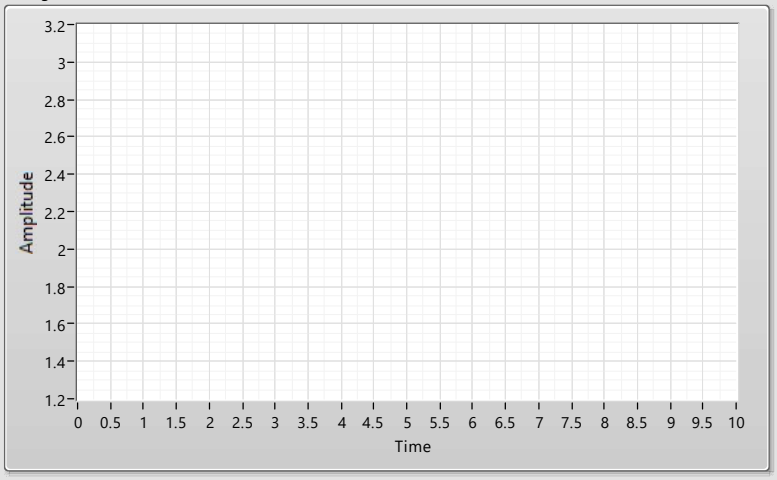

Saving Data 2

Force
Force

Module 2 Filename

Filename Out 2

error out 2
status
code 0
source

Force Sensors

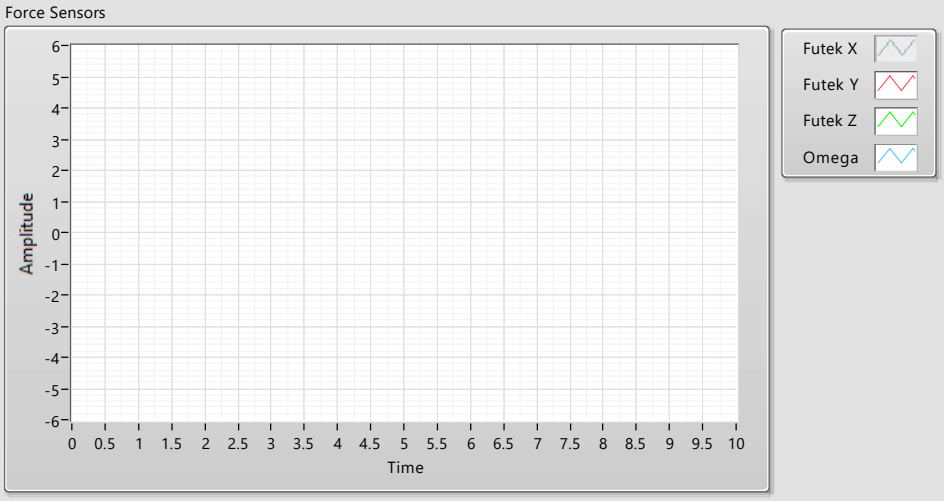

Saving Data 3

ACandPressure
ACandPressure

Module 3 Filename

Filename Out 3

error out 3
status
code 0
source

Accelerometers and Pressure Sensors

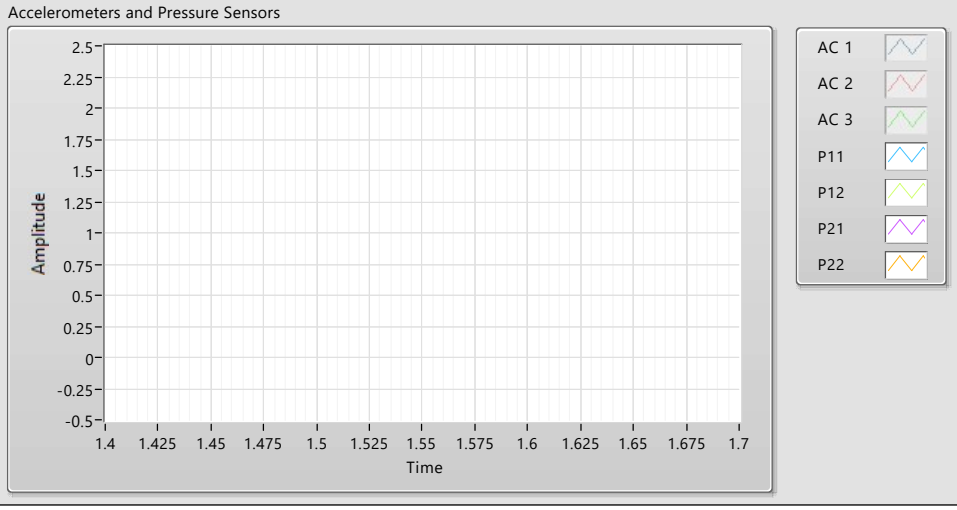

GPPH_Sensor_Data_v4.vi
C:\Users\towtankuser\Desktop\Tow Tank Sensors VI files\GPPH_Sensor_Data_v4.vi
Last modified on 3/18/2024 at 4:00 PM
Printed on 4/4/2024 at 10:35 AM

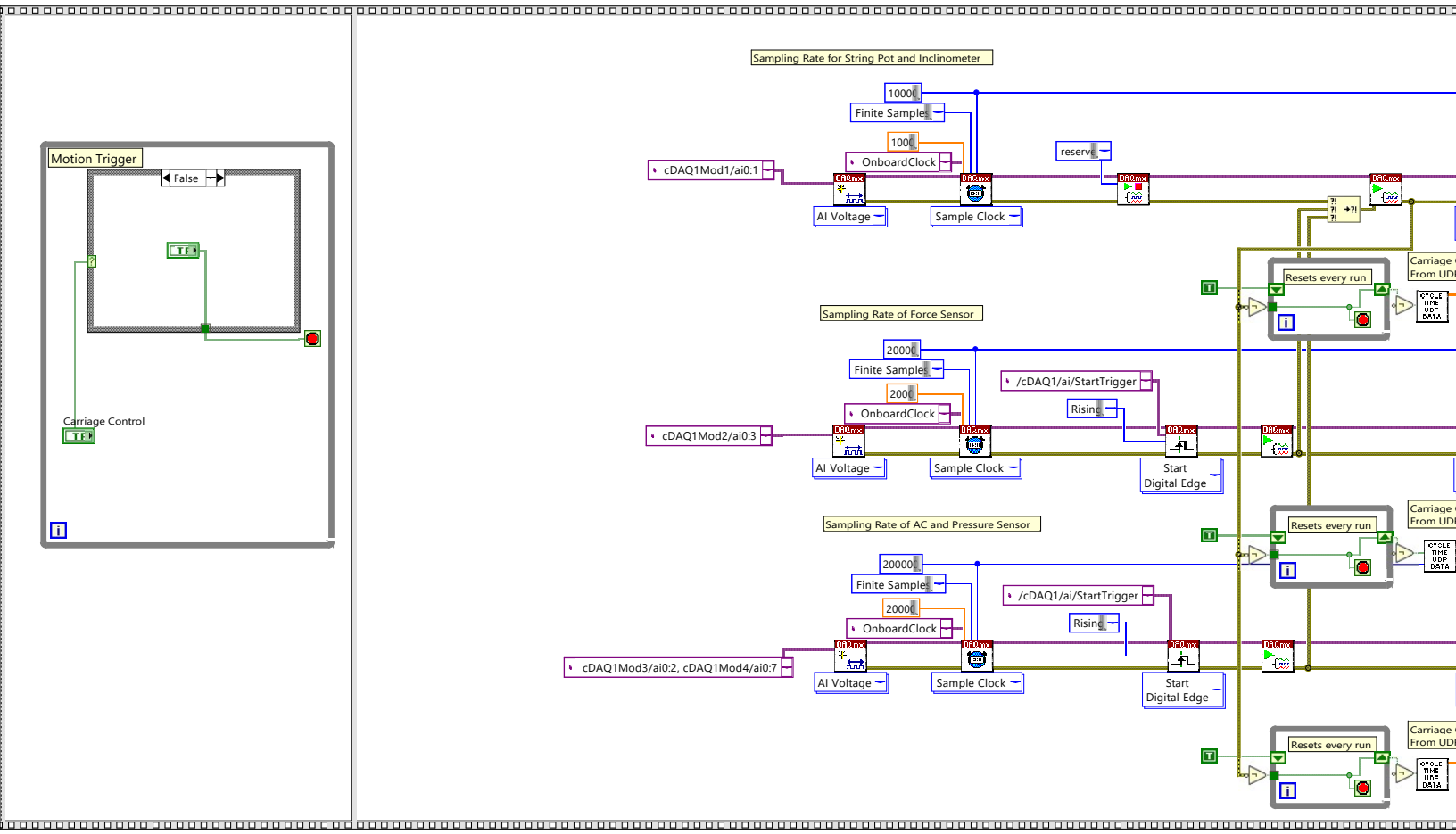

ex_subFileWrite.vi
C:\Program Files (x86)\National Instruments\LabVIEW 2020\vi.lib\express\express output\ExFileWriteBlock.llb\ex_subFileWrite.vi

usiDataType.ctl
C:\Program Files (x86)\National Instruments\LabVIEW 2020\vi.lib\express\express shared\ex_EditUserDefinedProperties\usiDataType.ctl

ex_userDefProperty.ctl
C:\Program Files (x86)\National Instruments\LabVIEW 2020\vi.lib\express\express shared\ExFile.llb\ex_userDefProperty.ctl

ex_propertySource.ctl
C:\Program Files (x86)\National Instruments\LabVIEW 2020\vi.lib\express\express shared\ExFile.llb\ex_propertySource.ctl

DialogType.ctl
C:\Program Files (x86)\National Instruments\LabVIEW 2020\vi.lib\Utility\error.llb\DialogType.ctl

ex_FileFormats.ctl
C:\Program Files (x86)\National Instruments\LabVIEW 2020\vi.lib\express\express shared\ExFile.llb\ex_FileFormats.ctl

Cycle Time test packet dissector.vi
C:\Users\towtankuser\Downloads\EdesignLabVIEW\LabVIEW\Cycle Time test packet dissector.vi

Velocity test packet dissector.vi
C:\Users\towtankuser\Downloads\EdesignLabVIEW\LabVIEW\Velocity test packet dissector.vi

SENSOR DATA

GPPH_Sensor_Data_v4.vi
C:\Users\towtankuser\Desktop\Tow Tank Sensors VI files\GPPH_Sensor_Data_v4.vi
Last modified on 3/18/2024 at 4:00 PM
Printed on 4/4/2024 at 10:35 AM

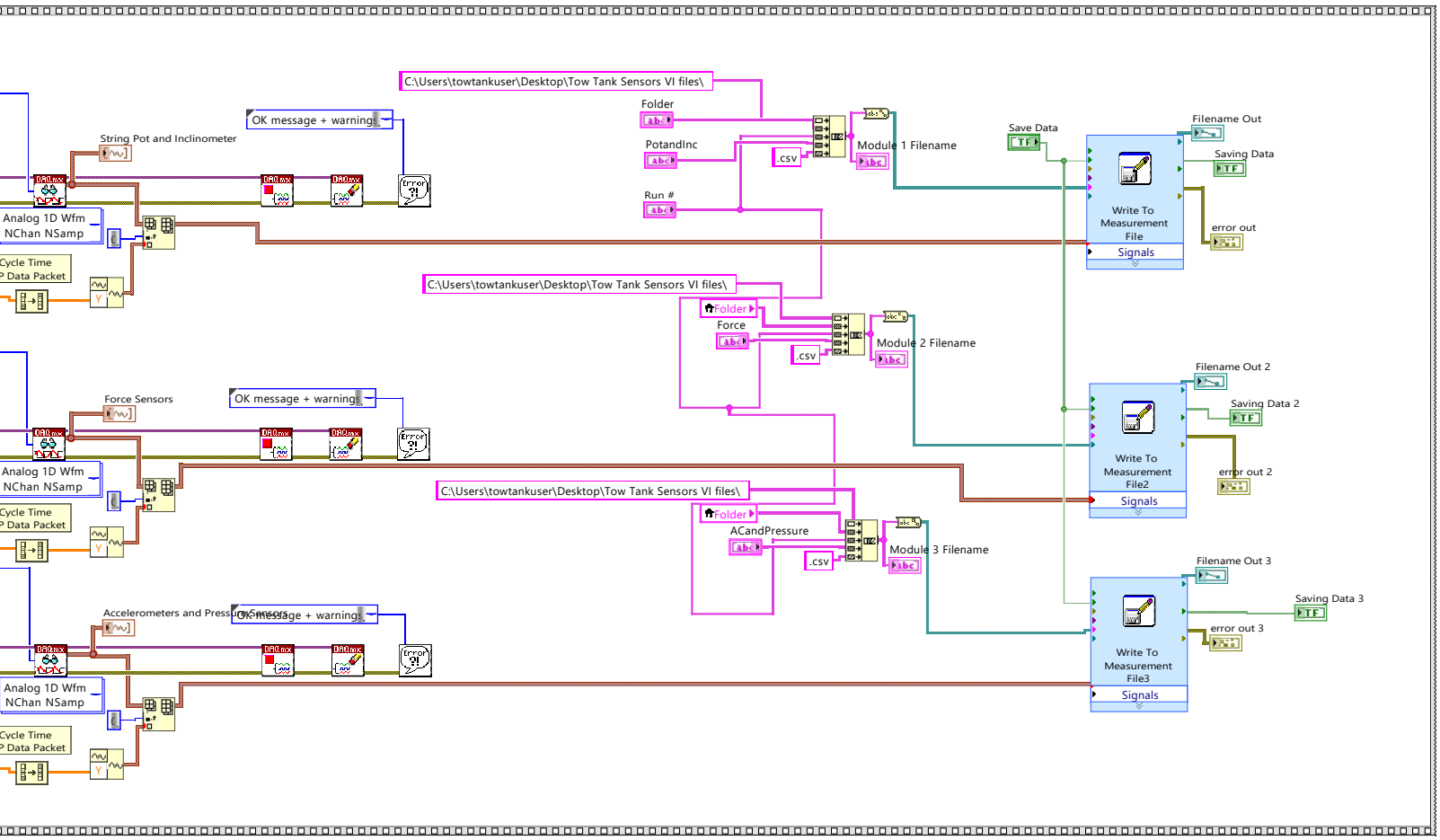

GPPH_Sensor_Data_v4.vi
C:\Users\towtankuser\Desktop\Tow Tank Sensors VI files\GPPH_Sensor_Data_v4.vi
Last modified on 3/18/2024 at 4:00 PM
Printed on 4/4/2024 at 10:35 AM

Simple Error Handler.vi
C:\Program Files (x86)\National Instruments\LabVIEW 2020\vi.lib\Utility\error.llb\Simple Error Handler.vi

DAQmx Timing (Sample Clock).vi
C:\Program Files (x86)\National Instruments\LabVIEW 2020\vi.lib\DAQmx\configure\timing.llb\DAQmx Timing (Sample Clock).vi

DAQmx Start Trigger (Digital Edge).vi
C:\Program Files (x86)\National Instruments\LabVIEW 2020\vi.lib\DAQmx\configure\trigger.llb\DAQmx Start Trigger (Digital Edge).vi

DAQmx Trigger.vi
C:\Program Files (x86)\National Instruments\LabVIEW 2020\vi.lib\DAQmx\configure\trigger.llb\DAQmx Trigger.vi

DAQmx Clear Task.vi
C:\Program Files (x86)\National Instruments\LabVIEW 2020\vi.lib\DAQmx\configure\task.llb\DAQmx Clear Task.vi

DAQmx Fill In Error Info.vi
C:\Program Files (x86)\National Instruments\LabVIEW 2020\vi.lib\DAQmx\miscellaneous.llb\DAQmx Fill In Error Info.vi

DAQmx Control Task.vi
C:\Program Files (x86)\National Instruments\LabVIEW 2020\vi.lib\DAQmx\configure\task.llb\DAQmx Control Task.vi

DAQmx Start Task.vi
C:\Program Files (x86)\National Instruments\LabVIEW 2020\vi.lib\DAQmx\configure\task.llb\DAQmx Start Task.vi

DAQmx Stop Task.vi
C:\Program Files (x86)\National Instruments\LabVIEW 2020\vi.lib\DAQmx\configure\task.llb\DAQmx Stop Task.vi

DAQmx Read.vi
C:\Program Files (x86)\National Instruments\LabVIEW 2020\vi.lib\DAQmx\read.llb\DAQmx Read.vi

DAQmx Read (Analog 1D Wfm NChan NSamp).vi
C:\Program Files (x86)\National Instruments\LabVIEW 2020\vi.lib\DAQmx\read.llb\DAQmx Read (Analog 1D Wfm NChan NSamp).vi

DAQmx Timing.vi
C:\Program Files (x86)\National Instruments\LabVIEW 2020\vi.lib\DAQmx\configure\timing.llb\DAQmx Timing.vi

DAQmx Create Channel (AI-Voltage-Basic).vi
C:\Program Files (x86)\National Instruments\LabVIEW 2020\vi.lib\DAQmx\create\channels.llb\DAQmx Create Channel (AI-Voltage-Basic).vi

DAQmx Create Virtual Channel.vi
C:\Program Files (x86)\National Instruments\LabVIEW 2020\vi.lib\DAQmx\create\channels.llb\DAQmx Create Virtual Channel.vi

SENSOR ZEROS

GPPH_Sensor_ZEROS_v4.vi
C:\Users\towtankuser\Desktop\Tow Tank Sensors VI files\GPPH_Sensor_ZEROS_v4.vi
Last modified on 2/29/2024 at 10:55 AM
Printed on 4/4/2024 at 10:36 AM

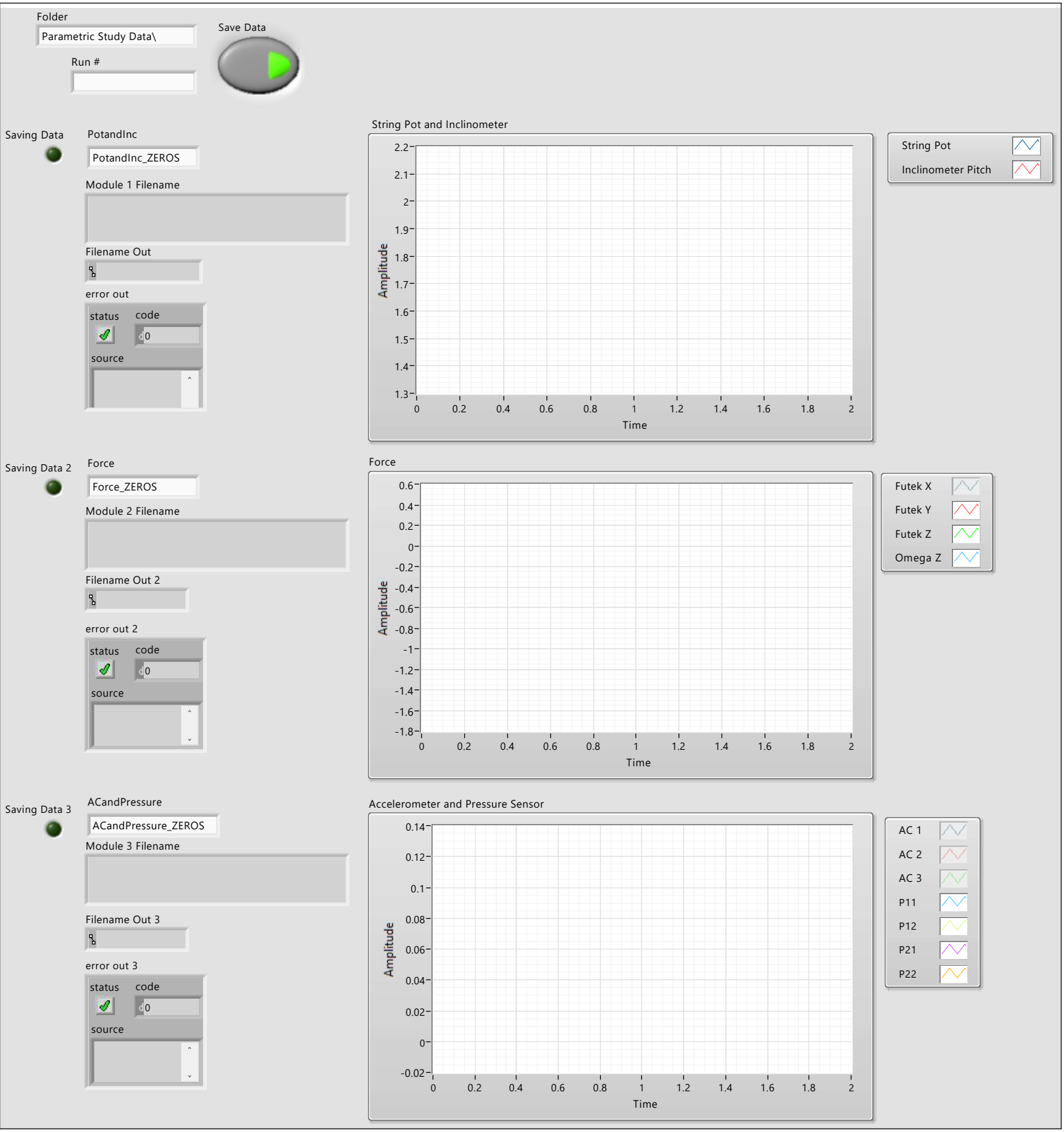

SENSOR ZEROS

GPPH_Sensor_ZEROS_v4.vi
C:\Users\towtankuser\Desktop\Tow Tank Sensors VI files\GPPH_Sensor_ZEROS_v4.vi
Last modified on 2/29/2024 at 10:55 AM
Printed on 4/4/2024 at 10:36 AM

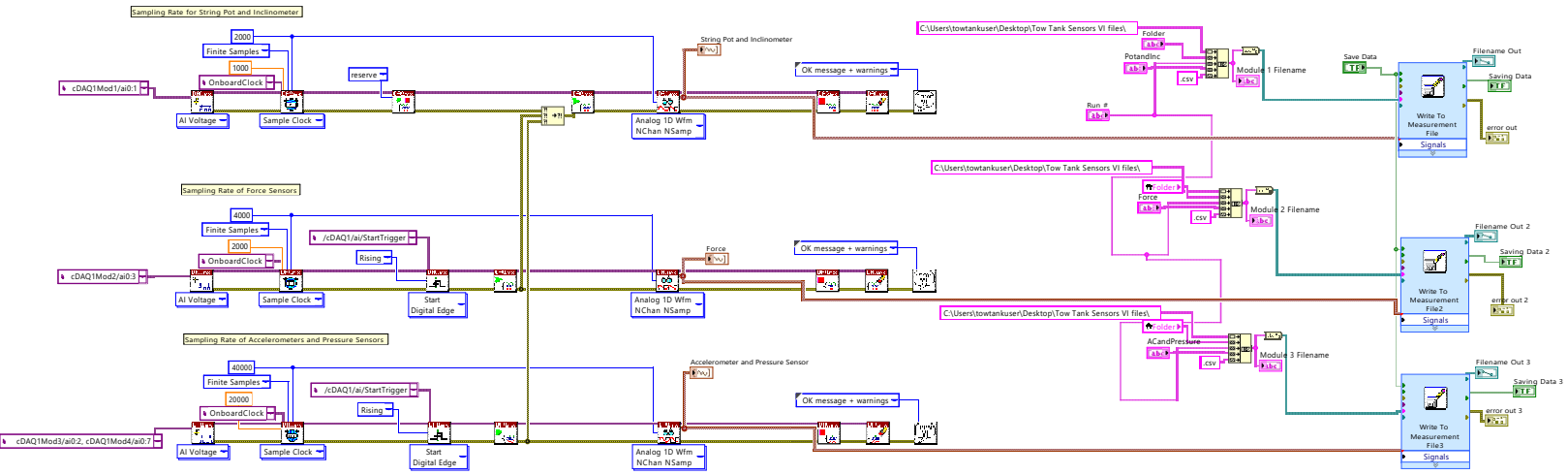

ex_subFileWrite.vi
C:\Program Files (x86)\National Instruments\LabVIEW 2020\vi.lib\express\express output\ExFileWriteBlock.llb\ex_subFileWrite.vi

usiDataType.ctl
C:\Program Files (x86)\National Instruments\LabVIEW 2020\vi.lib\express\express shared\ex_EditUserDefinedProperties\usiDataType.ctl

ex_userDefProperty.ctl
C:\Program Files (x86)\National Instruments\LabVIEW 2020\vi.lib\express\express shared\ExFile.llb\ex_userDefProperty.ctl

ex_propertySource.ctl
C:\Program Files (x86)\National Instruments\LabVIEW 2020\vi.lib\express\express shared\ExFile.llb\ex_propertySource.ctl

DialogType.ctl
C:\Program Files (x86)\National Instruments\LabVIEW 2020\vi.lib\Utility\error.llb\DialogType.ctl

ex_FileFormats.ctl
C:\Program Files (x86)\National Instruments\LabVIEW 2020\vi.lib\express\express shared\ExFile.llb\ex_FileFormats.ctl

Simple Error Handler.vi
C:\Program Files (x86)\National Instruments\LabVIEW 2020\vi.lib\Utility\error.llb\Simple Error Handler.vi

DAQmx Create Channel (AI-Voltage-Basic).vi
C:\Program Files (x86)\National Instruments\LabVIEW 2020\vi.lib\DAQmx\create\channels.llb\DAQmx Create Channel (AI-Voltage-Basic).vi

DAQmx Create Virtual Channel.vi
C:\Program Files (x86)\National Instruments\LabVIEW 2020\vi.lib\DAQmx\create\channels.llb\DAQmx Create Virtual Channel.vi

DAQmx Timing.vi
C:\Program Files (x86)\National Instruments\LabVIEW 2020\vi.lib\DAQmx\configure\timing.llb\DAQmx Timing.vi

DAQmx Clear Task.vi
C:\Program Files (x86)\National Instruments\LabVIEW 2020\vi.lib\DAQmx\configure\task.llb\DAQmx Clear Task.vi

GPPH_Sensor_ZEROS_v4.vi
C:\Users\towtankuser\Desktop\Tow Tank Sensors VI files\GPPH_Sensor_ZEROS_v4.vi
Last modified on 2/29/2024 at 10:55 AM
Printed on 4/4/2024 at 10:36 AM

DAQmx Fill In Error Info.vi
C:\Program Files (x86)\National Instruments\LabVIEW 2020\vi.lib\DAQmx\miscellaneous.llb\DAQmx Fill In Error Info.vi

DAQmx Start Trigger (Digital Edge).vi
C:\Program Files (x86)\National Instruments\LabVIEW 2020\vi.lib\DAQmx\configure\trigger.llb\DAQmx Start Trigger (Digital Edge).vi

DAQmx Start Task.vi
C:\Program Files (x86)\National Instruments\LabVIEW 2020\vi.lib\DAQmx\configure\task.llb\DAQmx Start Task.vi

DAQmx Stop Task.vi
C:\Program Files (x86)\National Instruments\LabVIEW 2020\vi.lib\DAQmx\configure\task.llb\DAQmx Stop Task.vi

DAQmx Trigger.vi
C:\Program Files (x86)\National Instruments\LabVIEW 2020\vi.lib\DAQmx\configure\trigger.llb\DAQmx Trigger.vi

DAQmx Control Task.vi
C:\Program Files (x86)\National Instruments\LabVIEW 2020\vi.lib\DAQmx\configure\task.llb\DAQmx Control Task.vi

DAQmx Timing (Sample Clock).vi
C:\Program Files (x86)\National Instruments\LabVIEW 2020\vi.lib\DAQmx\configure\timing.llb\DAQmx Timing (Sample Clock).vi

DAQmx Read.vi
C:\Program Files (x86)\National Instruments\LabVIEW 2020\vi.lib\DAQmx\read.llb\DAQmx Read.vi

DAQmx Read (Analog 1D Wfm NChan NSamp).vi
C:\Program Files (x86)\National Instruments\LabVIEW 2020\vi.lib\DAQmx\read.llb\DAQmx Read (Analog 1D Wfm NChan NSamp).vi

FPGA MASTER v3.vi
C:\Users\towtankuser\Documents\LabVIEWMC\examples\CompactRIO\FPGA Fundamentals\FPGA Math and Analysis\Floating-point PID\Multi-Rate PID\FPGA MASTER v3.vi
Last modified on 4/4/2024 at 10:33 AM
Printed on 4/4/2024 at 10:33 AM

POSITION SYSTEM 0

Pos Plant Sample Rate (Hz): 0
Max config pos 0: 1.33
Pos Plant Offset 0: 0
PID Static Gain 1: 0
Pos PV 0 (Unfiltered): 0
Pos PV 0 (Filtered): 0.00
Pos TPI: 0
FIR reinitialize? (F)

Velocity Sytem 0

Vel Plant Sample Rate (Hz): 0
Vel PID Rate (Hz): 0
Vel Plant Offset 0: 0
Vel Setpoint 0: 0
Expected Vel 0: 0
Max Config Vel 0: 1.33
PID Static Gain 0: 0
Vel Gains 0
- proportional gain: 0
- integral gain: 0
- derivative gain: 0
- filter coefficient: 0

Vel Output Range 0
- output high (Inf): 1.3
- output low (-Inf): -1.3

Vel PV 0 (Unfiltered): 0
Vel PV 0 (Filtered): 0.00
Vel PID TPI: 0
Vel PID output 0: 0
Vel Error 0: 0
Vel Plant TPI: 0
Vel 0 reset?
Disable Drive 0

POSITION SYSTEM 1

Pos Plant Offset 1: 0
Max config pos 1: 1.33
Pos PV 1 (Filtered): 0.00
Pos PV 1 (Unfiltered): 0

Velocity System 1

Vel Plant Offset 1: 0
Vel Setpoint 1: 0
Expected Vel 1: 0
Max Config Vel 1: 1.33
Vel Gains 1
- proportional gain: 0
- integral gain: 0
- derivative gain: 0
- filter coefficient: 0

Vel Output Range 1
- output high (Inf): 1.3
- output low (-Inf): -1.3

Vel PV 1 (Unfiltered): 0
Vel PV 1 (Filtered): 0.00
Vel PID output 1: 0
Vel Error 1: 0
Disable Drive 1
Vel 1 reset?

FPGA MASTER v3.vi
C:\Users\towtankuser\Documents\LabVIEWMC\examples\CompactRIO\FPGA Fundamentals\FPGA Math and Analysis\Floating-point PID\Multi-Rate PID\FPGA MASTER v3.vi
Last modified on 4/4/2024 at 10:33 AM
Printed on 4/4/2024 at 10:33 AM

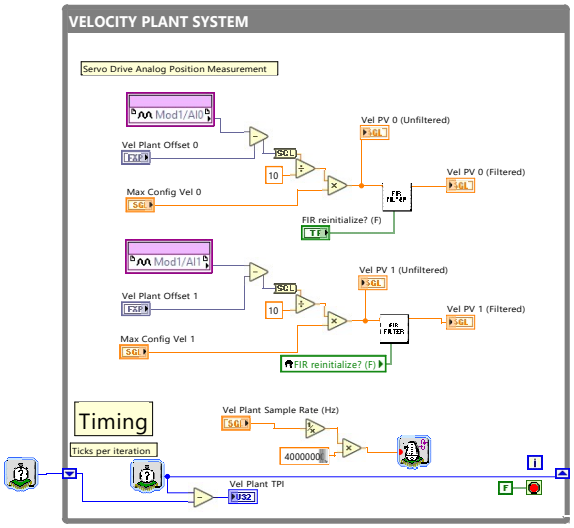

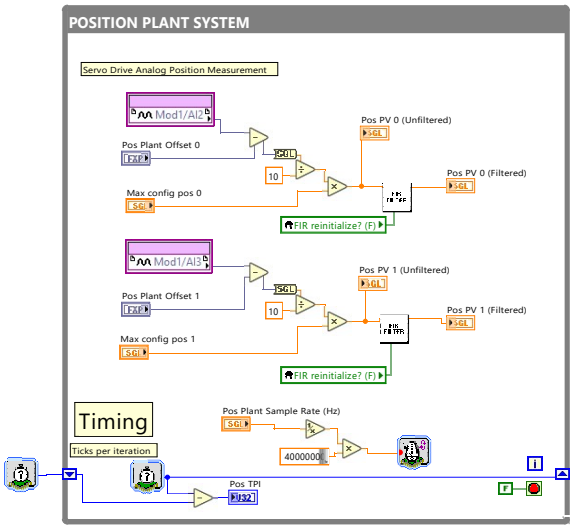

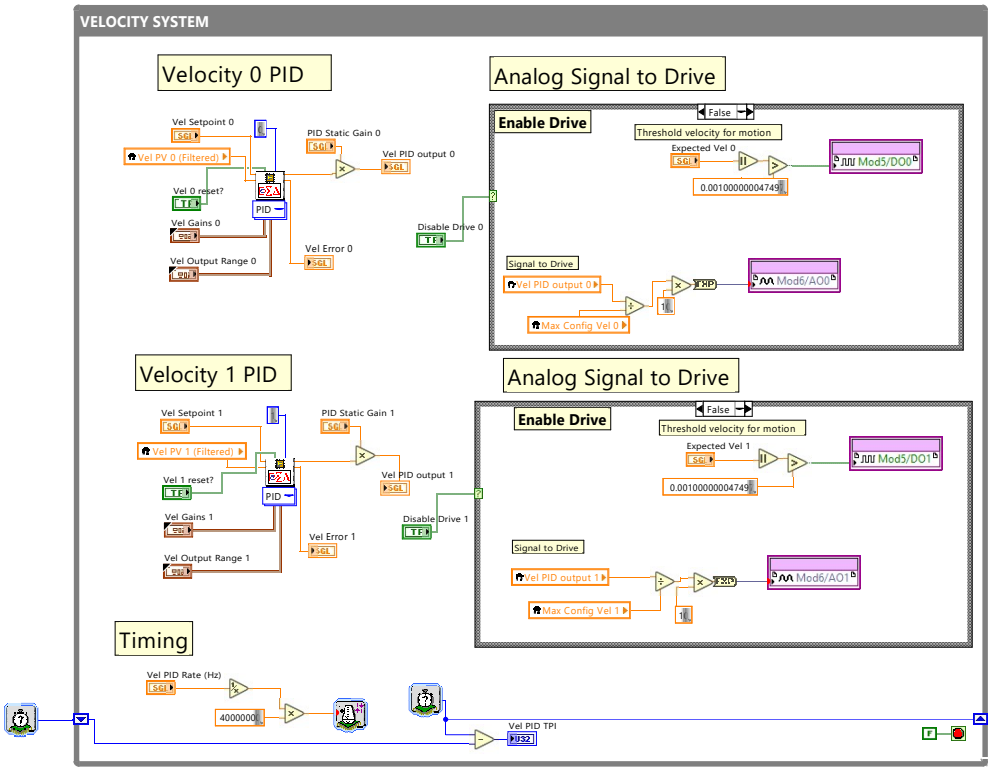

FPGA MASTER v3.vi
C:\Users\towtankuser\Documents\LabVIEWMC\examples\CompactRIO\FPGA Fundamentals\FPGA Math and Analysis\Floating-point PID\Multi-Rate PID\FPGA MASTER v3.vi
Last modified on 4/4/2024 at 10:33 AM
Printed on 4/4/2024 at 10:33 AM

FIR Filter.vi
C:\Users\towtankuser\Documents\LabVIEWMC\examples\CompactRIO\FPGA Fundamentals\FPGA Math and Analysis\Floating-point PID\Multi-Rate PID\FIR Filter.vi

FIR Filter.vi
C:\Users\towtankuser\Documents\LabVIEWMC\examples\CompactRIO\FPGA Fundamentals\FPGA Math and Analysis\Floating-point PID\Multi-Rate PID\FIR Filter.vi
Last modified on 4/3/2024 at 5:53 PM
Printed on 4/4/2024 at 10:32 AM

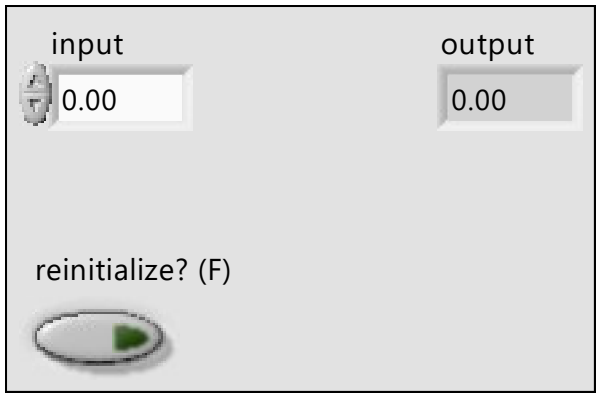

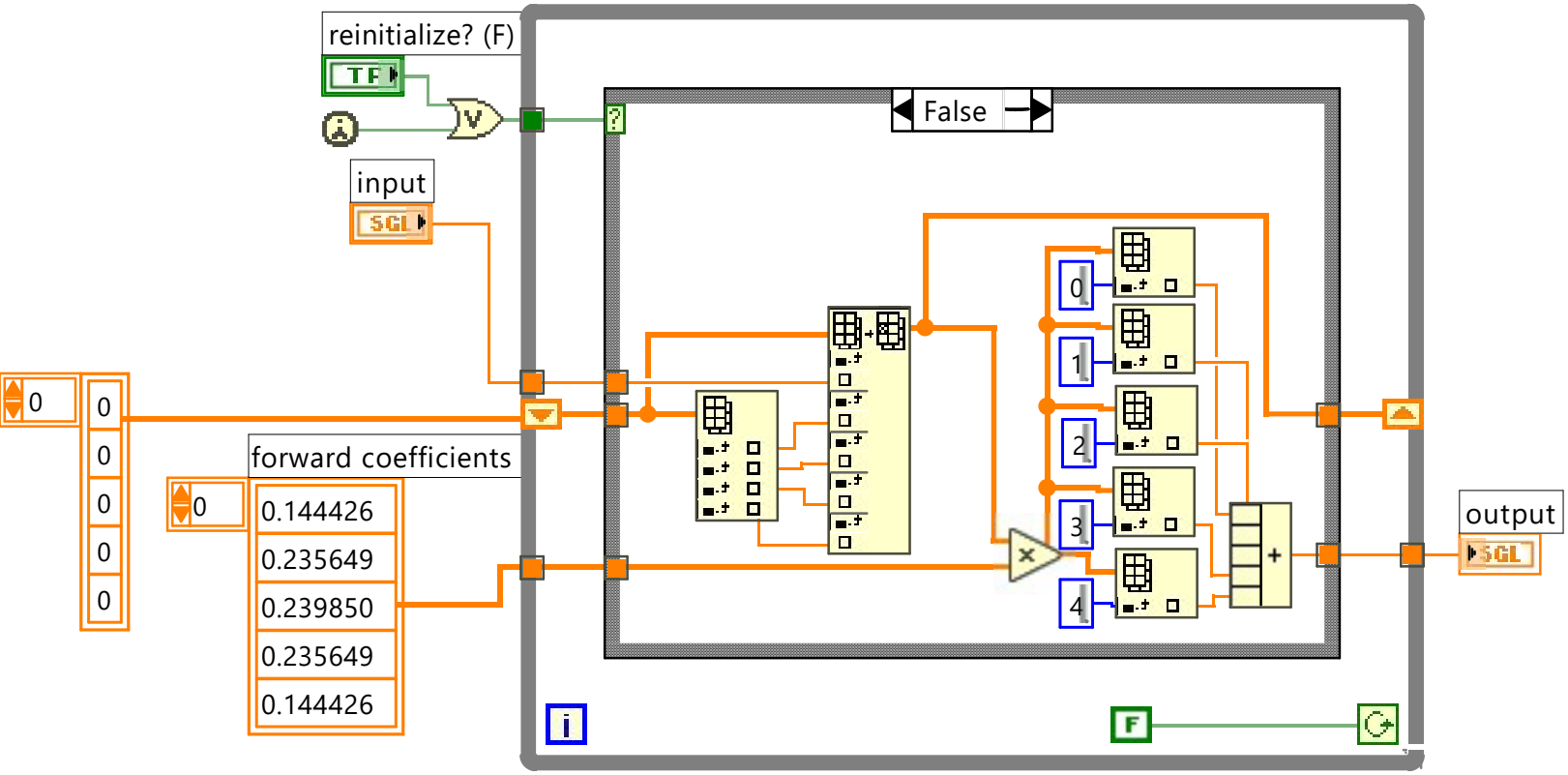

HomingJogging_v2.vi
C:\Users\towtankuser\Documents\LabVIEWMC\examples\CompactRIO\FPGA Fundamentals\FPGA Math and Analysis\Floating-point PID\Multi-Rate PID\HomingJogging_v2.vi
Last modified on 11/2/2023 at 2:46 PM
Printed on 4/3/2024 at 6:13 PM

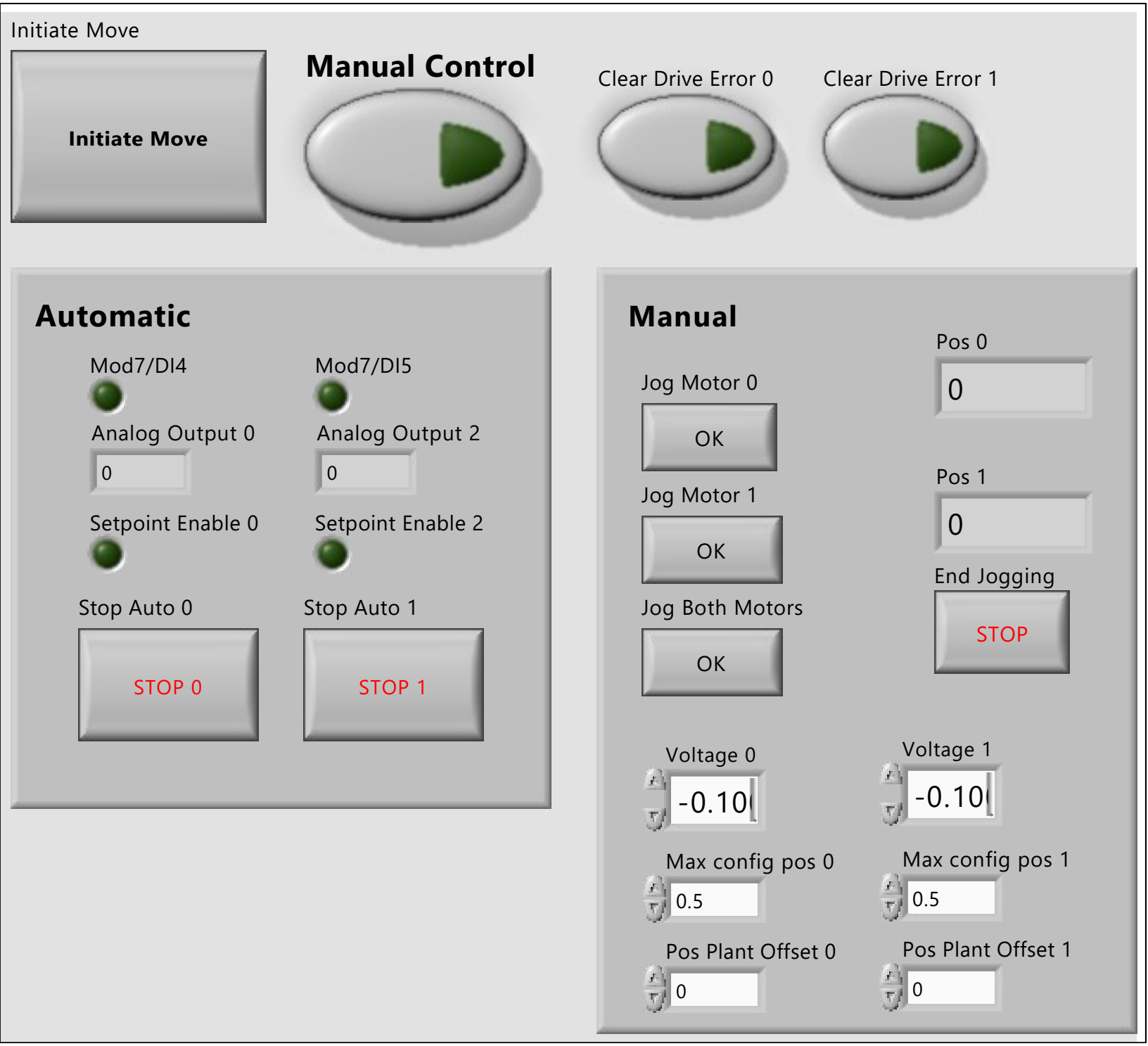

HomingJogging_v2.vi
C:\Users\towtankuser\Documents\LabVIEWMC\examples\CompactRIO\FPGA Fundamentals\FPGA Math and Analysis\Floating-point PID\Multi-Rate PID\HomingJogging_v2.vi
Last modified on 11/2/2023 at 2:46 PM
Printed on 4/4/2024 at 11:57 AM

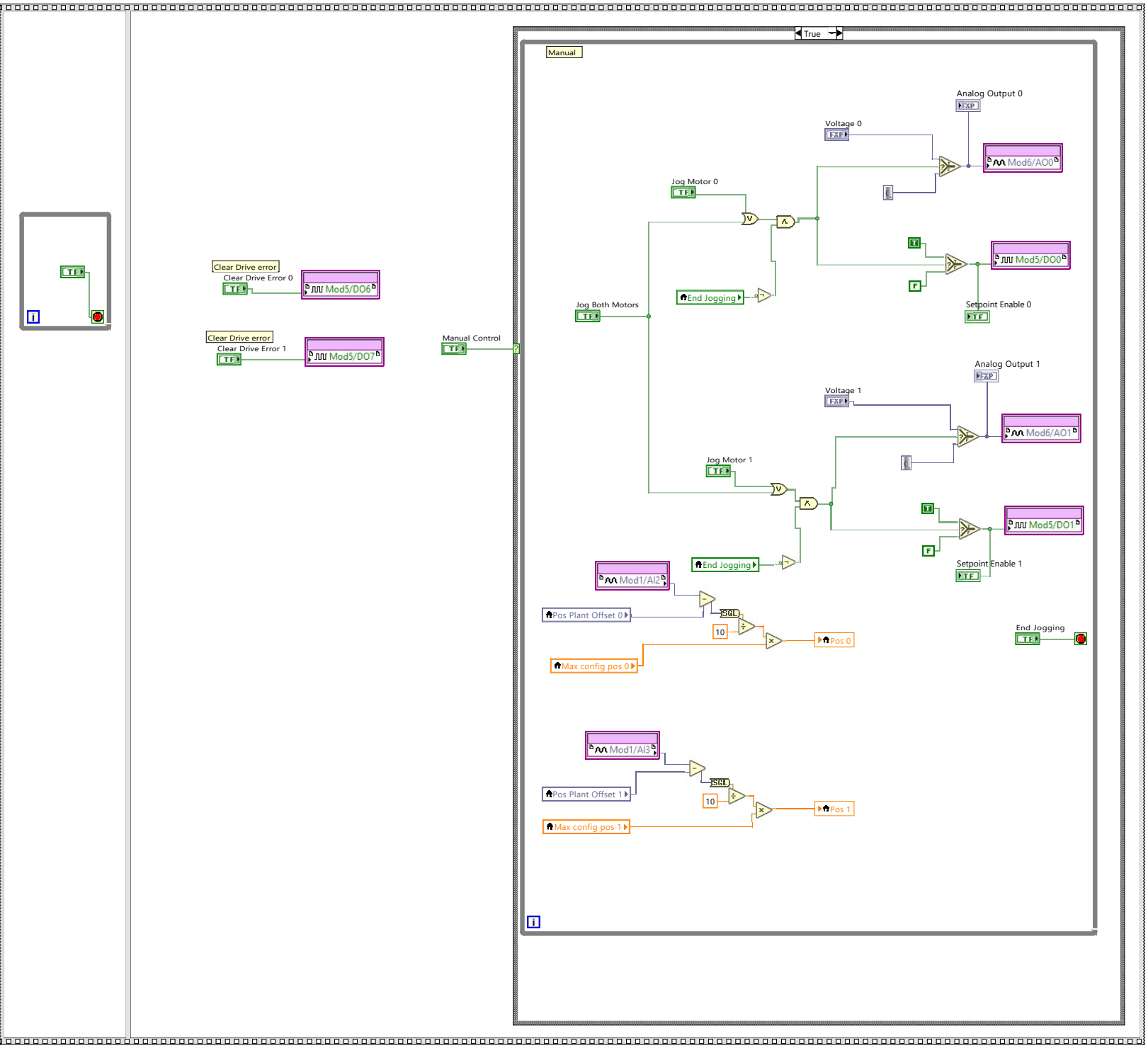

Analog Offset FPGA.vi
C:\Users\towtankuser\Documents\LabVIEWMC\examples\CompactRIO\FPGA Fundamentals\FPGA Math and Analysis\Floating-point PID\Multi-Rate PID\Analog Offset FPGA.vi
Last modified on 10/17/2023 at 5:30 PM
Printed on 4/4/2024 at 10:51 AM

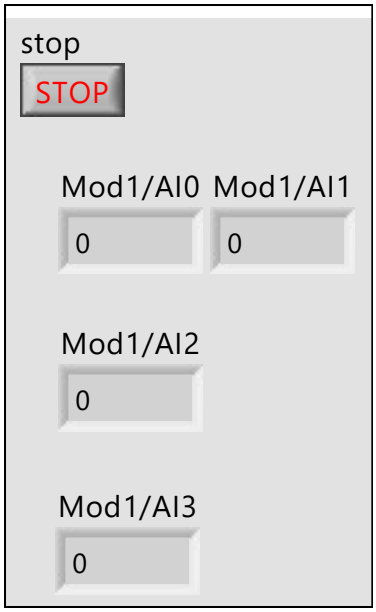

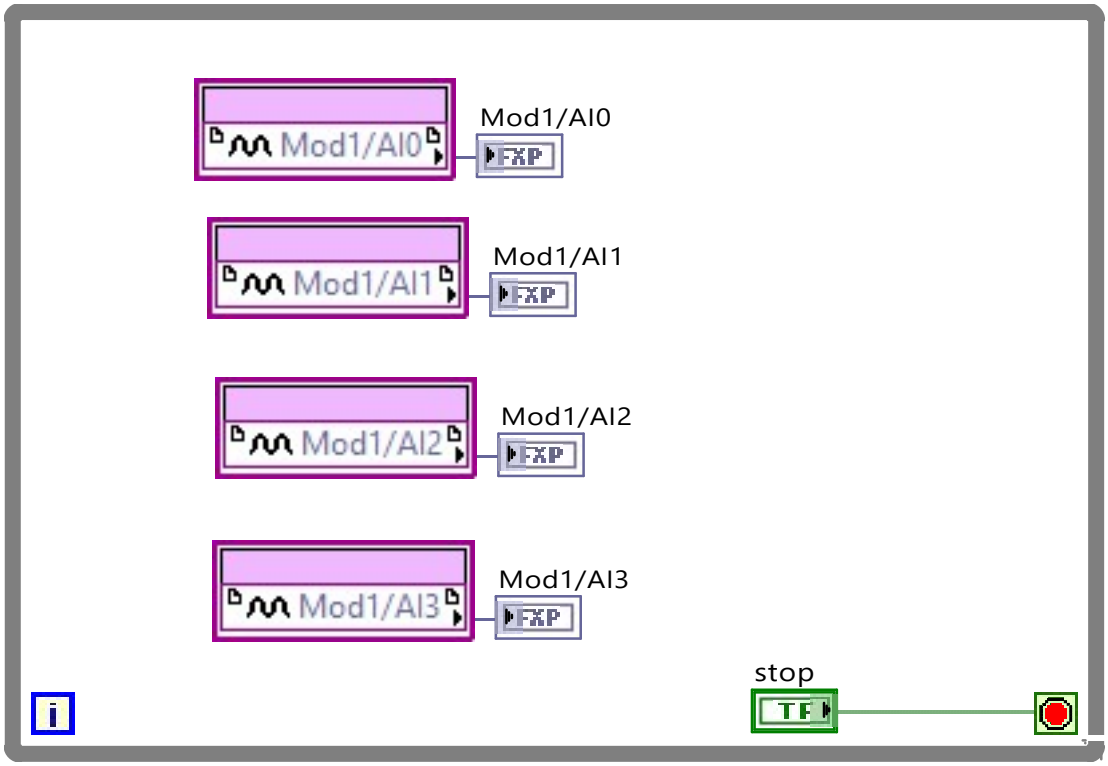

Appendix C

Relative Dynamic Model MATLAB Codes

```
clear; close all; clc;
%% Variables
% Inputs: Full Scale heading velocity, point of wave to impact, wave parameters, model↙
hull geometry points
% Outputs: Motion parameters for actuators and carriage
%% Event Parameters
runnumber = 97;

%Find slam from camera and DAQ data
if runnumber == 81
    camtime = [1.522, 1.737];
    lambdaratio = 1.55;
    carriagesurge= 6.39; % m/s (20.95 ft/s)
    initialangle = 4.8968; %deg, positive is bow up in this model
    initialsinkage = 0.0582; % m, at impact from initial draft
    %maxsinkage = 0.061; % m
elseif runnumber == 90
    camtime = [2.144, 2.385];
    lambdaratio = 1.55;
    carriagesurge= 6.39; % m/s (20.95 ft/s)
    initialangle = 4.4391; %deg, positive is bow up in this model
    initialsinkage = 0.0391; % m, at impact from initial draft
    %maxsinkage = 0.055; % m
elseif runnumber == 92
    camtime = [1.725, 1.946];
    lambdaratio = 1.55;
    carriagesurge= 6.39; % m/s (20.95 ft/s)
    initialangle = 3.6562; %deg, positive is bow up in this model
    initialsinkage = 0.0425; % m, at impact from initial draft
    %maxsinkage = 0.056; % m
elseif runnumber == 97
    %camtime = [2.61, 3];
    camtime = [2.264, 2.564];
    lambdaratio = 3.7;
    carriagesurge= 6.39; % m/s (20.95 ft/s)
    initialangle = 7.3192; %deg, positive is bow up in this model
    initialsinkage = 0.0496; % m, at impact from initial draft
    %maxsinkage = 0.11; % m
end

startslam= camtime(1); % sec
startnextslam = camtime(2); % sec


% image offset
xoffset = -1; %shift gpph image in x-direction
zoffset = initialsinkage; %-0.0508; %shift gpph image in z-direction
CWSshift = -0.01; %calm water surface tangent line vertical shift

%% GPPH Model Estimation
```

```
LOAf = 13; %m
LOAm = 48 / 39.37; %m
DeckHeightm = 7.875 / 39.37; %m
g = 9.81;

Fn = carriagesurge / (sqrt(LOAm * g));
FullScaleHeadingVelocity = Fn .* sqrt(g * LOAf) * 1.944; %kts
modelheadingvel = carriagesurge;
scalefactor = 1 / 10.6557;
% modelheadingvel = FullScaleHeadingVelocity .* sqrt(scalefactor) ./ 1.944; %m/s,↙
froude similitude

% Coords
M = readmatrix('KeelPoints.txt');
M = M';
[m, n] = size(M);

xcoords = M(1, :) ./ 39.37;
zcoords = M(3, :) ./ 39.37;
xcoords(n) = xcoords(2);
zcoords(n) = zcoords(2);
% Test coords
% xcoords = [LOA,          0,        0.05 * LOA,      0.2 * LOA, LOA, LOA ];
% zcoords = [DeckHeight, DeckHeight, .9 * DeckHeight, 0,         0, DeckHeight];

%offset image
Xcoords = xcoords + xoffset;
Zcoords = zcoords + zoffset;

GPPH = [Xcoords; Zcoords];

GPPH_center = [0.412 * LOAm , 0.709 * DeckHeightm]; % should be LCG and KG
center_original = repmat([GPPH_center(1); GPPH_center(2)], 1, length(GPPH(1)));

% Rotation
R = [cosd(initialangle), -sind(initialangle); sind(initialangle), cosd(initialangle)];↙
%rotation matrix
s = GPPH - center_original;     % shift points in the plane so that the center of↙
rotation is at the origin
so = R*s;              % apply the rotation about the origin
GPPH_initial = so + center_original;   % shift again so the origin goes back to the↙
desired center of rotation

%% Insert a wave train for specific USNA data
% load data
DAQ1=strcat('DAQ1_dataData',num2str(runnumber(1)-1),'.mat');
DAQ2=strcat('DAQ2_dataDAQ2_run',num2str(runnumber(1)-1),'.mat');
DAQ3=strcat('DAQ3_data',num2str(runnumber(1)-1),'.mat');
load ('RunCSVdata.csv')     % Run matrix file and corresponding details
load(DAQ1)
```

```
load(DAQ2)

% sync daq1 and daq2
[~,idxPeak1] = findpeaks(dataEng1(:,2),'minpeakheight',3,'minpeakdistance',↙
SampleRate1);
timshift1=time1(idxPeak1);

[~,idxPeak2] = findpeaks(dataEng2(:,1),'minpeakheight',3,'minpeakdistance',↙
SampleRate2);
timshift2=time2(idxPeak2);

[a1 bound21]=min(abs(time2-startslam+0.3));
[a2 bound22]=min(abs(time2-startslam-0.3));
% [idx2]=find(time2==sp-0.3)
[a3 idx]=max(dataEng2(bound21:bound22,4));
peak2time=time2(bound21+idx);
timeshift=peak2time-startslam;

 [~,idxPeak1] = findpeaks(dataEng1(:,2),'minpeakheight',3,'minpeakdistance',↙
SampleRate1);
 timeshift1=time1(idxPeak1);

 [~,idxPeak2] = findpeaks(dataEng2(:,1),'minpeakheight',3,'minpeakdistance',↙
SampleRate2);
 timeshift2=time2(idxPeak2);

 time1=time1-timeshift1;

startslam_cam = startslam - timeshift;
endslam_cam = startnextslam - timeshift;
windowstart = timshift1 + startslam_cam;
windowend = windowstart + (endslam_cam - startslam_cam);
%% Identifying Reference Wave
%Find index for the wave slam position
startslampos_index = find(time1>windowstart, 1);
endslampos_index = find(time1>windowend, 1);

% Find midpoints of steps
noisetol = 0.0005;
particular_wave = dataEng1(startslampos_index:endslampos_index, 5) ./ 39.37;
particular_time = time1(startslampos_index:endslampos_index);
midpoints = find(abs(diff(particular_wave)) > noisetol);
p = polyfit(particular_time, particular_wave, 4);
waveapprox = polyval(p, particular_time);

% % Fourier Transform to identify dominant frequencies and amplitudes
% Fs = 1 / (particular_time(2) - particular_time(1));  % Sampling frequency
% N = length(particular_wave);
% frequencies = Fs * (0:(N/2)) / N;
% wave_spectrum = abs(fft(particular_wave)) / N;
```

```
% dominant_frequencies = frequencies(1:4);%frequencies(wave_spectrum(1:N/2+1) == max↙
(wave_spectrum(1:N/2+1)));
%
% % Calculate corresponding wavelengths using the dispersion relationship
% wavelength = 2 * pi * sqrt(g ./ (2 .* pi .* dominant_frequencies));
% wavelength = 3.5;

% Wave length derived from parameters taken from Judge2020b
wavelength = LOAm * lambdaratio;
% particular_wavelength = linspace(-max(wavelength), max(wavelength), length↙
(particular_wave));
particular_wavelength = linspace(0, max(wavelength), length(particular_wave));

% Adding in Wave Celerity
celerity = sqrt((g * wavelength) / (2*pi))
modelheadingvel_relative = modelheadingvel + celerity;

eta = waveapprox;
xr = particular_wavelength';
% impactpos_index = round(length(particular_wavelength) / 2);
impactpos_index = 1;

%% Wave Reference Frame
% Center of Rotation
wave_center = [xr(impactpos_index); eta(impactpos_index)];
center = repmat([wave_center(1); wave_center(2)], 1, length(GPPH(1)));

% Angle of Impact
impactangle = -atand((eta(impactpos_index + 1) - eta(impactpos_index)) / (xr↙
(impactpos_index + 1) - xr(impactpos_index)));
impactangle = impactangle - initialangle % correction for initial trim, should double↙
check validity

% Rotation
R = [cosd(impactangle), -sind(impactangle); sind(impactangle), cosd(impactangle)]; %↙
rotation matrix
s = GPPH_initial - center;     % shift points in the plane so that the center of↙
rotation is at the origin
so = R*s;              % apply the rotation about the origin
GPPH_transformed = so + center;   % shift again so the origin goes back to the desired↙
center of rotation
TransformedVelocity = R .* modelheadingvel_relative;
TransformedSurge = abs(TransformedVelocity(1,1))
TransformedHeave = abs(TransformedVelocity(2,1))

% Calm Water Surface Representation
% Calculate the line passing through the point of rotation
CWSslope = -tand(impactangle); % Slope of the line
CWSintercept = wave_center(2) - CWSslope * wave_center(1); % Intercept of the line
```

```
% Calculate the x-values for the line extending beyond the current x-limits
xlimit = get(gca,'XLim');
extended_x = [-2 2]; % Extend the line beyond the current x-limits
extended_y = CWSslope * extended_x + CWSintercept;

% Calculate the y-values for the line based on the x-limits
% xlimit = get(gca,'XLim');
% y1 = CWSslope * xlimit(1) + CWSintercept;
% y2 = CWSslope * xlimit(2) + CWSintercept;

% xlimit = get(gca,'XLim');
% m = (eta(impactpos_index + 1) - eta(impactpos_index)) / (xr(impactpos_index + 1) - xr↙
(impactpos_index));
% b = eta(impactpos_index + 1) * m - xr(impactpos_index + 1) + CWSshift;
% y1 = m*xlimit(1) + b;
% y2 = m*xlimit(2) + b;

% Graph larger wave
mirroredwavelength = -xr(end:-1:1);
mirroredwaveheight = eta(end:-1:1);
multiplewavelengths = [mirroredwavelength; xr];
multiplewaveheights = [mirroredwaveheight; eta];

%% Plot
font = 20;
paperpos = [0 0 3 2.62];
papersize = [3 2.62];

figure(1)
hold on
wave = plot(multiplewavelengths, multiplewaveheights, '--b', 'LineWidth', 1);
OriginalHull = plot(GPPH_initial(1,:), GPPH_initial(2,:), '--k');
WFRHull = plot(GPPH_transformed(1,:), GPPH_transformed(2,:), 'Color', [0.9, 0.5, 0],↙
'LineWidth', 2); %wave reference frame
PointofRotation = plot(wave_center(1), wave_center(2), 'o', 'Color', [0.5, 0, 0],↙
'MarkerFaceColor', [0.5, 0, 0], 'LineWidth', 3);
% CalmWaterSurface = line([xlimit(1) xlimit(2)],[y1 y2]);
CalmWaterSurface = plot(extended_x, extended_y, 'Color', [0.5, 0, 0], 'LineWidth', 2);
axis equal
xlabel('X position [m]')
ylabel('Wave Amplitude [m]')
title('Wave Impact Model')
legend('Original Wave', 'Orginal Hull', 'Translated Hull', 'Impact Point', 'Calm↙
Water')
xlim([-1.5 1.5])
ylim([-0.2 0.5])
set(gca,'FontSize',font);
hold off

figure(1)
```

```
set(gcf,'PaperPosition',[0.36 0.42 7.78 10.15]);
print(strcat('DynamicModelVisual.pdf'),'-dpdf')
savefig(strcat('DynamicModelVisual'))
```

Appendix D

GPPH Modification for Mounting

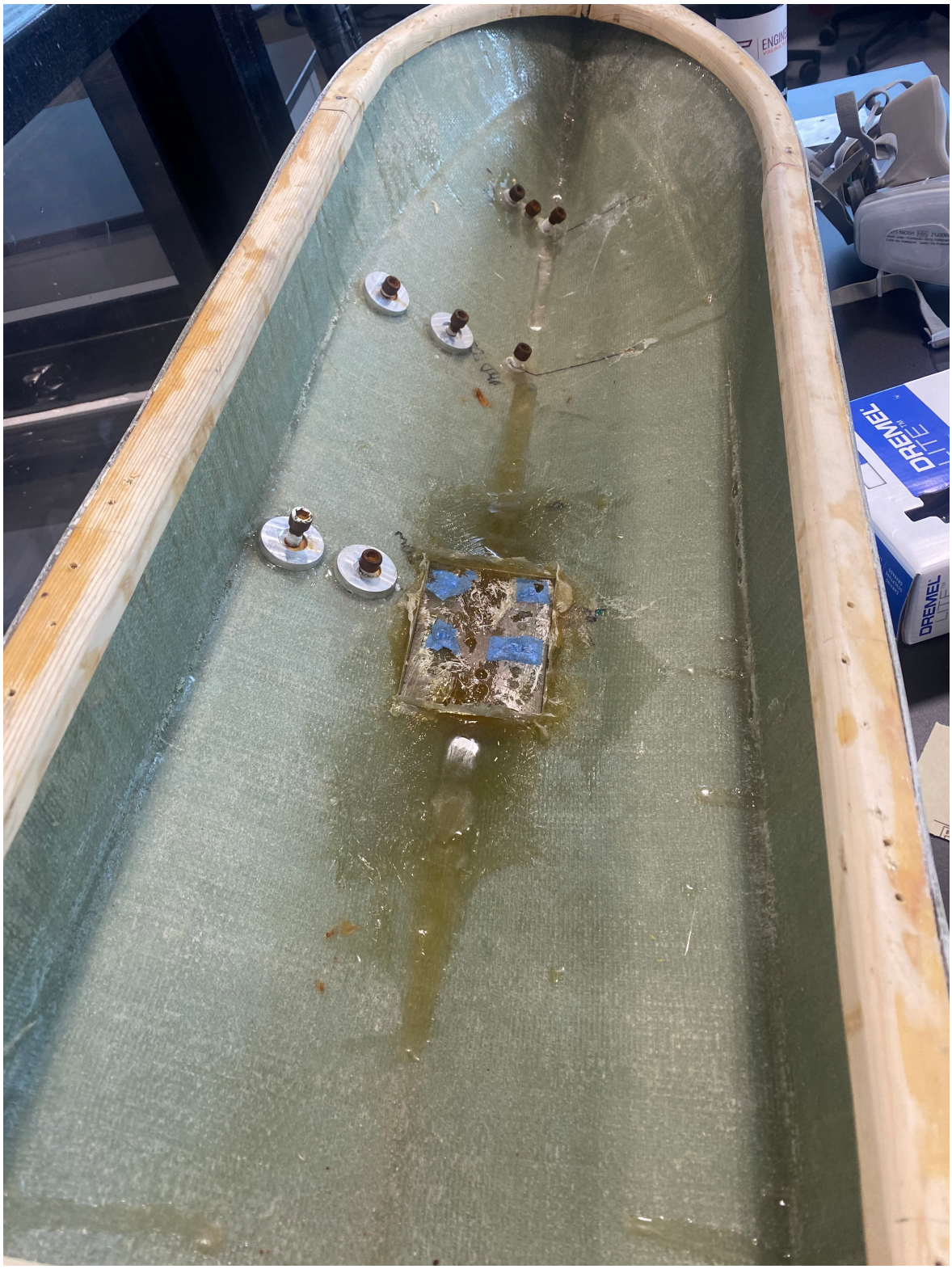
DREMEL
DREMEL